Two-dimensional nanomaterials as photocatalysts for solar-driven production of chemicals

Bingquan Xia

School of Chemical Engineering and Advanced Materials

Faculty of Sciences, Engineering and Technology

A thesis submitted for the degree of Doctor of Philosophy

The University of Adelaide

March 2022

Contents

Abstract

The utilisation of renewable solar energy shows great potential in tackling the problem of increasing carbon emission due to the combustion of traditional fossil fuels. To achieve carbon neutrality, more efforts need to be made on the exploration of efficient conversion of solar energy into chemical fuels/feedstocks. Particularly, chemical fuels with high energy density are ideal for storage and transportation. For the efficient transformation of solar energy into chemical fuels, high-performance photocatalysts are required to facilitate this process. Therefore, this thesis aims to find out a universal strategy for designing and fabricating novel nanomaterials as efficient photocatalysts for photocatalytic reactions. Besides, photocatalysts for emerging reactions fabricated via advanced delicate techniques and demonstrated for widespread applications are also reviewed and discussed comprehensively.

Thanks to the ultrathin layered structure and exposed uncoordinated atoms, the exposed edges of 2D nanomaterials have shown great potential in acting as reactive sites for various photocatalytic reactions. In this thesis, two-dimensional Co-MOF, Ni-MOF and FePS$_3$ (discussed in chapters 3-5) have been introduced to cooperate with the main photocatalysts for hydrogen evolution and it turns out that they have significantly improved the initial catalytic performances of the counterparts without them. These two-dimensional nanomaterials play key roles in improving the photocatalytic activity of the main photocatalyst by providing sufficient reactive sites and facilitating charge separation/transfer.

Also, the recent research progress of solar-driven simultaneous production of hydrogen and value-added chemicals (chapter 2), and the single-atom-based photocatalysts for emerging reactions (chapter 6) have been reviewed and discussed in

this thesis. The combination of searching for high-performance photocatalysts and adapting for emerging reactions will promote the transformation and utilisation of solar energy.

Probing into the origin of the structure-performance relationship and finding out a universal strategy for designing and screening outstanding high-performance photocatalysts for various reactions is of great importance for research on solar energy transformation. Meanwhile, finding approaches to improving solar-driven reaction efficiency will be of great benefit to the development of the solar energy industry as well.

Declaration

I certify that this work contains no material which has been accepted for the award of any other degree or diploma in my name, in any university or other tertiary institution and, to the best of my knowledge and belief, contains no material previously published or written by another person, except where due reference has been made in the text. In addition, I certify that no part of this work will, in the future, be used in a submission in my name, for any other degree or diploma in any university or other tertiary institution without the prior approval of the University of Adelaide and where applicable, any partner institution responsible for the joint-award of this degree.

I acknowledge that copyright of published works contained within this thesis resides with the copyright holder(s) of those works.

I also give permission for the digital version of my thesis to be made available on the web, via the University's digital research repository, the Library Search and also through web search engines, unless permission has been granted by the University to restrict access for a period of time.

Name of Candidate: Bingquan Xia

Signature:

Date: 31/03/2022

Acknowledgements

Chapter 1: Introduction

1.1 Significance of the Project

In recent decades, industrial development and population explosion have boosted the global energy demand. This demand is heavily dependent on fossil fuels, including oil, natural gas, and coal, which make up about 87% of global energy consumption.[1] Due to the large consumption of fossil fuels, their drawbacks should not be neglected. Considering the growing demand and supply, fossil fuels are non-renewable as the formation will take hundreds of years and would be depleted in the future. It has caused some obvious and hidden environmental problems. Also, carbon dioxide is released during the combustion of fossil fuel, which adds to the greenhouse effect and increases global warming. Besides, the burning of coal and oil could release sulfur dioxide, which may cause breathing problems for living creatures and contributes to acid rain. To address the shortage of fossil fuels and tackle relevant environmental issues, considerable exploration of pollution-free technologies and alternative clean energy sources have been made in recent decades. Renewable technologies provide many more advantages, such as reliability, lower costs, and smaller environmental impact. [2,3]

Compared with conventional fossil energy sources, solar energy is free, non-polluting, abundant and renewable. However, solar energy suffers from daily and seasonal variability, and it is difficult to be stored and utilized directly.[4-6] Therefore, it is of great significance to explore how to utilize solar energy efficiently. One promising way is to convert this solar energy to chemical fuels with high energy densities, because of their transportability and storability. Impacted by the greenhouse effects and drastic climate changes caused by carbon emissions, countries over the world have achieved agreements

on reducing carbon emissions. Thus, the conversion of solar energy into low-carbon and/or carbon-free chemical fuels is gaining increasingly intensive research attention.[7,8]

However, the direct solar-driven conversion is usually hindered by low efficiency and poor selectivity toward target products. To facilitate the process of transforming solar energy and storing it in the form of low-carbon and/or carbon-free chemical fuel, photocatalysts are required to enhance the conversion efficiency, including enhancing the light absorption, improving charge carrier separation, and promoting the photocatalytic reactions.[9,10] Also, the affordability of the photocatalysts and their stability under light illumination, need to be taken into consideration.

1.2 Research Objective

The major aim of this thesis is to mimic the photocatalytic synthesis of chemicals in nature, which uses solar energy to produce storable and transportable low-carbon fuels and/or value-added chemicals through photocatalysis. As mentioned above, the process of direct conversion of solar energy into chemical energy is slow and inefficient. To overcome the challenge of low efficiency in solar-driven conversion, the development of high-performance photocatalysts and a comprehensive understanding of reaction mechanisms are of great importance. In this regard, a combination of materials synthesis, physical characterizations, photocatalytic performance measurement and in-situ spectroscopy is employed to study the structure-activity relationship. In particular, the objectives of this thesis are:

1) To fabricate high-performance photocatalysts, non-noble metal-based two-dimensional nanomaterials would be introduced to photocatalytic systems.

2) To evaluate photocatalytic performance for hydrogen and ammonia production, relevant photocatalytic activity tests will be carried out.

3) To obtain the structural and compositional information about the as-prepared catalysts, advanced materials characterization tools will be used as evidence to elucidate the mechanisms of the performance enhancement.

1.3 Thesis Outline

This thesis is presented in the form of journal publications. It contains research results on the design of novel nanomaterials for photocatalytic hydrogen production. Recent progress and challenges for the application of photocatalysts for generating hydrogen and valuable chemicals. Also, several novel nanomaterials were reviewed for application in emerging solar-driven reactions. Specifically, the chapters in the thesis are presented in the following sequence:

Chapter 1 introduces the significance of this project and outlines the research objectives and key contributions to the field of photocatalysis.

Chapter 2 reviews the progress and challenges of the application of photocatalysts for hydrogen production and the production of valuable chemicals.

Chapter 3 presents two-dimensional Co-based metal-organic framework nanosheets enhancing photocatalytic hydrogen production

Chapter 4 presents metal-organic frameworks with atomically dispersed Ni-N$_4$ sites for boosting photocatalytic hydrogen production

Chapter 5 presents two-dimensional FePS$_3$ nanosheets for improving photocatalytic hydrogen production

Chapter 6 reviews the progress and challenges for the application of novel nanomaterials in emerging solar-driven reactions

Chapter 7 presents the conclusion and perspectives for future work on the design and application of novel nanomaterials for the photocatalytic production of value-added chemicals.

1.4 References

(1) Steven Chu; Yi Cui; Nian Liu. The path towards sustainable energy. *Nat. Mater.* **2017,** *16*, 16-22.

(2) Jinlong Gong; Can Li; Michael R. Wasielewski. Advances in solar energy conversion. *Chem. Soc. Rev.* **2019,** *48*, 1862-1864.

(3) Poul Alberg Østergaard; Neven Duic; Younes Noorollahi; Hrvoje Mikulcic; Soteris Kalogirou. Sustainable development using renewable energy technology. *Renew. Energ.* **2020,** *146*, 2430-2437.

(4) Nadarajah Kannan; Divagar Vakeesan. Solar energy for future world:-a review. *Renew. Sust. Energ. Rev.* **2016,** *62*, 1092-1105.

(5) Nathan S. Lewis. Research opportunities to advance solar energy utilization. *Science* **2016,** *351*, aad1920-aad1920.

(6) Arshian Sharif; Syed Ali Raza; Ilhan Ozturk; Sahar Afshan. The dynamic relationship of renewable and nonrenewable energy consumption with carbon emission: A global study with the application of heterogeneous panel estimations. *Renew. Energ.* **2019,** *133*, 685-691.

(7) Collin Smith; Alfred K. Hill; Laura Torrente-Murciano. Current and future role of haber–bosch ammonia in a carbon-free energy landscape. *Energy Environ. Sci.* **2020,** *13*, 331-344.

(8) Sonja van Renssen. The hydrogen solution? *Nat. Clim. Change* **2020,** *10*, 799-801.

(9) Konstantinos C. Christoforidis; Paolo Fornasiero. Photocatalytic hydrogen production: A rift into the future energy supply. *ChemCatChem* **2017,** *9*, 1523-1544.

(10) Priyanka Ganguly; Moussab Harb; Zhen Cao; Luigi Cavallo; Ailish Breen; Saoirse Dervin; Dionysios D Dionysiou; Suresh C Pillai. 2d nanomaterials for photocatalytic hydrogen production. *ACS Energy Lett.* **2019,** *4*, 1687-1709.

Chapter 2: Literature Review

2.1 Introduction and significance

Among renewable energies, solar energy has shown great potential for widespread application because of its availability and affordability. Normally, the unstable solar energy needs to be converted and stored in transportable energy carriers due to the vulnerability of sunlight changes. Currently, an increasing number of researches have been focused on the production of clean hydrogen fuel from water using renewable solar energy, thanks to the high energy density of H_2. However, conventional photocatalytic H_2 evolution from water splitting has low efficiency and poor stability. Hole scavengers are therefore added to boost the separation efficiency of photoexcited electron-hole pairs and improve stability by consuming the strongly oxidative photoexcited holes. The drawbacks of this approach are the increased cost and production of waste.

To overcome these drawbacks, a number of hole scavengers, including biomass, biomass-derived intermediates, plastic wastes and a range of alcohols have been reported for photocatalytic H_2 evolution, coupled with value-added chemicals production using semiconductor-based photocatalysts. It is timely, therefore, to comprehensively summarize the properties, performances, and mechanisms of these photocatalysts, and critically review recent advances, challenges, and opportunities in this emerging area.

Highlights of this Chapter include:

(1) Illustrating reaction mechanisms of photocatalysts for H_2 evolution coupled with selective oxidation, C–H activation and C–C coupling, together with nonselective oxidation, using hole-scavengers.

(2) Introducing equations to compute conversion/selectivity of selective oxidation.

(3) Summarizing and critically comparing recently reported photocatalysts with particular emphasis on correlation between physicochemical characteristics and performances, together with photocatalytic mechanisms.

(4) Appraising current advances and challenges.

2.2 Photocatalysts for Hydrogen Evolution Coupled with Production of Value-Added Chemicals

This chapter is included as it appears as a journal paper published by **Bingquan Xia,** Yanzhao Zhang, Bingyang Shi, Jingrun Ran, Kenneth Davey, Shi-Zhang Qiao Photocatalysts for Hydrogen Evolution Coupled with Production of Value-Added Chemicals. ***Small Methods*** 2020, *4*, 2000063.

Statement of Authorship

Title of Paper	Photocatalysts for Hydrogen Evolution Coupled with Production of Value-Added Chemicals
Publication Status	☑ Published ☐ Accepted for Publication ☐ Submitted for Publication ☐ Unpublished and Unsubmitted work written in manuscript style
Publication Details	Bingquan Xia, Yanzhao Zhang, Bingyang Shi, Jingrun Ran, Kenneth Davey, Shi-Zhang Qiao, Photocatalysts for Hydrogen Evolution Coupled with Production of Value-Added Chemicals, Small Methods, 2020, 4, 2000063

Principal Author

Name of Principal Author (Candidate)	Bingquan Xia
Contribution to the Paper	Proposed the review topic, reviewed and organised the literatures, and wrote the manuscript.
Overall percentage (%)	80
Certification:	This paper reports on original research I conducted during the period of my Higher Degree by Research candidature and is not subject to any obligations or contractual agreements with a third party that would constrain its inclusion in this thesis. I am the primary author of this paper.
Signature		Date	15/01/2022

Co-Author Contributions

By signing the Statement of Authorship, each author certifies that:

i. the candidate's stated contribution to the publication is accurate (as detailed above);

ii. permission is granted for the candidate in include the publication in the thesis; and

iii. the sum of all co-author contributions is equal to 100% less the candidate's stated contribution.

Name of Co-Author	Yanzhao Zhang
Contribution to the Paper	Helped to revise the figures
Signature		Date	15/01/2022

Name of Co-Author	Bingyang Shi
Contribution to the Paper	Helped to revise the manuscript
Signature		Date	15/01/2022

Name of Co-Author	Jingrun Ran		
Contribution to the Paper	Helped to revise the manuscript and organise the figures, and acted as the corrresponding author		
Signature		Date	15/01/2022

Name of Co-Author	Kenneth Davey		
Contribution to the Paper	Helped to edit the manuscript		
Signature		Date	15/01/2022

Name of Co-Author	Shizhang Qiao		
Contribution to the Paper	Supervised development of work, helped in manuscript evaluation and acted as corresponding author		
Signature		Date	15/01/2022

Photocatalysts for Hydrogen Evolution Coupled with Production of Value-Added Chemicals

Bingquan Xia, Yanzhao Zhang, Bingyang Shi, Jingrun Ran,* Kenneth Davey, and Shi-Zhang Qiao*

The conversion of water into clean hydrogen fuel using renewable solar energy can potentially be used to address global energy and environmental issues. However, conventional photocatalytic H_2 evolution from water splitting has low efficiency and poor stability. Hole scavengers are therefore added to boost separation efficiency of photoexcited electron–hole pairs and improve stability by consuming the strongly oxidative photoexcited holes. The drawbacks of this approach are increased cost and production of waste. Recently, researchers have reported the use of abundantly available hole scavengers, including biomass, biomass-derived intermediates, plastic wastes, and a range of alcohols for H_2 evolution, coupled with value-added chemicals production using semiconductor-based photocatalysts. It is timely, therefore, to comprehensively summarize the properties, performances, and mechanisms of these photocatalysts, and critically review recent advances, challenges, and opportunities in this emerging area. Herein, this paper: 1) outlines reaction mechanisms of photocatalysts for H_2 evolution coupled with selective oxidation, C–H activation and C–C coupling, together with nonselective oxidation, using hole-scavengers; 2) introduces equations to compute conversion/selectivity of selective oxidation; 3) summarizes and critically compares recently reported photocatalysts with particular emphasis on correlation between physicochemical characteristics and performances, together with photocatalytic mechanisms, and; 4) appraises current advances and challenges.

1. Introduction

Global energy demand continues to increase significantly. Due to the dwindling and possible exhaustion of nonrenewable fossil fuels, research emphasis is being directed to alternative and practically sustainable energy resources.[1–3] Solar energy is

B. Xia, Y. Zhang, Dr. J. Ran, Dr. K. Davey, Prof. S.-Z. Qiao
School of Chemical Engineering & Advanced Materials
The University of Adelaide
Adelaide, SA 5005, Australia
E-mail: jingrun.ran@adelaide.edu.au; s.qiao@adelaide.edu.au
Prof. B. Shi
School of Life Sciences
Henan University
Kaifeng, Henan 475004, China

The ORCID identification number(s) for the author(s) of this article can be found under https://doi.org/10.1002/smtd.202000063.

widely reckoned as an ideal substitute for present reliance on fossil fuels given its sustained availability.[4,5] The conversion of solar energy into clean and carbon-free hydrogen (H_2) fuel via semiconductor-based photocatalysis is environmentally benign and has therefore received significant attention.[6–8]

For semiconductor-based photocatalytic H_2 evolution in pure water, photoexcited electrons are used to reduce protons to evolve H_2 gas; while photoexcited holes oxidize the water to evolve oxygen (O_2).[9] Due to the ready recombination of photoexcited electron–hole pairs, sluggish water-oxidation kinetics, and high water-oxidation overpotential, the performance of photocatalytic H_2 evolution in pure water is significantly limited. This leads to low solar-to-H_2 conversion.[10] To boost efficiency and suppress photocorrosion of semiconductor photocatalysts, various hole scavengers have been reported as sacrificial electron donors.[11–13] The practical drawbacks of this strategy are an increased cost and production of waste. Additionally, the generated H_2 energy sometimes cannot offset the energy needed to acquire the hole scavengers. Therefore, it is practically necessary to use abundant and readily available feedstocks as hole scavengers to improve H_2 evolution and advantageously produce value-added chemicals simultaneously.

Abundantly available and renewable feedstocks include biomass (e.g., cellulose,[14,15] hemicellulose,[16] and lignin[17,18]) and biomass-derived intermediates[19,20] (e.g., furfuryl alcohols, 5-hydroxymethylfurfural, 2,5-dimethylfuran, and 2-methylfuran). These have been reported to consume the photoexcited holes and produce chemicals of high value, such as formate, furoic acid, 2,5-furandicarboxylic acid, and diesel-fuel precursors, through photocatalysts, including CdS/CdO$_x$,[16] TiO$_2$/NiO$_x$@graphitic carbon,[21] Ni deposited CdS ultrathin nanosheets,[19] Ru doped ZnIn$_2$S$_4$,[20] and CdSe quantum dots/Ni^{2+}.[22] At the same time, the photoexcited electrons reduce the protons to evolve H_2. Plastic wastes, such as poly(ethylene terephthalate), poly(lactic acid), and polyurethane, have also been used as abundant and readily available feedstocks to capture photoinduced holes and generate value-added products, such as formate, acetate, and pyruvate, in the presence of a range

**ADVANCED
SCIENCE NEWS**
www.advancedsciencenews.com

**small
methods**
www.small-methods.com

of photocatalysts (e.g., CdS/CdO_x quantum dots and carbon nitride/nickel phosphide) and alkaline solution.[23,24] Simultaneously, the photoinduced electrons left in these photocatalysts reduce water to evolve H_2.

In addition to readily available biomass and plastic wastes, a variety of alcohols, for example, methanol, benzyl alcohol, and 4-methyl benzyl alcohol, have been adopted as organic substrates to be selectively oxidized into corresponding aldehydes or ketones on a range of photocatalysts including Cu_2O,[25] ZnO,[25] Pt/TiO_2, $Pd/CdS-TiO_2$,[26] CoP/CdS,[27] Ni/CdS,[28] $ZnS-Ni_xS_y$,[29] $Zn_3In_2S_6$,[30] and; CdSe quantum dots/Ni^{2+}.[22] These alcohols are routinely produced in highly significant quantities in the chemical industry every year and selectively oxidized products including, for example, formaldehyde, benzyl aldehyde, and 4-methyl benzyl aldehyde are widely used in the fragrance, confectionery, beverage, and pharmaceutical industries. However, conventional oxidation requires strong oxidants that generate undesired and overoxidized products, and significant waste. In consequence, the efficient conversion of alcohols to aldehydes with simultaneous H_2 production via oxidant-free photocatalysis has attracted significant research attention.

Here, we critically review for the first time the development of photocatalysts to produce value-added chemicals with simultaneous evolution of clean and carbon-free H_2 fuel utilizing hole scavengers, such as biomass, biomass-derived intermediates, plastic wastes, and alcohols. In this work, we: 1) outline fundamental reaction mechanisms for H_2 evolution coupled with selective and nonselective oxidation using hole scavengers; 2) illustrate equations to compute conversion and selectivity of selective oxidation; 3) summarize and critically compare recently reported photocatalysts with an emphasis on the relationship between physicochemical characteristics and resulting performance, and; 4) appraise current advances and challenges.

2. Fundamental Photocatalytic H_2 Evolution Coupled with Production of Value-Added Chemicals

Semiconductor-based photocatalytic H_2 evolution that is advantageously coupled with value-added chemical production can be categorized into three (3) types based on differing reaction pathways and products. The fundamentals of these different types are outlined in the following:

2.1. Mechanisms of Photocatalytic H_2 Evolution Coupled with the Selective Oxidation Reaction

As shown in **Figure 1**a, the alcohol molecule is adsorbed initially on the surface of Ni loaded CdS nanoparticles (NPs). Under light irradiation, the photoexcited electron on the conduction band (CB) of CdS NPs migrates to the surface of Ni to reduce the proton extracted from the −OH of the alcohol molecule adsorbed on the surface of Ni to form an alkoxide anion and H atom adsorbed on the surface of Ni loaded CdS NPs. The photoexcited hole on the valence band (VB) of CdS

Bingquan Xia received his master's degree in chemistry from Wuhan University in 2016. He is currently a Ph.D. candidate under the supervision of Prof. Shi-Zhang Qiao at the University of Adelaide. His research is focused on the development of highly efficient photocatalysts for solar energy conversion.
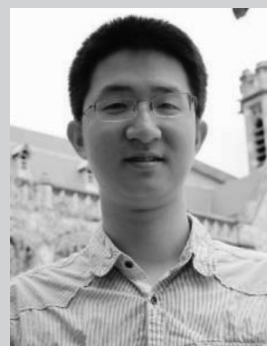
Jingrun Ran received his B.E. and M.E. degrees in materials science and engineering from Wuhan University of Technology and Ph.D. in chemical engineering from The University of Adelaide. He is now working as a postdoctoral research fellow supervised by Prof. Shi-Zhang Qiao and focusing on design and development of nanostructured photocatalysts for solar fuel production.

Shi-Zhang Qiao received his Ph.D. degree from Hong Kong University of Science and Technology in 2000. He is currently a Chair Professor and Australian Laureate Fellow at the School of Chemical Engineering & Advanced Materials at The University of Adelaide, Australia. His research expertise is in nanomaterials for new energy technologies (electrocatalysis, photocatalysis, batteries, and fuel cells).

NPs then migrates to its surface and oxidizes the alkoxide anion to form the corresponding aldehydes or ketones. In the meantime, the homolytic cleavage of C–H occurs. This leads to another H atom adsorbed on the surface of Ni loaded CdS NPs. Finally, the two adsorbed H atoms form a molecule of H_2.

In addition to this mechanism on photocatalysts without any linking to surfactant molecules, Zhao et al.[22] proposed another on $Ni^{2+}/CdSe$ capped with 3-mercaptopropionic acid (MPA, see Figure 1b). In this mechanism, under light illumination, the photoinduced hole on the VB of CdSe migrates to the absorbed thiolate anion or disulfide to produce a thiyl radical (RS·). The
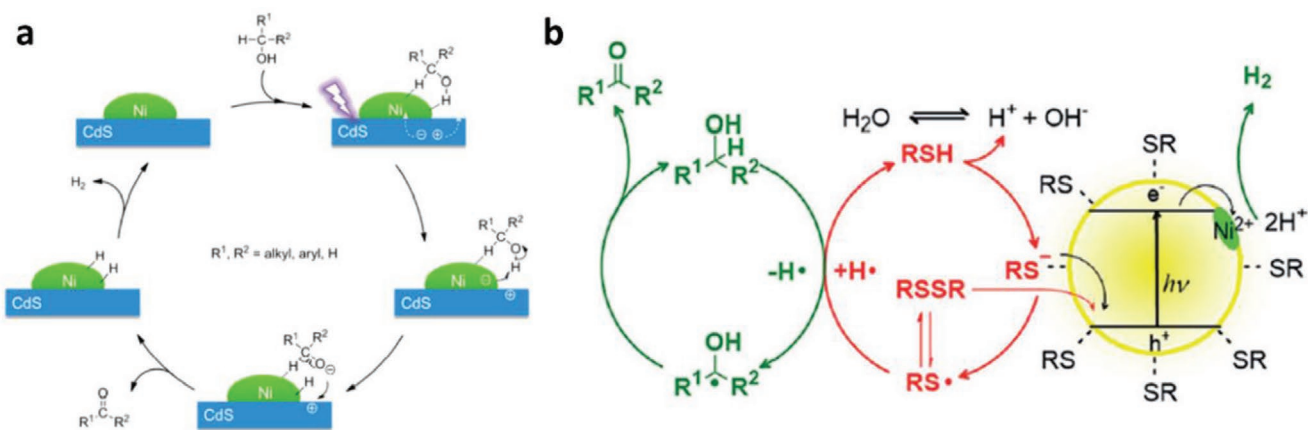
Figure 1. Mechanism of photocatalytic H$_2$ evolution coupled with selective oxidation on a) Ni loaded CdS nanoparticles[28] and b) Ni^{2+}/MPA capped CdSe quantum dot.[22] a) Reproduced with permission.[28] Copyright 2016, American Chemical Society. b) Reproduced with permission[22] Copyright 2017, Wiley-VCH.

H atom from the alcohol molecule is then extracted by the thiyl radical to produce a radical. Subsequently, the two radicals produced disproportionate to form one alcohol molecule and one aldehyde molecule. Through the equilibration of thiol (RSH) with bulk water the extracted H atoms are released as protons that finally are reduced to evolve H$_2$ by the Ni^{2+} adsorbed on the MPA-capped CdSe quantum dot.

2.2. Mechanisms of Photocatalytic H$_2$ Evolution Coupled with C–H Activation and C–C Coupling Reaction

As is shown in **Figure 2**a, Xie et al.[25] proposed a concerted proton–electron transfer mechanism in which the C—H bond was activated without affecting the O—H group for dehydrogenative C–C coupling of methanol (CH$_3$OH) to ethylene glycol (HOCH$_2$CH$_2$OH) on MoS$_2$ nanofoam coupled CdS nanorod (MoS$_2$/CdS) photocatalyst. Under light irradiation, the photoexcited hole in CdS oxidizes the CH$_3$OH to form ·CH$_2$OH radical and proton. The two ·CH$_2$OH radicals then combine via C–C coupling to form one HOCH$_2$CH$_2$OH. The two protons are finally reduced by the photoexcited electrons to evolve H$_2$.

Luo et al. reported photocatalytic H$_2$ evolution coupled with the production of diesel-fuel precursors through acceptor-less dehydrogenative C–C coupling using lignocellulose-derived methylfurans on Ru-doped ZnIn$_2$S$_4$ photocatalyst.[20] As is illustrated in Figure 2b, under visible-light irradiation the photoinduced hole oxidizes the furfuryl C—H bond of 2,5-dimethylfuran (2,5-DMF) to generate furfuryl radicals and protons. The furfuryl radicals undergo resonance to yield dimeric isomers via C–C coupling. The dimers then combine with 2,5-DMF, or actually themselves, to produce trimers and tetramers as diesel-fuel precursors. Simultaneously the photoinduced electrons on the CB of Ru doped ZnIn$_2$S$_4$ reduce the protons to evolve H$_2$.

2.3. Mechanisms of Photocatalytic H$_2$ Evolution Coupled with the Nonselective Oxidation Reaction

In the preceding two mechanisms the organic substrates are selectively converted into "target" products with high conversion. However, the organic substrates are, in some instances, converted into a range of products in photocatalysis. For example, Wakerley et al.[16] utilized CdS/CdO$_x$ photocatalyst
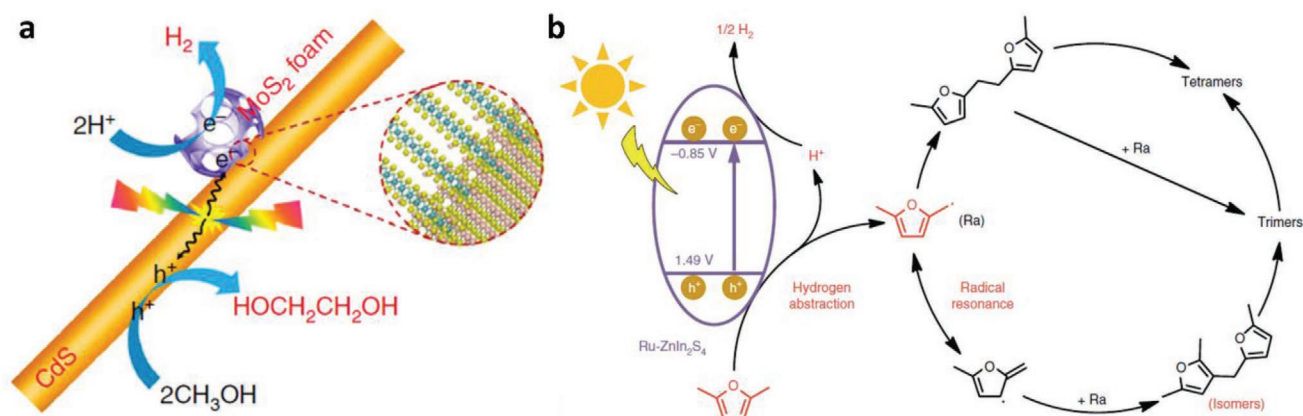
Figure 2. Mechanism of photocatalytic H$_2$ evolution coupled with C–H activation and C–C coupling on a) MoS$_2$ nanofoam coupled CdS nanorod and b) Ru doped ZnIn$_2$S$_4$. a) Reproduced with permission.[20] Copyright 2018, Springer Nature. b) Reproduced with permission[20] Copyright 2019, Springer Nature.

**ADVANCED
SCIENCE NEWS**

www.advancedsciencenews.com

**small
methods**

www.small-methods.com
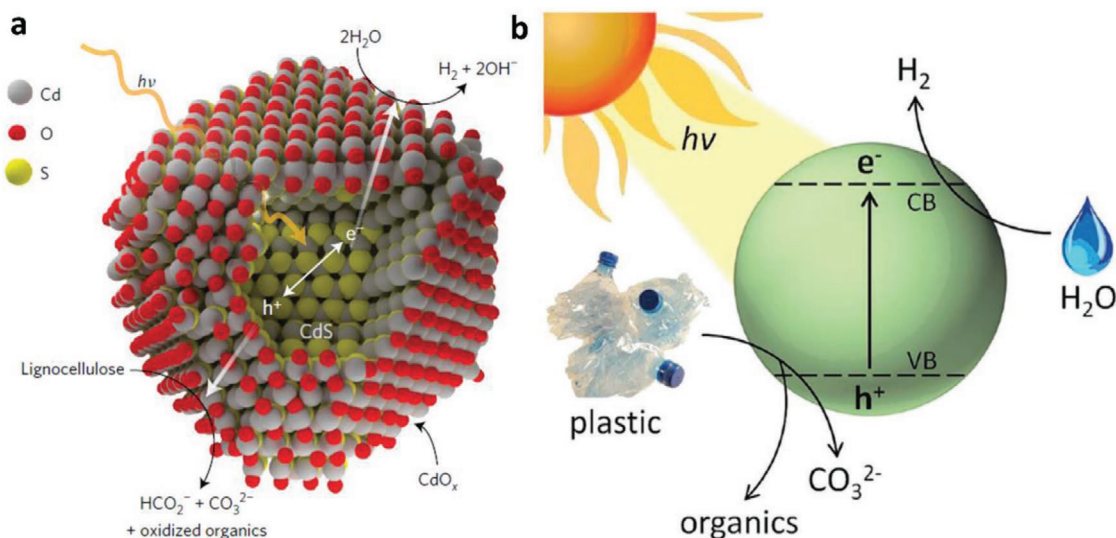
Figure 3. Mechanism of photocatalytic H_2 evolution coupled with nonselective oxidation reactions on a) CdS/CdO_x photocatalyst using lignocellulose[16] and b) CdS/CdO_x quantum dot using plastic waste.[24] a) Reproduced with permission.[16] Copyright 2017, Springer Nature. b) Reproduced with permission.[24] Copyright 2018, The Royal Society of Chemistry.

to photoreform lignocellulose to produce H_2. As is illustrated in **Figure 3**a, light irradiation on CdS/CdO_x leads to the production of photoexcited electrons and holes. The photoexcited electrons reduce the protons in the aqueous solution for H_2 evolution. The photoexcited holes oxidize the lignocellulose to generate a range of products, such as aldehydes, formate, HCO_3^- and CO_3^{2-}. In another example, CdS/CdO_x quantum dots were employed to photoreform plastic waste to evolve H_2 fuel.[24] Under visible-light irradiation, the photoexcited electrons reduce the H_2O to evolve H_2 gas. Plastic wastes including polylactic acid (PLA), polyethylene terephthalate (PET), polyurethane, and a PET water bottle, were oxidized by photoexcited holes to yield chemical products, e.g., pyruvate, formate, glycolate, ethanol, acetate, and lactate.

2.4. Conversion and Selectivity

The percentage conversion and selectivity of photocatalytic dehydrogenative oxidation of organic substrates to target oxidized products are computationally defined as follows:

$$\text{Conversion}(\%) = [(n_0 - n_t)/n_0] * 100 \tag{1}$$

$$\text{Selectivity}(\%) = [(n_{oxt})/(n_0 - n_t)] * 100 \tag{2}$$

$$\text{HER rate} = n(H_2)/(m_{cat} * t) \tag{3}$$

where
  n_0: the initial molar amount of the organic substrate
  n_t: the real-time molar amount of the organic substrate
  n_{oxt}: the molar amount of a target oxidized product
  $n(H_2)$: the molar amount of produced H_2
  m_{cat}: the initial mass of catalyst for the reaction
  t: reaction (light irradiation) time.

3. Photocatalyst for H_2 Evolution Coupled with the Selective Oxidation Reaction

The selective oxidation of alcohols, such as alkyl, aryl, and furfuryl, to corresponding oxidation products, such as aldehydes and ketones (**Figure 4**) via oxidant-free photocatalysis under mild conditions is important. This is because these oxidized products are used widely in the food and pharmaceutical industries. A number of photocatalysts (shown in **Table 1**) have been developed to drive the coproduction of H_2 gas and the selective oxidation of these alcohols to aldehydes or ketones.

3.1. Selective Oxidation of Alkyl Alcohol

In most instances of dehydrogenation of methanol, HCHO was formed as a major product with semiconductor-based photocatalysts. Xie and co-workers have reported the testing of a series of typical semiconductor-based photocatalysts for dehydrogenation and selective oxidation of methanol to obtain valuable chemical products.[25] Under UV–visible light illumination, ZnO showed a selectivity of 91% for obtaining HCHO, followed by TiO_2 (84%) and g-C_3N_4 (64%). 21% of HCOOH was produced with g-C_3N_4 photocatalyst, implying that some of the formed HCHO were oxidized further to HCOOH. For ZnS, the
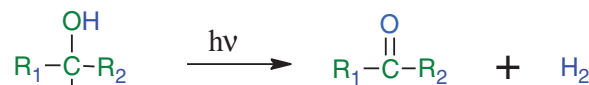
Figure 4. Photocatalytic H_2 evolution coupled with selective oxidation of alcohols (alky, aryl, and furfuryl) to aldehydes or ketones.

**ADVANCED
SCIENCE NEWS**

www.advancedsciencenews.com

**small
methods**

www.small-methods.com

Table 1. Comparative summary of performance on reported photocatalysts for H_2 evolution coupled with selective oxidation.

Photocatalyst	Cocatalyst	Substrate	Products[a] [Oxidized]	HER rate [mmol g_{cat}^{-1} h^{-1}]	Sel. [%]	Conv. [%]	Reaction condition	Light source [nm]	Ref
Cu_2O	–[b]	Methanol	Formaldehyde	0.42	100	–	H_2O	Vis(420–780)	[25]
ZnO	–	Methanol	Formaldehyde	3.1	91	–	H_2O	UV–vis(320–780)	[25]
Pt/TiO_2	Pt	Benzyl alcohol	Benzaldehyde	0.96	99	99	CH_3CN	UV	[37]
$Pd/CdS-TiO_2$	Pd	Benzyl alcohol	Benzaldehyde	1.2	96	99	H_2O	Blue LED(460 nm)	[26]
CoP/CdS	CoP	4-methlyl benzyl alcohol	4-methyl benzaldehyde	4.152	80.5	88	H_2O	Vis	[27]
Co-CdS	Co	Benzyl alcohol	Benzaldehyde	8.940	93.9	–	CH_3CN	Vis (>420 nm)	[38]
Ni/CdS	Ni	Benzyl alcohol	Benzaldehyde	–	96	96	CH_3CN	Blue LED	[28]
ZnS-Ni_xS_y	Ni_xS_y	Benzyl alcohol	Benzaldehyde	3.648	80.4	49.3	N_2	Xe lamp (>200 nm)	[29]
$Zn_3In_2S_6$	–	Benzyl alcohol	Benzaldehyde	0.167	93	–	benzotrifluoride	Vis (>420 nm)	[30]
CdSe–Ni^{2+}	Ni^{2+}	Benzyl alcohol	Benzaldehyde	–	98	92	H_2O, Ar	Vis (410 nm)	[22]
CdSe–Ni^{2+}	Ni^{2+}	Furfuryl alcohol	Furfural	–	14	95	H_2O, Ar	Vis (410 nm)	[22]
Ni/CdS	Ni	Furfuryl alcohol	Furfural	2.05	100	81.7	H_2O	Blue LED(455)	[19]
g-C_3N_4	Pt	Benzyl alcohol	Benzaldehyde	1.83	90	60	1.5×10^{-3} M, H_2O, Ar	UV-LED (392)	[39]
Pt-g-C_3N_4	Pt	Benzyl alcohol	Benzaldehyde	0.255	90	40	H_2O, Ar	Vis (>400 nm)	[31]
g-C_3N_4	–	Methanol	Formaldehyde	1.5	64	–	H_2O	UV–vis(320–780)	[25]

[a]Only major oxidized products are displayed; [b]–: not available.

selectivity for HCHO formation is 43%, and another 54% of methanol was converted to ethylene glycol. These results indicate that the photocatalytic dehydrogenation of methanol over ZnS might have additional reaction pathways to form ethylene glycol.

3.2. Selective Oxidation of Aromatic Alcohol

Benzaldehyde is an important chemical compound/precursor with a high added value because of widespread use in the food, pharmaceutical, and cosmetic industries. The synthesis of benzaldehyde is therefore significant. Since it is readily oxidized in the presence of O_2 (or other oxidants) it is difficult to obtain from benzyl alcohol or toluene while avoiding overoxidized products.

In 2016, Chai et al. reported utilization of Ni-modified CdS nanoparticles as a photocatalyst for splitting of alcohol into H_2 and corresponding aldehydes or ketones.[28] Following 20 h illumination, the conversion of benzyl alcohol was 96%. The selectivity for benzaldehyde was 96%. In comparison, 50% conversion for benzyl alcohol and 9% selectivity for benzaldehyde were observed over CdS photocatalyst without Ni. These researchers proposed a mechanism of formation of a C=O bond via Ni-assisted C–H activation (see Figure 1a). Success in this work was believed to be associated with the interface between the Ni nanocrystal and CdS (**Figure 5**a,b).

Hao et al. used ZnS-Ni_xS_y composites as photocatalysts for the dehydrogenation and selective oxidation of benzyl alcohol to produce H_2 and benzaldehyde.[29] High-resolution transmission electron microscopy (HRTEM) images of ZnS-Ni_xS_y (Figure 5c,d) corroborated intimate contact between ZnS

and Ni_xS_y, indicating efficient interfacial charge transfer. The overoxidation of benzyl alcohol was controlled by adding reaction media acetonitrile or benzotrifluoride to restrict the formation of nonselective and reactive •OH and overdependency on photogenerated holes. Compared with bare ZnS, the selectivity for the transformation of benzyl alcohol to benzaldehyde increased from 8.15% to 90.5% after Ni_xS_y was integrated with ZnS under UV light illumination (Figure 5d). The greatest photocatalytic H_2 evolution was also achieved on ZnS-Ni_xS_y (3) composite (Figure 5e).

Li et al. reported Pt-loaded g-C_3N_4 for photocatalytic dehydrogenation of benzyl alcohol.[31] After 20 h reaction, 0.051 mmol H_2 was produced, while 40% of benzyl alcohol was consumed with 90% converted to benzaldehyde.

3.3. Selective Oxidation of Furfuryl Alcohol

Furfuryl alcohol and its oxidative derivatives are important raw materials and intermediates in the chemical industries. They can be produced from abundant biomass resources.[32–34]

Han et al. reported the photocatalytic H_2 generation from furfuryl alcohol and obtained selective oxidative products using Ni/CdS.[19] Nearly all the furfuryl alcohol was converted to furfural after 22 h. However, under the same reaction condition, just 22% conversion was achieved with 2D Ni/CdS for the oxidation of 5-hydroxymethylfurfural (HMF). Results from controlled experiments indicated that aldehyde groups can inhibit the oxidation of alcohol groups in HMF. Because aldehyde groups are not stable in a high pH environment photocatalytic conversion of HMF to 2,5-furandicarboxylic acid reached 90% in 1 h.

ADVANCED
SCIENCE NEWS
www.advancedsciencenews.com

small
methods
www.small-methods.com
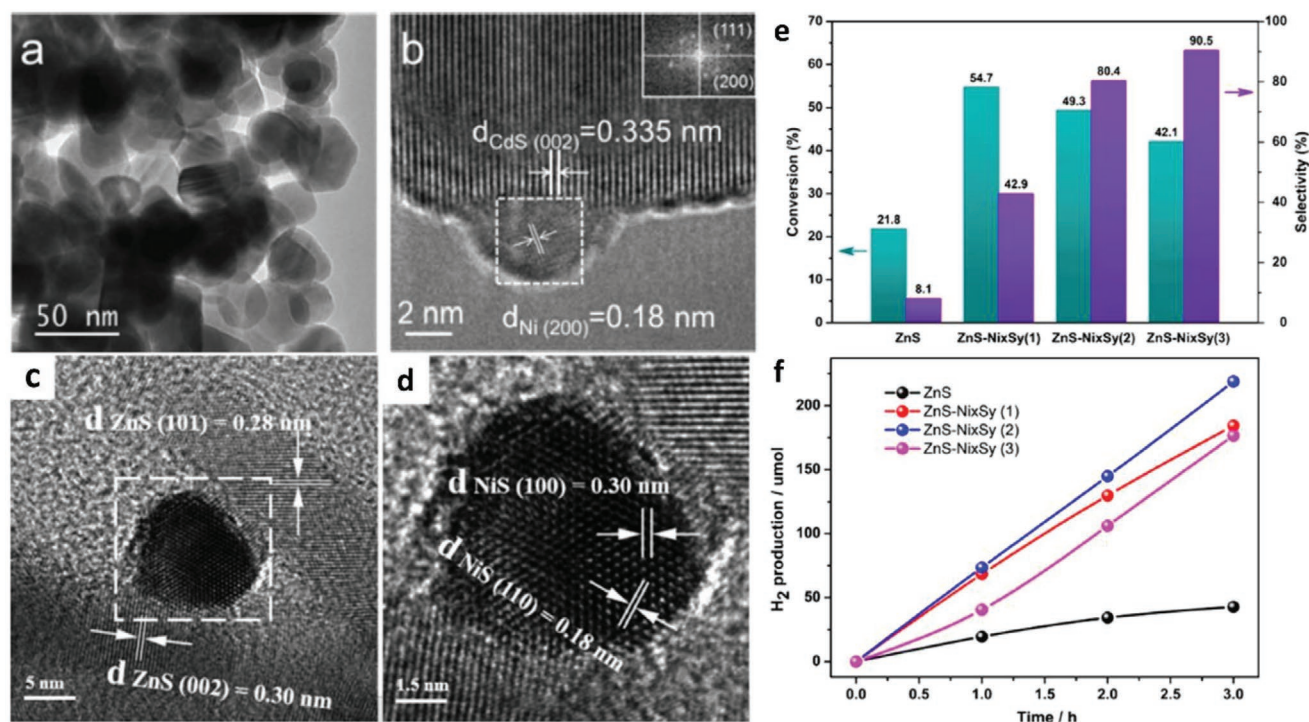
Figure 5. a) TEM image and b) HRTEM image of Ni/CdS (the inset in (b) shows the Fourier transform of the marked area).[29] HRTEM images of c) ZnS-Ni$_x$S$_y$ (3) composite and d) Ni$_x$S$_y$ nanoparticles. e) Conversion efficiencies for benzyl alcohol on various photocatalysts after a 3 h Xe lamp illumination in 5×10^{-3} M benzyl alcohol aqueous solution. f) Photocatalytic H$_2$ evolution of various photocatalysts in 5×10^{-3} M benzyl alcohol aqueous solution under Xe lamp illumination. Reproduced with permission.[29] Copyright 2019, American Chemical Society.

Zhao et al. reported an MPA-capped CdSe quantum dot with Ni^{2+} (NiCl$_2$) for the oxidation of furfuryl alcohol (2-furyl-methanol). Only 14% selectivity toward furfural was achieved while 95% furfuryl alcohol was consumed.[22]

4. Photocatalyst for H$_2$ Evolution Coupled with Selective C–H Activation and C–C Coupling

Generally, activation of inert C—H bonds is more difficult than activation of O—H bonds if the organic substrates contain hydroxyl groups. However, Xie et al. reported preferential activation of C—H bond and C—C coupling in methanol and obtained high-valued ethylene glycol (EG) with CdS as the photocatalyst under solar light irradiation.[25] In this work, the desired EG was demonstrated to be formed via the radical intermediate of •CH$_2$OH following C—H bond activation, while the byproduct HCHO was formed via radical intermediate CH$_3$O• after dissociation of the O—H bond. The lower formation

energy, smaller reaction energy barrier of •CH$_2$OH and, weak adsorption energy on CdS, make it favorable for the preferential generation of the intermediate •CH$_2$OH (over CH$_3$O•). The strong adsorption energy of •CH$_2$OH found on the surface of TiO$_2$ and CuS prevents the •CH$_2$OH formed from leaving the catalyst surface. The •CH$_2$OH intermediates can be further oxidized to chemical products, such as HCHO and HCOOH, as the case with ZnS and g-C$_3$N$_4$. Ethylene glycol can be formed because the OH group of CH$_3$OH on CdS energy is more difficult to deprotonate compared with that on TiO$_2$ which has greater adsorption energy. Additionally, the morphology and structure of the photocatalyst and cocatalyst can alter the reaction pathways and affect the selectivity. The selectivity toward forming ethylene glycol was 58% and 71% for CdS nanoparticles and CdS nanorods, respectively. As MoS$_2$ nanosheet and nanofoam were introduced, the selectivities increased to 84% and 90% (**Table 2**), respectively. They also mentioned that the produced EG may be further oxidized and a number of byproducts including glycolaldehyde, oxalic acid, HCHO, and

Table 2. Comparative summary of performance on reported photocatalysts for H$_2$ evolution and C–C coupling.

Photocatalyst	Cocatalyst	Substrate	Products[a] [Oxidized]	HER rate [mmol g_{cat}^{-1} h^{-1}]	Sel. [%]	Conv. [%]	Reaction cond.	Light source [nm]	Ref
NF-MoS$_2$/CdS	MoS$_2$	Methanol	Ethylene glycol	12	90	–	H$_2$O, N$_2$	Vis(420–780)	[25]
Ru-ZnIn$_2$S$_4$	—[b]	2,5-dimethylfuran	Diesel-fuel precursors	40	96	–	CH$_3$CN, Ar	Blue LED(455)	[20]

[a] Only major oxidized products are displayed; [b] –: not available.

**ADVANCED
SCIENCE NEWS**
www.advancedsciencenews.com

**small
methods**
www.small-methods.com
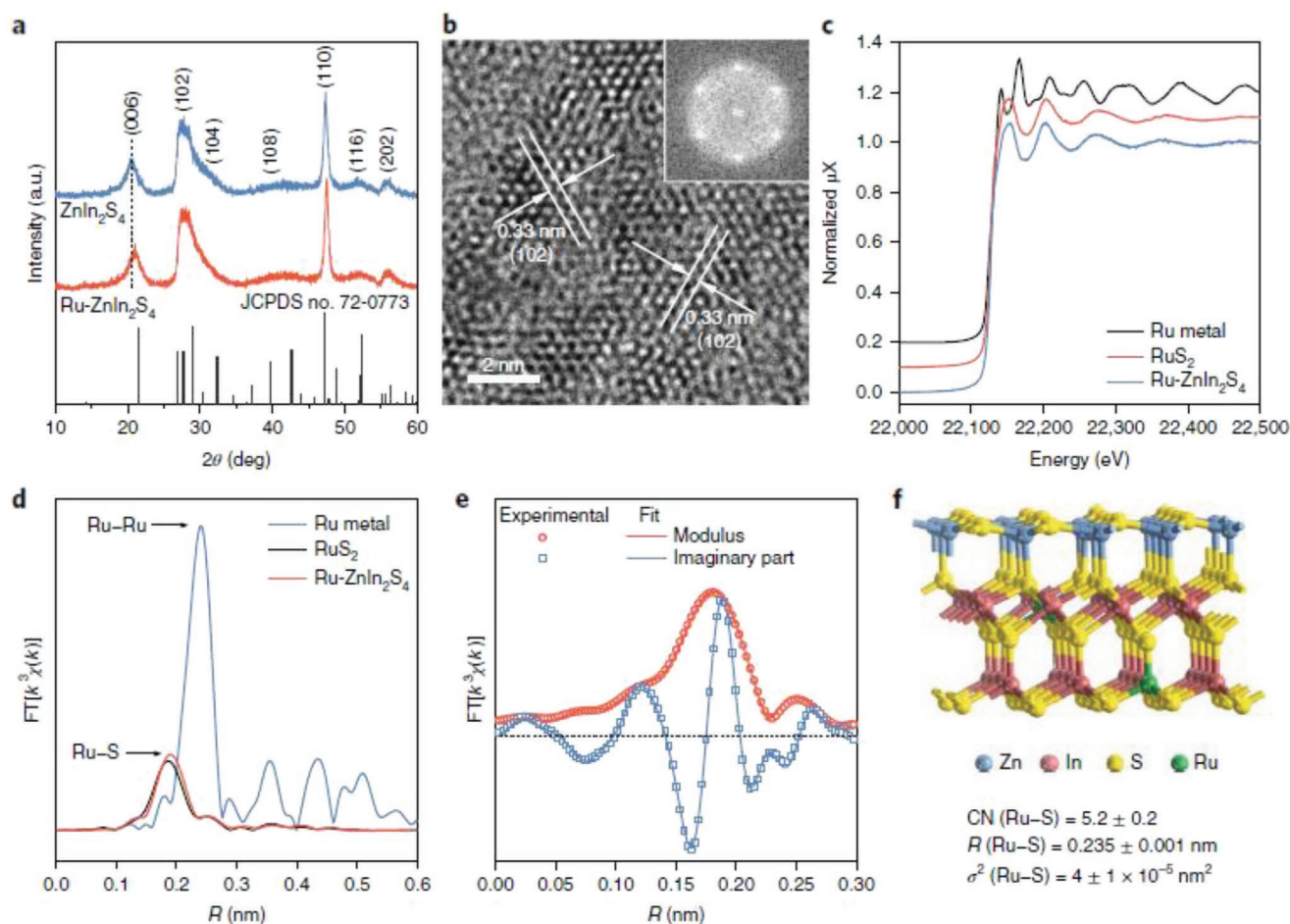
Figure 6. a) X-ray diffraction (XRD) patterns of Ru doped $ZnIn_2S_4$ and pure $ZnIn_2S_4$. b) HRTEM image of Ru doped $ZnIn_2S_4$. Inset in (b) shows the corresponding fast Fourier transform (FFT) of Ru doped $ZnIn_2S_4$. c) X-ray absorption near edge structure (XANES) of Ru K edge for, respectively, Ru metal, RuS_2, and Ru doped $ZnIn_2S_4$. d) Extracted extended X-ray absorption fine structure (EXAFS) signals for, respectively, Ru metal, RuS_2, and Ru doped $ZnIn_2S_4$. e) Fit of the Fourier transformed (FT) K^3-weighted $\chi(k)$ of the EXAFS signals of Ru K edge for Ru doped $ZnIn_2S_4$. f) Schematic of the Ru-$ZnIn_2S_4$ structure and the fitting results of Ru–S coordination. Reproduced with permission.[20] Copyright 2019, Springer Nature.

HCOOH were observed without the EG separator in the scaled-up production.

Luo et al. recently reported Ru-doped $ZnIn_2S_4$ as a photocatalyst for coproduction of diesel-fuel precursors and H_2 from methylfurans that were selectively obtained from lignocellulose.[20] X-ray diffraction (XRD) patterns of the Ru-doped $ZnIn_2S_4$ (**Figure 6**a) confirmed its hexagonal crystal structure (JCPDS no. 72-0773). The shift of the (006) reflection to a higher angle indicated that Ru is doped into the crystal structure of $ZnIn_2S_4$. The HRTEM image (Figure 6b) exhibited a lattice spacing of 0.33 nm, corresponding to the (102) facet of hexagonal structured $ZnIn_2S_4$. The X-ray absorption near edge structure (XANES) and extended X-ray absorption fine structure (EXAFS) of Ru K edge for Ru doped $ZnIn_2S_4$ are displayed in Figure 6c–e.

Overall results showed that the doped Ru is mainly located in the $ZnIn_2S_4$ lattice in a substitutional position for indium ions (see Figure 6f). When irradiated by the light, the furfuryl C–H of 2,5-dimethylfuran is oxidized by the photogenerated holes to form furfuryl radicals. Due to resonance, these radi-

cals migrate to the furan rings and the active C sites are then coupled by C−C bonds to form dimers, trimers, and tetramers. At the same time, the activated protons are reduced to gaseous H_2 by the photogenerated electrons in the CB of Ru doped $ZnIn_2S_4$.

It was concluded that the doping of Ru substitutes the indium ions in $ZnIn_2S_4$, narrows the bandgap of $ZnIn_2S_4$, inhibits the hole–electron recombination and thereby improves the efficiency of charge separation.

5. Photocatalyst for H_2 Evolution Coupled with the Nonselective Oxidation Reaction

In some instances added hole-scavengers are converted nonselectively into a range of chemical products, including over-oxidized products, such as CO_2, HCO_3^- and CO_3^{2-}.[11,16,23,35] For example, abundant and available hole-scavengers, such as lignocellulose and its derivatives, together with various plastic wastes (as shown in **Table 3**), are used to boost photocatalytic

ADVANCED
SCIENCE NEWS

www.advancedsciencenews.com

small
methods

www.small-methods.com

Table 3. Comparative summary of performance on reported photocatalysts for H_2 evolution coupled with nonselective oxidation.

Photocatalyst	Cocatalyst	Substrate	Products[a] [Oxidized]	HER rate [mmol g_{cat}^{-1} h^{-1}]	Sel. [%]	Conv. [%]	Reaction cond.	Light source [nm]	Ref
Cellulose@TiO_2	Pt	Cellulose	CO_2	2.16	–	–	H_2O, Ar	UV–vis	[15]
TiO_2/NiO_x@Cg	Ni NiO_x	Cellulose	CO_2, CO	0.27	–	65	H_2O	Xe lamp	[21]
Ni_2P/CN_x	Ni_2P	Polylactic acid	CO_2	0.097	–	1.6 ± 0.2	N_2, 10 M NaOH	Simulated Solar light	[23]
CdS/CdO_x	Co(BF$_4$)$_2$	lignin	CO_2	0.26	–	9.7	N_2, 10 M NaOH	Simulated Solar light	[16]
CdS/CdO_x QDs	–[b]	Polylactic acid	CO_2	64.3	–	38.8	N_2, 10 M NaOH	Simulated Solar light	[24]

[a]Only major oxidized products are displayed; [b]–: not available.

H_2 evolution and to generate a range of chemicals with high value.

Zhang et al. used cellulose coated TiO_2 with Pt for photocatalytic conversion of cellulose into sugars and carbon dioxide, with simultaneous H_2 evolution.[15] They found that the immobilization of cellulose onto TiO_2(Pt) is crucial to the conversion of cellulose, compared with a physical mixture of TiO_2(Pt) and cellulose that exhibited poor catalytic activity toward decomposition of cellulose. Based on reported results the oxidation potentials of organic carbohydrates are more negative than the potential of water oxidation, and the surface-bound cellulose was prone to be decomposed by the VB holes. The intermediates in water were further oxidized by the reactive and oxidative holes or OH radicals. Due to the complexity of the pathway of cellulose decomposition, it was difficult to determine the products generated.

Zhang et al. reported photocatalytic H_2 evolution from cellulose with TiO_2/NiO_x@C$_g$.[21] A proton dissociated from the –OH group adsorbed on the Ni surface was reduced by the photogenerated electron to form a Ni-H hydride and an alkoxide anion intermediate. Hydrogen was evolved at a reported rate of 0.967 mmol g_{cat}^{-1} h^{-1} by two Ni-H hydrides. The alkoxide anion was oxidized by the hole generating a mixture of CO_2, CO, and CH_4.

In 2017, Wakerley et al. used CdS/CdO_x quantum dots with Co(BF$_4$) as the cocatalyst for photocatalytic reforming lignocellulose (Equation (4)), earth's most abundant form of biomass, to H_2 at a rate of 5.31 mmol H_2 g_{cat}^{-1} h^{-1}.[16] A more detailed summary and comparison of photocatalysts for H_2 production from lignocellulose sources can be obtained from Kuehnel and Reisner[36]

$$C_6H_{12}O_6 + H_2O \rightleftharpoons 12H_2 + 6CO_2 \quad (4)$$
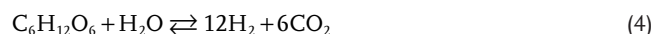
The practical utilization of CdS/CdO_x quantum dots as photocatalyst was reported for disposing of plastic waste, including PLA, PET, and polyurethane that are widely used in packaging and storage. These common plastic polymers were converted to H_2 and CO_2 under mild conditions compared with the harsh requirements for the decomposition of plastic waste.[24]

It is concluded that photocatalytic overoxidization of organic substrates could be practically useful for the disposal/decomposition of plastic wastes under mild conditions.

6. Conclusion

A number of photocatalysts have been developed for the evolution of hydrogen (H_2) coupled with selective oxidation reactions, C–H activation and C–C coupling as well as nonselective oxidation reactions.

Hole scavengers, such as abundantly available biomass, biomass-derived intermediates, plastic wastes, and alcohols, boost efficiency and long-term reliability of photocatalysts. These advantageously also yield high value-added chemicals that are presently widely used in the fragrance, confectionery, beverage, and pharmaceutical industries. Despite exciting advances in this emerging field further careful research to improve activity and selectivity, and to avoid overoxidation, is needed, however. As most researches were carried out with a relatively small amount of reactants in the laboratory, it is still challenging to realize the scaled-up production for the above-mentioned valuable chemicals. It is crucial to obtain the desired product with high selectivity. It needs to separate the product from a number of possible by-products. To improve the selectivity toward preferable products, designing suitable photocatalysts for the specific oxidation reaction is one viable approach. Also, facilitating the separation of the preferred product from reactants during the reaction could be another feasible approach.

In the future, state-of-art experimental techniques such as in operando/in situ characterizations, aberration-corrected atomic-resolution transmission electron microscopy, and synchrotron radiation-based X-ray absorption spectroscopy, could be usefully combined with theoretical computations to improve understanding of the structure-performance relationship of photocatalysts at the atomic level and to elucidate reaction mechanism(s) to guide development of high-performance photocatalysts for solar energy conversion and storage. In addition, flow-intensified chemical processing design and novel separation and purification technologies could also be utilized to obtain better outcomes and make it possible for large-scale production.

Conflict of Interest

The authors declare no conflict of interest.

Keywords

[1] J. Gong, C. Li, M. R. Wasielewski, *Chem. Soc. Rev.* **2019**, *48*, 1862.
[2] T. Arunkumar, Y. Ao, Z. Luo, L. Zhang, J. Li, D. Denkenberger, J. Wang, *Renewable Sustainable Energy Rev.* **2019**, *115*, 109409.
[3] J. Ran, M. Jaroniec, S.-Z. Qiao, *Adv. Mater.* **2018**, *30*, 1704649.
[4] P. Tao, G. Ni, C. Song, W. Shang, J. Wu, J. Zhu, G. Chen, T. Deng, *Nat. Energy* **2018**, *3*, 1031.
[5] S. K. Sansaniwal, V. Sharma, J. Mathur, *Renewable Sustainable Energy Rev.* **2018**, *82*, 1576.
[6] G. Knör, *Coord. Chem. Rev.* **2015**, *304–305*, 102.
[7] Y. Shiraishi, T. Takii, T. Hagi, S. Mori, Y. Kofuji, Y. Kitagawa, S. Tanaka, S. Ichikawa, T. Hirai, *Nat. Mater.* **2019**, *18*, 985.
[8] U. Aslam, V. G. Rao, S. Chavez, S. Linic, *Nat. Catal.* **2018**, *1*, 656.
[9] H. Zhang, G. Liu, L. Shi, H. Liu, T. Wang, J. Ye, *Nano Energy* **2016**, *22*, 149.
[10] J. Ran, J. Zhang, J. Yu, M. Jaroniec, S. Z. Qiao, *Chem. Soc. Rev.* **2014**, *43*, 7787.
[11] J. Kou, C. Lu, J. Wang, Y. Chen, Z. Xu, R. S. Varma, *Chem. Rev.* **2017**, *117*, 1445.
[12] X. Zhao, J. Feng, J. Liu, W. Shi, G. Yang, G. Wang, P. Cheng, *Angew. Chem., Int. Ed.* **2018**, *57*, 9790.
[13] G. Han, Y. Sun, *Nat. Energy* **2019**, *4*, 532.
[14] T. Wei, Z. Jin, F. Li, D. Yan, L. Xu, *Photochem. Photobiol. Sci.* **2020**, *19*, 80.
[15] G. Zhang, C. Ni, X. Huang, A. Welgamage, L. A. Lawton, P. K. J. Robertson, J. T. S. Irvine, *Chem. Commun.* **2016**, *52*, 1673.
[16] D. W. Wakerley, M. F. Kuehnel, K. L. Orchard, K. H. Ly, T. E. Rosser, E. Reisner, *Nat. Energy* **2017**, *2*, 17021.
[17] J. C. Colmenares, R. S. Varma, V. Nair, *Chem. Soc. Rev.* **2017**, *46*, 6675.
[18] M. D. Kärkäs, I. Bosque, B. S. Matsuura, C. R. J. Stephenson, *Org. Lett.* **2016**, *18*, 5166.
[19] G. Han, Y.-H. H. Jin, R. A. Burgess, N. E. Dickenson, X.-M. M. Cao, Y. Sun, G. Han, Y.-H. H. Jin, R. A. Burgess, N. E. Dickenson, X.-M. M. Cao, Y. Sun, *J. Am. Chem. Soc.* **2017**, *139*, 15584.
[20] N. Luo, T. Montini, J. Zhang, P. Fornasiero, E. Fonda, T. Hou, W. Nie, J. Lu, J. Liu, M. Heggen, L. Lin, C. Ma, M. Wang, F. Fan, S. Jin, F. Wang, *Nat. Energy* **2019**, *4*, 575.
[21] L. Zhang, W. Wang, S. Zeng, Y. Su, H. Hao, *Green Chem.* **2018**, *20*, 3008.
[22] L. M. Zhao, Q. Y. Meng, X. B. Fan, C. Ye, X. B. Li, B. Chen, V. Ramamurthy, C. H. Tung, L. Z. Wu, *Angew. Chem., Int. Ed.* **2017**, *56*, 3020.
[23] T. Uekert, H. Kasap, E. Reisner, *J. Am. Chem. Soc.* **2019**, *141*, 15201.
[24] T. Uekert, M. F. Kuehnel, D. W. Wakerley, E. Reisner, *Energy Environ. Sci.* **2018**, *11*, 2853.
[25] S. Xie, Z. Shen, J. Deng, P. Guo, Q. Zhang, H. Zhang, C. Ma, Z. Jiang, J. Cheng, D. Deng, Y. Wang, *Nat. Commun.* **2018**, *9*, 1181.
[26] S. Higashimoto, Y. Tanaka, R. Ishikawa, S. Hasegawa, M. Azuma, H. Ohue, Y. Sakata, *Catal. Sci. Technol.* **2013**, *3*, 400.
[27] Y. Xu, L. Z. Zeng, Z. C. Fu, C. Li, Z. Yang, Y. Chen, W. F. Fu, *Catal. Sci. Technol.* **2018**, *8*, 2540.
[28] Z. Chai, T.-T. T. Zeng, Q. Li, L.-Q. Q. Lu, W.-J. J. Xiao, D. Xu, *J. Am. Chem. Soc.* **2016**, *138*, 10128.
[29] H. Hao, L. Zhang, W. Wang, S. Qiao, X. Liu, *ACS Sustainable Chem. Eng.* **2019**, *7*, 10501.
[30] X. Ye, Y. Chen, Y. Wu, X. Zhang, X. Wang, S. Chen, *Appl. Catal., B* **2019**, *242*, 302.
[31] F. Li, Y. Wang, J. Du, Y. Zhu, C. Xu, L. Sun, *Appl. Catal., B* **2018**, *225*, 258.
[32] B. You, X. Liu, N. Jiang, Y. Sun, *J. Am. Chem. Soc.* **2016**, *138*, 13639.
[33] H. G. Cha, K. S. Choi, *Nat. Chem.* **2015**, *7*, 328.
[34] S. Li, K. Su, Z. Li, B. Cheng, *Green Chem.* **2016**, *18*, 2122.
[35] J. Zou, G. Zhang, X. Xu, *Appl. Catal., A* **2018**, *563*, 73.
[36] M. F. Kuehnel, E. Reisner, *Angew. Chem., Int. Ed.* **2018**, *57*, 3290.
[37] K. Imamura, H. Tsukahara, K. Hamamichi, N. Seto, K. Hashimoto, H. Kominami, *Appl. Catal., A* **2013**, *450*, 28.
[38] D. Jiang, X. Chen, Z. Zhang, L. Zhang, Y. Wang, Z. Sun, R. M. Irfan, P. Du, *J. Catal.* **2018**, *357*, 147.
[39] M. J. Lima, A. M. T. Silva, C. G. Silva, J. L. Faria, *J. Catal.* **2017**, *353*, 44.

Chapter 3: A two-dimensional metal–organic framework accelerating visible-light-driven H$_2$ production

3.1 Introduction and significance

The rapid consumption of non-renewable fossil fuels and the relevant critical environmental issues have significantly boosted the demand for clean, renewable and carbon-free energy sources. The conversion of solar energy into green hydrogen (H$_2$) via photocatalytic water splitting stands out as a promising, cost-effective and environmentally friendly technology. However, the realization of large-scale solar-driven photocatalytic H$_2$ production relies on the development of inexpensive, efficient and stable photocatalysts.

In this chapter, Zn$_{0.8}$Cd$_{0.2}$S (ZCS) nanoparticles (NPs) were dispersed on Co-based metal-organic layers (CMLs) using an easy self-assembly approach. A series of advanced characterization studies, e.g., synchrotron-based X-ray absorption near edge structure and time-resolved photoluminescence spectroscopy, disclose the strong electronic interaction between ZCS and CML and the abundant reactive sites on the CML lead to the significantly improved photocatalytic H$_2$-production activity. Our contribution not only demonstrates the application of CML as earth-abundant support and promoter to tremendously boost photocatalytic H$_2$ production without noble-metal co-catalysts, but also sheds light on the tailored design and synthesis of metal-organic layer-based materials for energy conversion and storage.

3.2 A two-dimensional metal–organic framework accelerating visible-light-driven H$_2$ production

This chapter is included as it appears as a journal paper published by **Bingquan Xia**; Jingrun Ran; Shuangming Chen; Li Song; Xuliang Zhang; Liqiang Jing; Shi-Zhang Qiao. A

two-dimensional metal–organic framework accelerating visible-light-driven H_2 production. *Nanoscale* 2019, 11, 8304-8309

Statement of Authorship

Title of Paper	A two-dimensional metal–organic framework accelerating visible-light-driven H2 production
Publication Status	☑ Published ☐ Accepted for Publication ☐ Submitted for Publication ☐ Unpublished and Unsubmitted work written in manuscript style
Publication Details	Bingquan Xia, Jingrun Ran, Shuangming Chen, Li Song, Xuliang Zhang, Liqiang Jing, Shi-Zhang Qiao, A two-dimensional metal–organic framework accelerating visible-light-driven H2 production, Nanoscale, 2019, 11, 8304-8309.

Principal Author

Name of Principal Author (Candidate)	Bingquan Xia
Contribution to the Paper	Research plan, materials synthesis, most of the physical characterization, photocatalytic performance tests, photoelectrochemical and electrochemical measurement, data analysis, and manuscript draft.
Overall percentage (%)	70
Certification:	This paper reports on original research I conducted during the period of my Higher Degree by Research candidature and is not subject to any obligations or contractual agreements with a third party that would constrain its inclusion in this thesis. I am the primary author of this paper.
Signature		Date	15/01/2022

Co-Author Contributions

By signing the Statement of Authorship, each author certifies that:

i.   the candidate's stated contribution to the publication is accurate (as detailed above);

ii.   permission is granted for the candidate in include the publication in the thesis; and

iii. the sum of all co-author contributions is equal to 100% less the candidate's stated contribution.

Name of Co-Author	Jingrun Ran
Contribution to the Paper	Discussion of research plan, help with data collection, manuscript revision
Signature		Date	15/01/2022

Name of Co-Author	Shuangming Chen
Contribution to the Paper	Helped with XAS measurement
Signature		Date	15/01/2022

Name of Co-Author	Li Song		
Contribution to the Paper	Helped with XAS result analysis		
Signature		Date	15/01/2022

Name of Co-Author	Xuliang Zhang		
Contribution to the Paper	Helped with SPS measurement		
Signature		Date	15/01/2022

Name of Co-Author	Liqiang Jing		
Contribution to the Paper	Helped with SPS result analysis		
Signature		Date	15/01/2022

Name of Co-Author	Shizhang Qiao		
Contribution to the Paper	Supervised development of work, helped in manuscript evaluation and acted as corresponding author		
Signature		Date	15/01/2022

Check for updates

A two-dimensional metal–organic framework accelerating visible-light-driven H$_2$ production†

Bingquan Xia, [ID] ‡[a] Jingrun Ran, [ID] ‡[a] Shuangming Chen,[b] Li Song, [ID] [b]
Xuliang Zhang,[c] Liqiang Jing [ID] [c] and Shi-Zhang Qiao [ID] *[a]

The rapid consumption of non-renewable fossil fuels and the relevant critical environmental issues have significantly boosted the demand for clean, renewable and carbon-free energy sources. The conversion of solar energy into green hydrogen (H$_2$) *via* photocatalytic water splitting stands out as a promising, cost-effective and environmentally friendly technology. However, the realization of large-scale solar-driven photocatalytic H$_2$ production relies on the development of inexpensive, efficient and stable photocatalysts. Here, for the first time, we report the fabrication of Zn$_{0.8}$Cd$_{0.2}$S (ZCS) nanoparticles (NPs) dispersed Co-based metal–organic layers (CMLs) using an easy self-assembly approach. The as-synthesized ZCS/ CML composite shows a remarkable visible-light-induced H$_2$-production activity of 18 102 μmol h^{-1} g^{-1}, 492% higher than that of pure ZCS. A series of advanced characterization studies, *e.g.*, synchrotron-based X-ray absorption near edge structure and time-resolved photoluminescence spectroscopy, disclose that the strong electronic interaction between ZCS and CML and the abundant reactive sites on the CML lead to the significantly improved photocatalytic H$_2$-production activity. Our contribution not only demonstrates the application of CML as an earth-abundant support and promoter to tremendously boost photocatalytic H$_2$ production without noble-metal co-catalysts, but also sheds light on the tailored design and synthesis of metal–organic-layer based materials for energy conversion and storage.

Introduction

Over the past decades, industrial development and population explosion have significantly driven the global demand for non-renewable fossil fuels. To address the shortage of fossil fuels and tackle relevant environmental issues due to fossil fuel consumption, aggressive exploration of clean, renewable and carbon-free energy sources has been made in recent decades.[1–3] Among them, hydrogen (H$_2$) has been considered as an ideal energy carrier because it is carbon-free and clean. Besides, as the lightest gas with a relatively high energy density in nature, H$_2$ can be compressed and stored and further transported by currently available facilities. Compared with conventional approaches for H$_2$ generation from chemical

hydrides[4] or electrolysis of water,[5] solar-driven H$_2$ production shows great potential in extracting H$_2$ from water under visible-light irradiation with photocatalysts.[6–8] It is promising to develop efficient, low-cost and robust photocatalysts for H$_2$ production considering the abundant solar light in nature.

Although considerable exploration of sunlight-driven H$_2$ generation has been made on semiconductor photocatalysts, it remains a big challenge to develop high-performance and cost-effective photocatalysts.[9–13] Currently, most of the developed photocatalysts suffer from insufficient H$_2$-production activity mainly due to the easy recombination of photo-excited electron/hole pairs and lack of highly active surface reactive centers.[14–21] An effective solution is to introduce co-catalysts for suppressing electron/hole recombination and providing sufficient active sites to catalyze the surface reactions by lowering the activation energies.[15,22–24] Generally, the noble metal Pt with a large work function is utilized as a co-catalyst in photocatalytic H$_2$ production. However, the high cost and scarcity of precious metals seriously restrict the practical application of photocatalysts. Therefore, it is of great significance to develop high-performance and inexpensive photocatalysts without using noble-metal co-catalysts.

Metal–organic frameworks (MOFs) are one kind of porous crystalline compounds constructed with metal-containing nodes and coordinating organic linkers.[25,26] The diverse com-

[a]*School of Chemical Engineering, The University of Adelaide, Adelaide, SA 5005, Australia. E-mail: s.qiao@adelaide.edu.au*
[b]*National Synchrotron Radiation Laboratory, CAS Center for Excellence in Nanoscience, University of Science and Technology of China, Hefei, Anhui 230029, China*
[c]*Key Laboratory of Functional Inorganic Material Chemistry (Ministry of Education), School of Chemistry and Materials Science, International Joint Research Center for Catalytic Technology, Heilongjiang University, Harbin, Heilongjiang 150080, China*
†Electronic supplementary information (ESI) available: Experimental section, supplementary figures and tables. See DOI: 10.1039/c9nr00663j
‡These authors contribute equally.

positions of MOFs make it possible to tune the structures and introduce specific functionalities. With relatively high surface area and high porosity, MOFs have widespread applications in medicine delivery, gas adsorption and separation, films and heterogeneous catalysis.[27–29] On the other hand, two-dimensional (2D) nanomaterials have gained intensive attention due to their ultrathin thickness, sheet-like structure and large surface area.[30] Benefiting from the strong in-plane covalent bond and atomic thickness, 2D materials with all atoms exposed for modification could obtain unique properties and functionalities at the atomic level through surface modification/functionalization, element doping, and/or defect/vacancy/strain engineering.[30–32] Inheriting the advantages of both MOFs and 2D nanomaterials, 2D MOFs with layered structures, large surface area, ultrathin thickness and high aspect ratio are anticipated to efficiently advance the charge carrier separation and transfer, promote the dispersion of nanosized photocatalysts and boost the surface catalytic procedures.[10,33–37]

Herein, we report a facile approach to fabricate a hybrid of $Zn_{0.8}Cd_{0.2}S$ (ZCS) and ultrathin 2D Co-based metal organic layers (CMLs) by a self-assembly process, yielding a ZCS/CML nanocomposite. This ZCS/CML nanocomposite exhibits a significantly enhanced photocatalytic H_2-production activity of 18 102 $\mu mol\ h^{-1}\ g^{-1}$, surpassing that of bare ZCS by 492%. A range of state-of-art characterization studies, such as synchrotron-based X-ray absorption near edge structure (XANES) and time-resolved PL spectroscopy, reveal that the strong electronic coupling between CML and ZCS greatly advances the interfacial charge dissociation and migration. In addition, the CML can accommodate numerous reduction-active sites. This study not only demonstrates that the CML can greatly advance the visible-light-driven H_2 evolution without noble-metal cocatalysts, but also enlightens the development of MOF-based hetero-structures for solar energy conversion and storage.

Results and discussion

First, the Co-based MOF (Co-MOF, Fig. S1†) was synthesized by a hydrothermal method according to the reported literature.[38] The powder X-ray diffraction (PXRD) pattern of solid Co-MOF is shown in Fig. S2.† The as-prepared solid Co-MOF was then dispersed in ethanol, probe-ultrasonicated and centrifuged to obtain the 2D Co-based MOF layers (abbreviated as CMLs) in the supernatant. The collected CML shows an ultrathin layered morphology in Fig. S3a.† The energy-dispersive X-ray spectroscopy (EDS) result shown in Fig. S3b† confirms the presence of C, N, O and Co elements in the CML, coincident with its chemical composition, which is also confirmed by the high-angle annular dark-field scanning transmission electron microscopy (HAADF-STEM) and elemental mapping images in Fig. S4.† The high-resolution X-ray photoelectron spectroscopy (XPS) recordings of Co 2p, N 1s, C 1s and O 1s spectra for CML are displayed in Fig. S5a, b, c and d,† respectively. Then, the $Zn_{0.8}Cd_{0.2}S$ (ZCS) nanoparticles (NPs) were synthesized by a precipitation-hydrothermal approach as introduced in the

ESI.† Finally, the ZCS NPs were combined with CML by a self-assembly technique through physical mixing at room temperature. The resulting composites were denoted as ZCS/CMLx, where x stands for the volumes (ml) of the CML ethanol solution used to combine with the as-prepared ZCS NPs (x = 0, 2.5, 10, 15 and 25). It can be observed in Fig. 1a that the ZCS NPs with a mean particle size of 21 ± 3 nm (Fig. 1a, inset) are uniformly anchored on the ultrathin CML nanosheet. The presence of ultrathin CML nanosheets can stabilize the ZCS NPs to reduce their aggregation. However, these CML nanosheets cannot direct the growth of ZCS NPs into smaller sizes because the post-synthesis physical coupling between the CML nanosheets and ZCS NPs at room temperature cannot alter the sizes of primary ZCS NPs. Moreover, the lattice spacing of ZCS was determined to be 0.30 nm, corresponding to the (101) plane of ZCS (Fig. 1b). The EDS spectrum of ZCS/CML15 corroborates the presence of Zn, Cd, S, C, N and O elements, in agreement with its elemental composition. The actual Co content was determined to be 0.2 wt% in the ZCS/CML15 using the inductively coupled plasma-optical emission spectrometer (ICP-OES). All the ZCS/CML hybrids exhibit PXRD patterns (Fig. 1d) similar to pristine ZCS. No other diffraction peaks were observed, ascribed to the low content and high dispersion of CML in all the ZCS/CML hybrids.

The photocatalytic H_2-production rates of ZCS/CML hybrids and pure ZCS were tested by measuring the amounts of H_2 produced in an hour. As shown in Fig. 2a, ZCS exhibits a photocatalytic H_2-production rate of 3683 $\mu mol\ h^{-1}\ g^{-1}$. After mixing with CML, the H_2-production rate of ZCS/CML2.5 is increased to 5871 $\mu mol\ h^{-1}\ g^{-1}$. The H_2-production rate of ZCS/CML15 reaches the highest value of 18 102 $\mu mol\ h^{-1}\ g^{-1}$, superior to those of most representative noble-metal-free $Zn_xCd_{1-x}S$ or
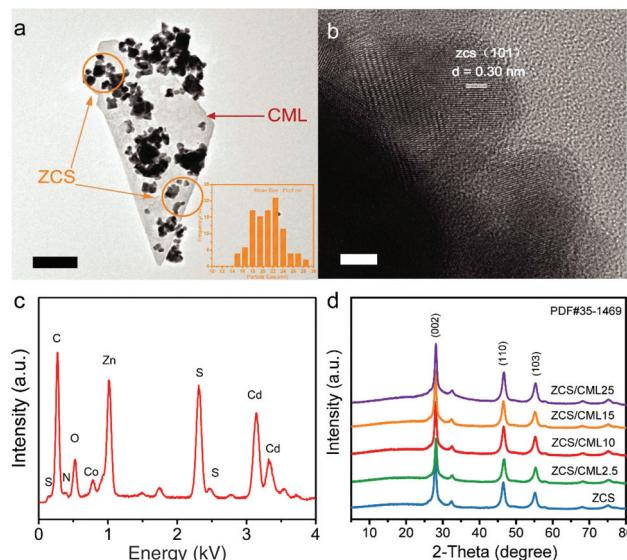
Fig. 1 (a) TEM image and particle size distribution (inset) of ZCS NPs, (b) HRTEM image of ZCS in ZCS/CML15, (c) the EDS spectrum of ZCS/CML15, and (d) PXRD patterns of ZCS and ZCS/CML hybrids (scale bar: a = 200 nm, b = 5 nm).
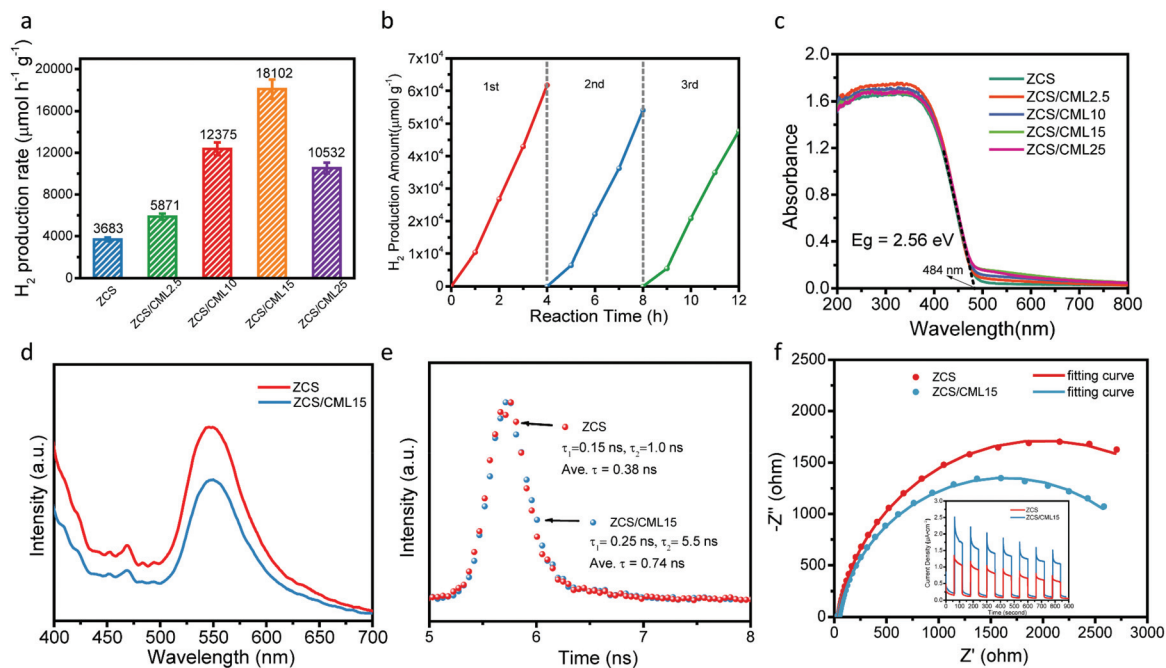
Fig. 2 (a) Photocatalytic H_2-production performance of ZCS and ZCS/CML hybrids in lactic acid aqueous solution under visible-light irradiation ($\lambda > 420$ nm), (b) durability test of ZCS/CML15, (c) UV-Visible diffuse reflectance spectra, (d) steady-state PL spectra, (e) time-resolved PL decay spectra and (f) EIS and (f inset) transient photocurrent response with light on/off.

CdS-based photocatalysts (see Table S1†). However, on further increasing the amount of CML, the H_2-production rate of ZCS/CML25 is decreased to 10 532 μmol h^{-1} g^{-1}. The decline of photocatalytic activity is ascribed to the covered active sites and blocked light absorption by the excessive amount of CML.

To examine the stability of ZCS/CML15, a 12 h photocatalytic reaction was carried out. As shown in Fig. 2b, the H_2-production amount of ZCS/CML15 in the third cycle still retains 77% of that in the first cycle, suggesting the good stability of ZCS/CML15. The slightly lowered photocatalytic activity in the third cycle probably arises from a combination of the following three reasons: (i) the aggregation of ZCS NPs resulting in the decrease of their exposed surface area and active sites, (ii) the consumption of the sacrificial reagent (lactic acid) leading to the reduction in its concentration and (iii) the adsorption of the lactic acid oxidation products on ZCS/CML15, resulting in the covering of its active sites.

To explore the origin of the enhanced photocatalytic activity, the light absorption of ZCS/CML15 was examined by UV-Vis diffuse reflectance spectroscopy. As presented in Fig. 2c, the ZCS/CML composites with various contents of incorporated CML display the unchanged onset absorption edge at 484 nm. No shift of the absorption edge of the ZCS/CML hybrids is found, suggesting that the elements in CML are not doped into the crystal structure of ZCS, in agreement with the above PXRD results. The band gaps of ZCS and CML are calculated to be 2.56 and 3.91 eV, respectively.

Furthermore, the efficiency of charge carrier separation and migration in ZCS/CML15 was studied by a range of characteriz-

ation techniques, such as steady-state and transient-state photo-luminescence (PL) spectroscopy, electrochemical impedance spectroscopy (EIS), transient photocurrent (TPC) density measurement and steady-state surface photovoltage (SPV) spectroscopy. After loading ZCS NPs on the surface of CML nanosheets, ZCS/CML15 exhibits an obviously decreased intensity of the steady-state PL peak at 550 nm, compared to that of pure ZCS (Fig. 2d), suggesting that the presence of CML can efficiently repress the recombination of charge carriers in ZCS. Moreover, the time-resolved PL decay spectra in Fig. 2e show that ZCS/CML15 possesses increased short ($\tau_1 = 0.25$ ns), long ($\tau_2 = 5.5$ ns) and intensity-average (ave. $\tau = 0.74$ ns) lifetimes, compared to those of pure ZCS ($\tau_1 = 0.15$ ns; $\tau_2 = 1.0$ ns; ave. $\tau = 0.38$ ns), indicating the enhanced charge separation and transfer in ZCS/CML15. In addition, as presented in the EIS spectra results (Fig. 2f), ZCS/CML15 presents a smaller semicircle, corresponding to the lower charge transfer resistance (R_t, Table S2†). Moreover, a higher TPC density (Fig. 2f, inset) is observed for ZCS/CML15 than that of ZCS alone, indicating that more efficient exciton dissociation and transportation are achieved in ZCS/CML15. Highly-sensitive steady-state SPV measurement is an effective and direct technique to disclose the properties of photo-induced charges of solid semiconductor materials. The SPV response is directly related to the efficiency of charge carrier separation on the surface of photocatalysts. In Fig. 3a, an apparently increased SPV response for ZCS/CML15 is perceived in comparison with that of ZCS, suggesting that the photo-induced charge carriers are more efficiently dissociated on the surface of ZCS/CML15, due to the combination of ZCS NPs and 2D CML. All the aforemen-

25
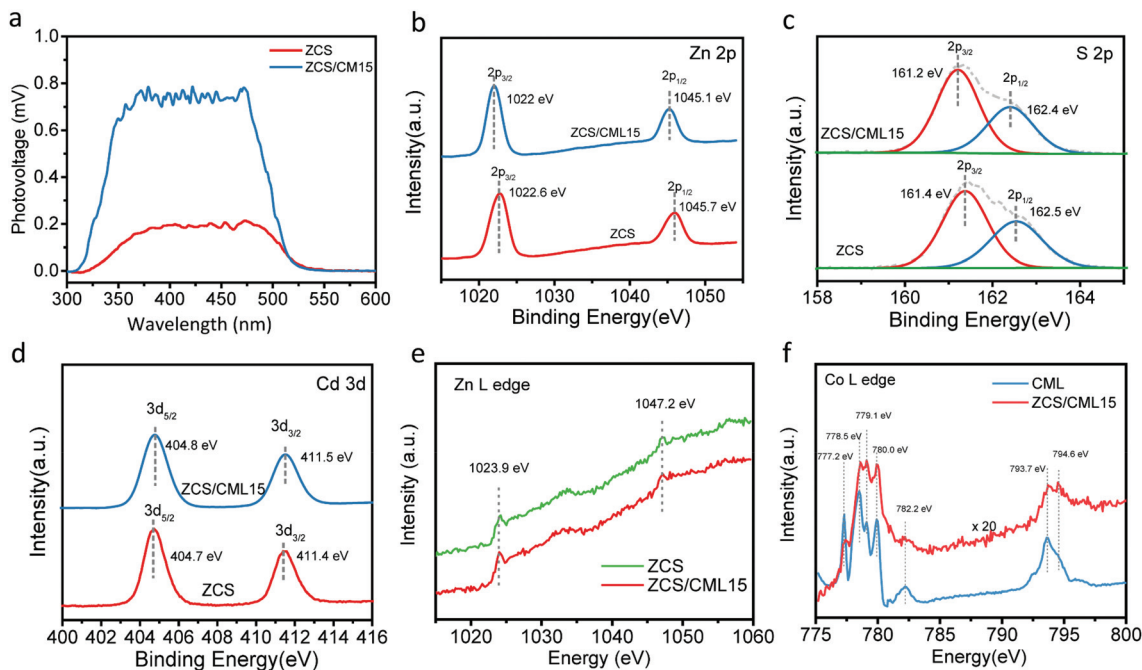
Fig. 3 (a) Surface photovoltage spectra, and high-resolution XPS spectra of (b) Zn 2p, (c) S 2p, and (d) Cd 3d spectra for ZCS and ZCS/CML15, and X-ray absorption near-edge spectra of (e) the Zn L edge and (f) the Co L edge.

tioned results corroborate the high-efficiency dissociation and transport of photo-excited charge carriers in ZCS/CML15.[39,40]

To explore the electronic interaction between ZCS and CML, both surface-sensitive XPS and synchrotron-based XANES studies were conducted. After loading ZCS on CML in ZCS/CML15, the Zn 2p peaks (Fig. 3b) at 1022.6 eV and 1045.7 eV shifted to 1022.0 eV and 1045.1 eV, respectively, suggesting the electron donation from 2D CML to ZCS. In addition, the S 2p peaks (Fig. 3c) of ZCS/CML also shifted in the low binding energy direction, compared to those of ZCS, also indicating the electron extraction from 2D CML to ZCS. Moreover, the Cd 3d peaks (Fig. 3d) of ZCS/CML exhibited a slight shift of 0.1 eV towards the high binding energy direction. Due to the much higher percentage of ZCS in ZCS/CML15, its Zn K edge showed no shift in comparison with that of pure ZCS after introducing CML. Nevertheless, the shift of the Co L edge towards the high photon energy direction reveals the electron migration from 2D CML to ZCS. The above results support electron donation from 2D CML to ZCS in ZCS/CML15.[41,42] The reason might be that ZCS attracts electrons from the electron-rich conjugated systems in the coordination linkers of 1,10-phenanthroline and 4,4′-oxybis(benzoic acid) in 2D CML.

The Brunauer–Emmett–Teller (BET) surface areas of ZCS and ZCS/CML15 acquired from the N_2 sorption isotherms (Fig. 4a and inset) are 93.82 m^2 g^{-1} and 49.38 m^2 g^{-1}, respectively, indicating the intimate contact between CML and ZCS. Then, the Mott–Schottky plots (Fig. 4b) of ZCS and 2D CML disclose that their flat band potentials are −0.99 V and −0.89 V vs. Ag/AgCl electrode, respectively. The calculated band gaps for ZCS and CML (Fig. 2c and 4c) are 2.56 eV and 3.91 eV,
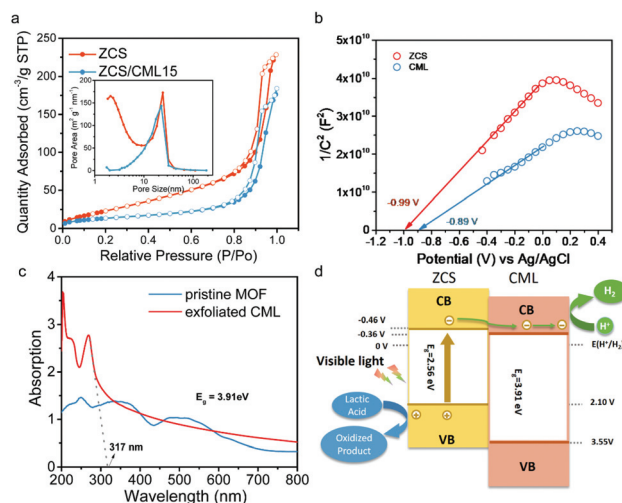
Fig. 4 (a) N_2 sorption isotherms, (inset) pore size distribution curves of ZCS and ZCS/CML15, (b) Mott–Schottky plots of ZCS and CML (c) UV-Vis absorption spectra of pristine Co-MOF and the exfoliated CML and (d) illustration of possible mechanism of photocatalytic H_2 production using the ZCS/CML composite.

respectively. Accordingly, their conduction band (CB) edge potentials are estimated to be −0.46 V and −0.36 V, respectively. Then their valence band (VB) edge potentials are calculated to be 2.10 V and 3.55 V, respectively. On the basis of the above comprehensive experimental results, a possible photocatalytic H_2-production mechanism in the ZCS/CML15 hybrid is proposed and illustrated in Fig. 4d where a type II (stagger-

ing type) hetero-junction consisting of ZCS and 2D CML is constructed.[43–45] The irradiation of visible light ($\lambda > 420$ nm) generates photo-excited electrons and holes on the CB and VB of ZCS, respectively. The strong electronic coupling between ZCS and 2D CML combined with their formation of a type II hetero-junction would promote the efficient separation and migration of photo-excited electron–hole pairs, resulting in the transfer of photo-excited electrons to the CB of the 2D CML and the remaining photo-excited holes in the VB of ZCS. Subsequently, the photo-excited electrons are further transported to the surface of ultrathin 2D CML nanosheets with numerous atomically dispersed single Co sites serving as catalytic sites to reduce the protons for H_2 evolution. In the meantime, the photo-excited holes left on the VB of ZCS NPs oxidize lactic acid to generate oxidation products.

Conclusions

In summary, we report the synthesis of a ZCS nanoparticle decorated Co-based metal organic layer (CML) by a simple self-assembly method through physical mixing at room temperature. The hybridized ZCS/CML nanocomposite presents a remarkable H_2-production rate of 18 102 μmol h^{-1} g^{-1}, about 492% higher than that of bare ZCS. Comprehensive characterization studies, such as synchrotron-based X-ray absorption near-edge spectroscopy and transient-state photoluminescence spectroscopy, reveal that the strongly interactive nature at the ZCS/CML interface, the high-efficiency interfacial charge transfer and the abundant reduction catalytic sites on CML, arouse the significant enhancement of photocatalytic performance. This work not only demonstrates that the interfacial engineering between the two-dimensional CML and the semiconductor photocatalyst can greatly increase its activity, but also pave a way to the exploration of noble-metal-free, high-performance and stable MOF-based photocatalysts for solar fuel production.

Conflicts of interest

There are no conflicts to declare.

Acknowledgements

References

1 E. G. Hertwich, T. Gibon, E. A. Bouman, A. Arvesen, S. Suh, G. A. Heath, J. D. Bergesen, A. Ramirez, M. I. Vega and L. Shi, *Proc. Natl. Acad. Sci. U. S. A.*, 2015, **112**, 6277–6282.

2 N. S. Lewis, *Science*, 2016, **351**, aad1920.

3 D. Larcher and J.-M. Tarascon, *Nat. Chem.*, 2014, **7**, 19.

4 Q.-L. Zhu and Q. Xu, *Energy Environ. Sci.*, 2015, **8**, 478–512.

5 Y. Zheng, Y. Jiao, A. Vasileff and S.-Z. Qiao, *Angew. Chem., Int. Ed.*, 2018, **57**, 7568–7579.

6 G. Han, Y.-H. Jin, R. A. Burgess, N. E. Dickenson, X.-M. Cao and Y. Sun, *J. Am. Chem. Soc.*, 2017, **139**, 15584–15587.

7 L. Li, J. Yan, T. Wang, Z.-J. Zhao, J. Zhang, J. Gong and N. Guan, *Nat. Commun.*, 2015, **6**, 5881.

8 Q. Li, B. Guo, J. Yu, J. Ran, B. Zhang, H. Yan and J. R. Gong, *J. Am. Chem. Soc.*, 2011, **133**, 10878–10884.

9 F. M. Zhang, J. L. Sheng, Z. Di Yang, X. J. Sun, H. L. Tang, M. Lu, H. Dong, F. C. Shen, J. Liu and Y. Q. Lan, *Angew. Chem., Int. Ed.*, 2018, **57**, 12106–12110.

10 Q. Li, F. Zhao, C. Qu, Q. Shang, Z. Xu, L. Yu, J. R. McBride and T. Lian, *J. Am. Chem. Soc.*, 2018, **140**, 11726–11734.

11 X. Zhao, J. Feng, J. Liu, W. Shi, G. Yang, G. Wang and P. Cheng, *Angew. Chem., Int. Ed.*, 2018, **57**, 9790–9794.

12 L. Cao, S. Sahu, P. Anilkumar, C. E. Bunker, J. Xu, K. A. S. Fernando, P. Wang, E. A. Guliants, K. N. Tackett and Y.-P. Sun, *J. Am. Chem. Soc.*, 2011, **133**, 4754–4757.

13 W. Wu, C. Jiang and V. A. L. Roy, *Nanoscale*, 2015, **7**, 38–58.

14 J. Ran, X. Wang, B. Zhu and S. Z. Qiao, *Chem. Commun.*, 2017, **53**, 9882–9885.

15 J. Ran, G. Gao, F.-T. Li, T.-Y. Ma, A. Du and S.-Z. Qiao, *Nat. Commun.*, 2017, **8**, 13907.

16 M. Ni, M. K. H. Leung, D. Y. C. Leung and K. Sumathy, *Renewable Sustainable Energy Rev.*, 2007, **11**, 401–425.

17 H. Liu, C. Xu, D. Li and H. L. Jiang, *Angew. Chem., Int. Ed.*, 2018, **57**, 5379–5383.

18 P. Lianos, *Appl. Catal., B*, 2017, **210**, 235–254.

19 J. Yang, D. Wang, H. Han and C. Li, *Acc. Chem. Res.*, 2013, **46**, 1900–1909.

20 X. Zong, J. Han, G. Ma, H. Yan, G. Wu and C. Li, *J. Phys. Chem. C*, 2011, **115**, 12202–12208.

21 B. Sun, W. Zhou, H. Li, L. Ren, P. Qiao, W. Li and H. Fu, *Adv. Mater.*, 2018, **30**, 1804282.

22 J. Ran, J. Zhang, J. Yu, M. Jaroniec and S. Z. Qiao, *Chem. Soc. Rev.*, 2014, **43**, 7787–7812.

23 T. Yoshinaga, M. Saruyama, A. Xiong, Y. Ham, Y. Kuang, R. Niishiro, S. Akiyama, M. Sakamoto, T. Hisatomi, K. Domen and T. Teranishi, *Nanoscale*, 2018, **10**, 10420–10427.

24 S. Patnaik, G. Swain and K. M. Parida, *Nanoscale*, 2018, **10**, 5950–5964.

25 T. Zhang and W. Lin, *Chem. Soc. Rev.*, 2014, **43**, 5982–5993.

26 S. Wang, B. Y. Guan and X. W. (David) Lou, *Energy Environ. Sci.*, 2018, **11**, 306–310.

27 K. S. Park, Z. Ni, A. P. Cote, J. Y. Choi, R. Huang, F. J. Uribe-Romo, H. K. Chae, M. O'Keeffe and O. M. Yaghi, *Proc. Natl. Acad. Sci. U. S. A.*, 2006, **103**, 10186–10191.

28 B. Liu, H. Shioyama, T. Akita and Q. Xu, *J. Am. Chem. Soc.*, 2008, **130**, 5390–5391.

29 Q.-L. Zhu and Q. Xu, *Chem. Soc. Rev.*, 2014, **43**, 5468–5512.

30 D. Feng, T. Lei, M. R. Lukatskaya, J. Park, Z. Huang, M. Lee, L. Shaw, S. Chen, A. A. Yakovenko, A. Kulkarni, J. Xiao,

K. Fredrickson, J. B. Tok, X. Zou, Y. Cui and Z. Bao, *Nat. Energy*, 2018, **3**, 30–36.

31 C. Tan, X. Cao, X.-J. Wu, Q. He, J. Yang, X. Zhang, J. Chen, W. Zhao, S. Han, G.-H. Nam, M. Sindoro and H. Zhang, *Chem. Rev.*, 2017, **117**, 6225–6331.

32 C. Tan, Z. Liu, W. Huang and H. Zhang, *Chem. Soc. Rev.*, 2015, **44**, 2615–2628.

33 X. Wang, L. Chen, S. Y. Chong, M. A. Little, Y. Wu, W.-H. Zhu, R. Clowes, Y. Yan, M. A. Zwijnenburg, R. S. Sprick and A. I. Cooper, *Nat. Chem.*, 2018, **10**, 1180–1189.

34 L. Peng, Z. Fang, Y. Zhu, C. Yan and G. Yu, *Adv. Energy Mater.*, 2018, **8**, 1–19.

35 M. Zhu, Z. Sun, M. Fujitsuka and T. Majima, *Angew. Chem., Int. Ed.*, 2018, **57**, 2160–2164.

36 G. S. Papaefstathiou, T. Friščić and L. R. MacGillivray, *J. Am. Chem. Soc.*, 2005, **127**, 14160–14161.

37 Y. Xiao, Y. Qi, X. Wang, X. Wang, F. Zhang and C. Li, *Adv. Mater.*, 2018, **30**, 1803401.

38 Z. B. Han, X. N. Cheng and X. M. Chen, *Cryst. Growth Des.*, 2005, **5**, 695–700.

39 J. Ran, H. Wang, H. Jin, C. Ling, X. Zhang, H. Ju, L. Jing, J. Wang, R. Zheng and S.-Z. Qiao, *J. Mater. Chem. A*, 2018, **6**, 23278–23282.

40 Y. Jiang, H. Ning, C. Tian, B. Jiang, Q. Li, H. Yan, X. Zhang, J. Wang, L. Jing and H. Fu, *Appl. Catal., B*, 2018, **229**, 1–7.

41 J. Ran, T. Y. Ma, G. Gao, X.-W. Du and S. Z. Qiao, *Energy Environ. Sci.*, 2015, **8**, 3708–3717.

42 K. Zhang, J. Ran, B. Zhu, H. Ju, J. Yu, L. Song and S.-Z. Qiao, *Small*, 2018, **14**, 1801705.

43 D. Wang, D. Han, Z. Shi, J. Wang, J. Yang, X. Li and H. Song, *Appl. Catal., B*, 2018, **227**, 61–69.

44 Y. Zhou, Z. Tian, Z. Zhao, Q. Liu, J. Kou, X. Chen, J. Gao, S. Yan and Z. Zou, *ACS Appl. Mater. Interfaces*, 2011, **3**, 3594–3601.

45 J. Fu, Q. Xu, J. Low, C. Jiang and J. Yu, *Appl. Catal., B*, 2019, **243**, 556–565.

Two-dimensional Metal-Organic Framework Accelerating Visible-Light-driven Hydrogen Production

Bingquan Xia, [a†] Jingrun Ran, [a†] Shuangming Chen, [b] Li Song, [b] Xuliang Zhang, [c] Liqiang Jing, [c] and Shi-Zhang Qiao *[a]

a. School of Chemical Engineering, The University of Adelaide, Adelaide, SA 5005, Australia
    E-mail: s.qiao@adelaide.edu.au

b. National Synchrotron Radiation Laboratory CAS Center for Excellence in Nanoscience, University of Science and Technology of China, Hefei, Anhui 230029, China

c. Key Laboratory of Functional Inorganic Material Chemistry (Ministry of Education), School of Chemistry and Materials Science, International Joint Research Center for Catalytic Technology, Heilongjiang University, Harbin, Heilongjiang 150080, China

I. Experimental Section

1.1 Materials synthetic procedures

All chemicals were purchased from Sigma-Aldrich without further purification.

Preparation of Co-MOF: Co-MOF was prepared according to the reported method.[1] Briefly, $Co(NO_3)_2 \cdot 3H_2O$ (0.119 g, 0.5 mmol), 1,10-phenanthroline (0.091 g, 0.5 mmol), 4,4′-oxybis(benzoic acid) (0.129 g, 0.5 mmol) and triethylamine (0.101 g, 1 mmol), were added into 10 mL H_2O. The suspension was then transferred into a Teflon-lined autoclave and heated to 160 °C and kept for 6 days and then cooled to room temperature at a rate of 5 K h^{-1}. Red crystals were obtained after being washed with water and dried in air.

Preparation of ultrathin Co-MOF layer (CML): 100 mg of the as-prepared Co-MOF was added into 100 mL ethanol and the suspension was then probe-ultrasonicated for 10 hours followed by high-speed centrifugation. Then the as-exfoliated 2D CML in the supernatant was preserved for further use.

Preparation of $Zn_{0.8}Cd_{0.2}S$ (ZCS): ZCS was prepared by a precipitation-hydrothermal approach. Briefly, 7.15 g $Zn(NO_3)_2 \cdot 2H_2O$ and 2.14 g $Cd(NO_3)_2 \cdot 4H_2O$ were dissolved in 217 mL deionized water and stirred at room temperature for 30 min. After that, 50 mL 0.9 M Na_2S aqueous solution was added dropwise into the above solution followed by stirring for about 2 hours at room temperature. Then the mixture was transferred into a 500 mL Teflon-lined stainless-steel autoclave and maintained at 180 °C for 12 h. The final products were washed with deionized water and ethanol, respectively, for two times to remove any residuals and then dried at 60 °C under vacuum.

Preparation of ZCS/CML hybrids: The ZCS/CML hybrids were fabricated by a self-assembly method using the as-synthesized ZCS and 2D CML ethanol solution. In a typical procedure, 50 mg ZCS nanoparticles were mixed with 2.5, 10.0, 15.0 and 25.0 mL of 2D CML ethanol solution, respectively. Then the suspension was mechanically ground for 5 min. After the ethanol naturally evaporated, the solid left was again ground into powders as the final products. The resulting samples were labelled as ZCS/CML2.5, ZCS/CML10, ZCS/CML15 and ZCS/CML25, respectively.

1.2 Physicochemical characterizations

PXRD was performed on Rigaku MiniFlex 600 X-Ray Diffractometer with Cu Kα to characterize the crystal structure. The morphologies and structures of as-prepared samples were observed by TEM (JEOL ARM-200CF with double Cs correctors, 200 kV). UV-Vis diffuse reflectance spectra were collected for the dry-pressed disk samples with an UV-Vis spectrophotometer (UV2600, Shimadzu, Japan) using $BaSO_4$ as the reflectance standard. The PL spectra were recorded on a RF-5301PC

spectrofluorophotometer (Shimadzu, Japan) at room temperature. Time-resolved PL decay curves were obtained on a FLS1000 fluorescence lifetime spectrophotometer (Edinburgh Instruments, UK). XPS measurement was conducted on a VG ESCALAB 210 XPS spectrometer with Mg Kα source. All the binding energies were referenced to the C 1s peak at 284.8 eV. XANES spectra of the samples were collected at the soft X-ray absorption beamline of the Australian Synchrotron (AS). Elemental contents were determined by ICP-OES (Inductively Coupled Plasma-Optical Emission Spectrometer) on Prodigy 7. The steady-state SPV spectra were acquired on a home-built apparatus.

1.3 Photocatalytic H_2 production measurement

The experimental measurements of photocatalytic H_2 production were carried out in a 100 ml Pyrex flask at room temperature and atmospheric pressure. A 300 W Xenon arc lamp with a UV-cutoff filter ($\lambda > 420$ nm) was utilized as a visible-light source to trigger the photocatalytic reaction. Briefly, 20 mg of the as-prepared photocatalyst was added into 80 ml of lactic acid (88 vol%) solution. Before irradiation, the suspension was purged with Argon for 0.5 h to remove any dissolved air and keep the reaction system under anaerobic conditions. Next, 0.2 ml gas was intermittently sampled through the septum, and H_2 content was analyzed by Gas chromatography (Clarus 480, PerkinElmer, USA, TCD, Ar as a carrier gas and 5 Å molecular sieve column). Before the experiment, all glassware was rinsed carefully with de-ionized water.

1.4 Electrochemical and photoelectrochemical measurements

EIS measurements were performed on an electrochemical analyzer (CHI650D instruments) in a standard three-electrode system utilizing the synthesized samples as the working electrodes, Ag/AgCl (saturated KCl) as a reference electrode, and Pt wire as the counter electrode. The EIS were recorded over a range from 1 to $2*10^5$ Hz with an AC amplitude of 0.02 V. 0.5 M Na_2SO_4 aqueous solution was utilized as the electrolyte. Transient photocurrent was measured in the same three-electrode system. A 300 W Xenon light with a UV-cutoff filter ($\lambda > 420$ nm) was applied as the light source. 0.5 M Na_2SO_4 aqueous solution was used as the electrolyte. The working electrodes were synthesized as follows: 0.01 g sample and 0.03 g polyethylene glycol (PEG; molecular weight: 20,000) were ground with 2.0 ml of ethanol to make a slurry. Then the slurry was coated onto a 1.2 cm * 0.8 cm FTO glass electrode by the doctor blade approach. The obtained electrode was dried in an oven and heated at 623 K for 0.5 h under flowing N_2.

S3

II. Supplementary Figures
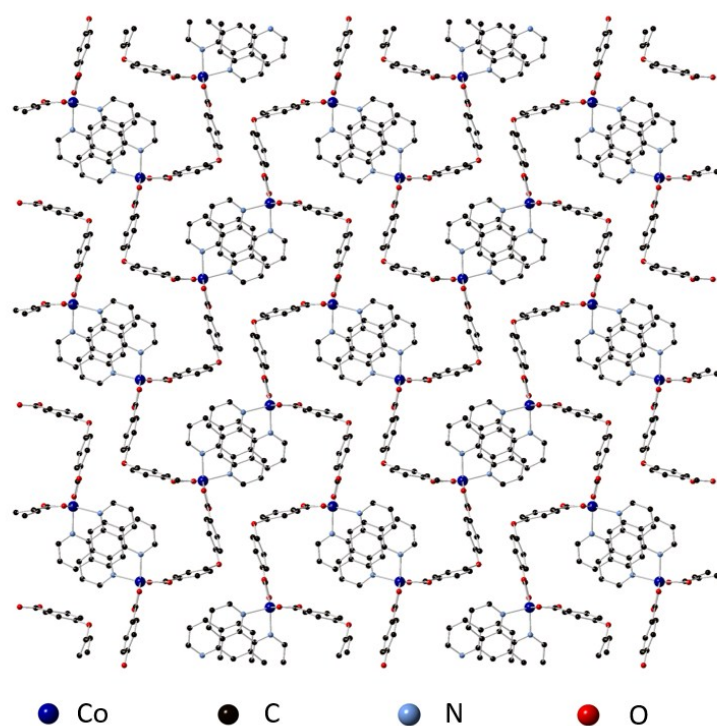
Figure S1. Crystal Structure of Co-MOF. (Note: Hydrogen atoms bonded to C, N and O are not shown.)
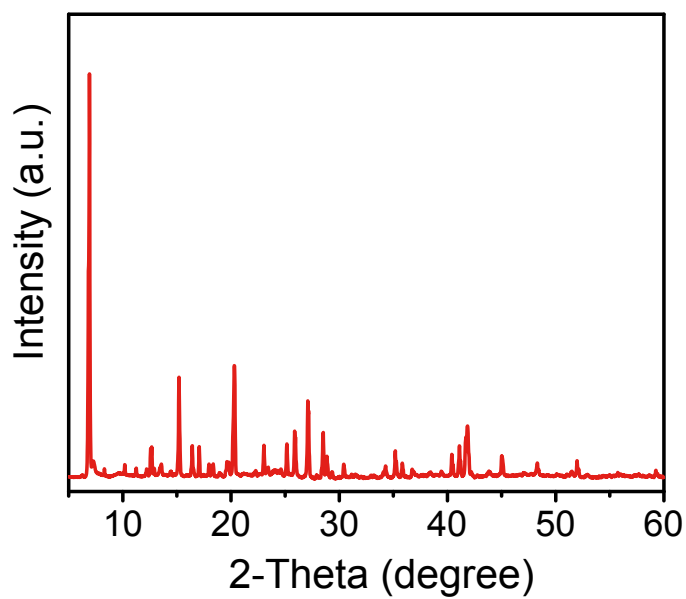
Figure S2. PXRD pattern of Co-MOF.
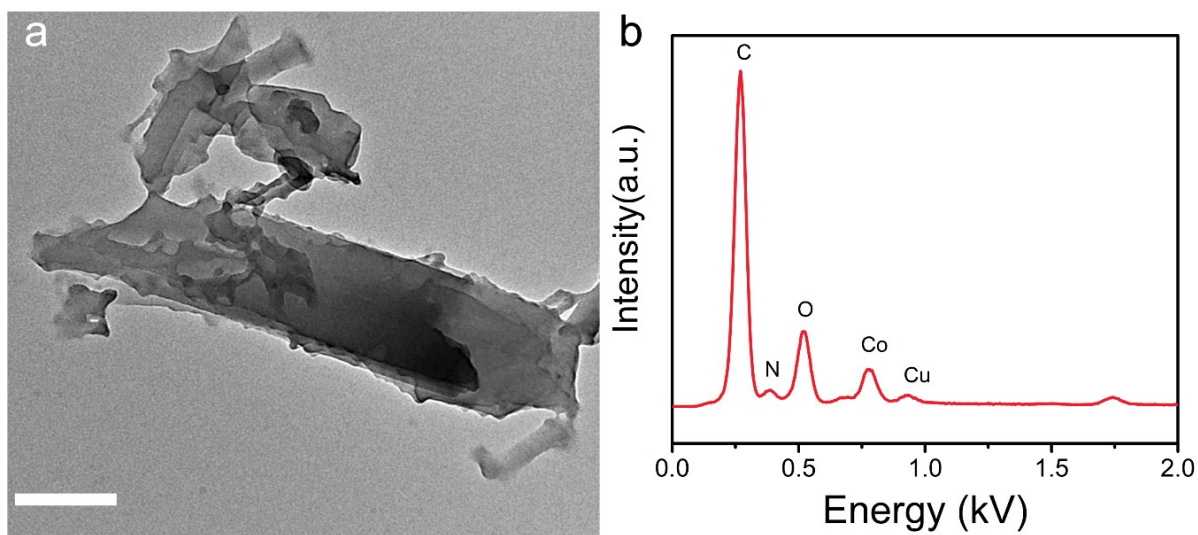
Figure S3. (a) TEM image and (b) EDS spectrum of 2D CML (scale bar in a: 200 nm).
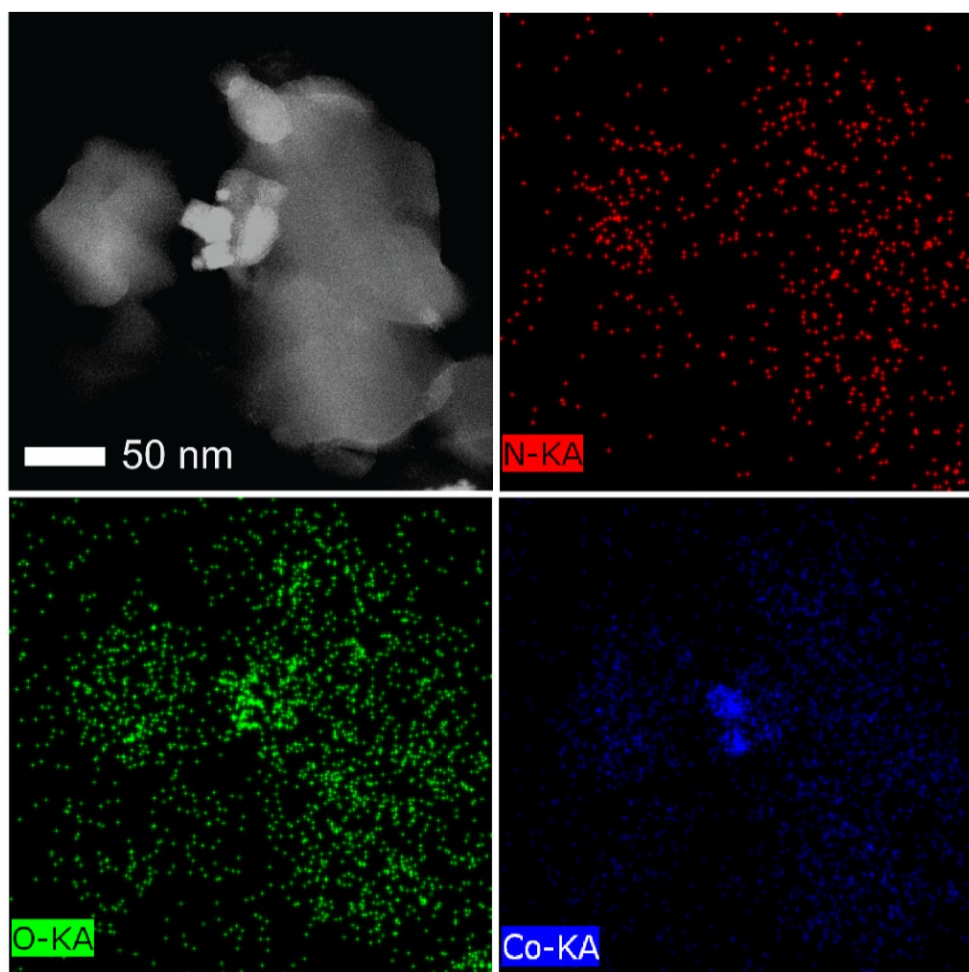
Figure S4. HAADF-STEM and the corresponding element mapping images of CML.

S5
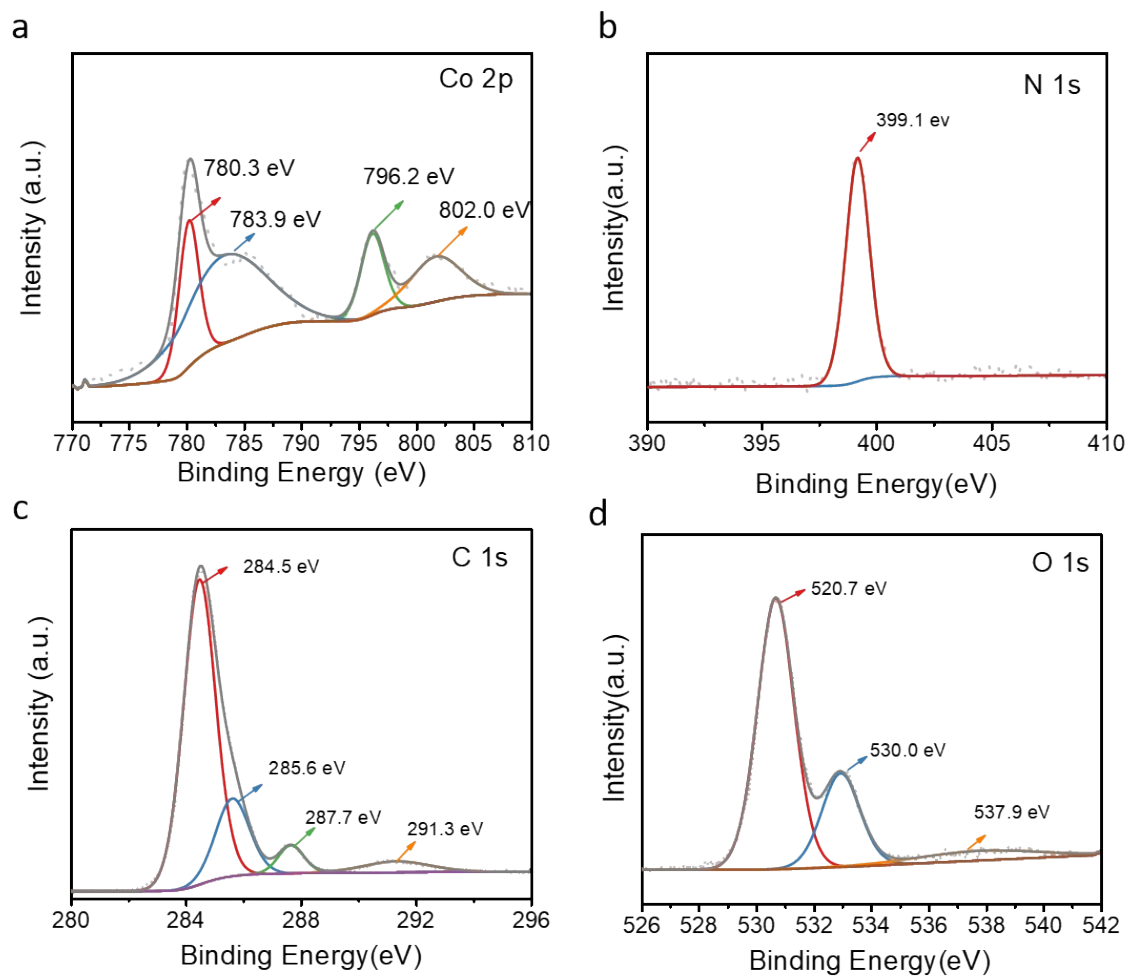
Figure S5. High-resolution XPS spectra of (a) Co 2p, (b) N 1s, (c) C 1s and (d) O 1s in CML.

III. Supplementary Tables

Table S1. A comparison of the photocatalytic H_2-production activities of the representative noble-metal-free $Zn_xCd_{1-x}S$ or CdS based systems

Photocatalyst	Co-catalyst	Enhancement factor	H_2 production rate ($\mu mol\ h^{-1}\ g^{-1}$)	Light/ dose	Ref.
$Zn_{0.8}Cd_{0.2}S/CML15$	CML	4.92	18100	$\lambda > 420$ nm/ 20 mg	This work
$Zn_{1-x}Cd_xS/10$ wt.% α-Fe_2O_3	α-Fe_2O_3	24	540	$\lambda > 420$ nm/ 100 mg	[2]
P-ZnCdS/CdS-VS_2	VS_2	7.6	192	$\lambda > 400$ nm/ 5 mg	[3]
0.5 wt% $Fe_{0.3}Pt_{0.7}$-ZnCdS	$Fe_{0.3}Pt_{0.7}$	3.06	2230	$\lambda > 400$ nm/ 100 mg	[4]
0.5 wt% Pt-ZnCdS	Pt	2.20	1630	$\lambda > 420$ nm/ 100 mg	[4]
CdS/CNT	CNT	2.23	1770	$\lambda > 420$ nm/ 20 mg	[5]
CdS/Graphene	Graphene	4.87	56000	$\lambda > 420$ nm/ 20 mg	[6]
CdS/N-Graphene	N-Graphene	5.25	1050	$\lambda > 420$ nm/ 200 mg	[7]
CdS/DWNT/s-MoS_2	DWNT/s-MoS_2	N/A	5730	$\lambda > 420$ nm/ 20 mg	[8]

Table S2. Fitted results of resistance obtained from electrochemical impedance spectra

Resistance	ZCS	ZCS/CML15
R_s (ohm)	47.15	43.10
R_t (ohm)	3818	3186

S7

IV. Supplementary references

1 Z. B. Han, X. N. Cheng and X. M. Chen, *Cryst. Growth Des.*, 2005, **5**, 695–700.

2 M. Imran, A. Bin Yousaf, P. Kasak, A. Zeb and S. J. Zaidi, *J. Catal.*, 2017, **353**, 81–88.

3 F.-T. Liu, K. Li, T. Li, Z.-X. Wang, Y.-Z. Lin and Y. Zhang, *Catal. Sci. Technol.*, 2018, **9**, 583–587.

4 D. Shu, H. Wang, Y. Wang, Y. Li, X. Liu, X. Chen, X. Peng, X. Wang, P. Ruterana and H. Wang, *Int. J. Hydrogen Energy*, 2017, **42**, 20888–20894.

5 J. Chen, Q. Chen, P. Guo, M. Liu, X. Wang, L. Guo, M. Wang and K. Zhang, *Int. J. Hydrogen Energy*, 2013, **38**, 13091–13096.

6 Q. Li, B. Guo, J. Yu, J. Ran, B. Zhang, H. Yan and J. R. Gong, *J. Am. Chem. Soc.*, 2011, **133**, 10878–10884.

7 L. Jia, D.-H. Wang, Y.-X. Huang, A.-W. Xu and H.-Q. Yu, *J. Phys. Chem. C*, 2011, **115**, 11466–11473.

8 M. Meng-Jung Li, P. Mills, S. M. Fairclough, A. Robertson, Y.-K. Peng, J. Warner, C. Nie, E. Flahaut and S. C. Edman Tsang, *Chem. Commun.*, 2016, **52**, 13596–13599.

Chapter 4: Metal-organic framework with atomically dispersed Ni–N$_4$ sites for greatly-raised visible-light photocatalytic H$_2$ production

4.1 Introduction and significance

The depletion of traditional fossil fuels and related environmental issues have spurred the demand for clean and sustainable energy resources to achieve carbon neutrality. Solar energy has been considered as an ideal sustainable alternative to the traditional carbon-based fuel, because of its affordability and availability. However, the intermittent and irregular sunlight and/or weather changes need to be taken into consideration. To overcome this difficulty, it has been proposed to transform solar energy into chemical fuels with higher energy densities. Hydrogen outstands as a promising energy carrier for transforming solar energy because of its high energy density and no by-product produced after combustion. It should also be noted that to facilitate the conversion process, active, robust and cheap photocatalysts are required for large-scale photocatalytic H$_2$ evolution reaction (p-HER), which transforms solar energy into chemical energy.

Based on the work of introducing Co-based MOF to Zn$_{0.8}$Cd$_{0.2}$S for photocatalytic hydrogen production in Chapter 3, an easily prepared Ni-imidazole framework (NiIm) with abundant Ni-N$_4$ reactive sites was proposed to improve the photocatalytic performance for hydrogen production. In this chapter, the decoration of the Ni-imidazole framework (NiIm) with CdS nanorods was fabricated and tested for p-HER. Highlights of this paper include:

(1) Physicochemical characterizations and theoretical calculations reveal strong interactions at the CdS/NiIm interface, and the presence of numerous Ni-N$_4$ active sites on NiIm leads to significant performance enhancement.

(2) NiIm is demonstrated to be an affordable and abundant cocatalyst that remarkably enhances the p-HER.

(3) The further development in the design and preparation of metal-organic framework-based materials for various applications in photocatalysis and related subjects is enlightened.

4.2 Metal-organic framework with atomically dispersed Ni–N$_4$ sites for greatly-raised visible-light photocatalytic H$_2$ production

This chapter is included as it appears as a journal paper published by **Bingquan Xia**, Yi Yang, Yanzhao Zhang, Yang Xia, Mietek Jaroniec, Jiaguo Yu, Jingrun Ran, Shi-Zhang Qiao. Metal–organic framework with atomically dispersed Ni–N$_4$ sites for greatly-raised visible-light photocatalytic H$_2$ production. ***Chemical Engineering Journal.*** 2022, 431, 133944.

Statement of Authorship

Title of Paper	Metal–organic framework with atomically dispersed Ni–N4 sites for greatly-raised visible-light photocatalytic H2 production
Publication Status	☑ Published ☐ Accepted for Publication ☐ Submitted for Publication ☐ Unpublished and Unsubmitted work written in manuscript style
Publication Details	Bingquan Xia, Yi Yang, Yanzhao Zhang, Yang Xia, Mietek Jaroniec, Jiaguo Yu, Jingrun Ran, Shi-Zhang Qiao; Chemical Engineering Journal, 2022, 431, 133944. https://doi.org/10.1016/j.cej.2021.133944

Principal Author

Name of Principal Author (Candidate)	Bingquan Xia	
Contribution to the Paper	Research plan, materials synthesis, most of the physical characterization,photocatalytic performance tests, photoelectrochemical and electrochemical measurement, data analysis, and manuscript draft.	
Overall percentage (%)	80	
Certification:	This paper reports on original research I conducted during the period of my Higher Degree by Research candidature and is not subject to any obligations or contractual agreements with a third party that would constrain its inclusion in this thesis. I am the primary author of this paper.	
Signature		Date 15/01/2022

Co-Author Contributions

By signing the Statement of Authorship, each author certifies that:

  i. the candidate's stated contribution to the publication is accurate (as detailed above);

  ii. permission is granted for the candidate in include the publication in the thesis; and

  iii. the sum of all co-author contributions is equal to 100% less the candidate's stated contribution.

Name of Co-Author	Yi Yang	
Contribution to the Paper	Help with materials synthesis	
Signature		Date 15/01/2022

Name of Co-Author	Yanzhao Zhang	
Contribution to the Paper	Help with data analysis	
Signature		Date 15/01/2022

Name of Co-Author	Yang Xia		
Contribution to the Paper	Help with physicochemcial characterisation		
Signature		Date	15/01/2022

Name of Co-Author	Mietek Jaroniec		
Contribution to the Paper	Helped to edit the manuscript.		
Signature		Date	15/01/2022

Name of Co-Author	Jiaguo Yu		
Contribution to the Paper	Helped to evaluate and edit the manuscript and acted as corresponding author.		
Signature		Date	15/01/2022

Name of Co-Author	Jingrun Ran		
Contribution to the Paper	Discussion of research plan, manuscript revision, and acted as corresponding author		
Signature		Date	15/01/2022

Name of Co-Author	Shizhang Qiao		
Contribution to the Paper	Supervised development of work, helped in manuscript evaluation and acted as corresponding author		
Signature		Date	15/01/2022

Metal–organic framework with atomically dispersed Ni–N$_4$ sites for greatly-raised visible-light photocatalytic H$_2$ production

Bingquan Xia [a], Yi Yang [b], Yanzhao Zhang [a], Yang Xia [b], Mietek Jaroniec [c], Jiaguo Yu [b,*], Jingrun Ran [a,*], Shi-Zhang Qiao [a,*]

[a] *School of Chemical Engineering and Advanced Materials, The University of Adelaide, Adelaide, SA 5005, Australia*
[b] *Laboratory of Solar Fuel, Faculty of Materials Science and Chemistry, China University of Geosciences, 388 Lumo Road, Wuhan 430074, PR China*
[c] *Department of Chemistry and Biochemistry & Advanced Materials and Liquid Crystal Institute, Kent State University, Kent, OH 44242, United States of America*

A B S T R A C T

The depletion of traditional fossil fuels and related environmental issues have increased the demand for clean and sustainable energy resources to achieve carbon neutrality. Active, robust and cheap photocatalysts are required for large-scale photocatalytic H$_2$ evolution reaction (p–HER), which transforms solar energy into chemical energy. Here we report the decoration of Ni-imidazole framework (NiIm) with CdS nanorods for p–HER. The p–HER rate of CdS/NiIm hybrid sharply increased by about 14.23 times to 21,712 μmol h^{-1} g^{-1} when compared with that of CdS alone. Physicochemical characterizations and theoretical calculations reveal strong interactions at the CdS/NiIm interface and the presence of numerous Ni–N$_4$ active sites on NiIm leading to the significant performance enhancement. This work demonstrates that NiIm acts as an affordable and abundant co-catalyst that remarkably enhances the p–HER, and enlightens the further development in the design and preparation of metal−organic framework-based materials for various applications in photocatalysis and related subjects.

1. Introduction

Single-atom catalysts (SACs) have attracted a lot of attention due to their distinctive performance in various chemical reactions linked to the abundance of single-atom active sites [1–5]. The distinct advantages of SACs arise from the following factors: i) the unsaturated coordination sites and unique electronic structures leading to the unusually high activity/selectivity; ii) the highest efficiency in the usage of single-atom sites leading to a tremendous decrease in the consumption of catalytic materials; iii) the single-atom reactive sites facilitate the exploration of the catalytic mechanisms, and iv) the well-defined atomic-level structure facilitates the understanding of structure–activity correlation [6,7]. Thus, SACs have been gaining increasing attention in many applications, *e.g.,* electrocatalysis [8–11], photocatalysis [12–17], thermo-catalysis [18,19], and photo-electrocatalysis [20,21].

In the past several decades, metal–organic frameworks (MOFs) have become one of the most attractive classes of nanomaterials because of their outstanding properties related to: i) the accessibility of reactive sites for catalysis and easy transfer of reactants/products due to the high porosity of MOFs [22]; ii) facile tunability of structures for acquiring ideal physicochemical properties toward desired catalytic reactions [23]; iii) the well-defined crystalline structures favoring the exploration of the structure–activity correlation [24]; iv) the porous structure creates short transfer pathways for electron-hole pairs before their contact with reactants, thus enhancing the electron-hole dissociation. Especially, the atomically-dispersed and under-coordinated metal sites in MOFs can greatly improve the catalytic reactions [25–28]. Thus, these MOFs are often coupled with the other materials to achieve synergistically-enhanced activity and selectivity.

In light of the present global energy/environmental issues caused by burning fossil fuels, great efforts have been devoted to seeking green and renewable energy resources. Photocatalysis is an environmentally benign, cost-effective and promising strategy, which can transform inexhaustible sunlight into carbon-free hydrogen (H$_2$) fuel via solar water splitting [29–37]. The large-scale application of this strategy relies upon the development of high-performance and inexpensive photocatalysts [38–44]. As a result, the utilization of MOFs with atomically dispersed metal sites to construct hybridized photocatalysts for boosted

---
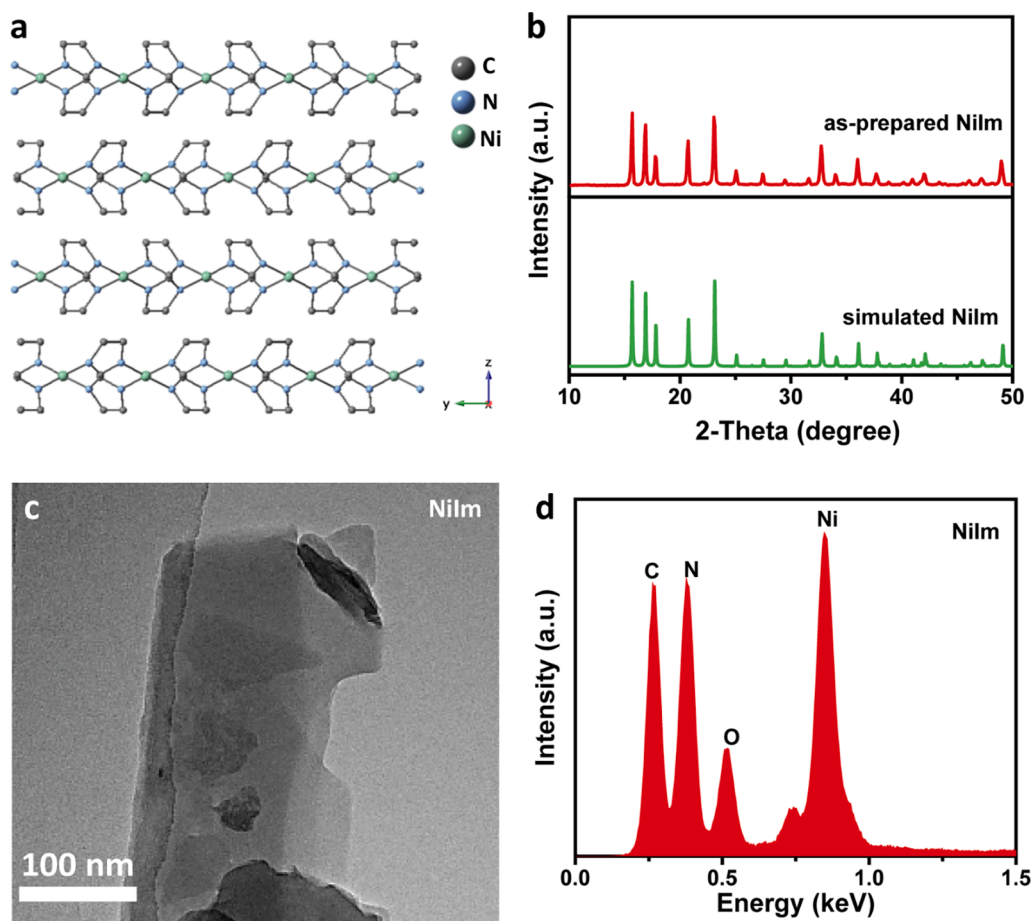
Fig. 1. (a) Atomic structure of NiIm viewed from [1 0 0] direction. (b) The experimental and simulated PXRD patterns of NiIm. (c) TEM image and (d) the corresponding EDS spectrum of NiIm.

photocatalytic H_2 production is of great interest [25,45–50]. However, previous works are more focused on utilizing MOF as the light harvester or support in photocatalysis [28,46]. Few works reported the utilization of MOF with atomically dispersed metal sites as a co-catalyst to advance the photocatalytic H_2 production.

Herein, we report the preparation of Ni-based MOF (NiIm) decorated with CdS nanorods (NRs) via a facile self-assembly procedure. The photocatalytic H_2 production rate over the NiIm/CdS hybrid is 21,712 μmol h^{-1} g^{-1}, about 14.23 times higher as compared to that on bare CdS. Experiments and theoretical calculations indicate that the tremendously increased photocatalytic H_2-production rate results from high dispersion of CdS NRs, better charge transport in the hybridized NiIm/CdS, as well as the abundant atomically-dispersed Ni–N$_4$ sites promoting the surface hydrogen production. Our work not only demonstrates that the Ni–N$_4$ sites in MOF co-catalyst can greatly promote photocatalytic H_2 generation, but also open new avenues for the design and synthesis of MOF-based materials for efficient solar energy transformation and utilization.

2. Experimental section

2.1. Materials synthesis

Preparation of NiIm: NiIm was prepared using a modified procedure based on a previous report [51]. 18 mmol of imidazole was added to an aqueous solution (50 mL) containing 2.8 mmol of nickel acetate tetrahydrate. Then, 10 mL of ammonium hydroxide (NH$_3$·H$_2$O) was added to the above solution. The mixed solution was then heated to 373 K and kept for 5 h. The precipitate was collected and then washed with deionized water and acetone, and then dried in a vacuum oven for 12 h.

The obtained yellow powder sample was labeled as NiIm.

Preparation of CdS nanorods (NRs): CdS NRs were prepared by using a modified solvothermal method [38]. Typically, 5.4 mmol of cadmium acetate dihydrate were added into 108 mL of ethylenediamine with stirring. 10.8 mmol of thiourea were then added to the above solution under stirring. After these solids were dissolved, the mixed solution was transferred to a sealed autoclave and kept at 433 K for 12 h. The yellow precipitates were collected after the autoclave cooling to 298 K, followed by washing with deionized water and ethanol 3 times and drying under 333 K for 24 h.

Preparation of CdS/NiIm hybrids: The CdS/NiIm hybrids were prepared by grinding at room temperature. At first, 100 mg of CdS was dispersed in 5 mL of ethanol. Then a certain amount (x = 0, 10, 20, 40 mg) of NiIm was added into the mixture. The mixed samples were collected after grinding for 10 min and drying under air for 2 h. The finally obtained powder samples were collected and stored for further use.

2.2. Photocatalytic H_2-production performance test

The evolved H_2 amount was analyzed and determined using gas chromatography (GC). 20 mg of the photocatalyst was added into 80 mL 10 vol% ethanol aqueous solution in a 100 mL reactor and kept stirring for 30 min and followed by a purge with N$_2$ for 30 min. The reaction system was then irradiated by a 300 W Xenon arc lamp with a 420 nm cut-off filter (λ > 420 nm). After a certain irradiation time, 400 μL of gas extracted from the reactor was immediately injected into the GC (GC-14C, Shimadzu, Japan). The real-time evolved hydrogen amount is determined by the peak area of produced hydrogen comparing with that
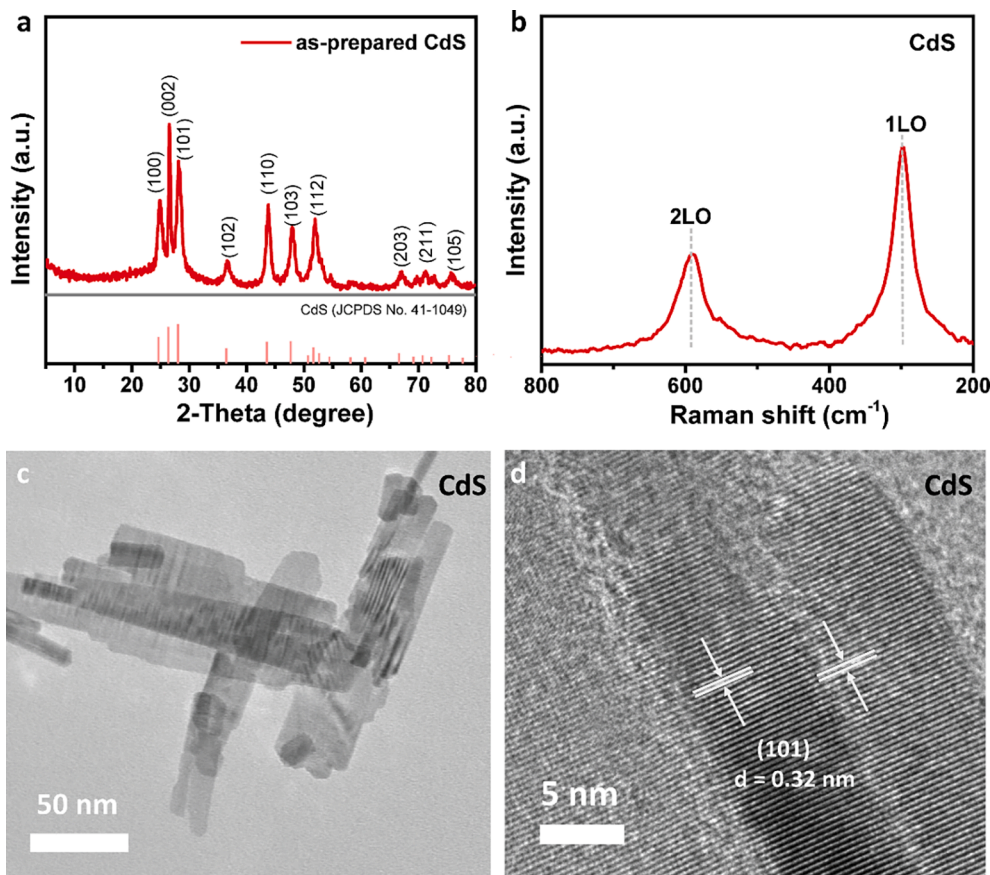
Fig. 2. (a) PXRD pattern and (b) Raman spectrum of CdS NRs. (c) TEM image and (d) HRTEM image of CdS NRs.

of standard H_2.

2.3. Electrochemical and photoelectrochemical measurements

These measurement details are described in supporting information.

2.4. Theoretical calculations

The theoretical computations details are described in supporting information.

2.5. Physicochemical characterization

The physicochemical characterization details are available in supporting information.

3. Results and discussion

3.1. Structures and morphologies

The metal–organic framework NiIm [bisimidazolato-nickel (II)] was fabricated via a modified hydrothermal approach using Ni as the metal node and imidazole as the organic linker [51]. The atomic structure of NiIm is displayed in Fig. 1a and Fig. S1, which show that each Ni atom coordinates with the adjacent four N atoms in imidazole (Im, $C_3H_4N_2$), affording a Ni-N_4 coordination structure. These atomically well-dispersed and under-coordinated Ni-N_4 sites could serve as highly active sites promoting H_2 evolution [26,52–54]. Moreover, the porous structure of NiIm also facilitates the adsorption/desorption of reactants/products as well as the mass transfer. As shown in Fig. 1b, the powder X-ray diffraction (PXRD) pattern of NiIm agrees well with the simulated

pattern based on its atomic structure in Fig. 1a, further confirming the successful synthesis of NiIm. The TEM image in Fig. 1c shows the layered structure of NiIm with an approximately 200–300 nm lateral size. The energy-dispersive X-ray spectroscopy (EDS) pattern for NiIm (Fig. 1d) indicates the presence of elements Ni, C and N, as expected based on the composition of NiIm. To test the water stability of the as-prepared NiIm, we dispersed the as-prepared NiIm in deionized water and stirred the dispersion for 3 h. Then we centrifuged and washed the NiIm by deionized water and ethanol for 3 times, respectively. After that, the washed NiIm was dried at 80 °C for 1 h, and then tested for the PXRD pattern. As shown in Fig. S2, no apparent difference is observed in the intensity and position of major diffraction peaks for the as-prepared NiIm and the NiIm dispersed in deionized water for 3 h. This result suggests the good water stability of the as-prepared NiIm.

Moreover, CdS nanorods (NRs) were prepared via a solvothermal method. The PXRD pattern of the as-prepared CdS NRs (Fig. 2a) is in good agreement with hexagonal wurtzite-structured CdS (JCPDS No. 41–1049) [55]. As can be seen in the scanning electron microscopy (SEM) image (Fig. S3), CdS displays a one-dimensional (1D) NR morphology. The Raman spectrum of CdS NRs (Fig. 2b) shows the fundamental (1LO) and overtone (2LO) peaks of CdS, in agreement with the reported data [56]. The TEM image in Fig. 2c further shows that CdS NRs possess the lengths of ~ 60–120 nm and diameters of ~ 10–20 nm. The presence of Cd and S elements in CdS NRs is confirmed by the EDS spectrum in Fig. S4, in agreement with the PXRD analysis (Fig. 2a) and Raman spectrum (Fig. 2b). The high-resolution transmission electron microscopy (HRTEM) image (Fig. 2d) shows the lattice spacing value of 0.32 nm attributed to the (1 0 1) facet of hexagonal wurtzite-structured CdS, also in agreement with the PXRD analysis (Fig. 2a). The 1D structure of CdS NRs with lengths of ~ 60–120 nm and diameters of ~ 10–20 nm facilitates the directed migration of charge carriers. This is also
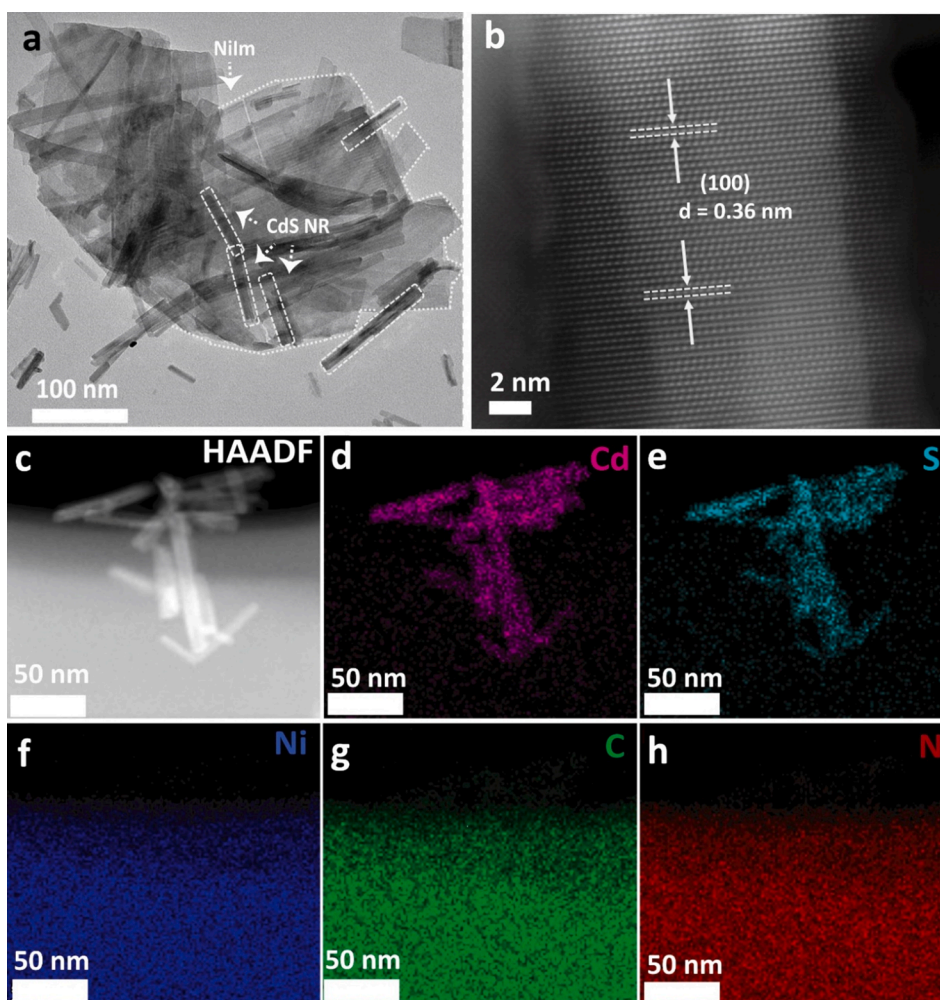
Fig. 3. (a) TEM image and (b) High-resolution HAADF-STEM image of CdS/0.2NiIm. (c) HAADF-STEM image of CdS/0.2NiIm and the elemental mapping images for Cd (Fig. 3d), S (Fig. 3e), Ni (Fig. 3f), C (Fig. 3g), and N (Fig. 3h).

supported by the previous reports on CdS NRs for photocatalytic H_2 production [57,58].

The as-synthesized CdS NRs are dispersed on the as-prepared NiIm by a facile physical mixing method at room temperature. The amounts of NiIm in the merged samples are, respectively, 10 wt%, 20 wt% and 40 wt% (based on the weight of CdS). Accordingly, the as-synthesized samples are denoted as CdS/0.1NiIm, CdS/0.2NiIm and CdS/0.4NiIm, respectively. As shown in Fig. S5, CdS exhibits a negative zeta potential of −0.06 mV; whilst NiIm shows a positive zeta potential of 20.42 mV. This result indicates that CdS and NiIm tend to combine with each other due to the opposite surface potential. This is also in agreement with the strong electronic interaction between CdS and NiIm in CdS/0.2NiIm confirmed by the XPS results. The TEM image of CdS/0.2NiIm (Fig. 3a) demonstrates the dispersion of CdS NRs on the surface of NiIm. More-over, the high-resolution high-angle annular dark-field scanning trans-mission electron microscopy (HAADF-STEM) image (Fig. 3b) of CdS/0.2NiIm exhibits a 0.36 nm d-spacing value, which could be ascribed to the (1 0 0) facet of hexagonal CdS. Additionally, the HAADF-STEM image of CdS/0.2NiIm (Fig. 3c) indicates that several CdS NRs are loaded onto the surface of NiIm. The corresponding mapping images of Cd, S, Ni, C, and N elements (Fig. 3d-h) and the EDS spectrum of CdS/0.2NiIm (Fig. S6) further verify the successful combination of CdS NRs and NiIm in CdS/0.2NiIm.

3.2. Photocatalytic H_2-production performance

The as-synthesized CdS, CdS/0.1NiIm, CdS/0.2NiIm, CdS/0.4NiIm and NiIm were tested for photocatalytic H_2 production in 10 vol% ethanol aqueous solution with visible-light illumination. As can be seen in Fig. 4a, CdS NRs display a limited photocatalytic H_2-production rate (1,525 μmol h^{-1} g^{-1}), as a consequence of the fast recombination of electrons and holes, and insufficient surface reactive sites. The disper-sion of CdS NRs onto NiIm results in the improved photocatalytic ac-tivity of 5,141 μmol h^{-1} g^{-1}. Then, the loading of CdS NRs onto the optimized amount (20 wt%) of NiIm exhibits the highest photocatalytic H_2-production rate (21,712 μmol h^{-1} g^{-1}). Compared with the H_2-pro-duction rate on CdS, this rate is about 14.23 times higher (Fig. 4a), which is also ranked amongst the most active earth-abundant CdS-based photocatalysts reported so far (Table S1). However, for samples with a larger amount of NiIm merged with CdS NRs, as in the case of CdS/0.4NiIm, a greatly reduced photocatalytic H_2-production rate (2,529 μmol h^{-1} g^{-1}) was observed, probably due to the partial blocking of reactive sites on CdS by excessive NiIm and the reduced amount of CdS as the light absorber. This is further supported by the negligible activity of pure NiIm under the same conditions (Fig. 4a). The stability of pho-tocatalytic H_2 production for CdS/0.2NiIm was also studied (Fig. S7). The photocatalytic H_2-production amount in the third hour accounts for 63.4% of that in the first hour, suggesting the acceptable stability of CdS/0.2NiIm. To gain insight into the reduced photocatalytic activity, the used CdS/0.2NiIm was collected for structural and morphological
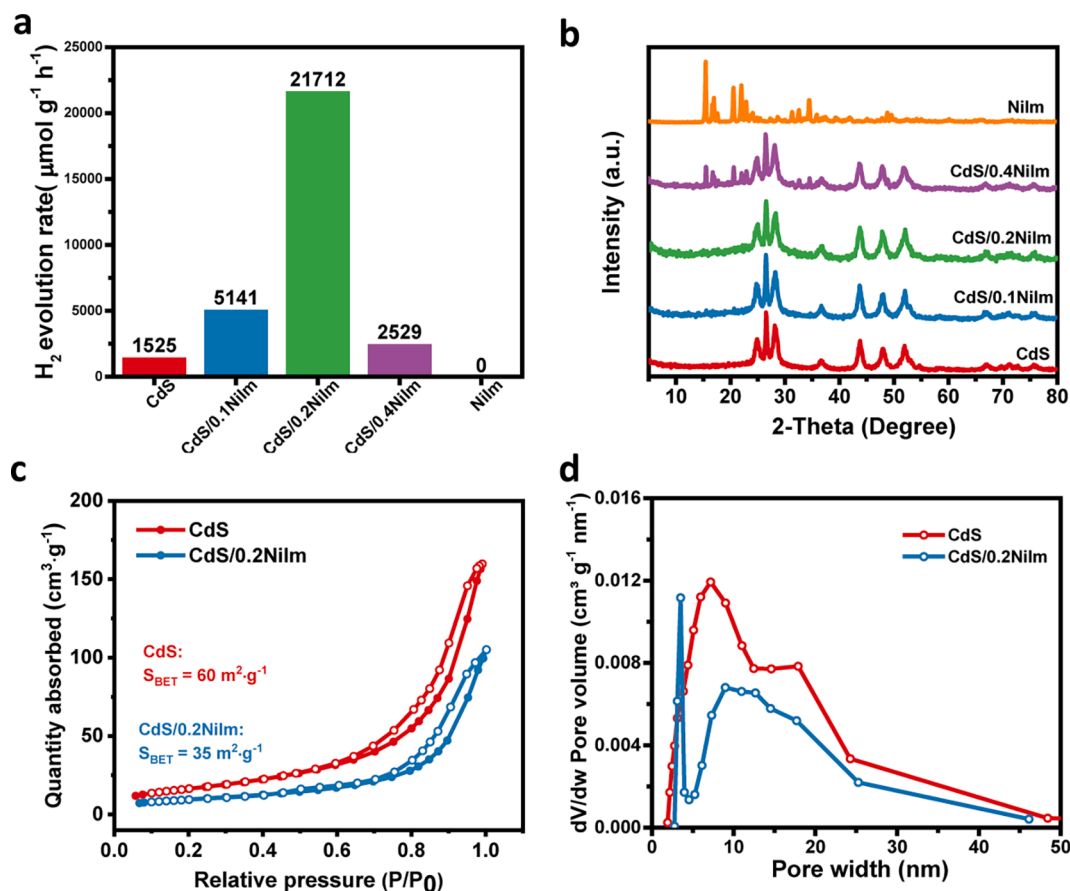
Fig. 4. (a) Photocatalytic H_2-production rates for CdS, CdS/0.1NiIm, CdS/0.2NiIm, CdS/0.4NiIm and NiIm in 10 vol% ethanol aqueous solution under visible light ($\lambda > 420$ nm). (b) PXRD patterns of CdS, CdS/0.1NiIm, CdS/0.2NiIm, CdS/0.4NiIm and NiIm. (c) N_2 sorption isotherms for CdS and CdS/0.2NiIm. The values of S_{BET} for CdS and CdS/0.2NiIm are presented in Fig. 4c. (d) Pore size distribution curves of CdS and CdS/0.2NiIm.

analysis. The PXRD patterns of the CdS/0.2NiIm-t (t stands for the reaction time) collected after reaction are shown in Fig. S8. The patterns of CdS/0.2NiIm-10min and CdS/0.2NiIm-1h are almost the same as that of CdS/0.2NiIm. The dominant peaks of CdS/0.2NiIm-3h remain unchanged, in comparison with those of CdS and CdS/0.2NiIm. However, the (2 0 3), (2 1 1) and (1 0 5) peaks of hexagonal wurtzite-structured CdS disappear for CdS/0.2NiIm-3h. The estimated crystallite sizes were calculated from the full width at half maximum (FWHM) of the three strong peaks in Fig. S8 (see Table S2). Only minor changes in the estimated crystallite sizes are observed. The relative crystallinity for the photocatalyst collected at different times was also calculated based on the area of the strongest (0 0 2) peak for CdS/0.2NiIm-t versus the counterpart of CdS/0.2NiIm (see Table S3). As shown in Table S3, the relative crystallinity for CdS/0.2NiIm-t is gradually decreased with the increasing reaction time. And the relative crystallinity of CdS/0.2NiIm-3h only accounts for ~ 55% of that for CdS/0.2NiIm, indicating the apparently reduced crystallinity of CdS/0.2NiIm-3h compared to that of CdS/0.2NiIm. These results indicate the reduced crystallinity of CdS NRs in CdS/0.2NiIm after the 3-hour reaction. It can be observed in Fig. S9a that some CdS NRs aggregate and lose their original shape in CdS/0.2NiIm-3h in comparison to the CdS NRs in CdS/0.2NiIm (Fig. 3a). The HRTEM image of CdS/0.2NiIm-3h (Fig. S9b) further confirms that some defects are produced in the CdS NRs, possibly due to the photo-induced corrosion of CdS NRs. This is different from the high-resolution HAADF-STEM image of CdS/0.2NiIm in Fig. 3b. The aggregation of CdS NRs and the produced defects in CdS NRs also contribute to the reduced photocatalytic activity of CdS/0.2NiIm-3h. Moreover, no apparent difference between the EDS spectra of CdS/0.2NiIm and CdS/0.2NiIm-3h can be observed in Fig. S6 and S10. As shown in Fig. S7, the

evolved H_2 amount of CdS/0.2NiIm in the third hour is 13,770 μmol g^{-1}, which is still much higher than the evolved H_2 amount of CdS in the first hour (1,525 μmol g^{-1}, Fig. 4a). On the other hand, it is well-known that CdS suffers from photo-corrosion and its crystallinity is reduced after photocatalytic reaction. This is reported in many previous works. [59–61]. Thus, it is supposed that much better stability can be achieved if NiIm co-catalyst is combined with robust photocatalyst, *e.g.*, TiO$_2$, for H_2 production.

3.3. Reason for outstanding photocatalytic H_2-production rate

To explore the reason for the greatly-raised photocatalytic H_2-production rate on CdS/0.2NiIm, both physicochemical characterization and theoretical computations were performed. The PXRD patterns obtained for CdS and NiIm/CdS samples are presented in Fig. 4b. Loading CdS NRs onto NiIm does not alter the intensity and positions of diffraction peaks, suggesting the crystal structure of CdS is not affected after merging with NiIm via physical mixing at room temperature. Furthermore, with the low loading of NiIm, no peaks of NiIm are found in CdS/0.1NiIm and CdS/0.2NiIm. Meanwhile, the diffraction peaks of NiIm appear in the pattern of CdS/0.4NiIm, also suggesting the merging of NiIm and CdS.

The N_2 sorption isotherm for CdS/0.2NiIm in Fig. 4c moves downwards compared with that for pure CdS, suggesting a decrease in the surface area of CdS/0.2NiIm. This can be probably attributed to the aggregation of CdS NPs and NiIm as ethanol evaporates during the mixing process. The N_2 sorption isotherm of NiIm is displayed in Fig. S11. The Brunauer–Emmett–Teller (BET) surface area (S_{BET}) of NiIm is 7 m^2 g^{-1} (Fig. S11 and Table S4), which is much lower than that of CdS
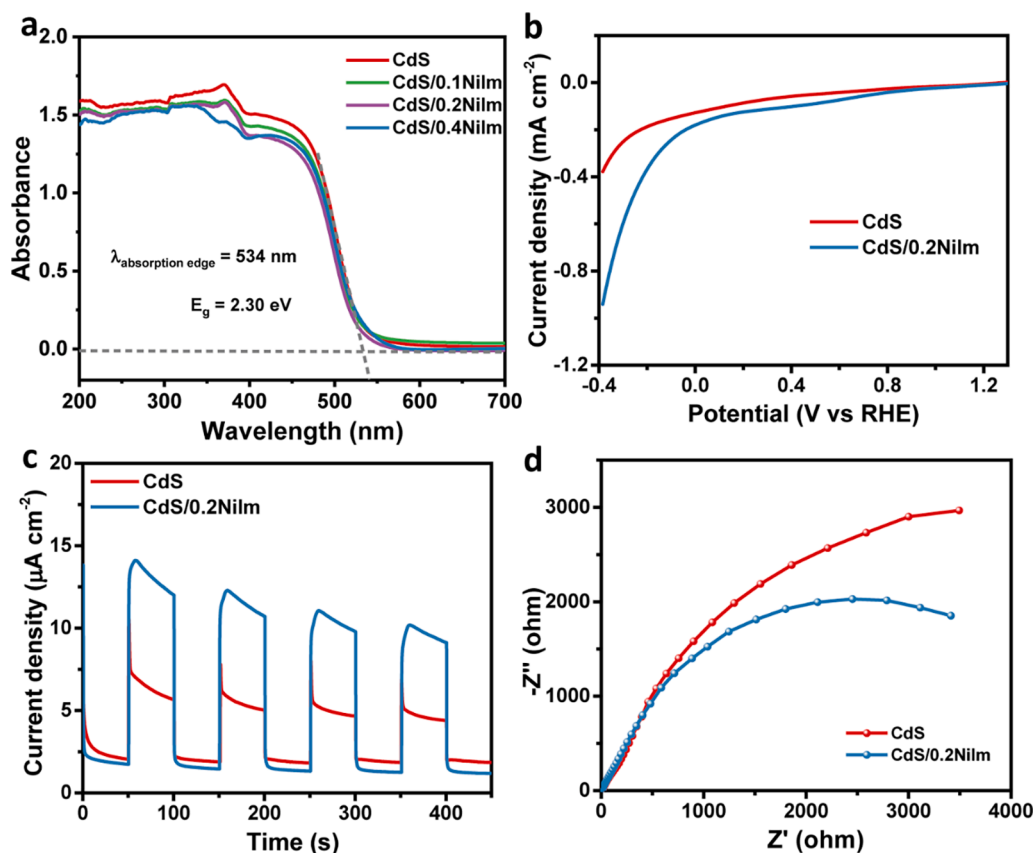
Fig. 5. (a) UV–Vis DRS spectra of CdS, CdS/0.1NiIm, CdS/0.2NiIm and CdS/0.4NiIm. (b) LSV curves of CdS and CdS/0.2NiIm electrodes in 0.5 M Na$_2$SO$_4$ aqueous solution. (c) Transient photocurrent response and (d) EIS spectra of CdS and CdS/0.2NiIm in 0.5 M Na$_2$SO$_4$ aqueous solution.

(60 m^2 g^{-1}, Table S4). Thus, the S$_{BET}$ of CdS/0.2NiIm apparently decreased to 35 m^2 g^{-1} after the hybridization of CdS and NiIm (Fig. 4c). The pore size distribution curves of CdS and CdS/0.2NiIm (Fig. 4d) show that the pore volume is also reduced after combining CdS and NiIm (Table S4). The reduced S$_{BET}$ of CdS/0.2NiIm compared to that of CdS indicates that the surface area is not the major factor deciding the photocatalytic H$_2$-production rate on CdS/0.2NiIm.

The ultraviolet–visible diffuse reflectance spectroscopy (UV–Vis DRS) was employed to measure the light absorption abilities of these hybrid photocatalysts. The UV–Vis DRS spectra of CdS and CdS/NiIm hybrids (Fig. 5a) indicate no apparent difference after combining CdS and NiIm, suggesting that the presence of NiIm does not result in the enhanced light absorption. This also suggests that light absorption is not the reason leading to the raised photocatalytic activity in this system. Besides, the UV–Vis DRS spectrum of NiIm (Fig. S12) suggests a bandgap width of 2.20 eV for NiIm. The CdS and CdS/0.2NiIm electrodes were tested for the HER activity via linear sweep voltammetry (LSV). As shown in Fig. 5b, CdS alone requires an overpotential of 230 mV to achieve a current density of 0.2 mA cm^{-2} while CdS/0.2NiIm requires an overpotential of 40 mV at the same current density. This result suggests the better HER activity of CdS/0.2NiIm in comparison to that of CdS alone. This further confirms that NiIm could boost the HER activity due to its abundant Ni–N$_4$ active sites.[49,52]. Since the C and N atoms in the imidazole linker are fully coordinated, these two sites are usually inactive for adsorption and reduction of protons for hydrogen evolution. In contrast, the undercoordinated Ni in Ni–N$_4$ sites could adsorb and reduce the protons for hydrogen evolution. So it is more likely that these rich Ni–N$_4$ sites in NiIm are the active sties for hydrogen evolution. The key role of Ni–N$_4$ as HER active sites is also supported by the recent works reporting the application of Ni–N$_4$ active sites for thermocatalytic/electrocatalytic H$_2$ evolution (Table S5). This is further

corroborated by the recent works reporting the application of metal–N$_4$ sites for hydrogen evolution (Table S6).

Then, a series of techniques including transient photocurrent (TPC) density measurement, electrochemical impedance spectroscopy (EIS), and time-resolved photoluminescence (TRPL) spectroscopy were adopted to gain insight into how charge carriers dissociate/migrate in CdS/0.2NiIm. As is shown in Fig. 5c, a much higher TPC density value is observed on CdS/0.2NiIm, compared to that of CdS, suggesting the higher efficiency of separation/migration of photo-generated electro-hole pairs in CdS/0.2NiIm than in CdS. Additionally, the EIS Nyquist plot of CdS/0.2NiIm (Fig. 5d) exhibits a smaller semicircle in contrast with that of CdS, suggesting the lower charge transfer resistance of CdS/0.2NiIm compared to that of CdS. This result also confirms the more efficient charge migration efficiency in CdS/0.2NiIm than in CdS. As displayed in Fig. 6a, the TRPL spectra of CdS and CdS/0.2NiIm were fitted with the triexponential decay, which involves a short charge-carrier lifetime, a middle charge-carrier lifetime and a long charge-carrier lifetime. The lifetimes of charge carriers for CdS/0.2NiIm (τ_1 = 0.25 ns; τ_2 = 2.89; τ_3 = 17.59 ns) are reduced in comparison to those obtained for CdS (τ_1 = 0.51 ns; τ_2 = 3.85; τ_3 = 34.09 ns). Besides, the average charge-carrier lifetime of CdS/0.2NiIm (τ_{ave} = 5.49 ns) is also decreased compared with that of CdS alone (τ_{ave} = 15.94 ns). These changes are attributed to the faster charge carrier transportation in CdS/0.2NiIm compared to that in CdS. All these confirm the improved separation/migration efficiency of charge carriers in CdS/0.2NiIm in comparison to that in CdS. The high efficiency in the separation/transfer of electron-hole pairs in CdS/0.2NiIm suggests the establishment of strong interfacial electronic coupling between NiIm and CdS.

As displayed in Fig. 6b, Ni 2p peaks of CdS/0.2NiIm in the XPS spectra are shifted to lower binding energy direction by 0.5 or 0.4 eV, in contrast with those for NiIm, indicating that electrons on CdS are
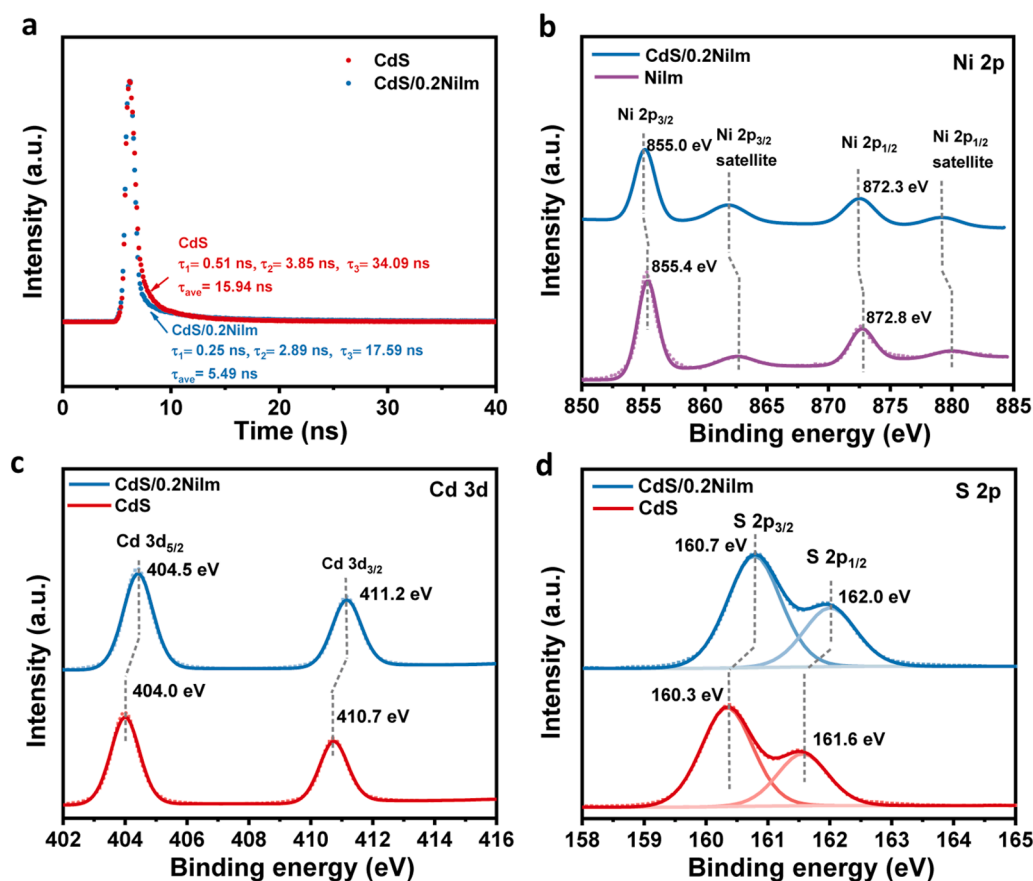
Fig. 6. (a) TRPL spectra of CdS and CdS/0.2NiIm. High-resolution XPS spectra of (b) Ni 2p, (c) Cd 3d and (d) S 2p obtained from CdS/0.2NiIm, NiIm or CdS.

transferred to NiIm after hybridization in CdS/0.2NiIm. Moreover, when comparing the peak shift of Cd 3d and S 2p in the XPS spectra for CdS and CdS/0.2NiIm (displayed in Fig. 6c and 6d), the CdS/0.2NiIm exhibits an obvious shift towards the higher binding energy direction, also suggesting transfer of electrons from CdS to NiIm after their contact in CdS/0.2NiIm. The high-resolution XPS spectra of CdS/0.1NiIm were also tested for comparison. The Cd 3d, S 2p and Ni 2p spectra of CdS/0.1NiIm are shown in Fig. S13a, b and c, respectively. The Cd 3d peaks and S 2p peaks move to the higher binding energy direction and Ni 2p peaks shift to the lower binding energy direction, compared with the counterparts of CdS or NiIm. All these results demonstrate the intimate electronic interaction at the interface between CdS and NiIm in CdS/0.1NiIm.

3.4. Positions of conduction/valence bands

Moreover, the flat band potentials for CdS and NiIm acquired from the Mott–Schottky plots (Ag/AgCl as reference electrode, shown in Fig. 7a and 7b) are −0.89 and −0.65 V vs. Ag/AgCl, which are equivalent to −0.26 and −0.02 V, respectively, after conversion with respect to the standard hydrogen electrode (SHE). As a result, the Fermi level of CdS is more negative than that of NiIm, suggesting that the electrons migrate from CdS to NiIm after their merging. Besides, theoretical computations indicate that the work function for the CdS (0 0 2) facet (Φ = 4.52 eV) is smaller than that for NiIm (0 0 1) facet (Φ = 4.89 eV), as shown in Fig. 7c and 7d. These theoretical results also support the electron migration from CdS to NiIm. Furthermore, the potentials of the conduction band (CB) edges for CdS is approximately −0.36 V vs. SHE. Thus, according to the UV–Vis DRS spectra of CdS (Fig. 5a), the valence band (VB) edge potential of CdS is 1.94 V vs. SHE, respectively.

3.5. Reaction mechanism

According to the afore-mentioned theoretical and experimental results, we propose the following mechanism of photocatalytic H_2 production for the CdS/NiIm hybrid system (Fig. 8). Visible-light irradiation (λ > 420 nm) leads to the excitation of CdS, producing photo-induced electrons and holes on the CB and VB of CdS, respectively. The layer-structured NiIm serves as the co-catalyst, which provides sufficient atomically dispersed Ni–N_4 sites boosting the reduction of protons to gaseous H_2 by the photo-induced electrons. Simultaneously, the photo-induced holes on the VB of CdS oxidize the sacrificial electron donor, ethanol, to form the oxidation product(s). Thus, CdS accommodates the oxidation sites for ethanol oxidation. The roles of NiIm in CdS/NiIm are summarized as follows: (i) NiIm can promote the electron-hole separation/migration and (ii) the atomically dispersed Ni–N_4 sites on NiIm can advance the surface H_2 evolution reaction.

4. Conclusions

In summary, Ni-based metal–organic framework (NiIm) coupled CdS nanorods (NRs) were prepared via physical mixing at room temperature. The as-prepared CdS/NiIm hybrid was shown to have an outstanding H_2-generation rate of 21,712 μmol h^{-1} g^{-1}, about 14.23 times larger than that on pure CdS NRs. Physicochemical characterization and theoretical computations disclose that the interactive nature at CdS/NiIm interface, efficient charge migration in the CdS/NiIm hybrid and numerous Ni–N_4 reduction sites in NiIm, work collaboratively to boost the photocatalytic activity. This study not only exemplifies the feasibility of interfacial engineering in photocatalysts for enhancing their catalytic performance, but also shows the path for seeking abundant, affordable and durable metal–organic framework-based photocatalysts for solar energy
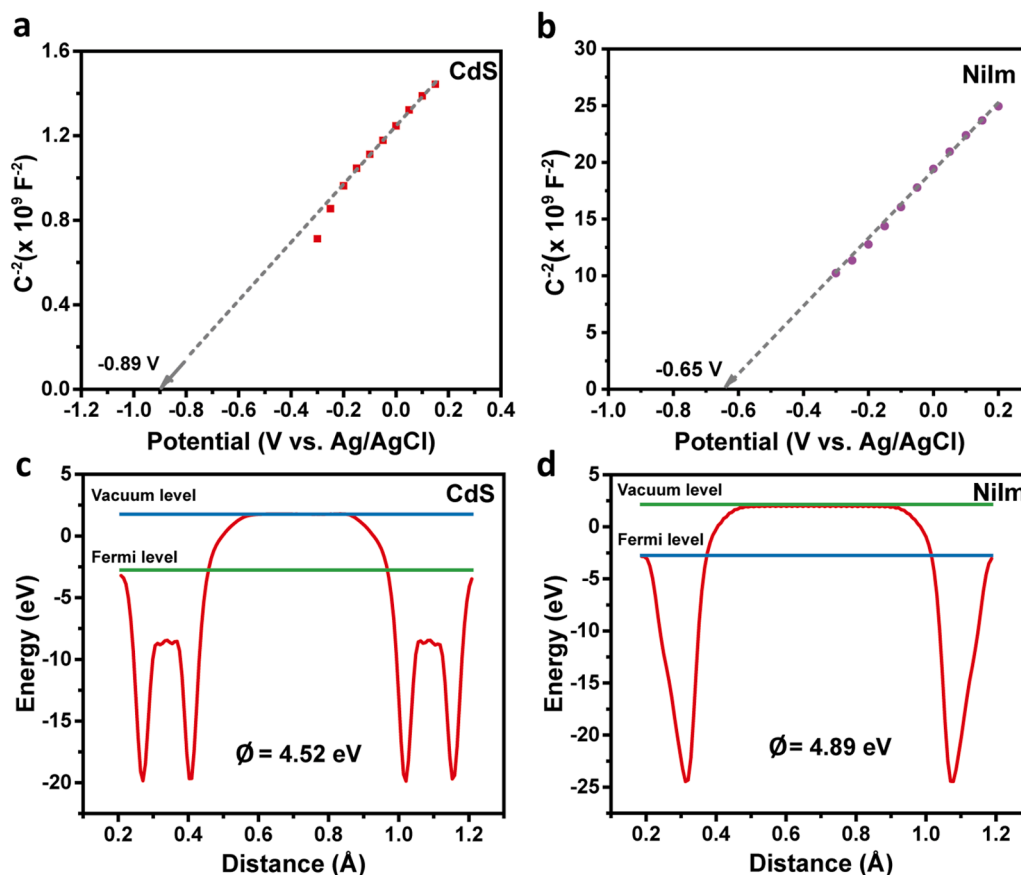
Fig. 7. Mott-Schottky plots for (a) CdS and (b) NiIm acquired at 2000 Hz in 0.5 M Na$_2$SO$_4$ aqueous solution. Work functions for (c) CdS (0 0 2) facet and (d) NiIm (0 0 1) facet acquired via theoretical computations.
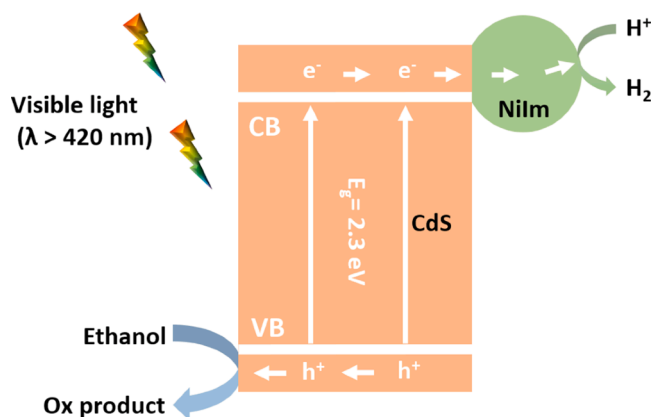
Fig. 8. Proposed mechanism for photocatalytic H$_2$ production on CdS/NiIm under visible light (λ > 420 nm).

transformation.

Declaration of competing interest

The authors declare that they have no known competing financial interests or personal relationships that could have appeared to influence the work reported in this paper.

Acknowledgements

The authors gratefully acknowledge financial support from the

Appendix A. Supplementary data

Supplementary data to this article can be found online at https://doi.org/10.1016/j.cej.2021.133944.

References

[1] E.C. Tyo, S. Vajda, Catalysis by clusters with precise numbers of atoms, Nat. Nanotechnol. 10 (7) (2015) 577–588.
[2] F. Zhang, Y. Zhu, Q. Lin, L. Zhang, X. Zhang, H. Wang, Noble-metal single-atoms in thermocatalysis, electrocatalysis, and photocatalysis, Energy Environ. Sci. 14 (5) (2021) 2954–3009.
[3] L. Jiao, H.-L. Jiang, Metal-organic-framework-based single-atom catalysts for energy applications, Chem 5 (4) (2019) 786–804, https://doi.org/10.1016/j.chempr.2018.12.011.
[4] Z. Song, L. Zhang, K. Doyle-Davis, X. Fu, J.-L. Luo, X. Sun, Recent advances in MOF-derived single atom catalysts for electrochemical applications, Adv. Energy Mater. 10 (38) (2020) 2001561, https://doi.org/10.1002/aenm.202001561.
[5] Y. Li, M. Karimi, Y.-N. Gong, N. Dai, V. Safarifard, H.-L. Jiang, Integration of metal-organic frameworks and covalent organic frameworks: Design, synthesis, and applications, Matter 4 (7) (2021) 2230–2265, https://doi.org/10.1016/j.matt.2021.03.022.
[6] Y.-S. Wei, M. Zhang, R. Zou, Q. Xu, Metal-organic framework-based catalysts with single metal sites, Chem. Rev. 120 (21) (2020) 12089–12174, https://doi.org/10.1021/acs.chemrev.9b00757.
[7] S.K. Kaiser, Z. Chen, D. Faust Akl, S. Mitchell, J. Pérez-Ramírez, Single-atom catalysts across the periodic table, Chem. Rev. 120 (21) (2020) 11703–11809, https://doi.org/10.1021/acs.chemrev.0c00576.
[8] C. Zhu, S. Fu, Q. Shi, D. Du, Y. Lin, Single-atom electrocatalysts, Angew. Chem. Int. Ed. 56 (45) (2017) 13944–13960, https://doi.org/10.1002/anie.201703864.
[9] Y. Chen, S. Ji, Y. Wang, J. Dong, W. Chen, Z. Li, R. Shen, L. Zheng, Z. Zhuang, D. Wang, Y. Li, Isolated single iron atoms anchored on N-Doped porous carbon as

an efficient electrocatalyst for the oxygen reduction reaction, Angew. Chem. Int. Ed. 56 (24) (2017) 6937–6941, https://doi.org/10.1002/anie.201702473.

[10] Y. Sun, Z. Xue, Q. Liu, Y. Jia, Y. Li, K. Liu, Y. Lin, M. Liu, G. Li, C.Y. Su, Modulating electronic structure of metal-organic frameworks by introducing atomically dispersed Ru for efficient hydrogen evolution, Nat. Commun. 12 (2021) 1369, https://doi.org/10.1038/s41467-021-21595-5.

[11] P. Kuang, Y. Wang, B. Zhu, F. Xia, C.-W. Tung, J. Wu, H.M. Chen, J. Yu, Pt single atoms supported on N-doped mesoporous hollow carbon spheres with enhanced electrocatalytic H₂-evolution activity, Adv. Mater. 33 (18) (2021) 2008599, https://doi.org/10.1002/adma.202008599.

[12] C. Gao, J. Low, R. Long, T. Kong, J. Zhu, Y. Xiong, Heterogeneous single-atom photocatalysts: Fundamentals and applications, Chem. Rev. 120 (21) (2020) 12175–12216, https://doi.org/10.1021/acs.chemrev.9b00840.

[13] C. Wang, K. Wang, Y. Feng, C. Li, X. Zhou, L. Gan, Y. Feng, H. Zhou, B. Zhang, X. Qu, H. Li, J. Li, A. Li, Y. Sun, S. Zhang, G. Yang, Y. Guo, S. Yang, T. Zhou, F. Dong, K. Zheng, L. Wang, J. Huang, Z.e. Zhang, X. Han, Co and Pt dual-single-atoms with oxygen-coordinated Co-O-Pt dimer sites for ultrahigh photocatalytic hydrogen evolution efficiency, Adv. Mater. 33 (13) (2021) 2003327, https://doi.org/10.1002/adma.202003327.

[14] Y. Hu, Y. Qu, Y. Zhou, Z. Wang, H. Wang, B.o. Yang, Z. Yu, Y. Wu, Single Pt atom-anchored C₃N₄: A bridging Pt–N bond boosted electron transfer for highly efficient photocatalytic H₂ generation, Chem. Eng. J. 412 (2021) 128749, https://doi.org/10.1016/j.cej.2021.128749.

[15] Z. Chen, S. Wu, J. Ma, S. Mine, T. Toyao, M. Matsuoka, L. Wang, J. Zhang, Non-oxidative coupling of methane: N-type doping of niobium single atoms in TiO₂–SiO₂ induces electron localization, Angew. Chem. Int. Ed. 60 (21) (2021) 11901–11909, https://doi.org/10.1002/anie.202016402.

[16] C. Ling, S. Niu, Q. Li, A. Du, J. Wang, Metal-free single atom catalyst for N₂ fixation driven by visible light, J. Am. Chem. Soc. 140 (43) (2018) 14161–14168, https://doi.org/10.1021/jacs.8b07472.

[17] G. Gao, Y. Jiao, E.R. Waclawik, A. Du, Single atom (Pd/Pt) supported on graphitic carbon nitride as an efficient photocatalyst for visible-light reduction of carbon dioxide, J. Am. Chem. Soc. 138 (19) (2016) 6292–6297, https://doi.org/10.1021/jacs.6b02692.

[18] L. Zhou, J.M.P. Martirez, J. Finzel, C. Zhang, D.F. Swearer, S. Tian, H. Robatjazi, M. Lou, L. Dong, L. Henderson, P. Christopher, E.A. Carter, P. Nordlander, N. J. Halas, Light-driven methane dry reforming with single atomic site antenna-reactor plasmonic photocatalysts, Nat. Energy 5 (1) (2020) 61–70, https://doi.org/10.1038/s41560-019-0517-9.

[19] D. Xia, H. Liu, B. Xu, Y. Wang, Y. Liao, Y. Huang, L. Ye, C. He, P.K. Wong, R. Qiu, Single Ag atom engineered 3D-MnO₂ porous hollow microspheres for rapid photothermocatalytic inactivation of E. coli under solar light, Appl. Catal. B 245 (2019) 177–189, https://doi.org/10.1016/j.apcatb.2018.12.056.

[20] Q. Song, J. Li, L. Wang, Y. Qin, L. Pang, H. Liu, Stable single-atom cobalt as a strong coupling bridge to promote electron transfer and separation in photoelectrocatalysis, J. Catal. 370 (2019) 176–185, https://doi.org/10.1016/j.jcat.2018.12.021.

[21] Y. Li, W. Cheng, H. Su, X.u. Zhao, J. He, Q. Liu, Operando infrared spectroscopic insights into the dynamic evolution of liquid-solid (photo)electrochemical interfaces, Nano Energy 77 (2020) 105121, https://doi.org/10.1016/j.nanoen.2020.105121.

[22] Y.-B. Huang, J. Liang, X.-S. Wang, R. Cao, Multifunctional metal-organic framework catalysts: Synergistic catalysis and tandem reactions, Chem. Soc. Rev. 46 (1) (2017) 126–157, https://doi.org/10.1039/c6cs00250a.

[23] Q. Yang, Q. Xu, H.-L. Jiang, Metal-organic frameworks meet metal nanoparticles: Synergistic effect for enhanced catalysis, Chem. Soc. Rev. 46 (15) (2017) 4774–4808, https://doi.org/10.1039/c6cs00724d.

[24] S. Yuan, L. Feng, K. Wang, J. Pang, M. Bosch, C. Lollar, Y. Sun, J. Qin, X. Yang, P. Zhang, Q.i. Wang, L. Zou, Y. Zhang, L. Zhang, Y.u. Fang, J. Li, H.-C. Zhou, Stable metal–organic frameworks: Design, synthesis, and applications, Adv. Mater. 30 (37) (2018) 1704303, https://doi.org/10.1002/adma.201704303.

[25] J. Chen, H. Li, C. Fan, Q. Meng, Y. Tang, X. Qiu, G. Fu, T. Ma, Dual single-atomic Ni–N₄ and Fe–N₄ sites constructing Janus hollow graphene for selective oxygen electrocatalysis, Adv. Mater. 32 (30) (2020) 2003134, https://doi.org/10.1002/adma.202003134.

[26] X. Li, W. Bi, M. Chen, Y. Sun, H. Ju, W. Yan, J. Zhu, X. Wu, W. Chu, C. Wu, Y.i. Xie, Exclusive Ni–N₄ sites realize near-unity CO selectivity for electrochemical CO₂ Reduction, J. Am. Chem. Soc. 139 (42) (2017) 14889–14892, https://doi.org/10.1021/jacs.7b09074.

[27] J. Li, P. Liu, J. Mao, J. Yan, W. Song, Two-dimensional conductive metal-organic frameworks with dual metal sites toward the electrochemical oxygen evolution reaction, J. Mater. Chem. A 9 (3) (2021) 1623–1629, https://doi.org/10.1039/d0ta10870g.

[28] M. Xu, D. Li, K. Sun, L. Jiao, C. Xie, C. Ding, H.-L. Jiang, Interfacial microenvironment modulation boosting electron transfer between metal nanoparticles and mofs for enhanced photocatalysis, Angew. Chem. Int. Ed. 60 (2021) 16372–16376, https://doi.org/10.1002/anie.202104219.

[29] Y.-H. Li, F. Zhang, Y. Chen, J.-Y. Li, Y.-J. Xu, Photoredox-catalyzed biomass intermediate conversion integrated with H₂ production over Ti₃C₂T: X/CdS composites, Green Chem. 22 (1) (2020) 163–169, https://doi.org/10.1039/c9gc03332g.

[30] X. Han, T. Si, Q. Liu, F. Zhu, R. Li, X. Chen, J. Liu, H. Sun, J. Zhao, H. Ling, Q. Zhang, H. Wang, 2D bimetallic RuNi alloy co-catalysts remarkably enhanced the photocatalytic H₂ evolution performance of g-C₃N₄ nanosheets, Chem. Eng. J. 426 (2021) 130824, https://doi.org/10.1016/j.cej.2021.130824.

[31] S. Li, Y.H. Ng, R. Zhu, S. Lv, C. Wu, Y. Liu, L. Jing, J. Deng, H. Dai, In situ construction of elemental phosphorus nanorod-modified TiO₂ photocatalysts for efficient visible-light-driven H₂ generation, Appl. Catal. B 297 (2021) 120412, https://doi.org/10.1016/j.apcatb.2021.120412.

[32] C. Li, H. Wu, D. Zhu, T. Zhou, M. Yan, G. Chen, J. Sun, G. Dai, F. Ge, H. Dong, High-efficient charge separation driven directionally by pyridine rings grafted on carbon nitride edge for boosting photocatalytic hydrogen evolution, Appl. Catal. B 297 (2021) 120433, https://doi.org/10.1016/j.apcatb.2021.120433.

[33] C. Bie, B. Cheng, J. Fan, W. Ho, J. Yu, Enhanced solar-to-chemical energy conversion of graphitic carbon nitride by two-dimensional cocatalysts, EnergyChem 3 (2021), 100051, https://doi.org/10.1016/j.enchem.2021.100051.

[34] X. Zhou, J. Luo, B. Jin, Z. Wu, S. Yang, S. Zhang, Y. Tian, Y. Fang, Y. Hou, X. Zhou, Sustainable synthesis of low-cost nitrogen-doped-carbon coated Co₃W₃C@g-C₃N₄ composite photocatalyst for efficient hydrogen evolution, Chem. Eng. J. 426 (2021) 131208, https://doi.org/10.1016/j.cej.2021.131208.

[35] M. Xiong, Y. Qin, B. Chai, J. Yan, G. Fan, F. Xu, C. Wang, G. Song, Unveiling the role of Mn-Cd-S solid solution and MnS in MnₓCd₁₋ₓS photocatalysts and decorating with CoP nanoplates for enhanced photocatalytic H₂ evolution, Chem. Eng. J. 428 (2022), 131069, https://doi.org/10.1016/j.cej.2021.131069.

[36] Y. Pan, Y. Qian, X. Zheng, S.-Q. Chu, Y. Yang, C. Ding, X. Wang, S.-H. Yu, H.-L. Jiang, Precise fabrication of single-atom alloy co-catalyst with optimal charge state for enhanced photocatalysis, Natl. Sci. Rev. 8 (2021) nwaa224, https://doi.org/10.1093/nsr/nwaa224.

[37] L. Zhang, Y. Li, Q. Li, J. Fan, S.A.C. Carabineiro, K. Lv, Recent advances on bismuth-based photocatalysts: Strategies and mechanisms, Chem. Eng. J. 419 (2021), 129484, https://doi.org/10.1016/j.cej.2021.129484.

[38] B. He, C. Bie, X. Fei, B. Cheng, J. Yu, W. Ho, A.A. Al-Ghamdi, S. Wageh, Enhancement in the photocatalytic H₂ production activity of CdS NRs by Ag₂S and NiS dual cocatalysts, Appl. Catal. B 288 (2021) 119994, https://doi.org/10.1016/j.apcatb.2021.119994.

[39] Z. Wang, Y. Luo, T. Hisatomi, J.J.M. Vequizo, S. Suzuki, S. Chen, M. Nakabayashi, L. Lin, Z. Pan, N. Kariya, A. Yamakata, N. Shibata, T. Takata, K. Teshima, K. Domen, Sequential cocatalyst decoration on BaTaO₂N towards highly-active Z-scheme water splitting, Nat. Commun. 12 (2021) 1005, https://doi.org/10.1038/s41467-021-21284-3.

[40] D. Wang, X.Q. Gong, Function-oriented design of robust metal cocatalyst for photocatalytic hydrogen evolution on metal/titania composites, Nat. Commun. 12 (2021) 158, https://doi.org/10.1038/s41467-020-20464-x.

[41] R. Chen, Y. Wang, Y. Ma, A. Mal, X.Y. Gao, L. Gao, L. Qiao, X.B. Li, L.Z. Wu, C. Wang, Rational design of isostructural 2D porphyrin-based covalent organic frameworks for tunable photocatalytic hydrogen evolution, Nat. Commun. 12 (2021) 1354, https://doi.org/10.1038/s41467-021-21527-3.

[42] S. Tang, Y. Xia, J. Fan, B. Cheng, J. Yu, W. Ho, Enhanced photocatalytic H₂ production performance of CdS hollow spheres using C and Pt as bi-cocatalysts, Chin. J. Catal. 42 (2021) 743–752, https://doi.org/10.1016/s1872-2067(20)63695-6.

[43] T. Di, L. Zhang, B. Cheng, J. Yu, J. Fan, CdS nanosheets decorated with Ni@ graphene core-shell cocatalyst for superior photocatalytic H₂ production, J. Mater. Sci. Technol. 56 (2020) 170–178, https://doi.org/10.1016/j.jmst.2020.03.032.

[44] X. Xiang, B. Zhu, B. Cheng, J. Yu, H. Lv, Enhanced photocatalytic H₂-production activity of CdS quantum dots using Sn²⁺ as cocatalyst under visible light irradiation, Small 16 (2020) 2001024, https://doi.org/10.1002/smll.202001024.

[45] X. Ma, L.i. Wang, Q. Zhang, H.-L. Jiang, Switching on the photocatalysis of metal–organic frameworks by engineering structural defects, Angew. Chem. Int. Ed. 58 (35) (2019) 12175–12179, https://doi.org/10.1002/anie.201907074.

[46] Q. Zuo, T. Liu, C. Chen, Y.i. Ji, Y.u. Wang, Y. Mai, Y. Zhou, Ultrathin metal–organic framework nanosheets with ultrahigh loading of single Pt atoms for efficient visible-light-driven photocatalytic H₂ evolution, Angew. Chem. Int. Ed. 58 (30) (2019) 10198–10203, https://doi.org/10.1002/anie.201904058.

[47] M. Kalaj, S.M. Cohen, Postsynthetic modification: An enabling technology for the advancement of metal-organic frameworks, ACS Cent. Sci. 6 (7) (2020) 1046–1057, https://doi.org/10.1021/acscentsci.0c00690.

[48] J. Xu, Y. Qi, L. Wang, In situ derived Ni₂P/Ni encapsulated in carbon/g-C₃N₄ hybrids from metal-organic frameworks/g-C₃N₄ for efficient photocatalytic hydrogen evolution, Appl. Catal. B 246 (2019) 72–81, https://doi.org/10.1016/j.apcatb.2019.01.045.

[49] H. Huang, Y. Zhao, Y. Bai, F. Li, Y. Zhang, Y.u. Chen, Conductive metal–organic frameworks with extra metallic sites as an efficient electrocatalyst for the hydrogen evolution reaction, Adv. Sci. 7 (9) (2020), 2000012, https://doi.org/10.1002/advs.202000012.

[50] B. Hu, X. Zhu, X. An, C. Wang, X. Wang, J. He, Y. Zhao, Separation of Metal–N₄ units in metal–organic framework for preparation of M–Nₓ/C catalyst with dense metal sites, Inorg. Chem. 59 (23) (2020) 17134–17142, https://doi.org/10.1021/acs.inorgchem.0c02420.

[51] J.-X. Wu, W.-W. Yuan, M. Xu, Z.-Y. Gu, Ultrathin 2D nickel zeolitic imidazolate framework nanosheets for electrocatalytic reduction of CO₂, Chem. Commun. 55 (77) (2019) 11634–11637, https://doi.org/10.1039/c9cc05487a.

[52] P. Sabhapathy, I. Shown, A. Sabbah, P. Raghunath, J.-L. Chen, W.-F. Chen, M.-C. Lin, K.-H. Chen, L.-C. Chen, Electronic structure modulation of isolated Co-N₄ electrocatalyst by sulfur for improved pH-universal hydrogen evolution reaction, Nano Energy 80 (2021), 105544, https://doi.org/10.1016/j.nanoen.2020.105544.

[53] Y.-N. Gong, L. Jiao, Y. Qian, C.-Y. Pan, L. Zheng, X. Cai, B.o. Liu, S.-H. Yu, H.-L. Jiang, Regulating the coordination environment of MOF-templated single-atom nickel electrocatalysts for boosting CO₂ Reduction, Angew. Chem. Int. Ed. 59 (7) (2020) 2705–2709, https://doi.org/10.1002/anie.201914977.

[54] Y. Cao, S.i. Chen, Q. Luo, H. Yan, Y. Lin, W. Liu, L. Cao, J. Lu, J. Yang, T. Yao, S. Wei, Atomic-level insight into optimizing the hydrogen evolution pathway over a Co$_1$-N$_4$ single-site photocatalyst, Angew. Chem. Int. Ed. 56 (40) (2017) 12191–12196, https://doi.org/10.1002/anie.201706467.

[55] P. Zhou, Q. Zhang, Z. Xu, Q. Shang, L. Wang, Y. Chao, Y. Li, H. Chen, F. Lv, Q. Zhang, L. Gu, S. Guo, Atomically dispersed Co–P$_3$ on CdS nanorods with electron-rich feature boosts photocatalysis, Adv. Mater. 32 (7) (2020) 1904249, https://doi.org/10.1002/adma.201904249.

[56] C. Bie, J. Fu, B. Cheng, L. Zhang, Ultrathin CdS nanosheets with tunable thickness and efficient photocatalytic hydrogen generation, Appl. Surf. Sci. 462 (2018) 606–614, https://doi.org/10.1016/j.apsusc.2018.08.130.

[57] J. Yu, Y. Yu, P. Zhou, W. Xiao, B. Cheng, Morphology-dependent photocatalytic H$_2$-production activity of CdS, Appl. Catal. B 156-157 (2014) 184–191, https://doi.org/10.1016/j.apcatb.2014.03.013.

[58] L. Cheng, Q. Xiang, Y. Liao, H. Zhang, CdS-Based photocatalysts, Energy Environ. Sci. 11 (6) (2018) 1362–1391, https://doi.org/10.1039/c7ee03640j.

[59] C. Wang, L. Wang, J. Jin, J. Liu, Y. Li, M. Wu, L. Chen, B. Wang, X. Yang, B.-L. Su, Probing effective photocorrosion inhibition and highly improved photocatalytic hydrogen production on monodisperse PANI@CdS core-shell nanospheres, Appl. Catal. B 188 (2016) 351–359, https://doi.org/10.1016/j.apcatb.2016.02.017.

[60] W. Zhen, X. Ning, B. Yang, Y. Wu, Z. Li, G. Lu, The enhancement of CdS photocatalytic activity for water splitting via anti-photocorrosion by coating Ni$_2$P shell and removing nascent formed oxygen with artificial gill, Appl. Catal. B 221 (2018) 243-257. https:/doi.org/10.1016/j.apcatb.2017.09.024.

[61] X. Ning, G. Lu, Photocorrosion inhibition of CdS-based catalysts for photocatalytic overall water splitting, Nanoscale 12 (3) (2020) 1213–1223, https://doi.org/10.1039/c9nr09183a.

Metal–organic framework with atomically dispersed Ni–N$_4$ sites for greatly-raised visible-light photocatalytic H$_2$ production

Bingquan Xia[a], Yi Yang[b], Yanzhao Zhang[a], Yang Xia[b], Mietek Jaroniec[c], Jiaguo Yu[b*], Jingrun Ran[a*], Shi-Zhang Qiao[a*]

[a] School of Chemical Engineering and Advanced Materials, The University of Adelaide, Adelaide, SA 5005, Australia

[b] Laboratory of Solar Fuel, Faculty of Materials Science and Chemistry, China University of Geosciences, 388 Lumo Road, Wuhan, 430074, P. R. China

[c] Department of Chemistry and Biochemistry & Advanced Materials and Liquid Crystal Institute, Kent State University, Kent, Ohio 44242, United States of America

E-mail addresses: s.qiao@adelaide.edu.au (S.-Z. Qiao), jingrun.ran@adelaide.edu.au (J. Ran), yujiaguo93@cug.edu.cn (J. Yu).

Section S1. Supplementary experimental and theoretical computation details

S1.1. Electrochemical and photoelectrochemical measurements

Electrochemical and photoelectrochemical measurements were performed on an electrochemical analyzer (CHI650D instruments) in a standard three-electrode system utilizing the as-synthesized samples as the working electrodes, Ag/AgCl (saturated KCl) as a reference electrode, and Pt wire as the counter electrode. The prepared samples were coated on the F-doped tin oxide (FTO) glass and used as the working electrodes. 20 mg of sample was dispersed in 0.5 mL of ethanol containing 10 μL of 5% Nafion solution (D-520, DuPont, USA) to make a slurry. Then the slurry was coated onto the conductive surface of FTO glass. Finally, the obtained working electrode was dried under room temperature overnight. A Xe lamp (300 W, $\lambda > 420$ nm) for ensuring that the effective irradiation area of 1 cm^2 on the sample was used as the light source. 50 mL of 0.5 M Na_2SO_4 aqueous solution was selected as the electrolyte for ion transport. The electrochemical impedance spectra and transient photocurrent response with the light on/off were obtained.

S1.2. Theoretical calculations

Similar to our previous work [1], density functional theory (DFT) calculations were performed with the CASTEP module based on the plane-wave-pseudo-potential approach. The Perdew-Burke-Ernzerhof (PBE) functional of the generalized gradient approximation (GGA) was used as the exchange-correlation function. The ultrasoft pseudo-potential was employed to describe the interaction between valence electrons and the ionic core. A kinetic energy cutoff of 450 eV and Monkhorst-Pack special k-point meshes of $3 \times 3 \times 1$ were proposed to carry out geometry optimization and electronic structure calculation. During the geometry optimization, all atoms were permitted to relax without any constraints until the convergence thresholds of maximum displacement, maximum force and energy were smaller than 0.001 Å, 0.05 eV/Å and 1.0×10^{-5} eV/atom, respectively.

S1.3. Physicochemical characterization

X-ray diffraction (XRD) patterns were recorded by an X-ray diffractometer (RU-200B/D/MAXRB, Rigaku, Japan). The microstructure investigation was performed on a field emission scanning electron microscope (FESEM) (JSM 7500F, JEOL, Japan) and (Scanning) Transmission electron microscope (S/TEM) images and corresponding energy dispersive X-ray (EDX) elemental mapping were collected on a scanning transmission electron microscope (Thermo Scientific Talos F200S G2, USA) equipped with EDX detector PV97-61850. The Brunauer-Emmett-Teller specific surface area (S_{BET}) was calculated based on N_2 adsorption isotherm measured on TriStar II 3020 (Micromeritics, USA). Raman spectra were collected on a Raman microscope (InVia, Renishaw, England) with a 633 nm Argon laser as an excitation source. The ultraviolet–visible diffuse reflectance spectra (UV–Vis DRS) were acquired on a UV–Vis spectrophotometer (UV-2600, Shimadzu, Japan). The X-ray photoelectron spectroscopy (XPS) spectra were obtained on an electron spectrometer (ESCALAB 210, VG, UK). The time-resolved photoluminescence (TRPL) spectra were acquired using FLS1000 fluorescence lifetime spectrophotometer (Edinburgh, Instruments, UK). Zeta potential measurement was performed on Malvern Zetasizer Nano ZS90.

Section S2. Supplementary results
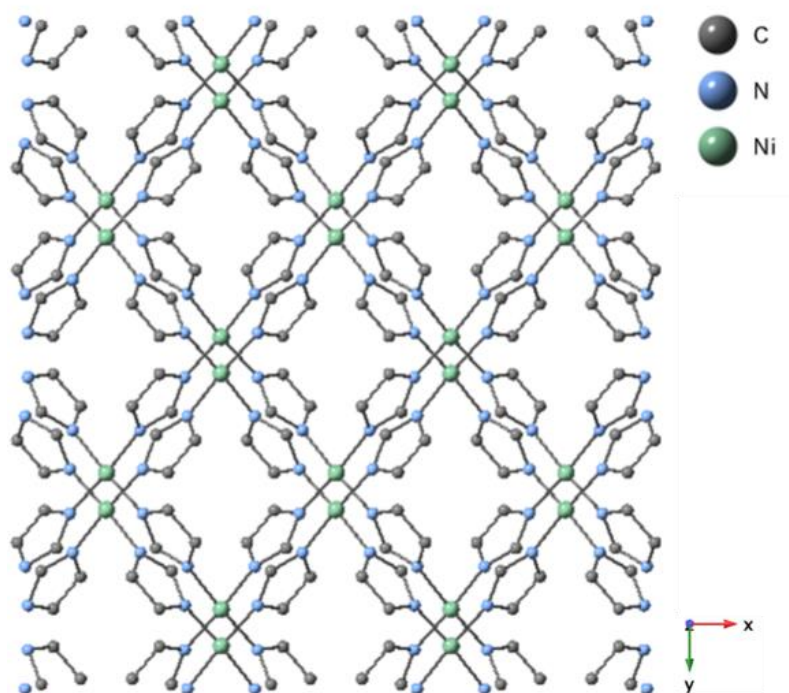
Fig. S1. Atomic structure of NiIm viewed from [001] direction.
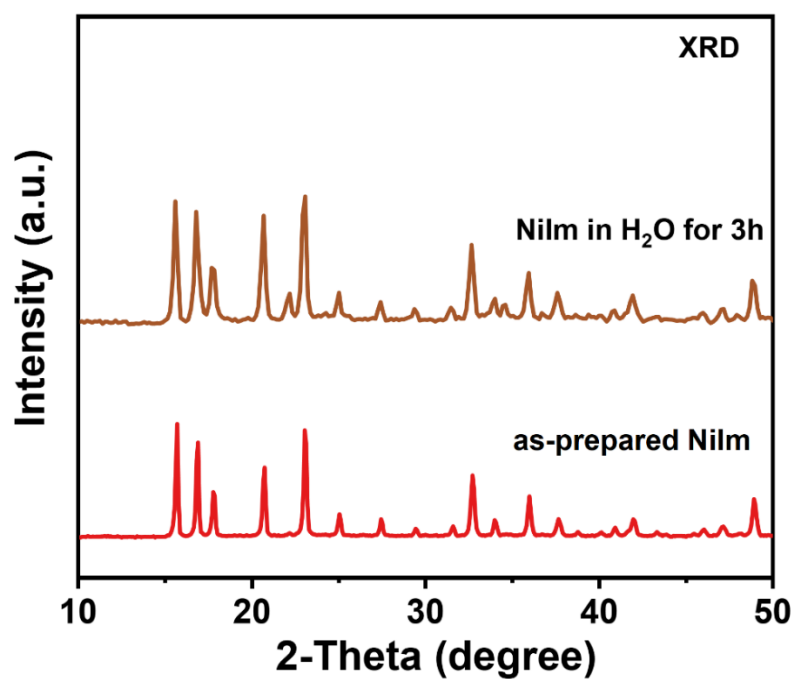
Fig. S2. PXRD patterns of the as-prepared NiIm and NiIm dispersed in water for 3 hours.
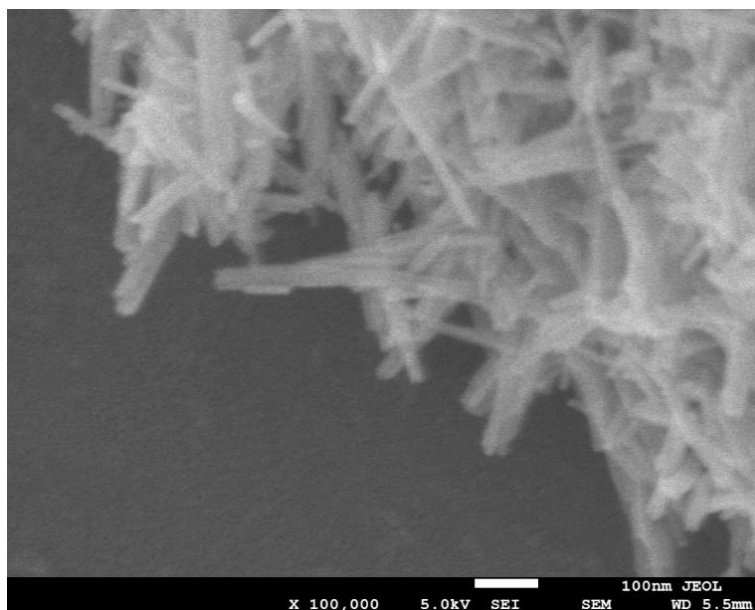
Fig. S3. SEM image of CdS NRs.
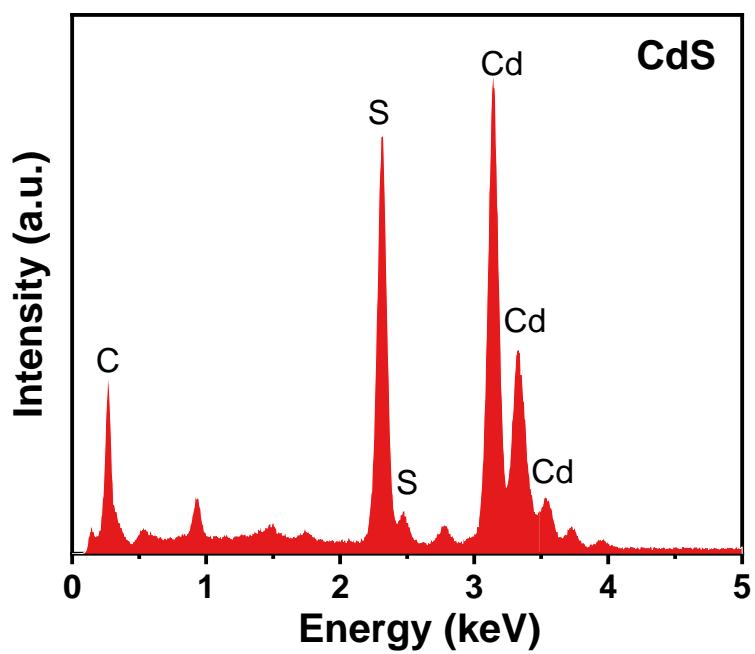
Fig. S4. EDS spectrum of CdS NRs.
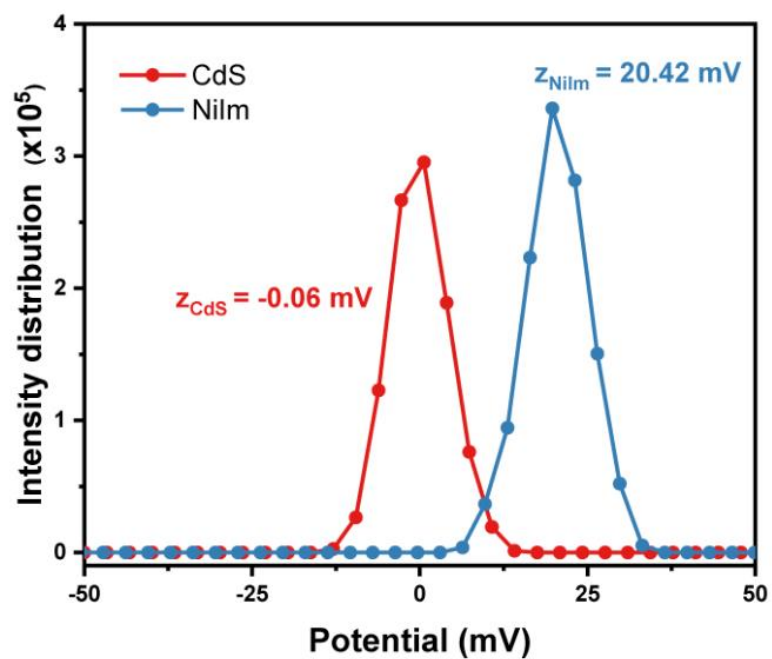
Fig. S5. Zeta potential acquired for NiIm and CdS in deionized water.
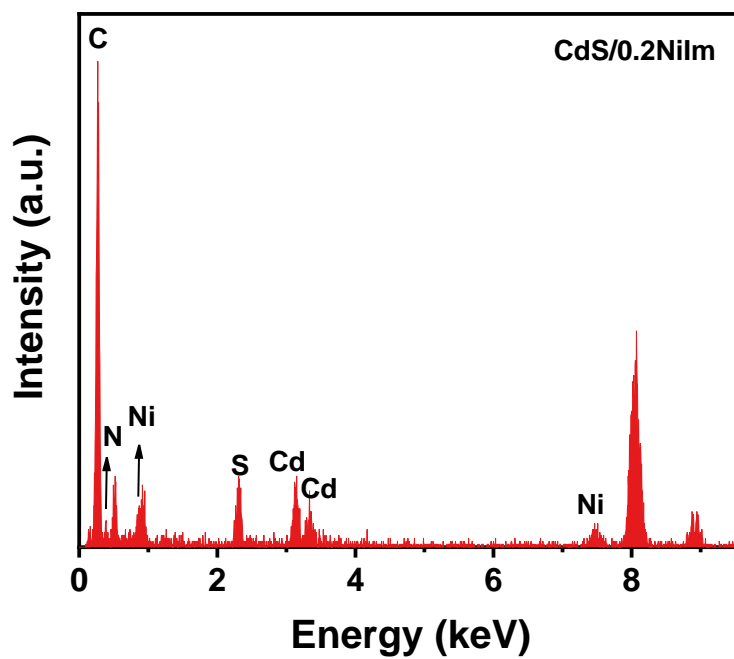
Fig. S6. EDS spectrum of CdS/0.2NiIm.
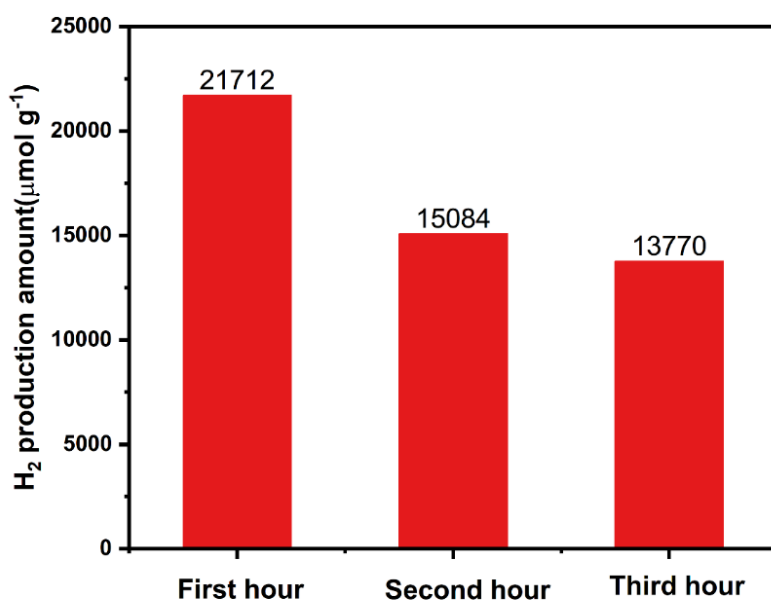
Fig. S7. Stability test of CdS/0.2NiIm for H_2 production in 10 vol% ethanol aqueous solution under visible light ($\lambda > 420$ nm).
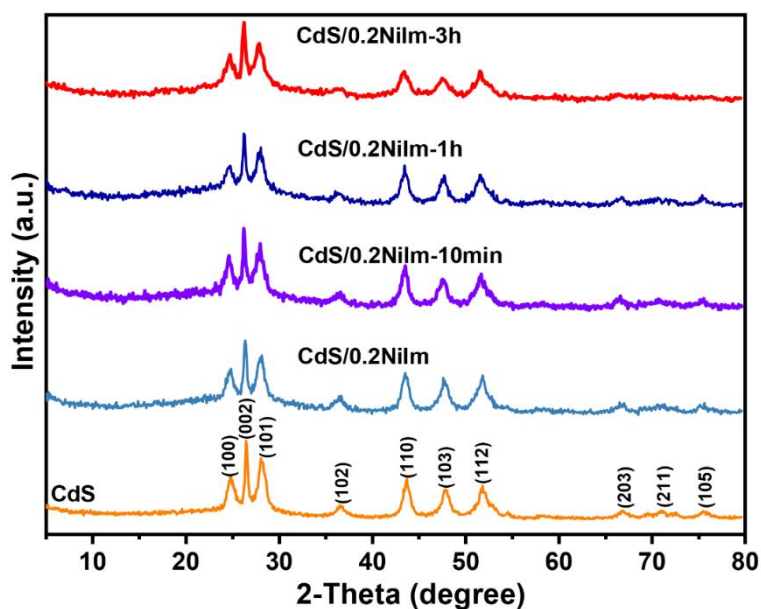
Fig. S8. PXRD patterns of CdS, CdS/0.2NiIm, CdS/0.2NiIm-10min, CdS/0.2NiIm-1h and CdS/0.2NiIm-3h.
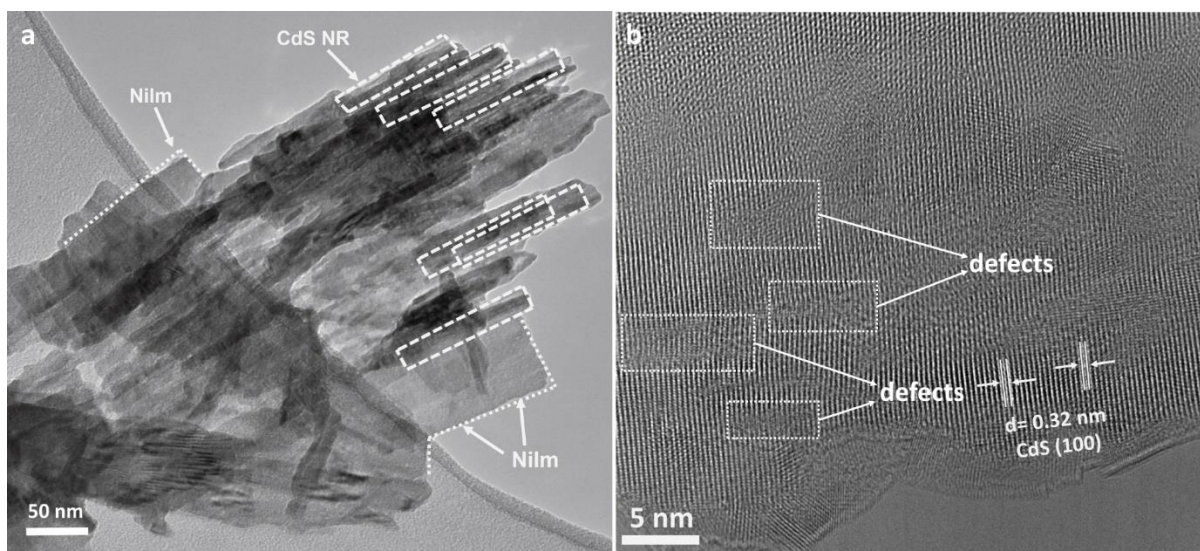
Fig. S9. (a) TEM image and (b) HRTEM image of CdS/0.2NiIm-3h.
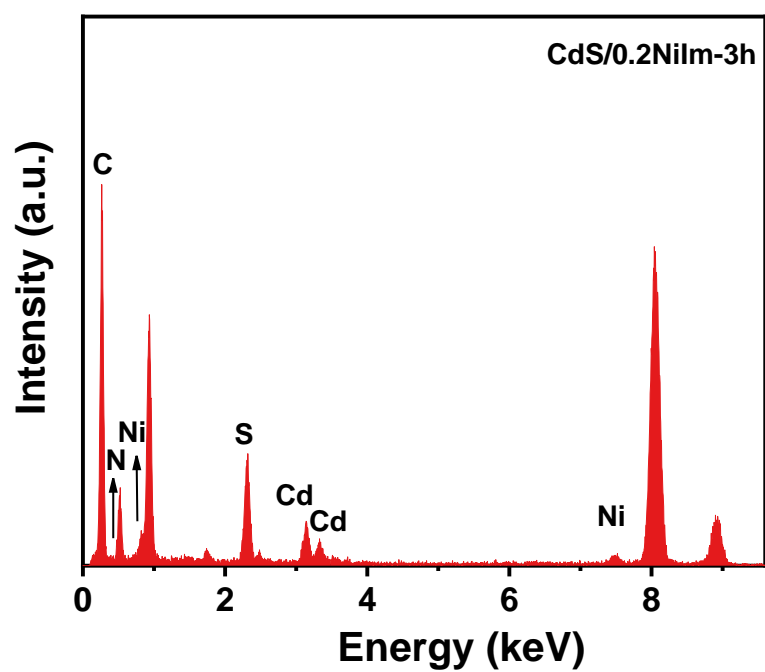
Fig. S10. EDS spectrum of the CdS/0.2NiIm-3h.
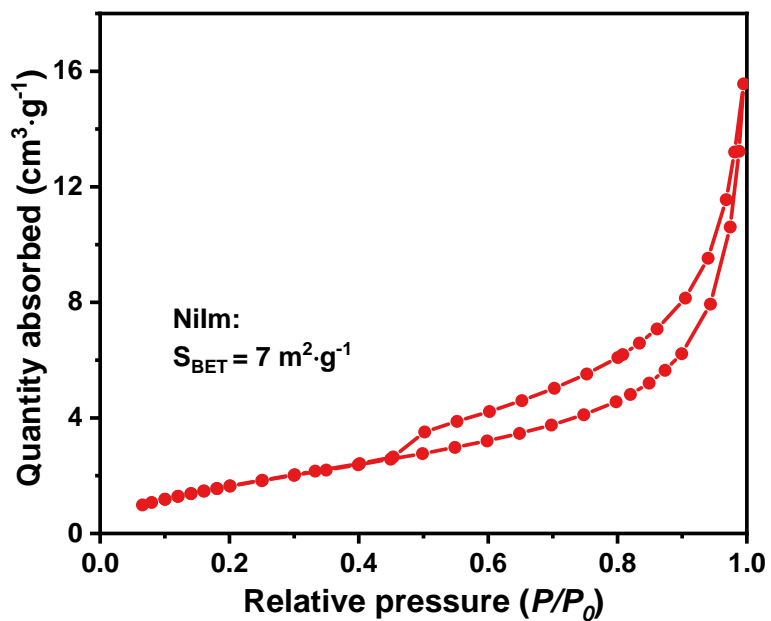
Fig. S11. N$_2$ sorption isotherm of NiIm.
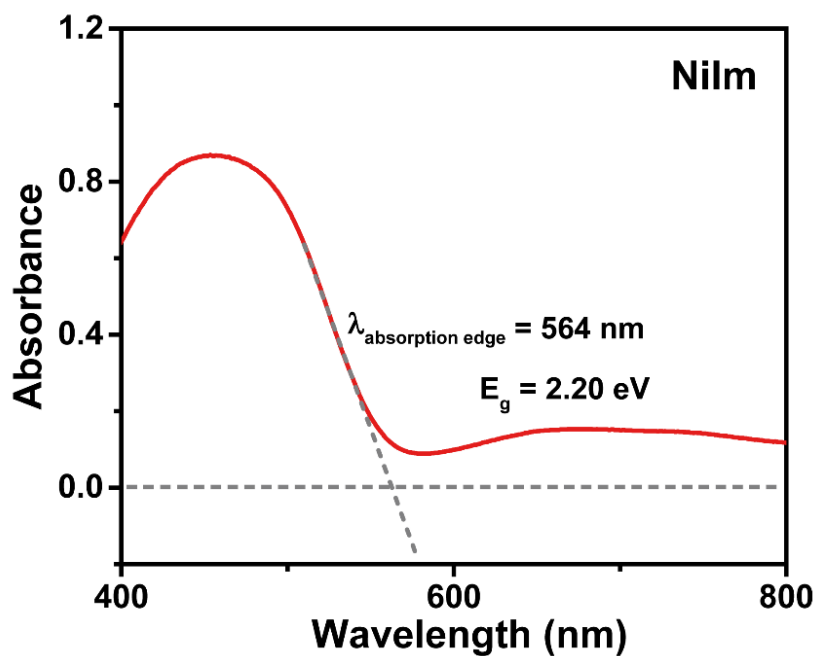
Fig. S12. UV-Vis DRS spectrum of NiIm.
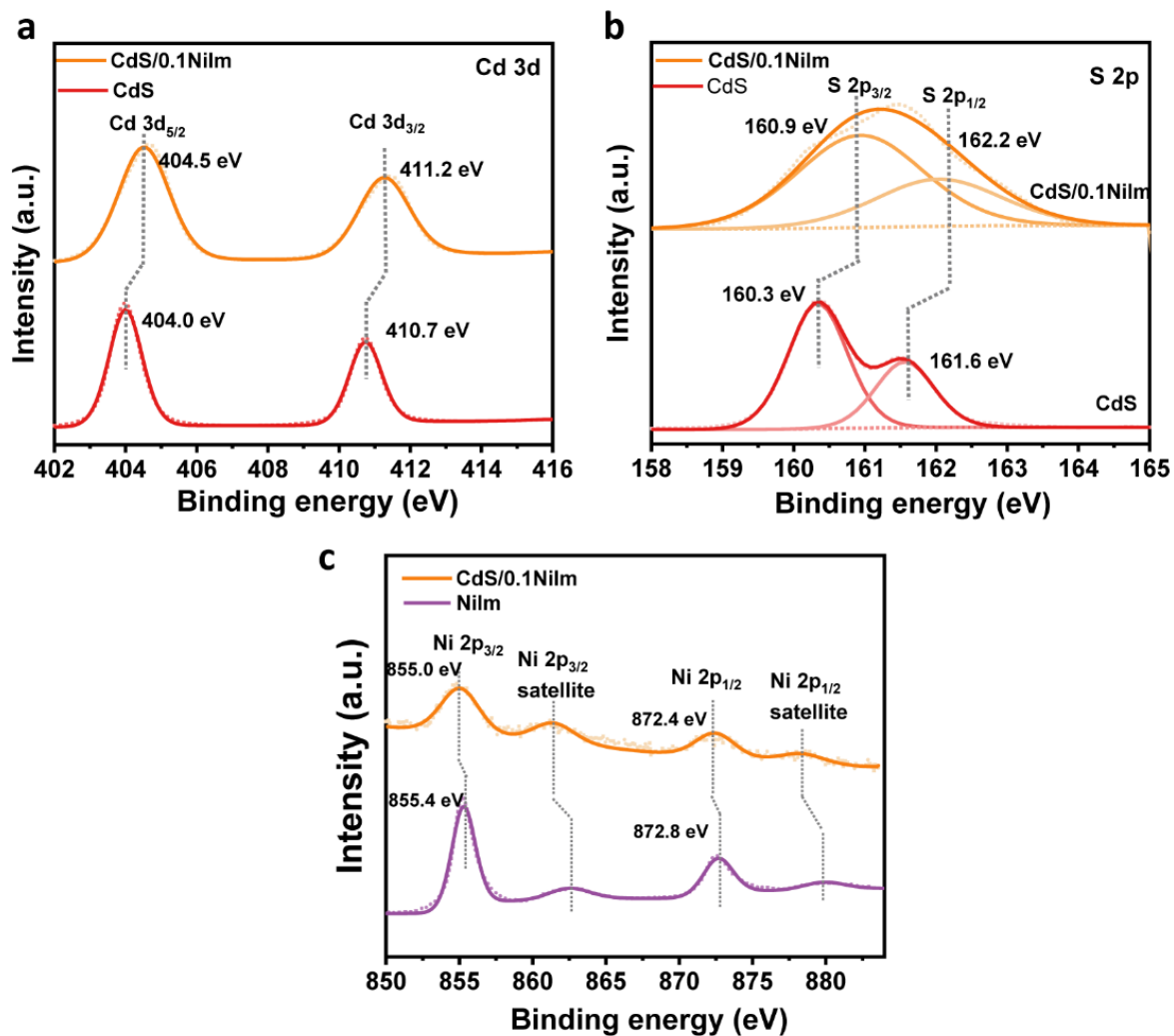
Fig. S13. High-resolution XPS spectra of (a) Cd 3d, (b) S 2p and (c) Ni 2p obtained from CdS/0.1NiIm, NiIm or CdS.

Table S1. H₂-production performances of the recently reported CdS-based photocatalysts.

Photocatalysts	Light sources	Reaction conditions	Photocatalytic performances (μmol h^{-1} g^{-1})	References
CdS/0.2NiIm	300 W Xe lamp, λ > 420 nm	10 vol.% ethanol solution	21,712	This work
MoS₂/Graphene-CdS	300 W Xe lamp, λ > 420 nm	20% lactic acid solution	1,600	[2]
Graphene oxide/CdS	300 W Xe lamp, λ > 420 nm	0.35 M Na₂S, 0.25 M Na₂SO₃	3,140	[3]
Cd/CdS/4%Pt	300 W Xe lamp, λ > 420 nm	0.35 M Na₂S, 0.25 M Na₂SO₃	16,800	[4]
MoS₂/CdS	300 W Xe lamp, λ > 420 nm	10% lactic acid solution	5,400	[5]
CdS/NiCo-LDH	300 W Xe lamp, λ > 400 nm	10% lactic acid solution	8,665	[6]
NiS/CDs/CdS	350 W Xe lamp, λ > 420 nm	0.25 M Na₂S, 0.35 M Na₂SO₃	1,444	[7]
Pt/TiO₂/CdS /Co₃O₄ spheres	300 W Xe lamp, λ > 420 nm	0.2 M Na₂S, Na₂SO₃	2,120	[8]
Ni(OH)₂/CdS	300 W Xe lamp, λ > 420 nm	20% triethanolamine solution	5,084	[9]
CdS/PT2/Pt	350 W Xe lamp, λ > 420 nm	10% lactic acid solution	9,280	[10]
CdS/Co₃O₄	350 W Xe lamp, λ > 420 nm	10% lactic acid solution	3,014	[11]
CdS-NRs/NMOF-Ni	300 W Xe lamp, λ > 420 nm	10% lactic acid solution	4500	[12]
CdS/ZIF-67-Co	5 W LED white light	15% lactic acid solution	65	[13]
CdS/UiO-66(10)	300 W Xe lamp, λ > 380 nm	CH₃CN/lactic acid/H₂O=27:3:1	1725	[14]

Table S2. Full width at half maximums of peaks and estimated crystallite sizes for CdS, CdS/0.2NiIm, CdS/0.2NiIm-10min, CdS/0.2NiIm-1h and CdS/0.2NiIm-3h acquired from PXRD patterns.

Photocatalysts	XRD Peaks			
	2θ*	24.8	26.3	28.1
	hkl	100	002	101
CdS	FWHM	0.86	0.31	0.92
	Crystallite**	9	28	9
CdS/0.2NiIm	FWHM	0.85	0.353	1.02
	Crystallite	9	24	8
CdS/0.2NiIm-10min	FWHM	1.1	0.28	1.22
	Crystallite	7	31	6
CdS/0.2NiIm-1h	FWHM	1.01	0.53	1.85
	Crystallite	8	29	7
CdS/0.2NiIm-3h	FWHM	1.01	0.36	1.18
	Crystallite	8	23	7

* The unit for 2θ is degree; ** The unit for crystallite size is nm.

Table S3. Relative crystallinity for CdS/0.2NiIm, CdS/0.2NiIm-10min, CdS/0.2NiIm-1h and CdS/0.2NiIm-3h acquired from the strongest XRD peak (002) in PXRD patterns.

Photocatalysts	Area of (002) peak	Relative crystallinity*
CdS/0.2NiIm	1575	1.00
CdS/0.2NiIm-10min	1212	0.77
CdS/0.2NiIm-1h	1145	0.73
CdS/0.2NiIm-3h	873	0.55

* The relative crystallinity is calculated based on the ratio of total peak area of the strongest crystalline peaks (002) of CdS/0.2NiIm-t versus the counterpart of the initial CdS/0.2NiIm.

Table S4. Surface areas, pore volumes and average pore sizes of CdS and CdS/0.2NiIm.

Samples	BET surface areas ($m^2 g^{-1}$)	Pore volumes ($cm^3 g^{-1}$)	Average pore sizes (nm)
CdS	60	0.25	16.5
CdS/0.2NiIm	35	0.16	18.5
NiIm	7	0.02	14.0

Table S5. Catalysts with Ni-N$_4$ active sites for H$_2$ evolution

Catalysts	Active sites	Reactions	Performances	References
1% Ni/NC	Ni-N$_4$	Thermocatalytic H$_2$ evolution from formic acid	50% conversion at 570 K	[15]
Ni SA/NP-NCF-800	Ni-N$_4$	Electrocatalytic H$_2$ evolution	$\eta_{10}^* = 137$ mV	[16]
Ni-N-C/EG	Ni-N$_4$	Electrocatalytic H$_2$ evolution	$\eta_{10} = 147$ mV	[17]

$^*\eta_{10}$ refers to the overpotential at the current density of 10 mA cm^{-2}

Table S6. Catalysts with M-N$_4$ active sites for H$_2$ evolution

Catalysts	Active sites	Reactions	References
Ru-NPC	Ru-N$_4$-P	Electrochemical H$_2$ evolution	[18]
Co-N$_x$-C@Co	Co-N$_4$	H$_2$ evolution	[19]

References

[1] B.C. Zhu, J.F. Zhang, C.J. Jiang, B. Cheng, J.G. Yu, First principle investigation of halogen-doped monolayer g-C_3N_4 photocatalyst, Appl. Catal. B 207 (2017) 27–34. https://doi.org/10.1016/j.apcatb.2017.02.020.

[2] K. Chang, Z. Mei, T. Wang, Q. Kang, S. Ouyang, J. Ye, MoS_2/graphene cocatalyst for efficient photocatalytic H_2 evolution under visible light irradiation, ACS Nano 8 (2014) 7078–7087. https://doi.org/10.1021/nn5019945.

[3] T. Peng, K. Li, P. Zeng, Q. Zhang, X. Zhang, Enhanced photocatalytic hydrogen production over graphene oxide–cadmium sulfide nanocomposite under visible light irradiation, J. Phys. Chem. C 116 (2012) 22720–22726. https://doi.org/10.1021/jp306947d.

[4] L. Shang, B. Tong, H. Yu, G.I.N. Waterhouse, C. Zhou, Y. Zhao, M. Tahir, L.-Z. Wu, C.-H. Tung, T. Zhang, CdS Nanoparticle-decorated Cd nanosheets for efficient visible light-driven photocatalytic hydrogen evolution, Adv. Energy Mater. 6 (2016) 1501241. https://doi.org/10.1002/aenm.201501241.

[5] X. Zong, H. Yan, G. Wu, G. Ma, F. Wen, L. Wang, C. Li, Enhancement of photocatalytic H_2 evolution on CdS by loading MoS_2 as cocatalyst under visible light irradiation, J. Am. Chem. Soc. 130 (2008) 7176–7177. https://doi.org/10.1021/ja8007825.

[6] S. Li, L. Wang, Y. Li, L. Zhang, A. Wang, N. Xiao, Y. Gao, N. Li, W. Song, L. Ge, J. Liu, Novel photocatalyst incorporating Ni-Co layered double hydroxides with P-doped CdS for enhancing photocatalytic activity towards hydrogen evolution, Appl. Catal. B 254 (2019) 145–155. https://doi.org/10.1016/j.apcatb.2019.05.001.

[7] R.-B. Wei, Z.-L. Huang, G.-H. Gu, Z. Wang, L. Zeng, Y. Chen, Z.-Q. Liu, Dual-cocatalysts decorated rimous CdS spheres advancing highly-efficient visible-light photocatalytic hydrogen production, Appl. Catal. B 231 (2018) 101–107. https://doi.org/10.1016/j.apcatb.2018.03.014.

[8] Z. Wang, W. Wu, Q. Xu, G. Li, S. Liu, X. Jia, Y. Qin, Z.L. Wang, Type-II hetero-junction dual shell hollow spheres loaded with spatially separated cocatalyst for enhancing visible light hydrogen evolution, Nano Energy 38 (2017) 518–525. https://doi.org/10.1016/j.nanoen.2017.05.046.

[9] J. Ran, J. Yu, M. Jaroniec, $Ni(OH)_2$ modified CdS nanorods for highly efficient visible-light-driven photocatalytic H_2 generation, Green Chem. 13 (2011) 2708–2713. https://doi.org/10.1039/c1gc15465f.

[10] C. Cheng, B. He, J. Fan, B. Cheng, S. Cao, J. Yu, An inorganic/organic s-scheme heterojunction H_2-production photocatalyst and its charge transfer mechanism, Adv. Mater. 33 (2021) 2100317. https://doi.org/10.1002/adma.202100317.

[11] D. Lang, F. Cheng, Q. Xiang, Enhancement of photocatalytic H_2 production activity of CdS nanorods by cobalt-based cocatalyst modification, Catal. Sci. Technol. 6 (2016) 6207–6216. https://doi.org/10.1039/c6cy00753h.

[12] H. Yang, C. Yang, N. Zhang, K. Mo, Q. Li, K. Lv, J. Fan, L. Wen, Drastic promotion of the photoreactivity of MOF ultrathin nanosheets towards hydrogen production by deposition with CdS nanorods, Appl. Catal. B 285 (2021) 119801. https://doi.org/10.1016/j.apcatb.2020.119801.

[13] Z. Jin, Z. Wang, H. Yuan, F. Han, Inserting MOF into flaky CdS photocatalyst forming special structure and active sites for efficient hydrogen production, Int. J. Hydrogen Energy 44 (2019) 19640–19649. https://doi.org/10.1016/j.ijhydene.2019.05.233.

[14] H.-Q. Xu, S. Yang, X. Ma, J. Huang, H.-L. Jiang, Unveiling charge-separation dynamics in cds/metal–organic framework composites for enhanced photocatalysis, ACS Catal. 8 (2018) 11615–11621. https://doi.org/10.1021/acscatal.8b03233.

[15] D.A. Bulushev, A.D. Nishchakova, S.V. Trubina, O.A. Stonkus, I.P. Asanov, A.V. Okotrub, L.G. Bulusheva, Ni-N$_4$ sites in a single-atom Ni catalyst on N-doped carbon for hydrogen production from formic acid, J. Catal. 402 (2021) 264–274. https://doi.org/10.1016/j.jcat.2021.08.044.

[16] J. Yu, J. Li, C.-Y. Xu, Q. Liu, J. Liu, R. Chen, J. Zhu, R. Li, J. Wang, Atomically dispersed Ni–N$_4$ species and Ni nanoparticles constructing N-doped porous carbon fibers for accelerating hydrogen evolution, Carbon 185 (2021) 96–104. https://doi.org/10.1016/j.carbon.2021.09.030.

[17] C. Lei, Y. Wang, Y. Hou, P. Liu, J. Yang, T. Zhang, X. Zhuang, M. Chen, B. Yang, L. Lei, C. Yuan, M. Qiu, X. Feng, Efficient alkaline hydrogen evolution on atomically dispersed Ni–N$_x$ Species anchored porous carbon with embedded Ni nanoparticles by accelerating water dissociation kinetics, Energy Environ. Sci. 12 (2019) 149–156. https://doi.org/10.1039/c8ee01841c.

[18] C. Wu, S. Ding, D. Liu, D. Li, S. Chen, H. Wang, Z. Qi, B. Ge, L. Song, A unique Ru–N$_4$–P coordinated structure synergistically waking up the nonmetal p active site for hydrogen production, Research 2020 (2020) 5860712. https://doi.org/10.34133/2020/5860712.

[19] M. Qin, S. Fan, X. Li, Z. Yin, L. Wang, A. Chen, Double Active Sites in Co–N$_x$–C@Co electrocatalysts for simultaneous production of hydrogen and carbon monoxide, ACS Appl. Mater. Interfaces 13 (2021) 38256–38265. https://doi.org/10.1021/acsami.1c08363.

Chapter 5: TiO$_2$/FePS$_3$ S-scheme heterojunction for greatly raised photocatalytic hydrogen evolution

5.1 Introduction and significance

The emerging extreme climate changes and increasing natural disasters have been a stimulus for seeking low-carbon alternatives to traditional carbon-based fossil fuels. Solar-to-hydrogen (STH) transformation has been considered as a promising approach to converting renewable solar energy into hydrogen. Restricted by the low efficiency and high cost of precious metal cocatalysts, high-performance and cost-effective photocatalysts are required to facilitate the STH transformation process.

According to the previous works in Chapters 3 and 4, the MOF-based photocatalysts suffer from instability under long-time light illumination. The inorganic two-dimensional FePS$_3$ with layered structure was introduced and proposed to overcome this challenge. In this chapter, TiO$_2$ nanoparticles anchored with the two-dimensional FePS$_3$ (FPS) nanosheets were prepared and tested for photocatalytic hydrogen evolution reaction (p-HER) under ultraviolet-visible light irradiation. Highlights of this chapter include:

(1) The improved performance of TiO$_2$-based photocatalysts for hydrogen production has been achieved by the introduction of FPS.

(2) A series of advanced characterization techniques have been employed to reveal the origin of the improved photocatalytic performance of TiO$_2$/FPS for p-HER.

(3) Particularly, the surface photovoltage spectroscopy integrated imaging techniques, the Kelvin probe force microscopy (KPFM), has been employed to visualize the electron migration pathway, revealing the separation of the electron-hole pairs.

5.2 TiO$_2$/FePS$_3$ S-scheme heterojunction for greatly raised photocatalytic hydrogen evolution

This chapter is included as it appears as a journal paper published by **Bingquan Xia**, Bowen He, Laiquan Li, Yanzhao Zhang, Jianjun Zhang, Jiaguo Yu, Jingrun Ran, Shi-Zhang Qiao. TiO$_2$/FePS$_3$ S-scheme heterojunction for greatly raised photocatalytic hydrogen evolution, unpublished work written in manuscript style (submitted to ***Advanced Energy Materials*** 2022).

Statement of Authorship

Title of Paper	TiO$_2$/FePS$_3$ S-scheme heterojunction for greatly raised photocatalytic hydrogen evolution
Publication Status	☐ Published ☐ Accepted for Publication ☐ Submitted for Publication ☑ Unpublished and Unsubmitted work written in manuscript style
Publication Details	Bingquan Xia, Bowen He, Jianjun Zhang, Laiquan Li, Yanzhao Zhang, Jiaguo Yu, Jingrun Ran, and Shi-Zhang Qiao, TiO$_2$/FePS$_3$ S-scheme heterojunction for greatly raised photocatalytic hydrogen evolution, Advanced Energy Materials, 2022, submitted.

Principal Author

Name of Principal Author (Candidate)	Bingquan Xia		
Contribution to the Paper	Research plan, materials synthesis, most of the physical characterization, photocatalytic performance tests, photoelectrochemical and electrochemical measurement, data analysis, and manuscript draft.		
Overall percentage (%)	80		
Certification:	This paper reports on original research I conducted during the period of my Higher Degree by Research candidature and is not subject to any obligations or contractual agreements with a third party that would constrain its inclusion in this thesis. I am the primary author of this paper.		
Signature		Date	15/01/2022

Co-Author Contributions

By signing the Statement of Authorship, each author certifies that:

i. the candidate's stated contribution to the publication is accurate (as detailed above);

ii. permission is granted for the candidate in include the publication in the thesis; and

iii. the sum of all co-author contributions is equal to 100% less the candidate's stated contribution.

Name of Co-Author	Bowen He		
Contribution to the Paper	Helped with KPFM data collection and analysis		
Signature		Date	15/01/2022

Name of Co-Author	Jianjun Zhang		
Contribution to the Paper	Helped with AFM data collection and analysis		
Signature		Date	15/01/2022

Please cut and paste additional co-author panels here as required.

Name of Co-Author	Laiquan Li		
Contribution to the Paper	Helped with XAS data collection and analysis		
Signature		Date	15/01/2022

Name of Co-Author	Yanzhao Zhang		
Contribution to the Paper	Helped to revise the manuscript		
Signature		Date	15/01/2022

Name of Co-Author	Jiaguo Yu		
Contribution to the Paper	Helped to evaluate and edit the manuscript		
Signature		Date	15/01/2022

Name of Co-Author	Jingrun Ran		
Contribution to the Paper	Discussion of research plan, manuscript revision, and acted as corresponding author		
Signature		Date	15/01/2022

Name of Co-Author	Shi-Zhang Qiao		
Contribution to the Paper	Supervised development of work, helped in manuscript evaluation and revision, and acted as corresponding author		
Signature		Date	15/01/2022

Please cut and paste additional co-author panels here as required.

TiO$_2$/FePS$_3$ S-scheme heterojunction for greatly raised photocatalytic hydrogen evolution

Bingquan Xia, Bowen He, Jianjun Zhang, Laiquan Li, Yanzhao Zhang, Jiaguo Yu, Jingrun Ran*, and Shi-Zhang Qiao*

B. Xia, L. Li, Y. Zhang, J. Ran, S.-Z. Qiao
School of Chemical Engineering and Advanced Materials, The University of Adelaide, Adelaide, SA 5005, Australia
E-mail: s.qiao@adelaide.edu.au, jingrun.ran@adelaide.edu.au

B. He, J. Zhang, J. Yu
Laboratory of Solar Fuel, Faculty of Materials Science and Chemistry, China University of Geosciences, 388 Lumo Road, Wuhan, 430074, P. R. China

The aggravating extreme climate changes and natural disasters stimulate the exploration of low-carbon/zero-carbon alternatives to traditional carbon-based fossil fuels. Solar-to-hydrogen (STH) transformation is considered as an appealing route to convert renewable solar energy into carbon-free hydrogen. Restricted by the low efficiency and high cost of noble-metal cocatalysts, high-performance and cost-effective photocatalysts are required to realize the realistic STH transformation. Herein, the two-dimensional $FePS_3$ (FPS) nanosheets anchored with TiO_2 nanoparticles ($TiO_2/FePS_3$) were synthesized and tested for photocatalytic hydrogen (H_2) evolution reaction. With the integration of FePS, the photocatalytic H_2-evolution rate on $TiO_2/FePS_3$ is radically increased by ~1686% times, much faster than that of TiO_2 alone. The origin of the greatly-raised activity is revealed by theoretical calculations and various advanced characterizations, such as transient-state photoluminescence spectroscopy/surface photovoltage spectroscopy, *in-situ* atomic force microscopy combined with Kelvin probe force microscopy (AFM-KPFM) and *in-situ* X-ray photoelectron spectroscopy (XPS), synchrotron-based X-ray absorption near edge structure (XANES). Especially, the *in-situ* AFM-KPFM and *in-situ* XPS together confirm the electron transport pathway in $TiO_2/FePS_3$ with light illumination, unveiling the efficient separation/transfer of charge carrier in $TiO_2/FePS_3$ step-scheme (S-scheme) heterojunction. This work sheds light on designing and fabricating novel two-dimensional material-based S-scheme heterojunction in the photocatalysis area.

1. Introduction

Recently, extreme climate changes and natural disasters have alerted humans to the impact of global warming, which has continually intensified and could be out of control. Therefore, it is urgent to greatly reduce the gigantic consumption of carbon-based fossil fuels,[1-2] which emit substantial greenhouse gases to tremendously aggravate global warming. Furthermore, it is of great significance to realize carbon neutrality in human society via replacing fossil fuels by low-carbon/carbon-free alternatives. Thus, the conversion of renewable solar energy[3-5] into clean and carbon-free hydrogen (H_2) fuel is highly attractive. Such a solar-to-H_2 (STH) conversion can be achieved utilizing photocatalytic H_2 evolution via water splitting,[6-10] which is regarded as an alluring, environmentally benign and low-cost strategy. Hence, a highly active, robust and affordable photocatalyst is the most sought after.[11-13] Rational design and synthesis of such a photocatalyst require not only the emerging nano-sized building blocks with desired features, but also efficient charge dissociation/transfer boosted by the strong built-in electric field in a favorable junction system.

In the past decades, two-dimensional (2D) materials have demonstrated a great capacity in achieving efficient and cost-effective photocatalysis for various reactions, due to their distinct physicochemical features.[14-20] Recently, an emerging 2D material, $FePS_3$ (FPS), [21-26] has displayed numerous attractive characteristics for catalysis: (i) ultrathin structure boosting rapid bulk-to-surface electron-hole transport; (ii) high specific surface area accelerating efficient adsorption/desorption of reactant and product, and benefiting the anchoring of other nano-building blocks; (iii) exposed under-coordinated edge atoms serving as active sites to advance the reactions; (iv) thickness-dependent electronic band structure benefiting the regulation of light absorption and redox abilities of charge carriers; (v) p-type semiconductor nature favoring the construction of certain junction system with a strong built-in electric field. Albeit the above alluring advantages,[27-29] 2D FPS is rarely adopted in the photocatalysis area.

It is a great challenge to accurately regulate the charge dissociation/transfer for realizing the high charge utilization efficiency and strong redox abilities of electrons and holes in semiconductor-based photocatalysts.[30-33] Recently, step-scheme (S-scheme) heterojunction emerges as a very effective junction system with a strong built-in electric field to simultaneously boost the splitting of electron-hole pairs and retain their high redox capacities.[34-40] Especially, the S-scheme junction based on a n-p junction system is rarely reported.[41] Additionally, the direct visualization of the charge carrier transport pathway in the S-scheme junction is challenging, but interesting and important for understanding the in-depth mechanism in photocatalytic reactions.[42-43] This will further guide the rational design and synthesis of an efficient junction system toward targeted photocatalytic reactions. Atomic force microscopy combined with Kelvin probe force microscopy (AFM-KPFM) could *in-situ* explore the charge transfer course in photocatalyst with light illumination. [44-47] Hence, it is particularly important to apply *in-situ* AFM-KPFM to study the charge transfer pathway in the S-scheme junction based on a n-p semiconductor system.

Herein, 2D FPS nanosheets (NSs) were decorated with TiO_2 nanoparticles (NPs) to form the S-scheme heterojunction of FPS/TiO_2 possessing a strong internal electric field, which significantly raises the photocatalytic H_2-evolution rate compared with TiO_2 NPs alone. The as-synthesized FPS/TiO_2 exhibited a H_2 evolving rate of 99.5 $\mu mol\ h^{-1}\ g^{-1}$, surpassing that of TiO_2 alone by ~1686%. The origin of the tremendously increased rate is studied by a series of cutting-edge characterizations, *e.g.,* transient-state photoluminescence/surface photovoltage spectroscopy, *in-situ* AFM-KPFM, *in-situ* X-ray photoelectron spectroscopy (XPS) and synchrotron-based X-ray absorption near edge structure (XANES). Notably, *in-situ* AFM-KPFM was carried out to visualize the photogenerated charge migration path and surface potential changes of the as-prepared TiO_2/FPS with light excitation. Additionally, *ex-situ* XPS and theoretical calculations reveal the intimate electronic interaction between TiO_2 and FPS. These results demonstrate that TiO_2 NPs coupling with novel 2D FPS NSs can form the S-

scheme heterojunction based on an n-p semiconductor system, which not only greatly advances the electron-hole separation/transport, but also reserves the electrons and holes with higher redox capabilities on the conduction band of FPS and valence band of TiO_2, respectively. Hence, the photocatalytic H_2-evolution rate of FPS/TiO_2 S-scheme heterojunction is significantly raised.

2. Results and discussion

2.1. Crystal structure, morphology and elemental composition of FPS and FPS/TiO₂

The flake-like bulk FPS was grounded for 0.5 hour and then added into ethanol for the subsequent sonication and centrifuge treatment to acquire the FPS nanosheets (NSs). The synthesis details can be found in the experimental section. As shown in **Figure 1a**, the X-Ray diffraction (XRD) pattern of FPS NSs is attributed to the monoclinic structured $Fe_2P_2S_6$ (JCPDS #33-0672). The top-view and side-view atomic structures of monoclinic $FePS_3$ are displayed in Figure 1b and Figure S1, respectively. Figure 1b indicates that in a typical unit cell, one Fe atom is connected to six neighboring S atoms, while the P atom is connected to one P atom and three S atoms. The side-view atomic structure of FPS (Figure S1) confirms the layered structure, suggesting that obtaining two-dimensional (2D) FPS from bulk FPS via exfoliation is feasible. The as-synthesized FPS NSs are characterized by transmission electron microscopy (TEM), energy-dispersive X-ray spectroscopy (EDS), high angle annular dark-field scanning transmission electron microscopy (HAADF-STEM), elemental mapping and atomic force microscopy (AFM). The TEM image of FPS NSs in Figure 1c confirms the sheet-like structure of FPS NSs with lateral sizes of ~320-380 nm. The EDS spectrum (Figure 1d) suggests the existence of Fe, P and S elements. And the HAADF-STEM image and the corresponding elemental mapping images of Fe, P and S (Figure 1e) together confirm the successful synthesis of FPS NSs. Furthermore, the AFM image of FPS NSs (Figure 1f) and the corresponding height profiles (Figure 1g) show the FPSs NSs with a thickness of ~20 nm, further supporting the successful fabrication of FPS NSs via the sonication treatment.
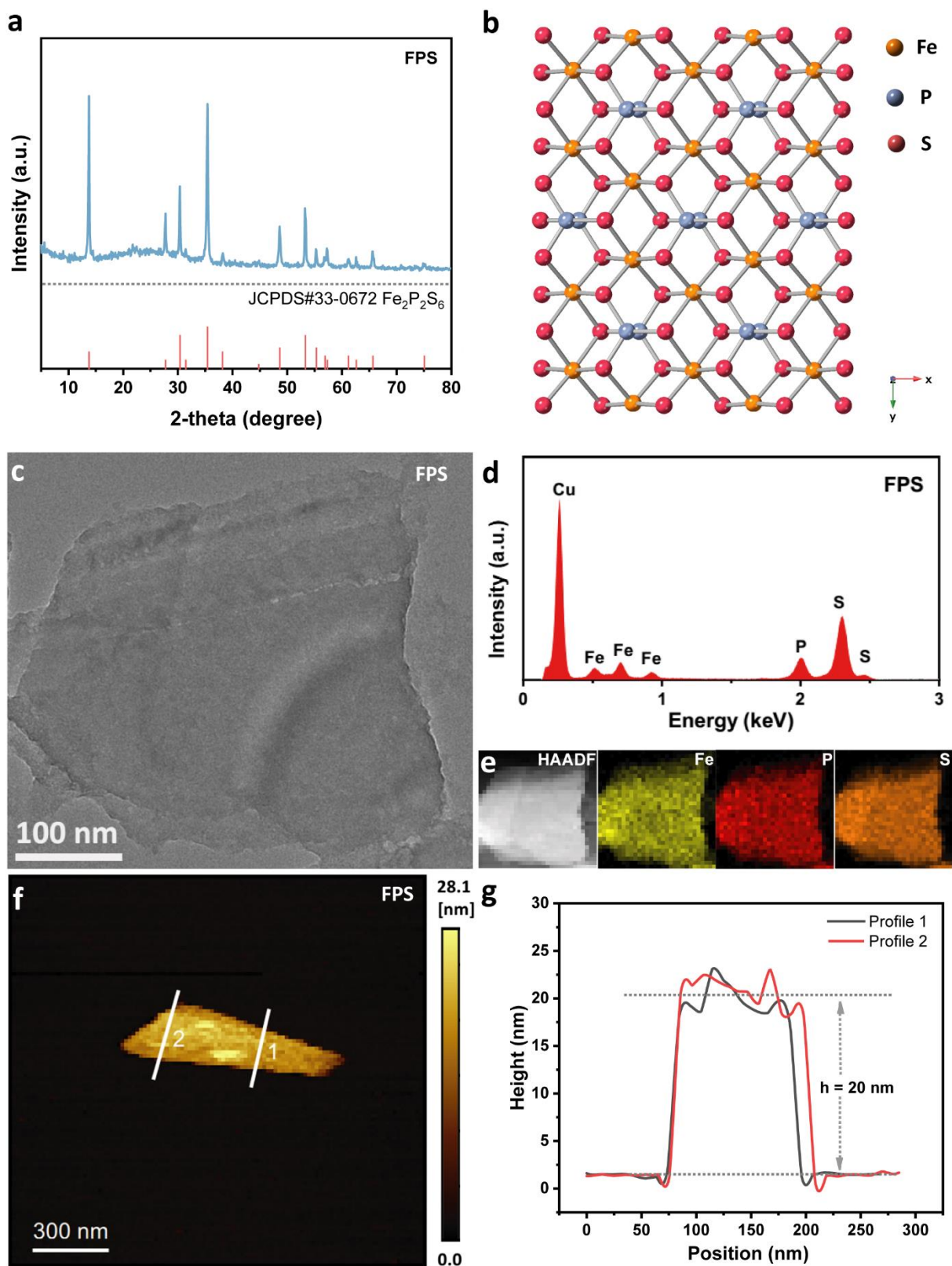
Figure 1. (a) XRD pattern of FPS NSs. (b) Top-view atomic structure of FPS viewed along [001] direction. (c) TEM image of FPS NSs. (d) EDS spectrum of FPS NSs. (e) HAADF-STEM image and mapping images of different elements in FPS NSs. (f) AFM image and (g) corresponding profiles of FPS NSs.

Then, we have anchored the TiO$_2$ NPs on the FPS NSs utilizing a facile physical grinding approach. In detail, 0.05 g TiO$_2$ NPs were coupled with 1, 2, 5 and 10 ml of FPS NSs ethanol suspension, respectively. The as-synthesized samples are annotated as TF1, TF2, TF5 and TF10, respectively. TiO$_2$ NPs alone is annotated as TF0. The XRD patterns of all the above samples are shown in **Figure 2a**. Both Rutile and Anatase structured TiO$_2$ can be observed in Figure 2a. No apparent diffraction peaks of FPS can be observed, possibly owing to the low content of FPS in the combined samples. This is also confirmed by the result obtained from inductively coupled plasma-optical emission spectrometry (ICP-OES) measurement, which indicates that FPS only accounts for ~0.94 wt% even in TF10. Raman spectroscopy was also conducted to acquire the structure information of TF0 and TF10. The Raman spectra for TF0 and TF10 are shown in Figure S2. The peaks around 144, 200, 396, 516, and 635 cm^{-1} could be assigned to the characteristic Raman modes of anatase TiO$_2$. No apparent difference of these peaks is observed for TF10 in comparison to those of TF0, suggesting the introduction of FPS does not impact the structure of TiO$_2$. The synchrotron-based X-ray absorption near edge structure (XANES) spectra of Ti L edge for TF5 and TF10 are displayed in Figure S3. Furthermore, the TEM image of TF10 is displayed in Figure 2b, which shows that the TiO$_2$ NPs are well dispersed on the FPS NSs. The 0.24 and 0.35 nm lattice spacings manifested in the high-resolution (HR)TEM image of TF10 (Figure 2c), are ascribed to the Anatase TiO$_2$ (103) and (101) facets, respectively. The EDS spectrum of TF10 (Figure 2d) confirms the existence of Ti, O, Fe, P, and S elements, corroborating the combination of TiO$_2$ NPs and FPS NSs in TF10. Furthermore, the HAADF-STEM image of TF10 and the element distribution mapping of Ti, O, Fe, P and S (Figure 2e) further support the intimate combination of TiO$_2$ NPs with FPS NSs. All the above results corroborate the successful anchoring of TiO$_2$ NPs on PFS surface.

2.2. Photocatalytic H$_2$ evolution rate

To evaluate the performance of photocatalytic hydrogen (H$_2$) evolution reaction (pHER), all the tests for as-synthesized photocatalysts were measured in 10 vol% ethanol aqueous solution
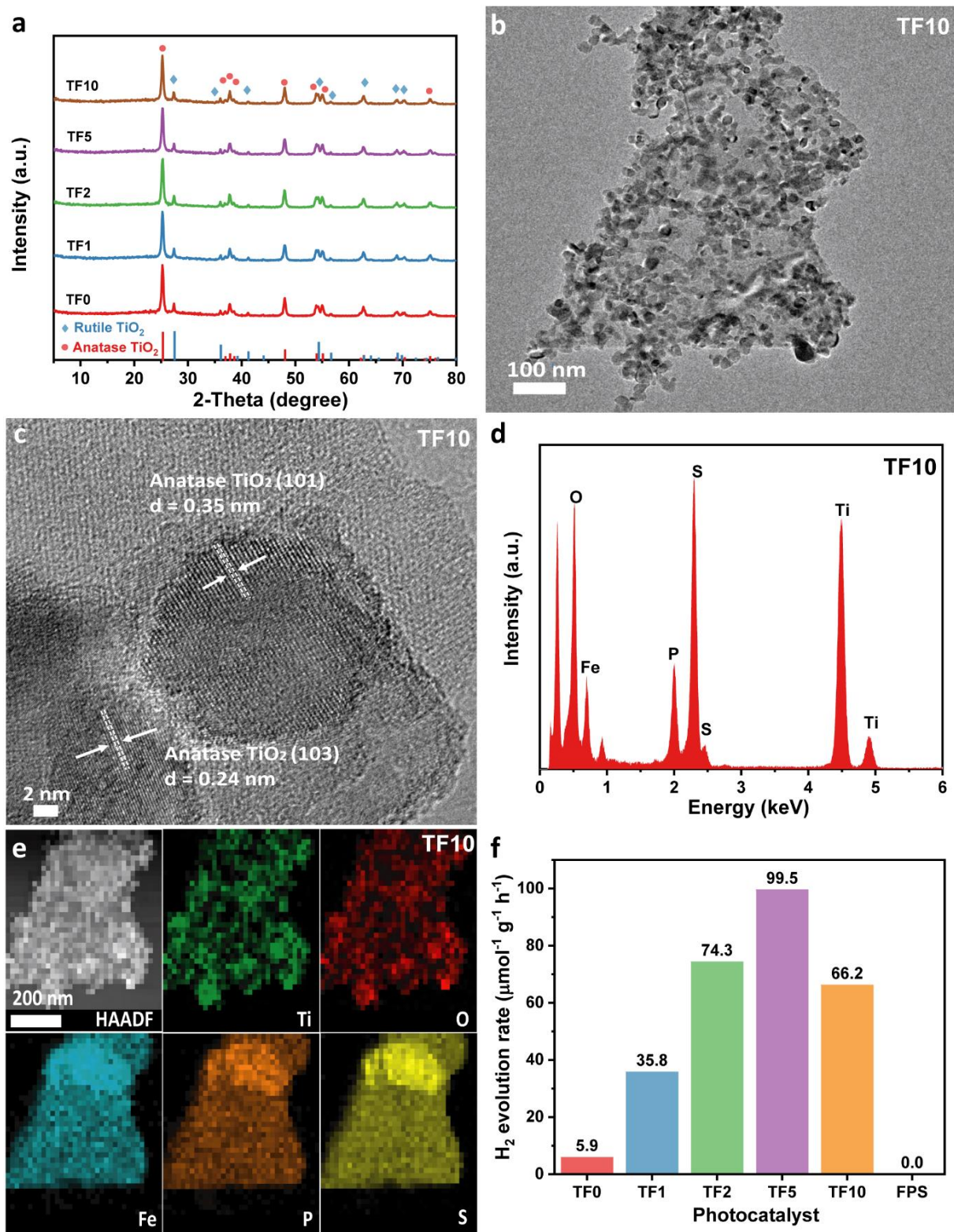
Figure 2. (a) XRD patterns of TF0, TF1, TF2, TF5 and TF10. (b) TEM, (c) HRTEM images and (d) EDS spectrum of TF10. (e) HAADF-STEM image and corresponding mapping images of elements in TF10. (f) Photocatalytic H_2-evolution rates of TF0, TF1, TF2, TF5, TF10 and FPS in 10 vol% ethanol aqueous solution under xenon light.

under xenon light irradiation. The pHER rate of pure TiO_2 (TF0) displayed in Figure 2f is about 5.9 µmol h^{-1} g^{-1}, while no H_2 was generated if bare FPS was used as the photocatalyst. As for the TFx (x = 1, 2, 5 and 10) composites, their pHER rates were improved by the introduction of FPS NSs. Compared with the rate of TiO_2, the rates of TF1 and TF2 are raised to 35.8 and 74.3 µmol h^{-1} g^{-1}, respectively. Strikingly, the rate of TF5 reaches the peak at 99.5 µmol h^{-1} g^{-1}, supassing the counterpart of TF0 by ~1686%. But further increasing the content of FPS does not arouse further activity enhancement, since TF10 only shows a rate of 66.2 µmol h^{-1} g^{-1}. This possibly results from the blockage of TiO_2 reactive sites and the weakened light-harvesting ability of TiO_2 by the excessive FPS NSs. Additionally, the TF5 shows an acceptable stability for pHER (Figure S4).

2.3. Charge carrier separation and transfer

Since the separation/transfer of charge carriers serves a key role in the overall photocatalytic reaction, a range of cutting-edge characterizations were conducted to explore the photogenerated electron-hole dissociation and transport. First, steady-state photoluminescence (PL) spectroscopy and time-resolved (TR)PL were used to investigate the separation/transfer of charge carriers. Both TF0 and TF5 show two distinct peaks around 408 and 467 nm in **Figure 3a**, which are equal to 3.04 and 2.66 eV, respectively. The emission peak around ~408 nm is attributed to the interband PL phenomenon. And the PL peak at ~468 nm could be attributed to the band edge-free excitons. The anchoring of TiO_2 NPs on FPS NSs apparently reduces the PL intensities of TiO_2, indicating that the charge recombination rate in TF5 is obviously reduced in contrast to that in TF0. Furthermore, insights into the charge carrier lifetimes in TF0 and TF5 can be acquired in the TRPL spectra (Figure 3b). As can be seen in Figure 3b and Table S1, the fitted and average charge carrier lifetimes (τ_1 = 0.75 ns, τ_2 = 3.04 ns, τ_3 = 11.11 ns and τ_{ave} = 3.71 ns) of TF5 are obviously raised in contrast to those of TF0 (τ_1 = 0.27 ns, τ_2 = 2.06 ns, τ_3 = 9.29 ns and τ_{ave} = 3.20 ns). These results further corroborate the higher charge carrier separation
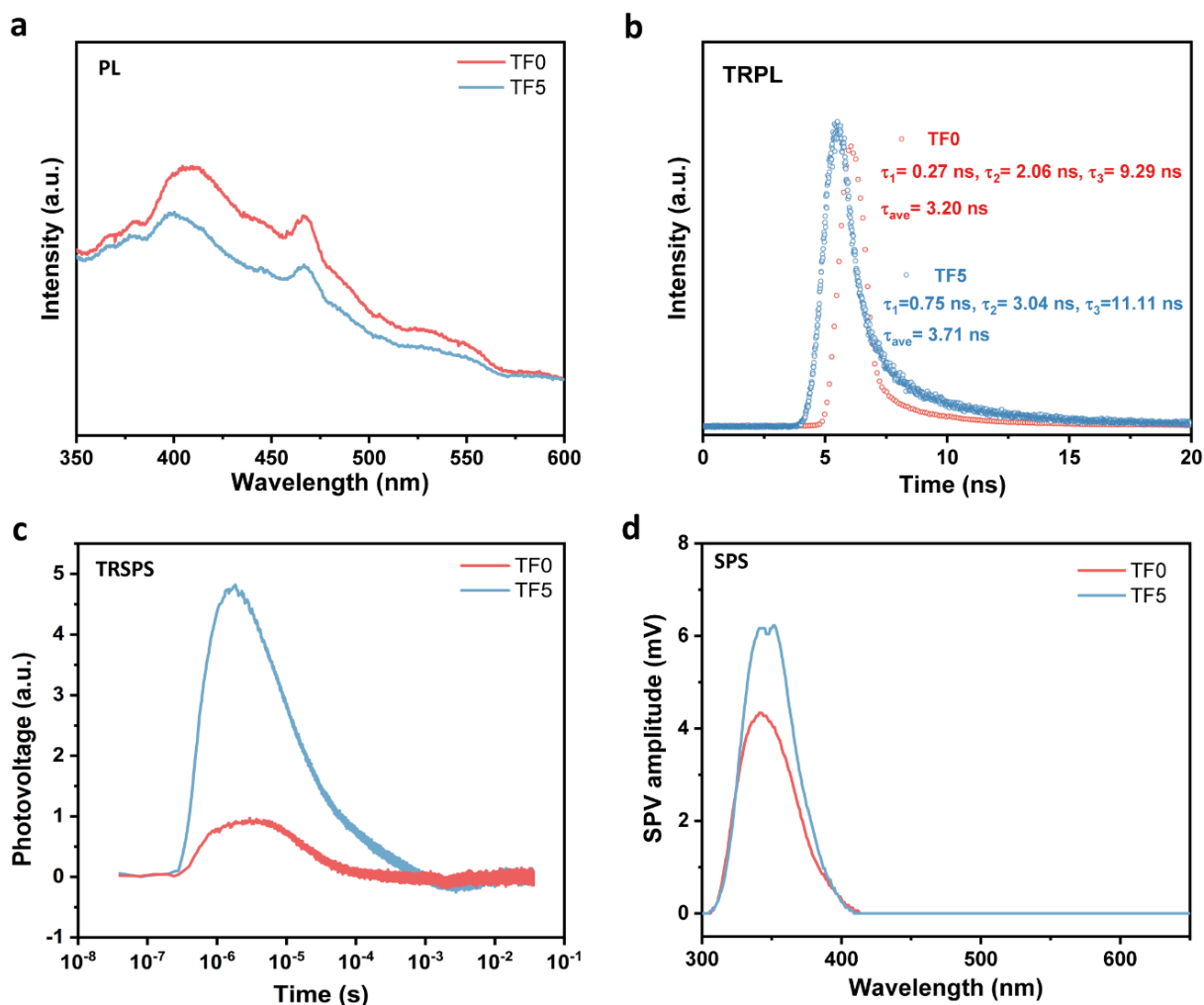
Figure 3. (a) steady-state PL spectra, (b) TRPL spectra, (c) TRSPS spectra and (d) steady-state SPS spectra of TF0 and TF5.

/transport efficiency in TF5 compared to that in TF0. Furthermore, the time-resolved surface photovoltage spectroscopy (TRSPS) and steady-state surface photovoltage spectroscopy (SPS) were performed to reveal the surface charge carrier separation/transfer in TF5. As displayed in Figure 3c, both TF0 and TF5 show the positive surface photovoltage signals, indicating that the photoinduced holes are accumulated on the surface after the light excitation. Furthermore, TF5 displays a much higher positive surface photovoltage signal than TF0, indicating that the anchoring of TiO_2 NPs on FPS NSs could greatly boost the accumulation of photogenerated holes on the surface. Considering that TiO_2 accounts for the most part of TF5, it can be inferred that the combination with FPS NSs advances dissociating electron-hole pairs in TiO_2 NPs and also accumulating photogenerated holes on the surface of TiO_2 NPs. The steady-state SPS

results in Figure 3d further confirm the higher surface photovoltage signal of TF5 compared with that of TF0, in agreement with the TRSPS result (Figure 3c). Besides, the surface photovoltage signal can only be observed as the excitation light wavelength is below ~410 nm, confirming that the positive surface photovoltage is due to the surface accumulation of photogenerated holes from TiO_2 rather than FPS NSs.

To reveal the charge transfer procedure, electrochemical impedance spectroscopy (EIS) was then performed on electrodes prepared with TF0 and TF5 in an electrochemical environ-
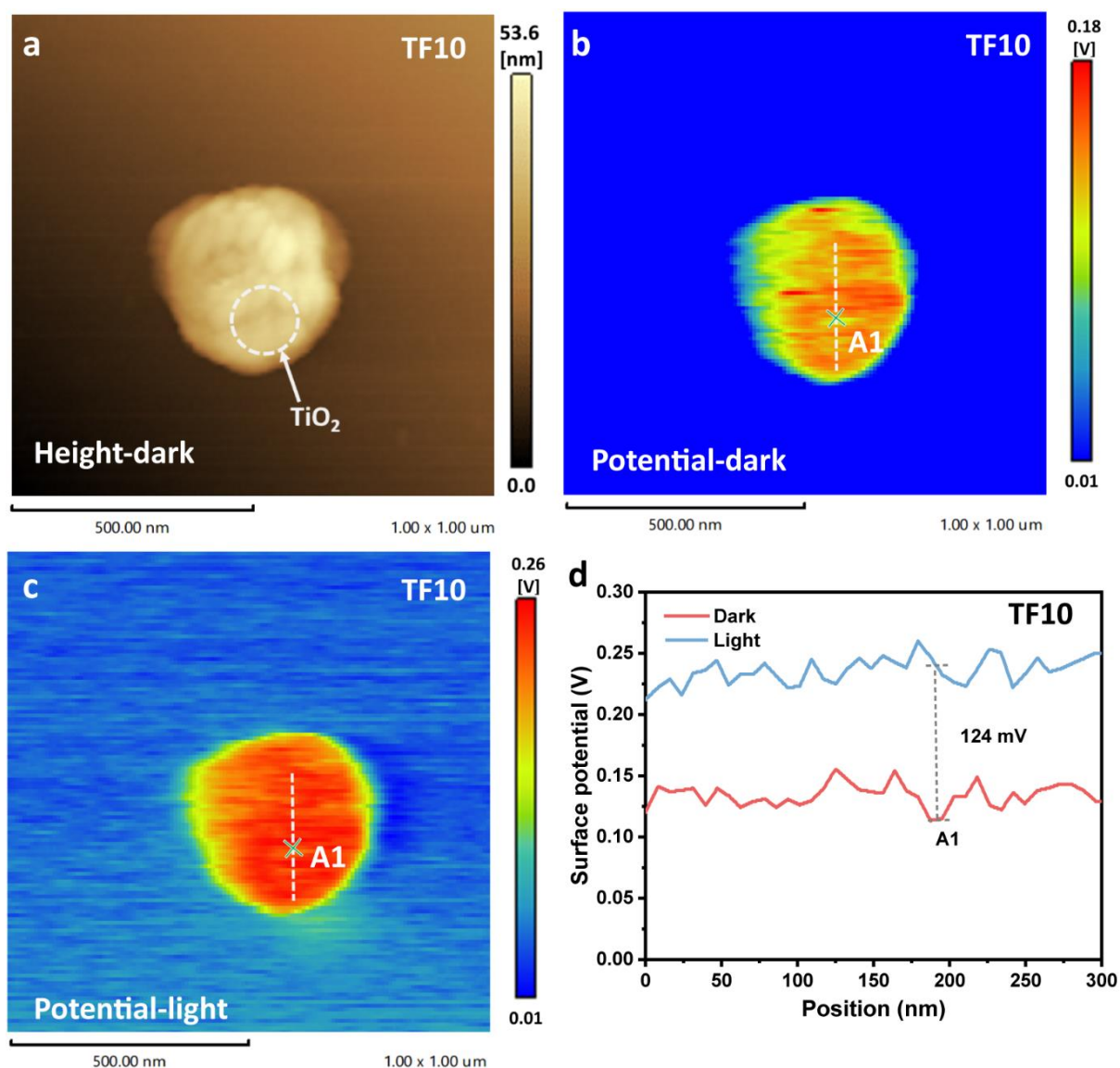
Figure 4. (a) AFM and (b) KPFM images of TF10 in darkness. (c) KPFM image of TF10 with 365-nm UV light illumination. (d) The corresponding surface potential profiles of TF10 in the dark and with 365-nm UV light illumination.

-ment. The Nyquist plots of TF0 and TF5 are displayed in Figure S5. TF5 exhibits a semicircle smaller than TF0 (TiO$_2$), indicating a reduced charge transfer resistance of TF5 compared with that of TF0 (TiO$_2$). The inset flowchart (Figure S5) illustrates the simulated equivalent circuit. Based on this simulation, the charge transfer resistance (R_{ct}) of TiO$_2$ is 6454 Ω, while the R_{ct} of TF5 is 5378 Ω. These results reveal that the introduction of FPS NSs decreases the charge transfer resistance of TiO$_2$ NPs, also supporting the better charge separation/transfer efficiency in TF5 compared with that of TF0.

The above results indicate the greatly-raised efficiency of charge separation/transfer after the coupling of TiO$_2$ NPs and FPS NSs in TF5. Hence, a variety of characterizations, such as *in-situ* Atomic force microscopy combined with Kelvin probe force microscopy (AFM-KPFM) and *in-situ* X-ray photoelectron spectroscopy (XPS), and theoretical computations were adopted to explore the reason. As presented in **Figure 4a**, the aggregation of TiO$_2$ NPs can be observed in the AFM image of TF10. Figure 4b and c show the corresponding KPFM images of TF10 in darkness and with 365-nm UV light illumination, respectively. Accordingly, the surface potential profiles of TF10 in the darkness and with 365-nm light irradiation are displayed in Figure 4d. It can be observed in Figure 4e that the surface potential at A1 is raised by 124 mV. Actually, the surface potentials across the line are all raised with the 365-nm light illumination compared to that in darkness. These results suggest that the photogenerated holes accumulate on the surface of TiO$_2$ NPs in TF10 with light excitation.

Furthermore, both *ex-situ* and *in-situ* XPS were also conducted. As displayed in **Figure 5a** and b, the high-resolution Ti 2p and O 1s XPS spectra for TF0 (TiO$_2$) and TF10 suggest the left shift of Ti 2p and O 1s peaks toward the low binding energy direction. These results imply the transfer of electrons from FPS NSs to TiO$_2$ NPs after their binding in TF10. Furthermore, with UV light excitation, both Ti 2p and O 1s peaks of TF10 move towards higher binding energy positions, compared with those of TF10 without light excitation. These results suggest that photogenerated holes are accumulated on the surface of TiO$_2$ NPs in TF10 after light excitation,
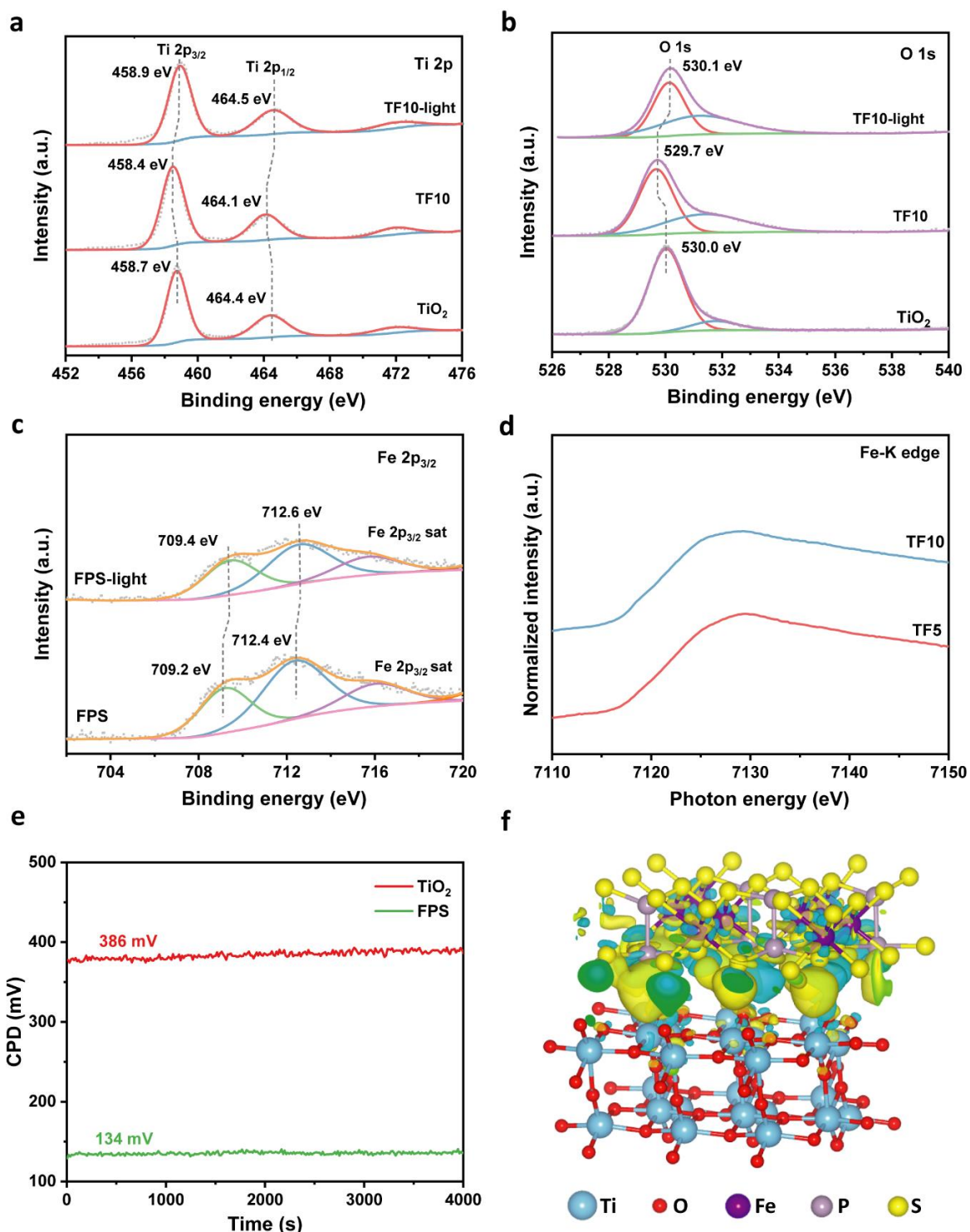
Figure 5. High-resolution XPS spectra of (a) Ti 2p and (b) O 1s for TF0 (TiO$_2$) and TF10 without/with UV light illumination. (c) high-resolution XPS spectrum of Fe 2p$_{3/2}$ for FPS NSs without/with UV light illumination. (d) synchrotron-based XANES spectra of Fe K edge for TF5 and TF10. (e) CPD of TiO$_2$ and FPS in the dark. (f) The differential charge density map (side view) of TiO$_2$ (101) facet/FPS (001) facet with an iso-surface of 2.7*10^{-4} e/Å^3. The charge accumulation is shown as the yellow region, and the charge depletion is shown as the cyan region.

agreeing with the TRSPS results (Figure 3c) and AFM-KPFM results (Figure 4d). Furthermore, the peaks of FPS NSs in the high-resolution XPS spectra of Fe $2p_{3/2}$ shift positively to higher binding energy positions under UV light excitation (Figure 5c), suggesting the accumulation of photogenerated holes on the surface of FPS NSs with light illumination. Since the XPS technique cannot detect any Fe, P and S signal in TF5 or TF10 due to the low content of FPS in them, the synchrotron-based XANES test was performed to explore the Fe K edge for TF5 and TF10. As shown in Figure 5d, the Fe K edge can be observed for both TF5 and TF10, confirming the existence of the Fe element in these two samples. Furthermore, the contact potential difference (CPD) for FPS NSs and TiO_2 (TF0) in darkness are shown in Figure 5e. And the work functions (Φ) of FPS NSs and TF0 are calculated to be 4.38 and 4.64 eV (Table S2), respectively. This also supports the electron transport from FPS NSs to TF0 (TiO_2) after the contact in TF5 and TF10, in agreement with the XPS spectra in Figure 5a and b. Furthermore, the differential charge density map of FPS and TiO_2 also bolsters the electron accumulation on TiO_2 at the interface of FPS/TiO_2 (Figure 5f). Thus, all the above experimental and theoretical results support the extraction of electrons from FPS to TiO_2 after their contact in TiO_2/FPS system. This confirms the intimate electronic coupling between TiO_2 and FPS in TiO_2/FPS system.

2.4. Light absorption and surface redox reactions

In addition to the charge separation and migration, light absorption and redox reactions on the surface of the TiO_2/FPS system are also studied. All these samples were explored by ultraviolet-visible diffuse reflectance spectroscopy (UV-Vis DRS). The DRS spectra of all the samples (**Figure 6a**) exhibit an absorption edge around 387 nm, attributed to the absorption edge of TiO_2 with a bandgap energy of ~3.20 eV. Compared to the DRS spectra, all the TiO_2/FPS samples (TF1, TF2, TF5 and TF10) show the apparently increased absorption ranging from ~400-1000 nm, ascribed to the absorption by FPS NSs. This confirms the intimate electronic interaction between FPS and TiO_2, promoting the separation/transfer of photoinduced electrons
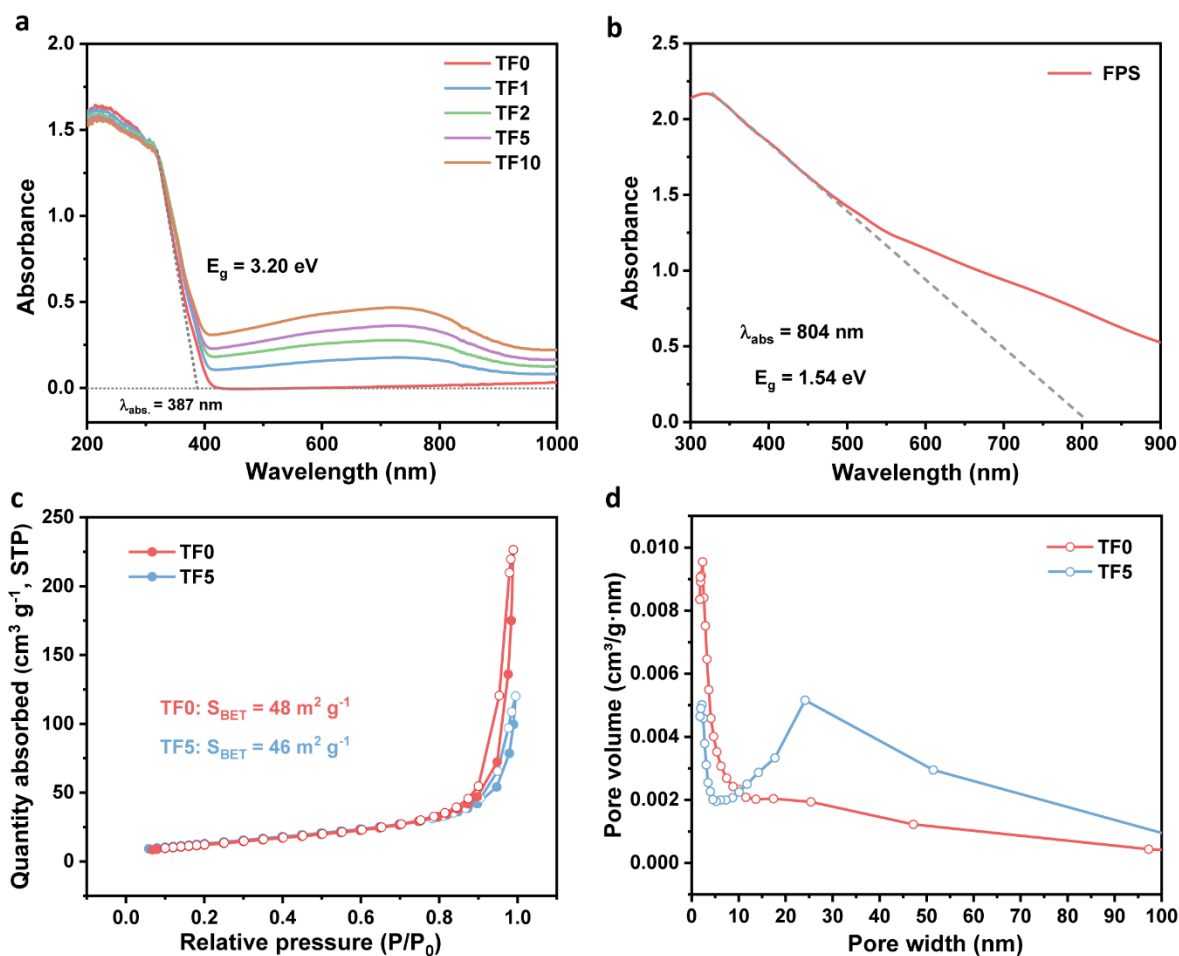
Figure 6. (a) UV-Vis DRS spectra of TF0, TF1, TF2, TF5 and TF10. (b) UV-Vis absorption spectrum of FPS NSs in ethanol solution. (c) N_2 sorption isotherms of TF0 and TF5 and (d) the corresponding pore size distribution plots of TF0 and TF5.

and holes. This is confirmed by the long absorption edge of FPS NSs (804 nm; Figure 6b) possessing a narrow bandgap (1.54 eV).

The surface redox reactions on the TiO_2/FPS system are closely related to the surface area and reactive sites. The nitrogen (N_2) adsorption-desorption isotherms for TF0 (TiO_2) and TF10 are shown in Figure 6c. The apparent shift up of sorption isotherm for TF10 is observed in the range of ~0.8-1.0 of the relative pressure, suggesting that the introduction of FPS NSs would increase the macropores due to the aggregation of large-sized FPS NSs. However, the Brunauer-Emmett-Teller surface area (S_{BET}) for TF5 is slightly reduced to 46 m^2 g^{-1}, slightly lower than the S_{BET} of TF0 (48 m^2 g^{-1}, Table S3). The corresponding pore width distribution plots and parameters are displayed in Figure 6d and Table S3, respectivley. To investigate the intrinsic

H₂ evolution reaction (HER) activities of TF0 and TF10, linear sweep voltammetry (LSV) test was further conducted. As displayed in Figure S6, the HER overpotential of TF5 is apparently reduced compared to that of TF0 at the same current density of -0.5 mA cm^{-2}. This result indicates that the introduction of FPS NSs with active sites in TF5 could raise the HER activity.

2.5. Reaction mechanism based on S-scheme heterojunction

The above experimental and theoretical calculation results confirm the construction of heterojunction between TiO₂ and FPS in the TiO₂/FPS system. To reveal the details of this heterojunction, further characterizations were carried out. First, the band structures of TiO₂ and FPS are calculated. As shown in Table S2, the work functions (Φ) of TiO₂ and FPS are 4.64 and 4.38 eV, respectively. Thus, the Fermi level (E_F) values of TiO₂ and FPS are 4.64 and 4.38 V $vs.$ vacuum level, equal to 0.2 and -0.06 V $vs.$ standard hydrogen electrode (SHE). Based on the valence band (VB) spectra of FPS and TiO₂ (**Figure 7a**), the VB edge potentials of FPS and TiO₂ are 0.56 and 2.58 V $vs.$ SHE. Since the bandgap energies of FPS and TiO₂ are 1.54 and 3.20 eV, the potentials for conduction band (CB) edge of FPS and TiO₂ are -0.98 and -0.62 V $vs.$ SHE. Second, the Mott-Schottky (MS) plots of TF5 at different frequencies are shown in Figure 7b. The curves with both positive and negative slopes are observed in Figure 7b, suggesting the construction of an n-p heterojunction in TiO₂/FPS system. Hence, a S-scheme heterojunction mechanism based on the n-p semiconductor system is raised in this work. Before contact, the initial state of band structures diagram of n-type TiO₂ and p-type FPS is shown in Figure 7c (i). Since the Fermi level potential (E_F) of FPS (-0.06 V $vs.$ SHE) is higher than that of TiO₂ (0.2 V $vs.$ SHE), the contact between TiO₂ and FPS leads to electron migration from FPS to TiO₂, thus forming the built-in electric field causing the upward curving of the CB and VB of FPS and the downward curving of the CB and VB of TiO₂ near the interface of FPS and TiO₂ as displayed in Figure 7c (ii). Upon light illumination, the electrons and holes are generated in both TiO₂ and FPS. Then, the photogenerated electrons of FPS are reserved in the CB of FPS and the photoinduced holes are retained in the VB of TiO₂, owing to the strong built-
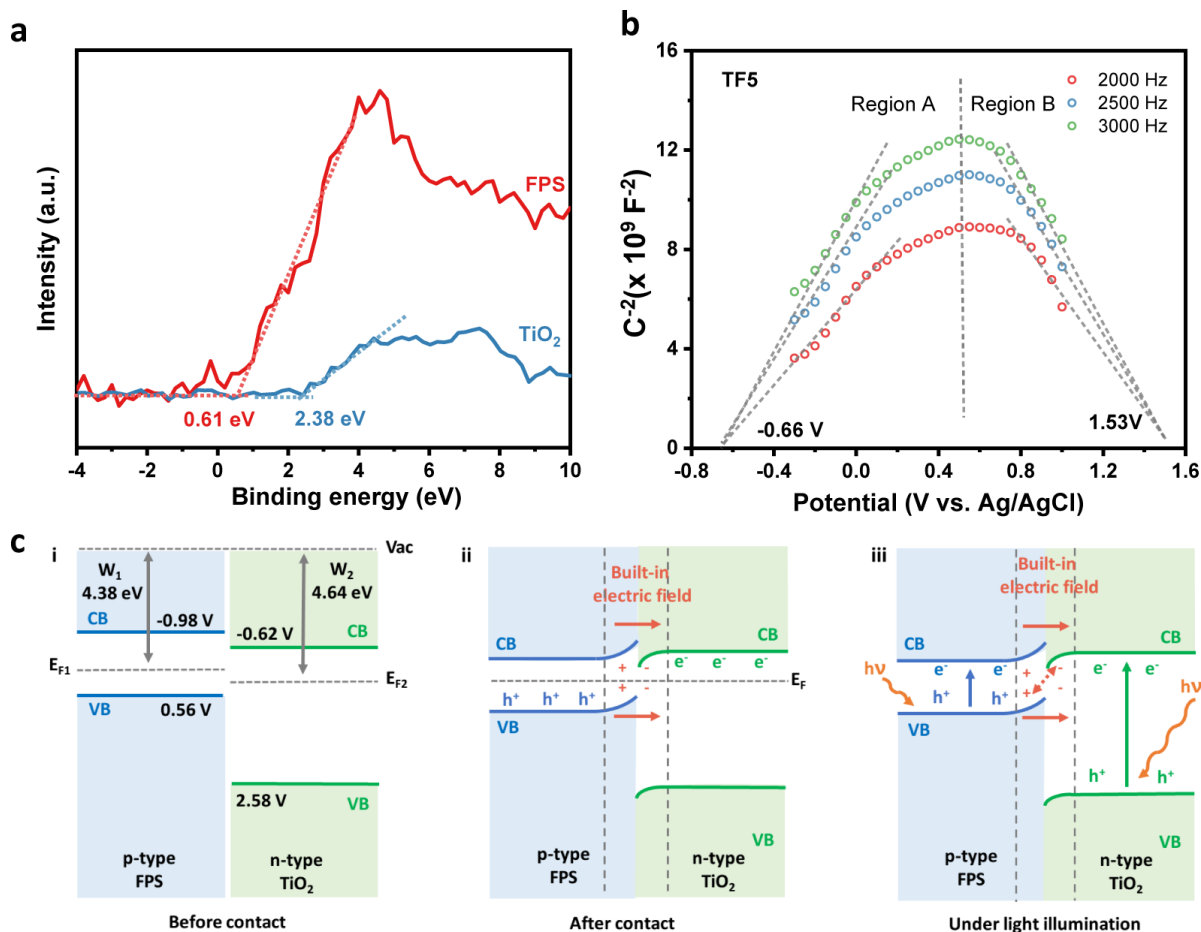
Figure 7. (a) XPS VB spectra of TiO_2 and FPS. (b) Mott-Schottky plots for TF5 acquired in 0.5 M Na_2SO_4 aqueous solution at different frequencies of 2000, 2500 and 3000 Hz. (c) Reaction mechanism for photocatalytic H_2 evolution on S-scheme TiO_2/FPS heterojunction: (i) before contact (ii) after contact and (iii) under light illumination.

in electric field near the interface of FPS and TiO_2. Meanwhile, photogenerated electrons at the CB of TiO_2 are driven by the built-in electric field to recombine with the photogenerated holes in the VB of FPS. Hence, stronger reduction ability derived from the photogenerated electrons in FPS and stronger oxidation ability derived from the photogenerated holes are retained. And the high charge separation/transfer efficiency in TiO_2/FPS system is achieved simultaneously. Besides, the photoexcited electrons at the CB of FPS could efficiently reduce the water molecules to generate H_2 gas due to the FPS surface active sites. And ethanol at TiO_2 can be easily oxidized by the strongly oxidative photogenerated holes in the VB to generate oxidized products.

3. Conclusions

In summary, the S-scheme $TiO_2/FePS_3$ heterojunction was successfully fabricated by the self-assembly of TiO_2 nanoparticles (NPs) and $FePS_3$ (FPS) nanosheets (NSs). The formation of TiO_2/FPS S-scheme heterojunction leads to establishing a strong internal electric field, which not only retains the stronger redox capabilities of the photo-excited electrons and holes, but also achieves higher electron-hole separation efficiency via recombining the photogenerated electrons and holes with weaker redox abilities. Besides, the FPS NSs accommodate the reactive sites for hydrogen (H_2) generation reaction. Thus, the apparently raised photocatalytic H_2 evolution activity was achieved on $TiO_2/FePS_3$ S-scheme heterojunction. These are supported by both theoretical calculations and cutting-edge characterizing techniques, *e.g.,* synchrotron-based X-ray absorption near edge structure (XANES), transient-state surface photovoltage spectroscopy/photoluminescence spectroscopy, *in-situ* atomic force microscopy combined with Kelvin probe force microscopy (AFM-KPFM) and *in-situ* X-ray photoelectron spectroscopy (XPS). This work not only demonstrates the great capacity of increasing photocatalytic activity by the construction of S-scheme heterojunction with a strong internal electric field, but also highlights the new way for the development of efficient, affordable, and durable high-activity photocatalysts with new two-dimensional materials.

4. Experimental

All chemicals were used without purification if not specified.

Preparation of FPS nanosheets (NSs): The bulk $FePS_3$ was bought from a commercial supplier. First, 100 mg bulk $FePS_3$ was grounded into black powder for 0.5 hour and added into 100 mL ethanol. The mixed solution was then sonicated by a 600 W ultrasonic cell crusher (Ningbo Xinzhi Biotechnology Ltd. Co.) for 10 hours. After centrifugation at 3000 rpm for 5 mins , the upper solution was collected and centrifugated at 10,000 rpm for another 5 mins. Finally, the obtained black precipitates were well dispersed in 100 mL ethanol and used as FPS NSs.

Preparation of TiO₂/FPS: The TiO₂/FPS samples were prepared by grinding at room temperature. Typically, 50 mg TiO₂ (P25, Degussa AG) was added into a certain amount ($x =$ 1, 2, 5, and 10 mL) of FPS NSs suspension. The mixture was then grounded for 0.5 hour followed by 3-hour natural drying, and the final products were collected and annotated as TFx.

Evaluation of photocatalytic H₂ evolution activity: Briefly, 20 mg photocatalyst TFx was added into a 100 mL sealed reactor contaning 80 mL 10 vol% ethanol aqueous soution. The mixed solution was bubbled with nitrogen (N_2) for 0.5 hour. A 350 W Xenon arc lamp ($\lambda \geq 350$ nm) was employed for light irradiation while the reactor was 10 cm away from the lamp. 0.4 mL evolved gas under light irradation was extracted intermittently with a syringe and injected into the detector of the Shimadzu gas chromatograph (GC-14C). The amount of generated H_2 was calculated by analyzing the peak area of evolved H_2 and standard H_2.

Details about physicochemical characterization, electrochemical measurements and theoretical calculations are available in Supporting Information.

Data availability

The data supporting the findings of this study are available in the paper and Supporting Information.

Conflict of interest

The authors declare no conflict of interest.

Supporting Information

Supporting Information is available from the Wiley Online Library or from the authors.

Received: ((will be filled in by the editorial staff))

Revised: ((will be filled in by the editorial staff))

Published online: ((will be filled in by the editorial staff))

References

[1]   R. R. Hernandez, A. Armstrong, J. Burney, G. Ryan, K. Moore-O'Leary, I. Diédhiou, S. M. Grodsky, L. Saul-Gershenz, R. Davis, J. Macknick, D. Mulvaney, G. A. Heath, S. B. Easter, M. K. Hoffacker, M. F. Allen, D. M. Kammen, *Nat. Sustain.* **2019**, *2*, 560.

[2]   S. D. Tilley, *Adv. Energy Mater.* **2019**, *9*, 1802877.

[3]   J. Gong, C. Li, M. R. Wasielewski, *Chem. Soc. Rev.* **2019**, *48*, 1862.

[4]   O. A. Al-Shahri, F. B. Ismail, M. A. Hannan, M. S. H. Lipu, A. Q. Al-Shetwi, R. A. Begum, N. F. O. Al-Muhsen, E. Soujeri, *J. Clean. Prod.* **2021**, *284*, 125465.

[5]   D. K. Dogutan, D. G. Nocera, *Acc. Chem. Res.* **2019**, *52*, 3143.

[6]   S. Ye, C. Ding, M. Liu, A. Wang, Q. Huang, C. Li, *Adv. Mater.* **2019**, *31*, 1902069.

[7]   T. Keijer, T. Bouwens, J. Hessels, Joost N. H. Reek, *Chem. Sci.* **2021**, *12*, 50.

[8]   S. Chen, Y. Qi, C. Li, K. Domen, F. Zhang, *Joule* **2018**, *2*, 2260.

[9]   W. Zhong, D. Gao, H. Yu, J. Fan, J. Yu, *Chem. Eng. J.* **2021**, *419*, 129652.

[10]   S. Tang, Y. Xia, J. Fan, B. Cheng, J. Yu, W. Ho, *Chin. J. Catal.* **2021**, *42*, 743.

[11]   Q. Wang, K. Domen, *Chem. Rev.* **2020**, *120*, 919.

[12]   K. Takanabe, *ACS Catal.* **2017**, *7*, 8006.

[13]   B. Xia, Y. Zhang, B. Shi, J. Ran, K. Davey, S. Z. Qiao, *Small Methods* **2020**, *4*, 2000063.

[14]   J. Xiong, J. Di, J. Xia, W. Zhu, H. Li, *Adv. Funct. Mater.* **2018**, *28*, 1801983.

[15]   G. Guan, E. Ye, M. You, Z. Li, *Small* **2020**, *16*, 1907087.

[16]   Z. Xie, Y.-P. Peng, L. Yu, C. Xing, M. Qiu, J. Hu, H. Zhang, *Solar RRL* **2020**, *4*, 1900400.

[17]   Y. Zhou, Z. Wang, L. Huang, S. Zaman, K. Lei, T. Yue, Z. a. Li, B. You, B. Y. Xia, *Adv. Energy Mater.* **2021**, *11*, 2003159.

[18]   D. Qin, Y. Zhou, W. Wang, C. Zhang, G. Zeng, D. Huang, L. Wang, H. Wang, Y. Yang, L. Lei, S. Chen, D. He, *J. Mater. Chem. A* **2020**, *8*, 19156.

[19] R. Hu, G. Liao, Z. Huang, H. Qiao, H. Liu, Y. Shu, B. Wang, X. Qi, *J. Hazard. Mater.* **2021**, *405*, 124179.

[20] Y. Xia, B. Cheng, J. Fan, J. Yu, G. Liu, *Sci. China Mater.* **2020**, *63*, 552.

[21] S. Ghosh, F. Kargar, A. Mohammadzadeh, S. Rumyantsev, A. A. Balandin, *Adv. Electron. Mater.* **2021**, *7*, 2100408.

[22] C. R. S. Haines, M. J. Coak, A. R. Wildes, G. I. Lampronti, C. Liu, P. Nahai-Williamson, H. Hamidov, D. Daisenberger, S. S. Saxena, *Phys. Rev. Lett.* **2018**, *121*, 266801.

[23] J. Xu, W. Li, Y. Hou, *Trends Chem.* **2020**, *2*, 163.

[24] W. Zhu, W. Gan, Z. Muhammad, C. Wang, C. Wu, H. Liu, D. Liu, K. Zhang, Q. He, H. Jiang, X. Zheng, Z. Sun, S. Chen, L. Song, *Chem. Commun.* **2018**, *54*, 4481.

[25] Z. Yu, J. Peng, Y. Liu, W. Liu, H. Liu, Y. Guo, *J. Mater. Chem. A* **2019**, *7*, 13928.

[26] H. Wang, Z. Li, Y. Li, B. Yang, J. Chen, L. Lei, S. Wang, Y. Hou, *Nano Energy* **2021**, *81*, 105613.

[27] Z. Cheng, T. A. Shifa, F. Wang, Y. Gao, P. He, K. Zhang, C. Jiang, Q. Liu, J. He, *Adv. Mater.* **2018**, *30*, 1707433.

[28] J. Zhang, F. Feng, Y. Pu, X. a. Li, C. H. Lau, W. Huang, *ChemSusChem* **2019**, *12*, 2651.

[29] P. Sen, R. K. Chouhan, *Electron. Struct.* **2020**, *2*, 025003.

[30] R. Chen, F. Fan, T. Dittrich, C. Li, *Chem. Soc. Rev.* **2018**, *47*, 8238.

[31] M. J. Shearer, M.-Y. Li, L.-J. Li, S. Jin, R. J. Hamers, *J. Phys. Chem. C* **2018**, *122*, 13564.

[32] B. He, C. Bie, X. Fei, B. Cheng, J. Yu, W. Ho, A. A. Al-Ghamdi, S. Wageh, *Appl. Catal. B* **2021**, *288*, 119994.

[33] J. Bian, Z. Zhang, J. Feng, M. Thangamuthu, F. Yang, L. Sun, Z. Li, Y. Qu, D. Tang, Z. Lin, F. Bai, J. Tang, L. Jing, *Angew. Chem. Int. Ed.* **2021**, *60*, 20906.

[34] L. Zhang, J. Zhang, H. Yu, J. Yu, *Adv. Mater.* **2022**, *34*, 2107668.

[35] C. Cheng, B. He, J. Fan, B. Cheng, S. Cao, J. Yu, *Adv. Mater.* **2021**, *33*, 2100317.

[36] Q. Xu, S. Wageh, A. A. Al-Ghamdi, X. Li, *J. Mater. Sci. Technol.* **2022**, *124*, 171.

[37] F. Y. Xu, K. Meng, S. Cao, C. H. Jiang, T. Chen, J. S. Xu, J. G. Yu, *ACS Catal.* **2022**, *12*, 164.

[38] M. Sayed, B. Zhu, P. Kuang, X. Liu, B. Cheng, A. A. A. Ghamdi, S. Wageh, L. Zhang, J. Yu, *Adv. Sustain. Syst.* **2021**, *6*, 2100264.

[39] S. Wageh, A. A. Al-Ghamdi, O. A. Al-Hartomy, M. F. Alotaibi, L. Wang, *Chin. J. Catal.* **2022**, *43*, 586.

[40]   X. Li, B. Kang, F. Dong, Z. Zhang, X. Luo, L. Han, J. Huang, Z. Feng, Z. Chen, J. Xu, B. Peng, Z. L. Wang, *Nano Energy* **2021**, *81*, 105671.

[41]   J. Fu, Q. Xu, J. Low, C. Jiang, J. Yu, *Appl. Catal. B* **2019**, *243*, 556.

[42]   L. Wang, B. Cheng, L. Zhang, J. Yu, *Small* **2021**, *17*, 2103447.

[43]   P. Xia, S. Cao, B. Zhu, M. Liu, M. Shi, J. Yu, Y. Zhang, *Angew. Chem. Int. Ed.* **2020**, *59*, 5218.

[44]   J. Li, Y. Long, Z. Hu, J. Niu, T. Xu, M. Yu, B. Li, X. Li, J. Zhou, Y. Liu, C. Wang, L. Shen, W. Guo, J. Yin, *Nat. Commun.* **2021**, *12*, 4998.

[45]   V. Donchev, *Mater. Res. Express* **2019**, *6*, 103001.

[46]   M. A. Melo, Z. Wu, B. A. Nail, A. T. De Denko, A. F. Nogueira, F. E. Osterloh, *Nano Lett.* **2018**, *18*, 805.

[47]   Z.-K. Xin, Y.-J. Gao, Y. Gao, H.-W. Song, J. Zhao, F. Fan, A.-D. Xia, X.-B. Li, C.-H. Tung, L.-Z. Wu, *Adv. Mater.* **2022**, *34*, 2106662.

Supporting Information

FePS$_3$/TiO$_2$ S-scheme heterojunction for greatly raised photocatalytic hydrogen evolution

Bingquan Xia, Bowen He, Jianjun Zhang, Laiquan Li, Yanzhao Zhang, Jiaguo Yu, Jingrun Ran*, and Shi-Zhang Qiao *

B. Xia, L. Li, Y. Zhang, J. Ran, S.-Z. Qiao
School of Chemical Engineering and Advanced Materials, The University of Adelaide, Adelaide, SA 5005, Australia
E-mail: s.qiao@adelaide.edu.au, jingrun.ran@adelaide.edu.au

B. He, J. Zhang, J. Yu
Laboratory of Solar Fuel, Faculty of Materials Science and Chemistry, China University of Geosciences, 388 Lumo Road, Wuhan, 430074, P. R. China

S1. Experimental and theroretical calculation details

S1.1 Physicochemical characterization:

X-ray diffraction (XRD) patterns were recorded by an X-ray diffractometer (RU-200B/D/MAXRB, Rigaku, Japan). The microstructure investigation is taken on (Scanning) Transmission electron microscope (S/TEM) images and corresponding Energy dispersive X-ray (EDX) elemental mapping were collected on a scanning transmission electron microscope (Thermo Scientific Talos F200S G2, USA) equipped with EDX detector PV97-61850. The Brunauer-Emmett-Teller specific surface area (S_{BET}) was calculated based on N_2 adsorption-desorption measurement conducted on TriStar II 3020 (Micromeritics, USA). Raman spectra were collected on a Raman microscope (InVia, Renishaw, England) with a 633 nm Ar laser as an excitation source. The ultraviolet-visible diffuse reflectance spectra (UV-vis DRS) were acquired on a UV-vis spectrophotometer (UV-2600, Shimadzu, Japan). The X-ray photoelectron spectroscopy (XPS) and *in situ* irradiated X-ray photoelectron spectroscopy (ISI-XPS) were conducted on an electron spectrometer (ESCALAB 210, VG, UK). The XPS valence band spectra were collected with a light source with 21.2 eV He ultraviolet light. The steady-state surface photovoltage (SPV) spectra were acquired with a homemade apparatus, consisting of a monochromatic light source, a lock-in amplifier (SR830-DSP) with a light chopper (SR540), a sample cell, and a computer. The transient-state surface photovoltage response was collected using the reported method.[S1] Photoluminescence (PL) spectroscopy measurements were carried out by a fluorescence spectrophotometer (F-7000, Hitachi, Japan). The time-resolved photoluminescence (TRPL) spectra were acquired using FLS1000 fluorescence lifetime spectrophotometer (Edinburgh, Instruments, UK). The inductively coupled plasma–optical emission spectrometry (ICP-OES) (Prodigy 7, Leeman Labs Inc., USA) was used to quantify element content. Contact potential difference (CPD) was measured on a Kelvin probe apparatus (Instytut Fotonowy, Poland). Atomic force microscopy (AFM) and Kelvin probe force microscopy (KPFM) measurements were both finished at SPM-9700 surface probe system (Shimadzu, Japan). Before the test, the probe is calibrated with the iron plate, which was base when testing. The light source for *in-situ* KPFM is a 365-nm LED light. The XANES spectra were acquired at the Australian Synchrotron.

S1.2 Electrochemical measurements

EIS measurements were performed on an electrochemical analyzer (CHI650D instruments) in a standard three-electrode system utilizing the synthesized samples as the working electrodes, Ag/AgCl (saturated KCl) as a reference electrode, and Pt wire as the counter electrode. The

synthesized samples were coated on the In-doped tin oxide (ITO) glass and used as the working electrode. Briefly, 20 mg of sample was dispersed in 0.5 mL of ethanol which contained 10 μL of 5% Nafion solution (D-520, DuPont, USA) to make a slurry. Then the slurry was coated onto the conductive surface of FTO glass. Finally, the obtained working electrode was dried at room temperature overnight. 50 mL of electrolyte containing 0.5 M Na_2SO_4 was selected as the carrier for ion transport.

S1.3 Theoretical calculations

DFT calculations were conducted through the Vienna ab initio Simulation Package (VASP) with the projector augment wave method. Generalized gradient approximation of the PBE functional was used as the exchange-correlation functional. The cutoff energy was set as 500 eV, and structure relaxation was performed until the convergence criteria of energy and force reached 1×10^{-5} eV and 0.02 eV $Å^{-1}$, respectively. Kmesh-resolved value was set to 0.04 2*PI/Angstrom. A vacuum layer of 15 Å was constructed to eliminate interactions between periodic structures of surface models. The van der Waals (vdW) interaction was amended by the DFT-D3 method of Grimme.

S2. Supplementary figures
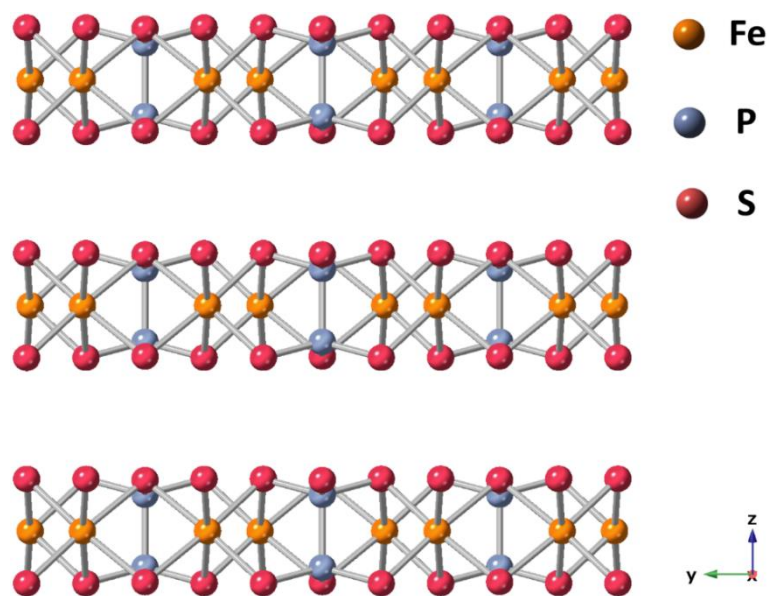
Figure S1. Side-view atomic structure of FPS viewed along [100] direction.
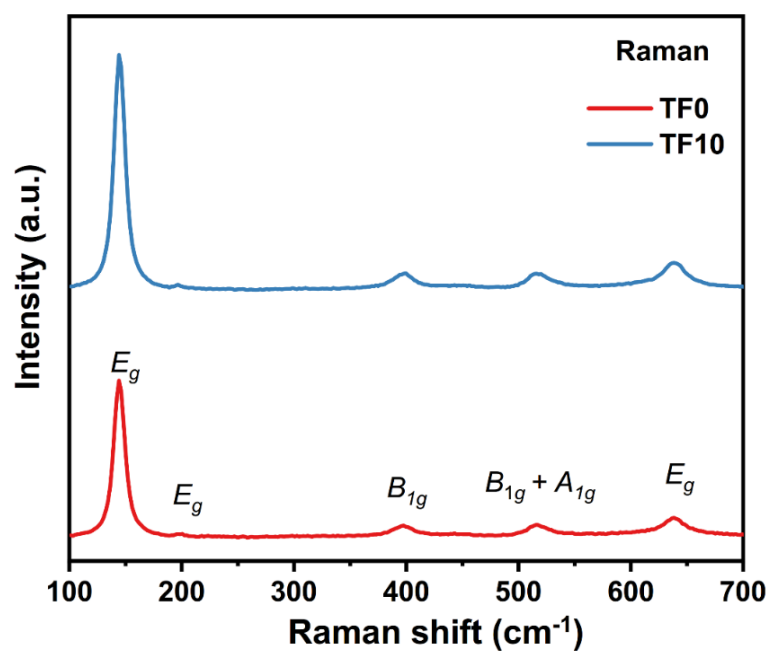
Figure S2. Raman spectra of TF0 and TF10.
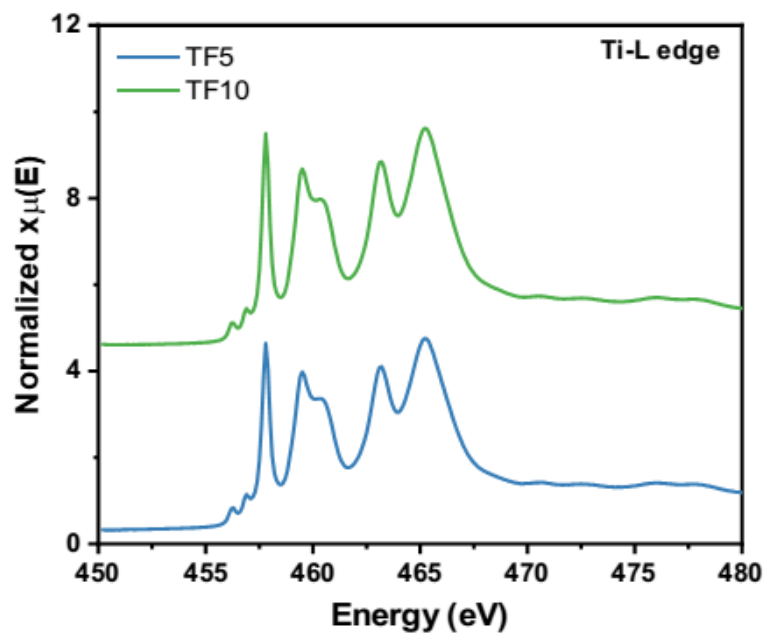
Figure S3. Synchrotron-based XANES spectra of Ti L edge for TF5 and TF10.
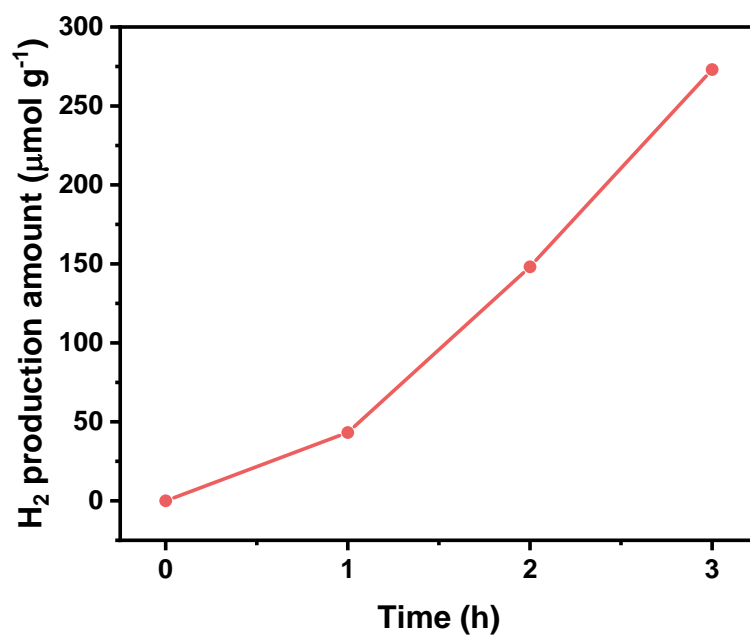
Figure S4. Photocatalytic H_2 evolution test of TF5 in 3 hours.
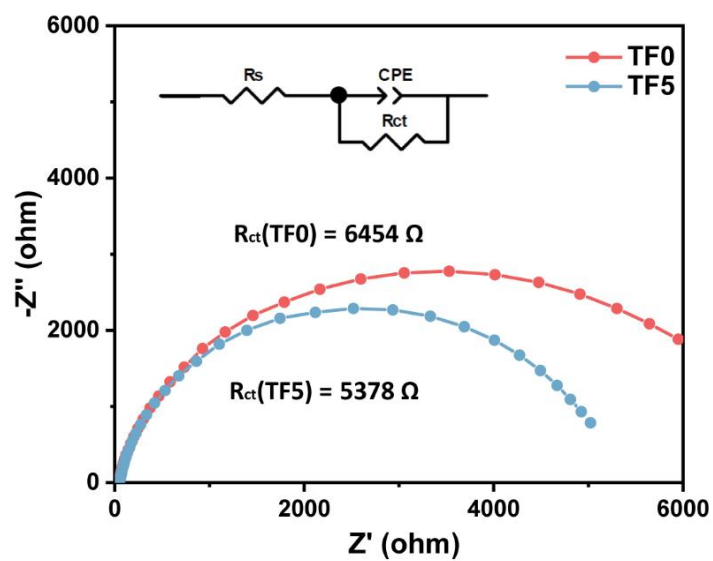
Figure S5. EIS spectra for TF0 and TF5 in 0.5 M Na$_2$SO$_4$ aqueous solution.
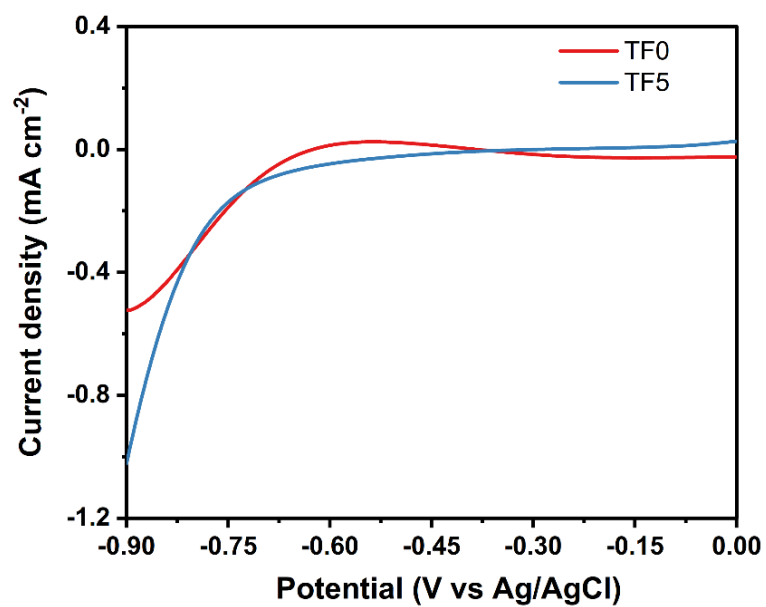
Figure S6. LSV curves for TF0 and TF5 in 0.5 M Na$_2$SO$_4$.

S3. Supplementary tables

Table S1. Charge carrier lifetimes derived from TRPL decay plots

Photocatalyst	Parameter	Value/ns	Rel.%
TF0	τ_1	0.27	30.2
	τ_2	2.06	46.5
	τ_3	9.29	23.3
	τ_{ave}	3.20	
TF5	τ_1	0.75	38.1
	τ_2	3.04	42.84
	τ_3	11.11	19.07
	τ_{ave}	3.71	

Table S2. Contact Potential changes and work function (W) and Fermi level potentials obtained from Kelvin probe.·

Sample	CPD_{dark} /mV	W /eV	E_F /V
TiO_2	386	4.64	4.64
FPS	134	4.38	4.38

The work function is calculated following the equation below:[S2]

$W_{sample} = CPD_{sample} * 0.001 * e + W_{probe}$ (W_{probe} = 4.25 eV)

Table S3. physicochemical features of TF0 and TF5 acquired from the N_2 sorption analysis

photocatalyst	Average pore size (nm)	pore volume (cm³/g)	surface area (m²/g)
TF0	15.21	0.18	49
TF5	30.26	0.35	46

References

[S1]   J. Bian, Z. Zhang, J. Feng, M. Thangamuthu, F. Yang, L. Sun, Z. Li, Y. Qu, D. Tang, Z. Lin, F. Bai, J. Tang, L. Jing, *Angew. Chem. Int. Ed.* **2021**, *60*, 20906.

[S2]   B. He, C. Bie, X. Fei, B. Cheng, J. Yu, W. Ho, A. A. Al-Ghamdi, S. Wageh, *Appl. Catal. B* **2021**, *288*, 119994.

Chapter 6: Single-atom photocatalysts for emerging reactions

6.1 Introduction and significance

Single-atom photocatalysts have demonstrated enormous potential in producing value-added chemicals and/or fuels using sustainable and clean solar light to replace fossil fuels causing global energy and environmental issues. These photocatalysts not only exhibit outstanding activities, selectivity, and stabilities due to their distinct electronic structures and unsaturated coordination centers but also tremendously reduce the consumption of catalytic metals owing to the atomic dispersion of catalytic species. Besides, the single-atom active sites facilitate the elucidation of reaction mechanisms and understanding of the structure-performance relationships.

Apart from the well-known reactions (H_2 production, N_2 fixation, and CO_2 conversion), various novel reactions that are successfully catalyzed by single-atom photocatalysts possessing high efficiency, selectivity, and stability, have been reviewed and discussed in this chapter. The highlights of this chapter include:

(1) summarizing the strategy for designing and fabricating single-atom photocatalysts for three different kinds of emerging reactions (i.e., reduction reactions, oxidation reactions, as well as redox reactions) to generate desirable chemicals and/or fuels.

(2) revealing relationships between the composition/structure of single-atom photocatalysts and their activity/selectivity/stability.

(3) probing into the reaction mechanisms of single-atom photocatalysts

(4) forecasting possible opportunities for the design and fabrication of brand-new high-performance single-atom photocatalysts.

6.2 Single-atom photocatalysts for emerging reactions

This chapter is included as it appears as a journal paper published by **Bingquan Xia**; Yanzhao Zhang; Jingrun Ran; Mietek Jaroniec; Shi-Zhang Qiao. Single-atom photocatalysts for emerging reactions. *ACS Central Science* 2021, 7, 39-54.

Statement of Authorship

Title of Paper	Single-Atom Photocatalysts for Emerging Reactions
Publication Status	☑ Published ☐ Accepted for Publication ☐ Submitted for Publication ☐ Unpublished and Unsubmitted work written in manuscript style
Publication Details	Bingquan Xia, Yanzhao Zhang, Jingrun Ran, Mietek Jaroniec, Shi-Zhang Qiao, Single-atom photocatalysts for emerging reactions, ACS Central Science 2021, 7, 1, 39–54. https://doi.org/10.1021/acscentsci.0c01466

Principal Author

Name of Principal Author (Candidate)	Bingquan Xia
Contribution to the Paper	Proposed the review topic, reviewed and organised the literatures, and wrote the manuscript.
Overall percentage (%)	85
Certification:	This paper reports on original research I conducted during the period of my Higher Degree by Research candidature and is not subject to any obligations or contractual agreements with a third party that would constrain its inclusion in this thesis. I am the primary author of this paper.
Signature	Date 15/01/2022

Co-Author Contributions

By signing the Statement of Authorship, each author certifies that:

    i.   the candidate's stated contribution to the publication is accurate (as detailed above);

    ii.   permission is granted for the candidate in include the publication in the thesis; and

    iii.   the sum of all co-author contributions is equal to 100% less the candidate's stated contribution.

Name of Co-Author	Yanzhao Zhang
Contribution to the Paper	Helped to revise the manuscript
Signature	Date 15/01/2022

Name of Co-Author	Jingrun Ran
Contribution to the Paper	Helped to revise the manuscript and organise the figures, and acted as the corrresponding author
Signature	Date 15/01/2022

Name of Co-Author	Mietek Jaroniec		
Contribution to the Paper	Helped to edit the manuscript		
Signature		Date	1-15-2022

Name of Co-Author	Shizhang Qiao		
Contribution to the Paper	Supervised development of work, helped in manuscript evaluation and acted as corresponding author		
Signature		Date	15/01/2022

Single-Atom Photocatalysts for Emerging Reactions

Bingquan Xia, Yanzhao Zhang, Jingrun Ran,* Mietek Jaroniec, and Shi-Zhang Qiao*

Read Online

ACCESS | Metrics & More | Article Recommendations

ABSTRACT: Single-atom photocatalysts have demonstrated an enormous potential in producing value-added chemicals and/or fuels using sustainable and clean solar light to replace fossil fuels causing global energy and environmental issues. These photocatalysts not only exhibit outstanding activities, selectivity, and stabilities due to their distinct electronic structures and unsaturated coordination centers but also tremendously reduce the consumption of catalytic metals owing to the atomic dispersion of catalytic species. Besides, the single-atom active sites facilitate the elucidation of reaction mechanisms and understanding of the structure-performance relationships. Presently, apart from the well-known reactions (H_2 production, N_2 fixation, and CO_2 conversion), various novel reactions are successfully catalyzed by single-atom photocatalysts possessing high efficiency, selectivity, and stability. In this contribution, we summarize and discuss the design and fabrication of single-atom photocatalysts for three different kinds of emerging reactions (i.e., reduction reactions, oxidation reactions, as well as redox reactions) to generate desirable chemicals and/or fuels. The relationships between the composition/structure of single-atom photocatalysts and their activity/selectivity/stability are explained in detail. Additionally, the insightful reaction mechanisms of single-atom photocatalysts are also introduced. Finally, we propose the possible opportunities in this area for the design and fabrication of brand-new high-performance single-atom photocatalysts.
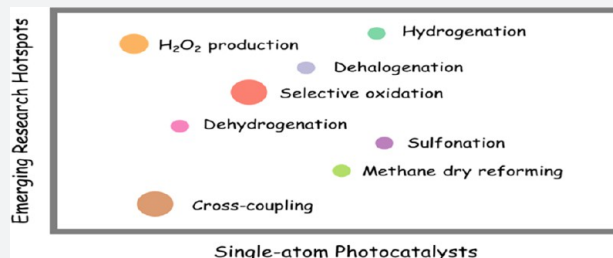
1. INTRODUCTION

To resolve the potential global energy and environmental issues, enormous efforts have been made to explore alternative energy resources for fossil fuels. Solar energy has exhibited great potential as a promising alternative to substituting the traditional energy sources because it is clean, renewable, abundant, affordable, and everlasting.[1,2] Due to the unpredictable nature of weather, it is challenging to make use of solar light under poor weather conditions and/or at night; therefore, it is necessary to transform solar energy into new forms of energy that are storage-stable. Up to date, solar energy has been extensively utilized to produce storable and transportable fuels with high energy capacity as well as value-added chemicals.[3−11] Among various solar energy conversion techniques, photocatalysis is deemed as a promising, environmentally benign, and cost-effective strategy to generate both fuels and high-value chemicals.[12−18] During the past decades, numerous studies have been focused on several well-known reactions (e.g., H_2 production,[19−26] N_2 fixation[27−30] and CO_2 conversion[31−34]) achieved via photocatalysis. Recently, a range of emerging photocatalytic reactions generating fuels and/or valuable chemicals has been attracting increasing attention.[35−37] These emerging reactions can be categorized into three different types, i.e., reduction reactions, oxidation reactions, and redox reactions, based on their specific photocatalytic reaction mechanisms. For instance, several studies demonstrate the production of hydrogen peroxide

(H_2O_2) as a value-added chemical and potential energy carrier, using only water (H_2O) and oxygen (O_2) via photocatalytic reduction reaction.[38−40] Moreover, phenol, as a key organic chemical intermediate and precursor, can be achieved via photocatalytic selective oxidation of benzene.[41] In another study, low-cost biomass-derived acetone is subject to oxidative C−C coupling to form 2,5-hexanedione (HDN) as an important chemical and redox agent to generate H_2 fuel through a photocatalytic redox reaction.[42] Thus, the above three classes of emerging photocatalytic reactions used to produce desirable chemicals and/or fuels are of both great interest and importance.

Recently, single-atom photocatalyst has become one of the most groundbreaking and dynamic research hotspots in heterogeneous photocatalysis.[43,44] Single-atom photocatalysts have attracted tremendous attention primarily owing to the following fascinating benefits in comparison to the nanoclusters, nanoparticles, and bulk counterparts: (i) exceptionally high activity and selectivity originating from their distinct electronic structures and unsaturated coordination centers;[45,46]

Table 1. Single-Atom Photocatalysts for Emerging Reduction Reactions

| Photocatalyst | Light source | Reactants | Reduction reaction | | | | ref |
			Reaction	Main product	Activity	Stability	
Co/C_3N_4	xenon lamp	O_2, H_2O	H_2O_2 production	H_2O_2	62 $\mu M\ h^{-1}$	8 h	38
Co Phthalocyanine/g-C_3N_4	xenon lamp	Benzyl alcohol	O_2 activation	Benzyl aldehyde			85
Ag/AgF	425 nm LED	4-iodoanisole	Dehalogenation reactions	Biphenyl derivative	92% conversion	12 h	88

(ii) tremendous reduction in the usage of catalytic metals achieved by their atomic dispersion;[47,48] (iii) easy to follow reaction mechanisms because of single-atom reactive sites;[49,50] and (iv) an excellent platform to apprehend the structure−performance correlation based on their atomic-level structures.[51−53] The metal−support interactions are crucial for maintaining the stability of single-atom-based photocatalysts, where metal atoms are usually stabilized by neighboring surface atoms or ligands on the support, thus preventing the diffusion and aggregation of the well-dispersed metal single atoms.[43,54−56] A universal strategy for designing and fabricating single-atom-based photocatalysts is to strengthen the effect of the metal−support interaction on single-atom photocatalysts.[57,58] Generally, the enhancement of interactions between isolated metal single-atoms and support is achieved by alteration of supporting materials, including anchoring surface sites (e.g., defects and vacancies), heteroatom doping, coordinating with organic bridging ligands, and anchoring on metal−organic frameworks.[43,59−61] Therefore, the selection and adaption of the support are critical before their utilization in photocatalytic reactions.

Up until now, the majority of reports in the area of single-atom photocatalysts are focused on several well-known reactions, e.g., H_2 production,[62−68] N_2 fixation,[69−74] and CO_2 conversion.[32,34,47,50,59,75] In contrast, there are fewer works on the application of single-atom photocatalysts for emerging reactions to generate the value-added chemicals and/or energy sources, such as H_2O_2,[38] phenol,[76] imines,[77] syngas (CO and H_2),[78] HDN,[42] and β-ketosulfones.[79] In this contribution, for the first time we review and discuss the recent progress in the design and fabrication of single-atom photocatalysts for a variety of emerging reactions, which are categorized into three different types: (i) reduction reactions, (ii) oxidation reactions, and (iii) redox reactions. The structure−performance relationships for some specific reactions on single-atom photocatalysts are discussed and summarized. Also, we elucidate reaction mechanisms for single-atom photocatalysts, as revealed by the state-of-art characterization techniques and/or theoretical calculations. Moreover, new opportunities in this emerging research area, especially those merging theoretical computations and advanced characterizations are proposed.

2. SINGLE-ATOM PHOTOCATALYSTS FOR EMERGING REDUCTION REACTIONS

Recently, single-atom photocatalysts have been reported to catalyze a series of emerging reduction reactions.[42−44] The production of fuels and/or value-added chemicals, such as H_2O_2 and aniline, via single-atom photocatalysis, have been investigated utilizing experimental and/or density functional theory (DFT)-based calculations.[38,80] Also, it has been reported that the effective activation of O_2 for aerobic organic conversion was achieved over single-atom photocatalysts. Moreover, the single-atom photocatalysts are applied for the dehalogenation reaction of organic halides, thus achieving

detoxification and removal of harmful organic halides. A detailed discussion of the above-mentioned developments (summarized in Table 1) in single-atom photocatalysis is presented below.

H_2O_2, a common commodity chemical product, has various industrial and commercial applications, such as an oxidizing agent for chemical production, preventing infections in medical practice, and removing pollutants/contaminants in the environment.[81−83] Due to its relatively high oxidation potential (E_0 = 1.763 V vs NHE at pH = 0),[39] H_2O_2 is utilized as an environmentally friendly and widely available oxidant with only H_2O and O_2 produced after usage. Owing to its high energy density, liquid H_2O_2 shows great potential for storing energy and can be further used in fuel cells. However, the conventional techniques for producing H_2O_2 on an industrial scale suffer from toxic emissions and/or large energy consumption. Thus, the low-cost generation of H_2O_2 by using an environmentally friendly photocatalytic process under ambient conditions is highly desirable. Recently, two-dimensional (2D) carbon nitride (C_3N_4) loaded with single-atom cobalt (Co) and anthraquinone (AQ) was synthesized for solar-light-driven H_2O_2 generation.[38] Specifically, bulk C_3N_4 was first exfoliated into C_3N_4 nanosheets by ultrasonication. Then, single-atom Co was anchored onto the C_3N_4 surface through Co ion coordination and pyrolysis in the N_2 atmosphere followed by phosphorylation. Finally, AQ was linked to the edge of the as-prepared single-atom Co-anchored C_3N_4 nanosheets (Co_1/C_3N_4) via forming amide bonds between the carboxylic groups in AQ and primary/secondary amine groups on the edge of C_3N_4, thus yielding $Co_1/AQ/C_3N_4$ composite photocatalyst. As displayed in Figure 1a, the single-atom Co species on the surface of C_3N_4 nanosheets serve as the H_2O oxidation centers, while AQ at the edge of C_3N_4 nanosheets acts as the O_2 reduction center. The ultrathin few-layer morphology of C_3N_4 nanosheets is shown in the TEM image (Figure 1b) of $Co_1/AQ/C_3N_4$. The dispersion of isolated Co atoms on C_3N_4 nanosheets is further confirmed by the atomic-resolution high-angle annular dark-field scanning transmission electron microscopy (HAADF-STEM) image in Figure 1c. Moreover, the HAADF-STEM image of $Co_1/AQ/C_3N_4$ (Figure 1d) and the corresponding elemental mapping images (Figure 1e−h) further corroborate the good dispersion of Co across the C_3N_4 nanosheet surface. Besides, no Co−Co coordination observed in the Fourier transform (FT) extended X-ray absorption fine structure (EXAFS) spectrum of $Co_1/AQ/C_3N_4$ (Figure 1i) further supports the atomic dispersion of Co. The results in Figure 1i further suggest that P is mainly coordinated with Co in $Co_1/AQ/C_3N_4$, which supports the complete phosphorylation. Moreover, as displayed in Figure 1j, the absorption edge position and spectral line shape of $Co_1/AQ/C_3N_4$ and CoO are quite similar, indicating that the valence state of the single-atom Co is near +2. The photocatalytic H_2O_2 generation was tested utilizing simulated solar light illumination under O_2-saturated conditions. Figure 1k indicates that the H_2O_2 production rate was improved by
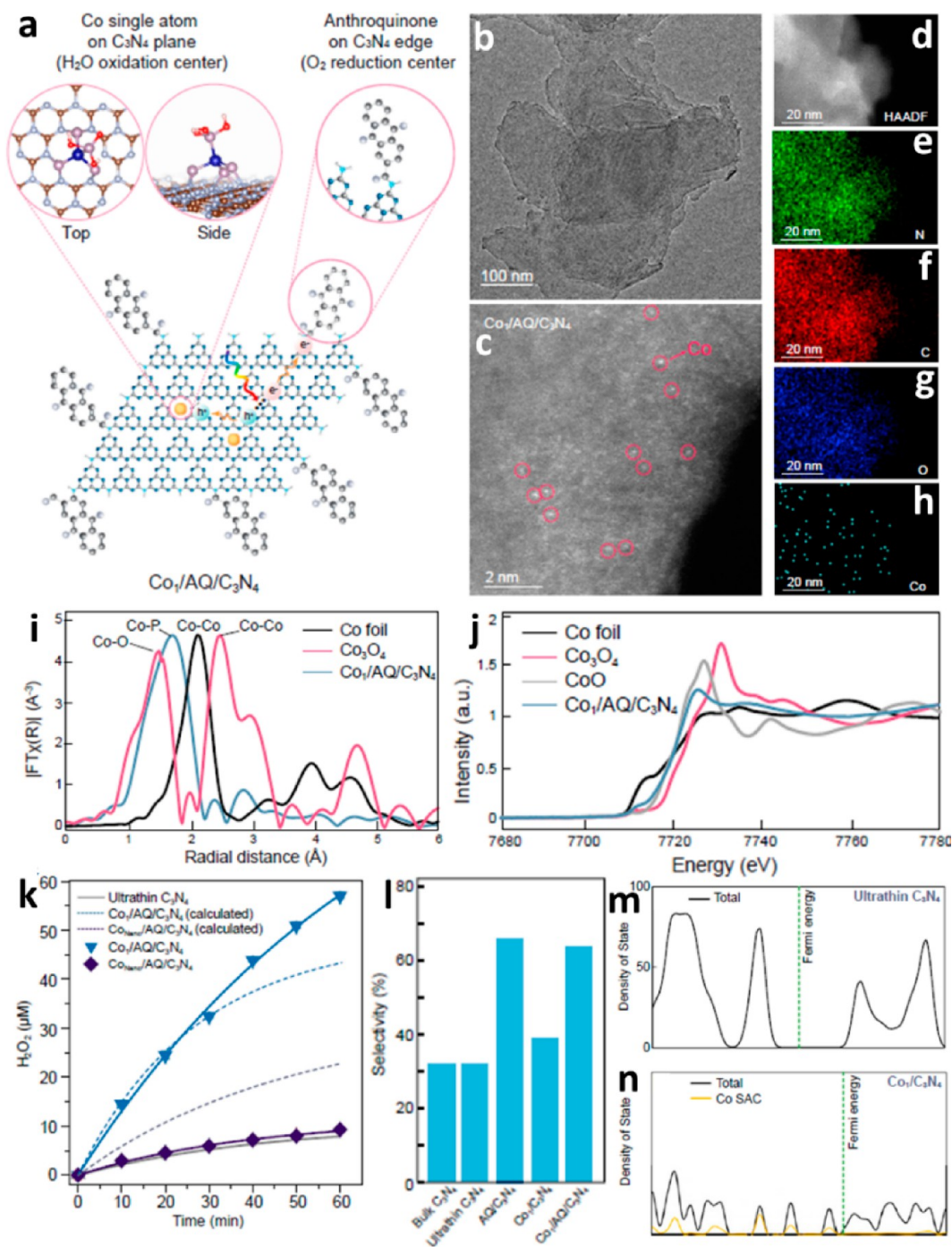
Figure 1. (a) 2D C_3N_4 nanosheets with spatially separated single-atom Co and AQ species as the H_2O oxidation centers and the O_2 reduction centers, respectively. (b) TEM image of $Co_1/AQ/C_3N_4$. (c) Atomic-resolution HAADF-STEM image of $Co_1/AQ/C_3N_4$. (d) HAADF-STEM image of $Co_1/AQ/C_3N_4$ and the corresponding EDS elemental mapping images of (e) N element, (f) C element, (g) O element, and (h) Co element. (i) Fourier transform (FT) EXAFS spectra of Co K edge for $Co_1/AQ/C_3N_4$, Co foil, and Co_3O_4. (j) Normalized XANES of Co K edge for $Co_1/AQ/C_3N_4$, Co foil, Co_3O_4, and CoO. (k) Time course of H_2O_2 generation utilizing simulated solar light illumination on $Co_1/AQ/C_3N_4$ and $Co_{Nano}/AQ/C_3N_4$. Dotted lines ($Co_1/AQ/C_3N_4$ and $Co_{Nano}/AQ/C_3N_4$) are H_2O_2 generation estimated assuming additive improvement of each cocatalyst. Solid line (ultrathin C_3N_4) in Figure 1k is the fitting result of the kinetic model. (l) H_2O_2 generation selectivity of bulk C_3N_4, ultrathin C_3N_4, AQ/C_3N_4, Co_1/C_3N_4, and $Co_1/AQ/C_3N_4$. Density of states calculated using the DFT-based theory for (m) ultrathin C_3N_4 and (n) Co_1/C_3N_4. Reproduced with permission from ref 38 (with CC BY-NC-ND License). Copyright 2020 National Academy of Sciences.

7.3 times after coloading single-atom Co species and AQ simultaneously. Besides, $Co_1/AQ/C_3N_4$ exhibits a high selectivity of over 60%, much higher than other samples, such as bulk C_3N_4, ultrathin C_3N_4, and Co_1/C_3N_4 (Figure 1l). The greatly enhanced photocatalytic H_2O_2 generation activity and selectivity are ascribed to the simultaneous loading of both

single-atom Co species as H_2O oxidation centers and AQ as the O_2 reduction center, respectively. Moreover, the DFT-based computations show two distinct and occupied midgap states about 0.5 and 0.9 eV above the valence band edge as the H_2O is absorbed, thus boosting the localization of photo-
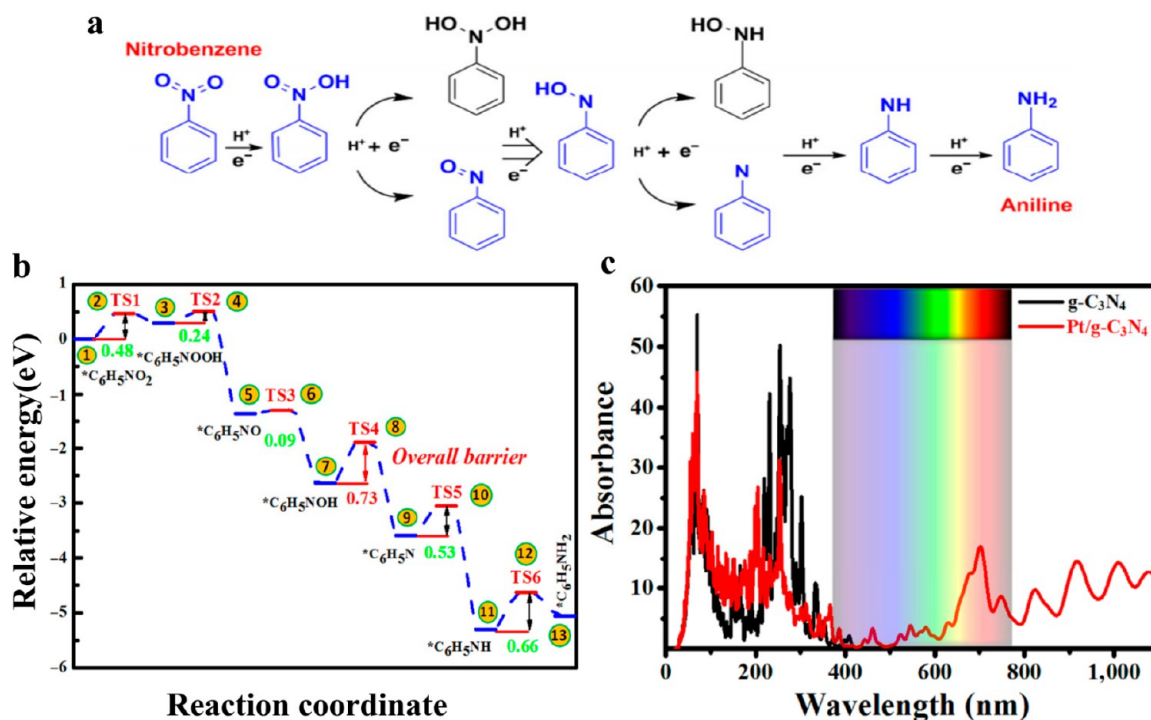
Figure 2. (a) Possible reaction routes for the nitrobenzene hydrogenation producing aniline (the preferential one is in blue). (b) Energy diagrams of the reaction routes for nitrobenzene hydrogenation producing aniline over Pt/g-C$_3$N$_4$ single-atom photocatalyst and (c) light absorption spectra of the g-C$_3$N$_4$ with and without Pt single-atom loading. Reproduced with permission from ref 80. Copyright 2020 Springer Nature.

induced holes and the dissociation of photoinduced electrons and holes (Figure 1m and n).

Aniline is a significantly widely used raw material in the modern chemical industry and pharmaceutical industry.[84] Due to the lack of efficient and excellent catalysts, He et al. used the DFT calculations to predict the possible highly active photocatalyst for the synthesis of aniline from nitrobenzene under solar light irradiation.[80] Based on their calculation results, a single-atom Pt decorated graphitic carbon nitride (Pt@g-C$_3$N$_4$) showed excellent catalytic performance for the hydrogenation of nitrobenzene and high selectivity for forming aniline. They explored four possible reaction pathways in Figure 2a to find the most suitable one. According to the calculation results of reaction energies and the activation energies required for all the possible intermediates, the preferential thermodynamic route over Pt@g-C$_3$N$_4$ is hydrogenation of nitrobenzene producing aniline. Hence, the activation barrier for each reaction step was computed and the corresponding energy profiles are shown in Figure 2b. The N−O bonds on Pt single atom of Pt@g-C$_3$N$_4$ are cracked by a single hydrogen atom, followed by the Ph-NO → Ph-NOH → Ph-N hydrogenation pathway, while in the conventional dissociation of N−O bonds on the Pt (111) surface, these bonds are attacked by two hydrogen atoms and undergo the Ph-NO$_2$ → Ph-NOOH → Ph-NO → Ph-NOH → Ph-N → Ph-NH → Ph-NH$_2$ hydrogenation pathway. The DFT-based calculations also indicate that the energy barriers for hydrogenations of phenyl, -C=C, -C≡C, and -CHO substituents on single-atom Pt@g-C$_3$N$_4$ photocatalyst are 1.05, 1.49, 1.29, and 1.53 eV, higher than those for the overall hydrogenation of nitrobenzene. Besides, the incorporation of single Pt atom narrows the bandgap of g-C$_3$N$_4$ from 2.7 to 0.72 eV, suggesting that both visible light and infrared light could be

harvested by Pt@g-C$_3$N$_4$ (Figure 2c), thus enhancing the light-capturing ability of the pristine g-C$_3$N$_4$.

The efficient activation of O$_2$ is of great importance for achieving sunlight-driven aerobic organic conversion under atmospheric pressure. Recently, Chu et al. reported the photocatalytic O$_2$ activation by cophthalocyanine/g-C$_3$N$_4$(CoPc−g-C$_3$N$_4$) heterostructure with single Co−N$_4$ (II) sites.[85] Based on theoretical calculations, they utilized melamine and cyanuric acid as the raw materials to fabricate carbon nitride nanosheets, followed by phosphate modification and introduction of CoPc to obtain the CoPc-g-C$_3$N$_4$ heterojunction (shown in Figure 3a). The rough dark shadows in Figure 3b could be assigned to the loaded CoPc, which is confirmed by the HAADF-STEM image (Figure 3c) and the corresponding elemental mapping images (Figure 3d). The UV−vis absorption spectra and FT-IR and Raman spectra indicate that the thinner assemblies and high dispersion of CoPc are induced by phosphates and CoPc could interact with g-C$_3$N$_4$ and P-doped g-C$_3$N$_4$(P-CN) via the H-bonding. The interfacial charge transfer between CoPc and P-doped g-C$_3$N$_4$ was confirmed by the steady-state surface photovoltage spectroscopy and photoluminescence (PL) and fluorescence spectral (FS) data. The electron paramagnetic resonance (EPR) results in Figure 3e indicate that 0.5CoPc/9P-CN is the optimized photocatalyst for O$_2$ activation where O$_2$ is reduced to produce •O$_2^-$ radicals. As regards the catalytic performance test for O$_2$ activation, the optimized CoPc-g-C$_3$N$_4$ with abundant single-atom Co−N$_4$ sites exhibits excellent photocatalytic activity for 2,4-dichlorophenol (DCP) degradation (shown in Figure 3f) and the possible mechanism of the oxidative degradation of 2,4-DCP over CoPc/P-CN is illustrated in Figure 3g. Moreover, the optimized 1.8CoPc/12P-CN photocatalyst was tested for selective oxidation of
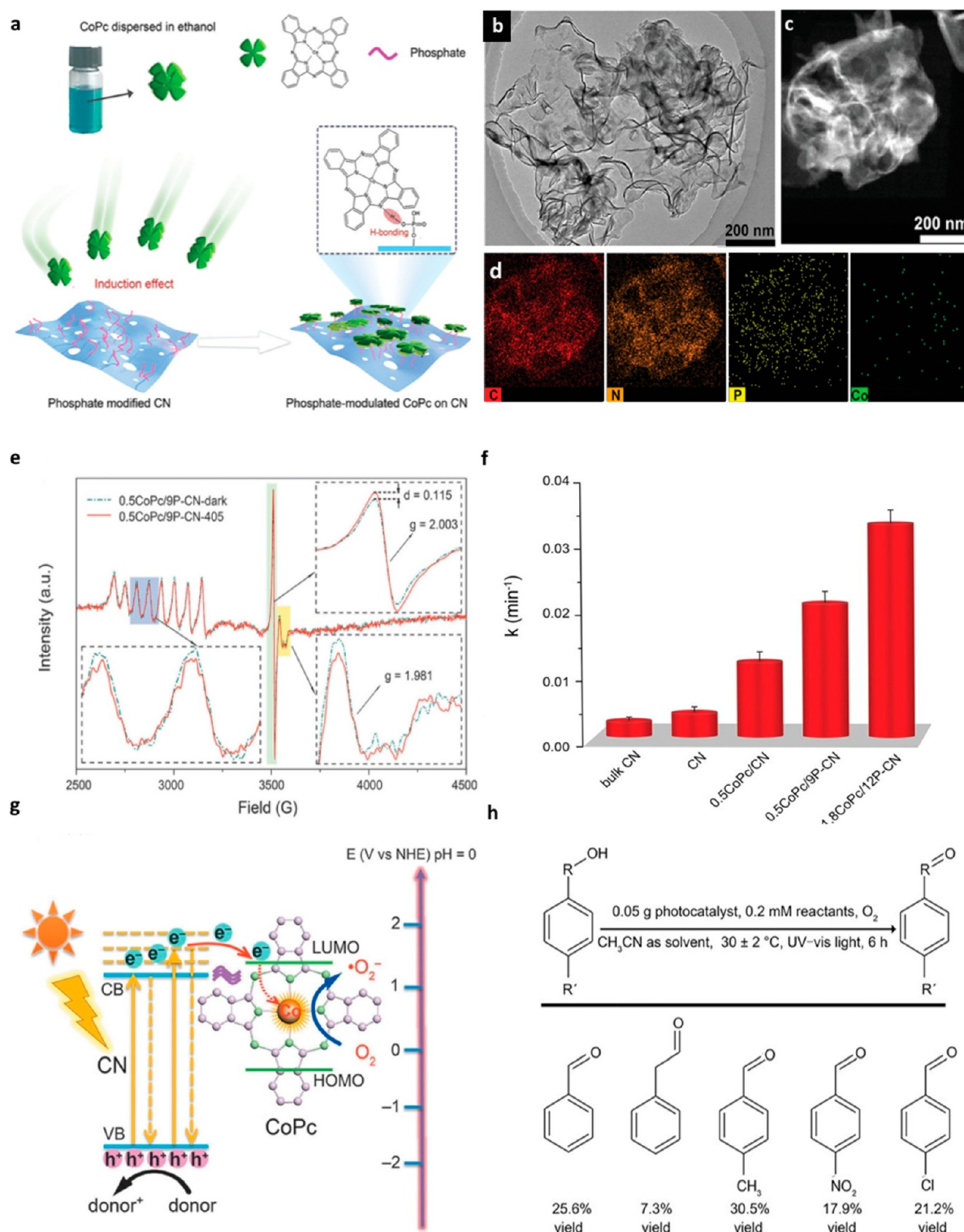
Figure 3. (a) Scheme of the process of preparation of CoPc/P-CN nanostructures; (b) TEM and (c) HAADF-STEM images of 0.5CoPc/9P-CN and (d) the corresponding elemental mapping images; (e) EPR spectra of 0.5CoPc/9P-CN under light irradiation (λ = 405 nm); (f) photocatalytic performance test for 2,4-DCP degradation by CoPc/P-CN; (g) diagram of O_2 activation on the CoPc/P-CN heterojunction under visible-light irradiation; (h) selective photocatalytic oxidation of different aryl-alcohols over 1.8CoPc/12P-CN. (Photocatalytic reaction conditions: in the presence of O_2, under visible-light irradiation). Reproduced with permission from ref 85 (with CC BY 4.0 License). Copyright 2020 John Wiley & Sons, Inc.

aromatic alcohols, exhibiting a 25.6% yield for producing benzaldehyde (Figure 3h).

Dehalogenation reaction of organic halides is considered as one of the most important transforming processes because of

its potential use for detoxification and removal of harmful organic halides.[86,87] Wu et al. used AgF as a photocatalyst for the selective dehalogenation of various organic halides under visible light illumination.[88] Irradiated by visible light, AgF

> The reduction reactions of widely available raw materials into fuels and value-added chemicals, such as H₂O₂ and aniline, have been successfully achieved on single-atom photocatalysts.

would be converted to Ag single atoms (Ag-SAs) and Ag nanoparticles, which could trigger hydro-deiodination or deiodination-phenylation of organic halides in a specific solvent. Recycling tests were performed to understand the key role of this photocatalytic reaction. The *in situ* electron spin resonance (ESR) spectroscopy studies and contrast experiment data confirm that Ag-SAs acts as the reactive center for photocatalytic deiodination reactions.

3. SINGLE-ATOM PHOTOCATALYSTS FOR EMERGING OXIDATION REACTIONS

As discussed in our previous work,[13] selective photocatalytic oxidation is a promising strategy to produce various value-added chemicals. Although photocatalytic selective oxidation of organic compounds to form valuable chemicals has been extensively investigated, it is still challenging to achieve the high-selectivity yield of desired chemical products. Recent studies (shown in Table 2) indicate that single-atom photocatalysts can achieve the efficient activity, high selectivity, and strong stability toward selective oxidation reaction, thus generating target chemicals, such as phenol and imines.

> Photocatalytic selective oxidation of organic compounds on single-atom photocatalysts is a promising strategy to produce various desirable value-added chemicals.

Phenol is utilized as a pivotal organic chemical intermediate and precursor to synthesize many important industrial products, e.g., phenolic resins, bisphenol A, cyclohexanol, polysulfone, carbonate, aniline, and *o*-cresol.[89] However, the current industrial procedure to synthesize phenol from benzene requires multiple steps and indirect preparation, thus suffering from many drawbacks, e.g., complex preparation processes, severe depletion of raw materials, and serious environmental contamination.[90] Hence, it is of great importance to discover cost-effective strategies for phenol production via benzene oxidation utilizing H₂O₂ from the industrial and social perspectives. This is also one of the most challenging tasks in the green chemistry field. Recently, Xiao et al. anchored single-atom Cu (SA-Cu) on tubular carbon nitride (TCN) for visible-light-induced photocatalytic benzene

oxidation to generate phenol using H₂O₂.[41] As demonstrated in Figure 4a, SA-Cu-TCN is synthesized via thermal treatment of melamine-based precursor containing chlorophyll sodium copper (CSC). The TEM results of SA-Cu-TCN and the enlarged marked area are displayed in Figure 4b and 4c. The corresponding elemental mapping images of N, C, and Cu are presented in Figure 4d−f, respectively. In particular, the uniform distribution of Cu element on the whole carbon nitride is confirmed in Figure 4f. The aberration-corrected HAADF-STEM image (Figure 4g) displays the detection of single-atom Cu, confirming the fabrication of single-atom Cu in SA-Cu-TCN. Moreover, X-ray absorption spectroscopy (XAS; see Figure 4h) study reveals the valence state of Cu in SA-Cu-TCN, as well as the coordination environment. Since its absorption edge is located in the middle of those edges of CuO and Cu₂O, both Cu(I) and Cu(II) are supposed to be present in SA-Cu-TCN. Figure 4i displays the Fourier transform of the K²-weighted EXAFS spectra for the Cu K edge on Cu foil, CSC, and SA-Cu-TCN. The predominant peak at *ca.* 1.6 Å is assigned to the Cu−N bond in SA-Cu-TCN, again confirming the loading of single-atom Cu on TCN. Since the local coordination environment intimately affects the form of X-ray absorption near edge structure (XANES) spectra, the authors employed FEFF9.6 code to calculate the spectra of two coordination structures (denoted as Cu−N₃ and Cu−N₄) as shown in Figure 4j and k, respectively. Also, the XANES results of SA-Cu-TCN are verified by the simulated spectra shown in Figure 4j and k. The construction of the Cu−N₃ structure is attributed to the interaction of Cu atom and three N atoms in the TCN layer. Meanwhile, the interaction between four N atoms from two CN monolayers and a single atom results in Cu−N₄ coordination. The calculated charge density differences between the Cu−N₃ and Cu−N₄ coordination of SA-Cu-TCN are shown in Figure 4l and m, respectively. The charge migration in Cu and its adjacent N atoms is disclosed. In Cu−N₄ coordination, the apparent charge migration along the *z*-direction is also manifested in Figure 4m. Hence, the aforementioned results indicate that these Cu−N configurations in SA-Cu-TCN generate novel charge migration channels for enhancing the charge movement within and between the carbon nitride planes. This will boost the photocatalytic performance. Moreover, the benzene-to-phenol conversion was used to test the photocatalytic oxidation performance on SA-Cu-TCN. No benzene-to-phenol conversion happened without the catalyst. In dark conditions, SA-Cu-TCN attained a benzene-to-phenol conversion efficiency of 41.2% with a selectivity of 88.3%. Using visible light, SA-Cu-TCN shows the conversion and selectivity of 92.3% and 99.9%, respectively (Figure 4n), much larger than those obtained on CN and TCN. Besides, SA-Cu-TCN also possesses good robustness for benzene oxidation to phenol. The outstanding photocatalytic performance arises from the formation of the Cu−N_x electron/hole migration path in SA-Cu-TCN, thus

Table 2. Single-Atom Photocatalysts for Emerging Oxidation Reactions

| Photocatalyst | Light source | Reactants | Oxidation reaction | | Activity | Stability | ref |
			Reaction	Main product			
Cu/C₃N₄	λ > 420 nm	benzene, H₂O₂ CH₃CN	Benzene oxidation	Phenol	92.3% conversion	12 h	41
Co/carbon quantum dots	460 nm LED	Benzylamine, CH₃CN	Oxidative coupling	(E)-*N*-benzyl-1-phenylmethanimine	83% conversion	4 cycles	93
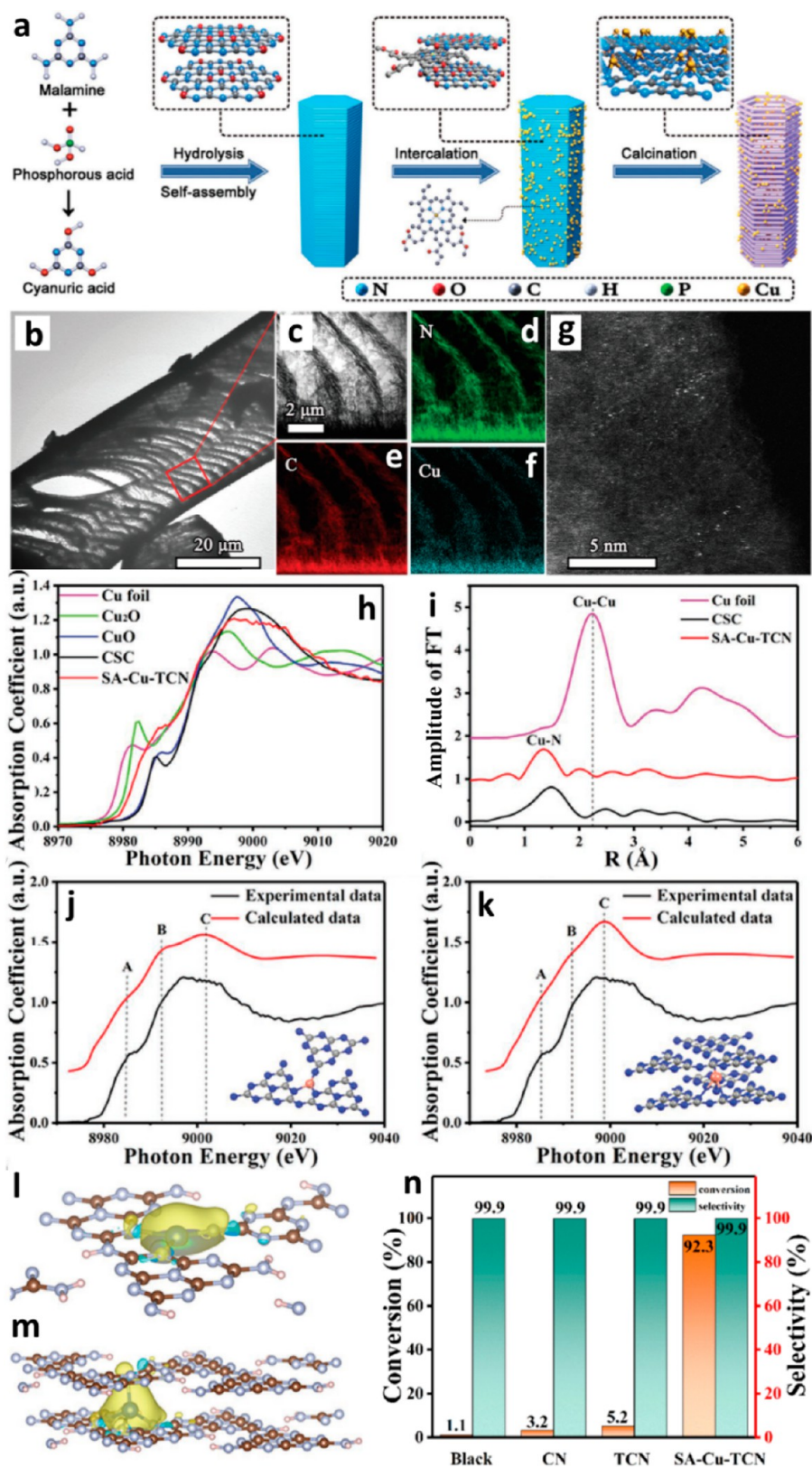
Figure 4. (a) The synthesis process of SA-Cu-TCN. (b) TEM image of SA-Cu-TCN and (c) the enlarged TEM image of the marked area in Figure 4b and the elemental mapping images of (d) N, (e) C, and (f) Cu elements. (g) A typical HAADF-STEM image of SA-Cu-TCN. (h) XANES spectra of the Cu K edge for SA-Cu-TCN, CSC, Cu foil, Cu$_2$O, and CuO samples. (i) Fourier transform (FT) of the K^2-weighted EXAFS Cu K edge of SA-Cu-TCN, Cu foil, and CSC. (j, k) Experimental and computed XANES spectra of the Cu K edge for the samples with the corresponding structure models (inset). (l, m) Differential charge surfaces of the Cu−N$_3$ and Cu−N$_4$ coordination structures. (n) Catalytic activity of SA-Cu-TCN for oxidation of benzene performed at 50 °C using visible light illumination for 12 h. Reproduced with permission from ref 41. Copyright 2020 John Wiley & Sons, Inc.
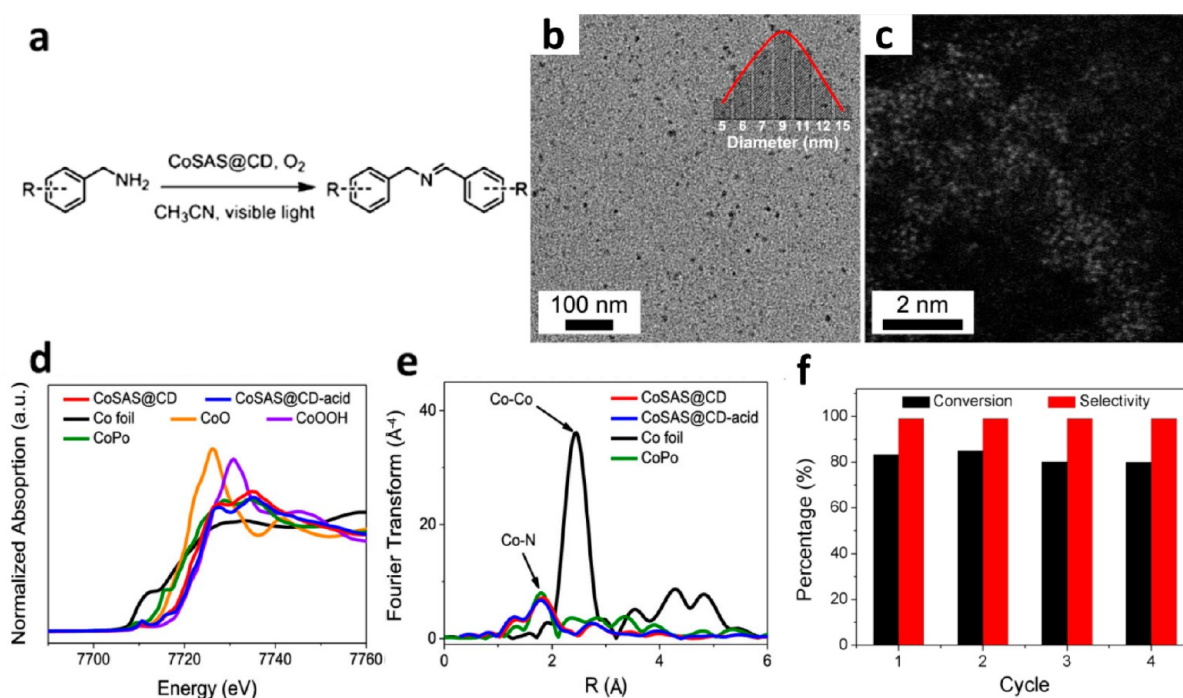
Figure 5. (a) Photocatalytic oxidative coupling of benzylamines with CoSAS@CD using visible light. (b) TEM image of CoSAS@CD; Figure 5b inset displays the size distribution of CoSAS@CD. (c) A typical HAADF-STEM image of CoSAS@CD. (d) XANES spectra of Co K edge for CoSAS@CD, CoSAS@CD-acid, Co foil, CoO, CoOOH, and Co-porphyrin (CoPo). (e) Fourier transform EXAFS spectra of Co K edge for CoSAS@CD, CoSAS@CD-acid, Co foil and CoPo. (f) The reaction conversion and selectivity of oxidative photocatalytic coupling of benzylamines on CoSAS@CD using visible light over 4 repeating cycles. Reproduced with permission from ref 93 (with CC-BY license). Copyright 2020 American Chemical Society.

Table 3. Single-Atom Photocatalysts for Emerging Redox Reactions

Photocatalyst	Light source	Reactants	Redox reaction				
			Reaction	Main Product	Activity	Stability	ref
Ru/Cu	White light	CH_4 and CO_2	methane dry reforming	CO, H_2	34 mol H_2 mol^{-1} s^{-1}	50 h	78
Co−P_3/CdS	λ > 420 nm	formic acid	dehydrogenation of formic acid	CO_2, H_2	102.9 mmol g^{-1} h^{-1}	24 h	94
Pt/TiO_2	Xe lamp	acetone	acetone dehydrogenation and C−C coupling	2,5-hexanedione, H_2	3.87 mmol g^{-1} h^{-1}	16 h	42
Fe/carbon nitride	460 nm LED	Styrene, p-methyl-benzenesulfinic acid	sulfonation of alkenes	β-ketosulfones	94% conversion		79

tremendously advancing the in-plane and interplane charge migration.

It is of great importance to selectively oxidize benzylamine as well as its derivatives to form imines since they are pivotal electrophilic intermediates in pharmaceutical synthesis.[91,92] In recent work, Wang et al. fabricated single-atom Co dispersed on carbon quantum dots (CoSAS@CD) for selective photocatalytic oxidation of benzylamine together with a range of its derivatives to yield imines in the presence of O_2 using visible light illumination (Figure 5a).[93] CoSAS@CD was fabricated through pyrolyzing vitamin B12 followed by hydrolysis in NaOH solution. CoSAS@CD was treated with an acid to yield the acid-treated CoSAS@CD (CoSAS@CD-acid). The TEM image of CoSAS@CD (Figure 5b) discloses that the as-prepared carbon dots are spherical with an averaged 9.0 nm diameter. Many bright dots (diameter <0.2 nm) observed in the aberration-corrected HAADF-STEM image (Figure 5c) could be ascribed to the single Co atoms. This result suggests that individual Co atoms are distributed on the carbon dots

surface. Furthermore, the XANES Co K edge was recorded to study the chemical state of Co sites. As presented in Figure 5d, the absorption edges of CoSAS@CD and CoSAS@CD-acid are positioned between those for CoO and CoOOH, suggesting the existence of Co(II) and Co(III). Moreover, the Fourier transform (FT) k^3-weighted EXAFS results show that only one major peak at *ca.* 1.9 Å is observed for both samples. This could be the first coordination shell of Co−N/C as that present in Co-porphyrin (CoPo). In particular, no apparent Co−Co peak located around *ca.* 2.5 Å and the HAADF-STEM result (Figure 5e) indicate the atomic dispersion of Co in CoSAS@CD. Then, benzylamine and its derivatives were selectively oxidized to yield imines in high conversion efficiency and excellent selectivity utilizing CoSAS@CD as the photocatalyst using visible light in the existence of O_2. Moreover, CoSAS@CD exhibited excellent stability over four cycles (Figure 5f).

## 4. SINGLE-ATOM PHOTOCATALYSTS FOR EMERGING REDOX REACTIONS

The emerging reduction or oxidation reactions presented in the previous two sections yield the target products by utilizing either photoinduced electrons or holes alone. As a result, it is highly desirable to utilize both photoinduced electrons and holes simultaneously in single-atom photocatalysts, thus generating both reduction and oxidation products via redox reactions. For example, Zhou et al. adopted a single-atom photocatalyst to achieve methane dry reforming (MDR: CH_4 + CO_2 = $2H_2$ + 2CO) and produce syngas composed of CO and H_2.[78] Also, the dehydrogenation of formic acid to yield H_2 and CO_2 (HCOOH = H_2 + CO_2) is conducted via single-atom photocatalysis.[94] Moreover, another work demonstrates the coproduction of H_2 and value-added 2,5-hexanedione through the C−C coupling of acetone.[42] Furthermore, Wen et al. demonstrated that β-ketosulfones could be produced via sulfonation of olefins utilizing photoinduced holes as well as $O_2^{\bullet-}$ and singlet oxygen $^1O_2$ generated via reduction of molecular oxygen using photoinduced electrons.[79] The above four studies (summarized in Table 3) are presented below.

> The reduction and oxidation products via redox reactions could be obtained as the target products simultaneously by utilization of photo-generated electrons and holes over single-atom photocatalysts.

Syngas comprised of CO and H_2 is extensively utilized in industrial-scale processing. Syngas can be generated by MDR reaction, where two greenhouse gases could be transformed into a high-value chemical feedstock.[95] However, the MDR reaction is not only kinetically and thermodynamically unfavorable but also suffering from coke deposition and the subsequent deactivation of catalysts. Moreover, high temperatures (700−1000 °C) are required to attain efficient reaction rates and reduce coke deposition. Thus, the photocatalytic MDR under light irradiation and tremendously milder reaction conditions is of great significance. Recently, Zhou et al. have prepared single-atom site Ru−Cu alloy as an antenna-reactor plasmonic photocatalyst via coprecipitation on the surface of a MgO/Al_2O_3 substrate (Figure 6a).[78] In detail, a series of Cu_xRu_y photocatalysts (i.e., Cu_{20}, $Cu_{19.95}Ru_{0.05}$, $Cu_{19.9}Ru_{0.1}$, $Cu_{19.8}Ru_{0.2}$, and $Cu_{19.5}Ru_{0.5}$) was fabricated, where x and y are the percentages of Cu and Ru of metal contents in the photocatalysts. The as-synthesized photocatalysts were tested for light-driven MDR using white light illumination. Single-atom Ru−Cu alloy ($Cu_{19.8}Ru_{0.2}$) exhibited much higher photocatalytic MDR activity, stability, and selectivity than bare Cu NPs (Figure 6b and c). Besides, $Cu_{19.8}Ru_{0.2}$ shows a turnover frequency (TOF) of 34 mol_{H_2} mol_{Ru}^{-1} s^{-1} and excellent photocatalytic stability over 50 h. Moreover, due to the low coverage of Ru on the surface of $Cu_{19.95}Ru_{0.05}$, the exposed Cu on the surface (Figure 6d) catalyzed a large fraction of the reaction. However, the Cu atoms exposed are susceptible to coking. Since the Ru content is smaller than 0.2%, it is postulated that Ru is atomically loaded onto the surface of Cu, separating carbon intermediates on the surface and inhibiting

the graphitic carbon generation (Figure 6e). For comparison, with larger Ru content ($Cu_{19.5}Ru_{0.5}$), the generated Ru assembles or some islands can be formed, which promote the carbon formation considering their proximity. Thus, dehydrogenated derivatives of CH_4 (CH_x) oligomerize and yield coke (Figure 6f). The robustness tests are also repeated to corroborate the above conclusions. Both CO probe molecule diffuse reflectance infrared Fourier transform spectroscopy (CO-DRIFTS) and DFT-based computations are combined to support the single-atom Ru dispersion in Cu (Figure 6g). Moreover, the authors conducted periodic DFT +D3 calculations to further probe the reaction mechanism. They found that the most likely rate-limiting steps of FA dehydrogenation on Cu and CuRu are the first step of hydrogen dissociating from CH_4 (CH_4 → CH_3 + H) and the fourth step of hydrogen dissociating from CH intermediate (CH → C + H) (see Figure 6h and i). Hence, the embedded multiconfigurational n-electron valence second-order perturbation theory (e-NEVPT2) was applied to study the above two steps. It was predicted that the first dehydrogenation step on Cu and the fourth dehydrogenation step on CuRu possess the largest barriers. Their ground-state barriers are 2.51 and 1.10 eV, respectively (Figure 6j and k). Hence, the barrier of CH_4 dissociation can be reduced by incorporating Ru. In the above photocatalytic MDR process, the generation of hot carriers is deemed as the principal mechanism, thus leading to significantly different behavior from the thermocatalytic MDR process. Hot carriers play a key role in improving the activation rates of C−H on Ru sites and H_2 desorption off from the catalysts surface. The observed improvement results from the kinetic matching of production rates of H_2 and CO, thus minimizing the coking formation and reverse water gas shift (RWGS) rates. Thus, the reported photocatalytic MDR process is robust and selective.

The photocatalytic formic acid (FA) dehydrogenation to produce hydrogen (H_2) was achieved on the atomic-level well-dispersed Co−P_3 on CdS nanorods (NRs) photocatalyst.[94] A facile impregnation−phosphorization strategy was adopted to prepare Co−P_3 with atomic dispersion onto CdS NRs. The distinct hexagonal-phase structured CdS NRs with ordered lattice spacings can be seen in the HAADF-STEM result (Figure 7a). This indicates that CdS crystal structure was not affected much in the aforementioned phosphatizing treatment at elevated temperature. The elemental mapping images in Figure 7a confirm the uniform dispersion of Co and P on the CdS NRs, and no apparent nanoparticles of Co and/or CoP are observed. Moreover, CoPSA-CdS exhibits a Co K edge higher than that of Co foil in the XANES spectra (Figure 7b). In addition, the main peak of CoPSA-CdS located around *ca.* 1.63 Å in the EXAFS spectra (Figure 7c) is ascribed to the Co−P bond. The EXAFS fitting results further indicate that the centered Co atoms in CoPSA-CdS possess one Co−P_1 and two Co−P_2, again supporting the atomic dispersion of Co atoms in CoPSA-CdS. Based on the aforementioned XAFS results, the theoretical computation was executed to construct the atomic geometry structure of CoPSA-CdS in Figure 7d. As displayed in Figure 7d, the Co atom is coordinated with one Co−P_1 and two Co−P_2 bonds. Then the catalytic performance of these samples was investigated via dehydrogenation of FA into H_2 and CO_2 under visible-light illumination at room temperature. In Figure 7e, CoPSA-CdS manifests the highest photocatalytic performance for FA dehydrogenation with a rate of 102.9 mmol·g^{-1}·h^{-1}, much higher than pristine CdS,
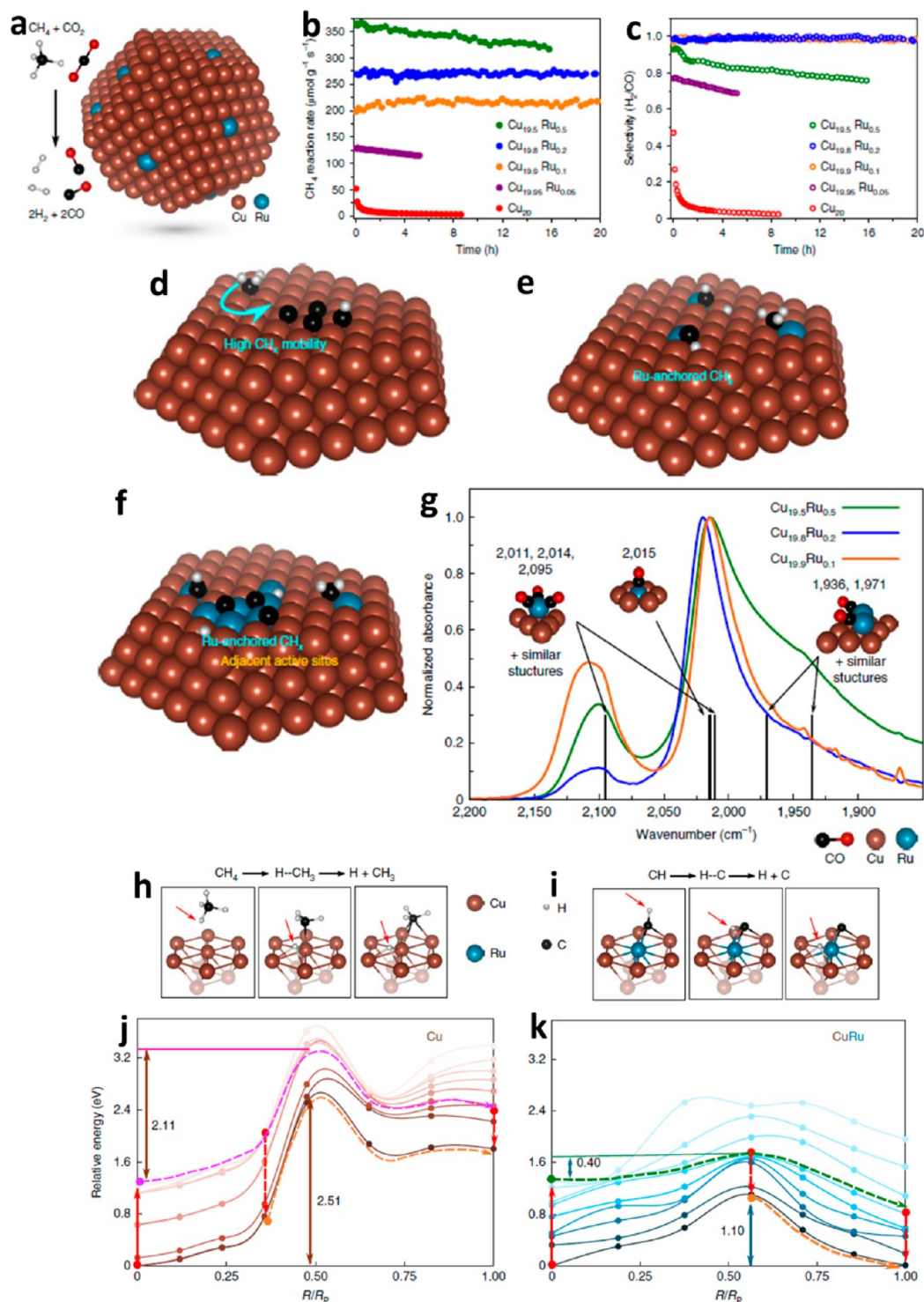
Figure 6. (a) Illustration of a single-atom Ru embedded Cu alloy photocatalyst. The reactants and products of MDR are displayed on the left panels. (b) Photocatalytic MDR activities and stabilities of pure Cu NPs (Cu_{20}) and Ru/Cu alloys with different Ru contents ($Cu_{19.95}Ru_{0.05}$, $Cu_{19.9}Ru_{0.1}$, $Cu_{19.8}Ru_{0.2}$ and $Cu_{19.5}Ru_{0.5}$) using white light irradiation. The reactor for conducting the photocatalytic MDR reaction was maintained at room temperature. (c) Photocatalytic MDR selectivity of pure Cu NPs (Cu_{20}) and Ru/Cu alloys with different Ru contents ($Cu_{19.95}Ru_{0.05}$, $Cu_{19.9}Ru_{0.1}$, $Cu_{19.8}Ru_{0.2}$, and $Cu_{19.5}Ru_{0.5}$) using white light irradiation. The reactor for conducting the photocatalytic MDR reaction was maintained at room temperature. The formation rate ratio of H_2 to CO is defined as the selectivity. Schematic illustration for the influence of Cu_xRu_y composition on the coke resistance for (d) Cu alone, (e) Cu_xRu_y with low Ru loading content, and (f) Cu_xRu_y with high Ru loading content. (g) Infrared spectra of CO adsorbed on single-atom Ru embedded Cu alloy surface at room temperature and saturation coverage following pretreatment at 200 °C in 10% CO in Ar (100 mL min^{-1}) for 60 min. Rate-determining (h) CH_4 and (i) CH activation on Cu (111) and CuRu (111), respectively. Left, middle, and right panels indicate reactant, transient state, and product structure, respectively. Ground- and excited-state energy curves for CH_4 activation on (j) Cu (111) and (k) CH activation on CuRu (111) from e-NEVPT2. From the ground to the highest energy excited state, the color saturation of the curves turns from dark to light. Reproduced with permission from ref 78. Copyright 2020 Springer Nature.
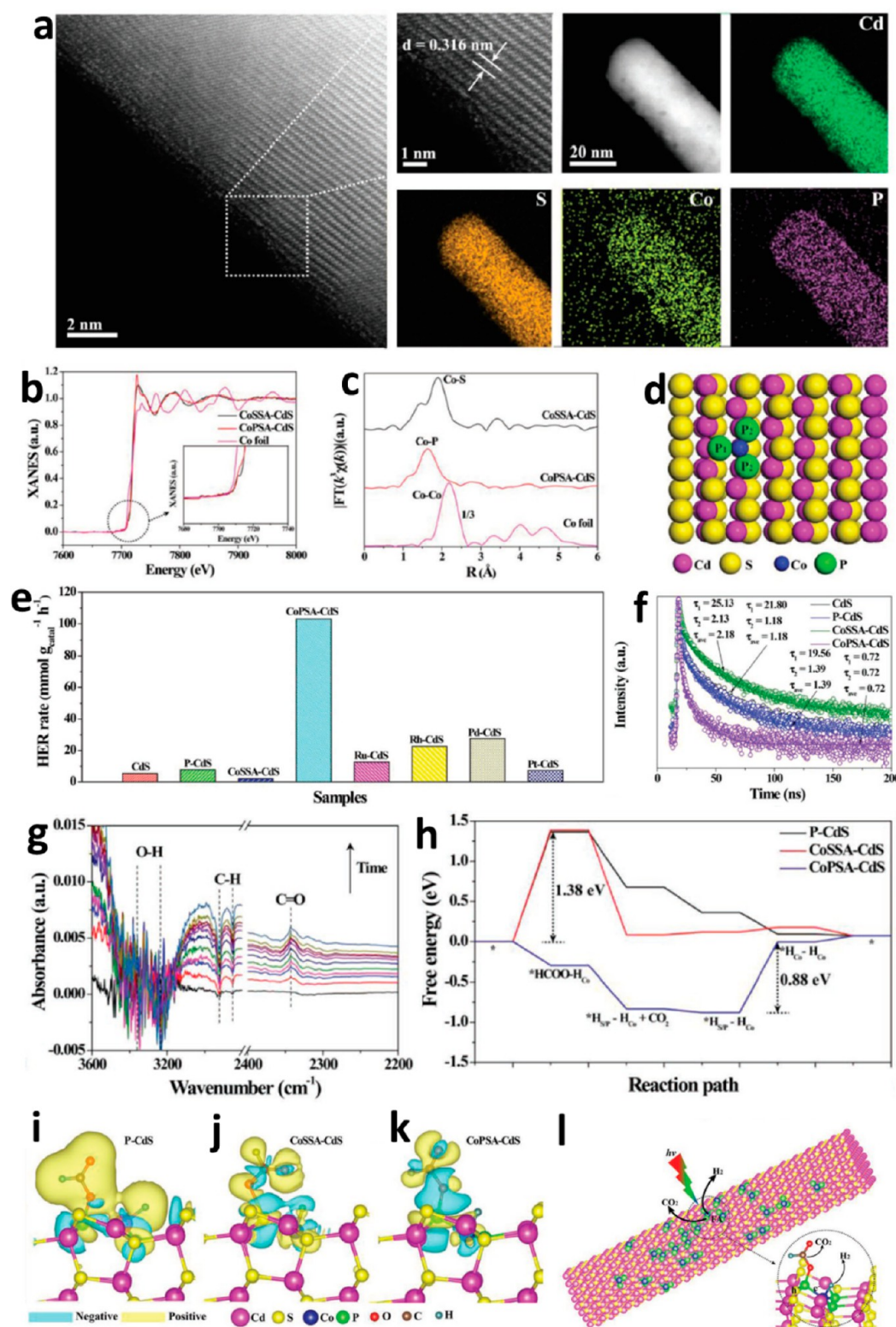
Figure 7. (a) HAADF-STEM image and the relevant elemental mapping images of CoPSA-CdS. (b) X-ray absorption spectra of Co and (c) the corresponding k^3-weighted FT space at R space. (d) Atomic-level structure configuration of CoPSA-CdS based on first-principles simulation. (e) Comparison of the photocatalytic activities for FA dehydrogenation on all the as-prepared samples. The test of photocatalytic FA dehydrogenation reaction was conducted in the 100 mL 20 vol % FA aqueous solution using visible light illumination ($\lambda > 420$ nm) at room temperature. (f) Transient-state photoluminescence spectra of the as-prepared samples. (g) *In situ* IR spectrum analysis for photocatalytic dehydrogenation of FA on (g) CoPSA-CdS. (h) Free energy profiles calculated for the photocatalytic FA dehydrogenation process on P-CdS, CoSSA-CdS, and CoPSA-CdS. The differential charge density maps between CdS and adsorbed FA on (i) P-CdS, (j) CoSSA-CdS, and (k) CoPSA-CdS. (l) Photocatalytic FA dehydrogenation and H$_2$ evolution mechanism on CoPSA-CdS. Reproduced with permission from ref 94. Copyright 2020 John Wiley and Sons, Inc.

phosphatized CdS NRs (P-CdS), or S-coordinated Co singe atom on CdS NRs (CoSSA-CdS). Besides, CoPSA-CdS presents an *ca.* 100% product selectivity for CO_2 and H_2 with a 1:1 ratio. Thus, the generation of byproducts was efficiently suppressed on CoPSA-CdS. Furthermore, CoPSA-CdS shows much higher activity than Ru-loaded CdS (Ru-CdS), Rh-loaded CdS (Rh-CdS), Pd-loaded CdS (Pd-CdS), or Pt loaded CdS (Pt-CdS) as displayed in Figure 7e. Additionally, CoPSA-CdS displays the highest mass activity of Co (34,309 mmol g_{Co}^{-1} h^{-1}), in contrast to the previous record. Such an outstanding activity of CoPSA-CdS was explored by both experimental characterizations and theoretical computations. Transient-state photoluminescence spectra (Figure 7f) indicate the most efficient charge migration in CoPSA-CdS compared to CdS, P-CdS, or CoSSA-CdS. Moreover, the *in situ* IR spectrum study of the photodriven FA dehydrogenation on CoPSA-CdS (Figure 7g) shows the apparent peak intensity reduction of the C−H bond in the IR spectra, suggesting the effective FA adsorption and C−H bond activation on CoPSA-CdS. Additionally, the apparent IR peak intensity improvement around 2324 cm^{-1} was found for CoPSA-CdS (Figure 7g), indicating the marked generation of CO_2. Moreover, the DFT-based computations were executed to further probe into the reaction mechanism of the photocatalytic FA dehydrogenation. Figure 7h displays that the hydroxyl group of FA is inclined to dissociate between the adjacent P and Co atoms, ascribed to the *HCOO-H_{Co}. Thus, the P-HCOO generation along with the H adsorption on Co atom are achieved on CoPSA-CdS. As presented in Figure 7h, this is a spontaneous reaction step based on the negative reaction energy (−0.29 eV). In comparison, both CoSSA-CdS and P-CdS show positive reaction energy. As regards CoPSA-CdS, its FA dehydrogenation activity is restricted by the hydrogen migration process between P atom and the adjacent Co atom during the reaction, with positive reaction energy (0.88 eV). Thus, CoPSA-CdS displays a smaller energy barrier toward FA dehydrogenation compared to that observed for P-CdS or CoSSA-CdS, agreeing with its highest photocatalytic performance. Moreover, Figure 7i−k exhibits the differential charge density between the CdS surface and FA owing to the pivotal role of the FA dissociation adsorption on the CdS surface. In comparison to CoSSA-CdS and P-CdS, CoPSA-CdS possesses the best capacity to transport electrons from FA to Co atom and the ability to bind with HCOO via a robust P−O bond as well (shown in Figure 7i−k). Based on these results, the proposed reaction route is illustrated in Figure 7l. When illuminated by visible-light, the photoinduced electrons and holes are transported to Co−P sites and adjacent Cd−S sites, respectively. Subsequently, photoinduced electrons on Co atoms reduce the adsorbed proton to generate H_2. Meanwhile, the photoinduced holes on Cd−S sites migrate to P sites and the adsorbed HCOO group is dehydrogenatively oxidized to generate CO_2.

As a key chemical extensively applied in biofuel and medicinal chemistry, 2,5-hexanedione (HDN) is usually prepared using costly chemicals through complicated and harsh reaction processes.[96] Hence, it is of great significance to prepare HDN from renewable and inexpensive biomass, e.g., acetone, via cost-effective and environmentally benign solar photocatalysis under mild conditions. Recently, C−H activation of the methyl group in acetone and the subsequent cross-coupling of two $CH_3COCH_2^\bullet$ radicals to produce HDN was achieved on single-atom Pt dispersed P25 TiO_2(PtSA-TiO_2).[41] H_2, as a green fuel and important chemical, was also

generated via dehydrogenation of acetone in the above photocatalytic process. In detail, the DFT computation was first performed to acquire the energy profiles of the acetone dehydrogenation reaction on various single metal atoms dispersed on P25 TiO_2. The computation results indicate that the methyl dehydrogenation and generation of a $CH_3COCH_2^\bullet$ radical are the major rate-limiting processes. Thus, among the TiO_2-supported single metal atoms, PtSA-TiO_2 possesses the smallest energy barrier toward dehydrogenation of acetone. Indeed, PtSA-TiO_2 is confirmed to be the most effective photocatalyst with 3.87 mmol·g^{-1}·h^{-1} of 2,5-hexanedione production rate and 93% selectivity. In the reaction procedure, the photoinduced holes from TiO_2 activated methyl groups, thus leading to their dehydrogenation into H species on Pt single atoms and $CH_3COCH_2^\bullet$ radicals on TiO_2. Subsequently, two $CH_3COCH_2^\bullet$ radicals can achieve C−C coupling and produce 2,5-hexanedione; while two photoinduced electrons reduce two H to H_2 gas. Both *in situ* IR and ESR techniques confirm the above process.

As a pivotal category of organic molecules containing sulfone, β-ketosulfones have been extensively applied for synthesizing pharmaceuticals and organic functional materials. Especially, significant attention has been drawn recently by β-ketosulfones owing to their interesting biological activities and key preparation applications.[97,98] Unfortunately, the previously reported homogeneous photocatalytic preparation and functionalization processes of β-ketosulfones suffer from a narrow light absorption range, restricted substrate scope, and unrecoverable catalysts. Hence, it is important to explore highly efficient, recoverable, and environmentally friendly heterogeneous photocatalysts to prepare β-ketosulfones. Wen et al. adopted a facile molecule coupling approach to fabricate carbon nitride-hemin (CNH) composite photocatalyst.[79] The atomic-resolution HAADF-STEM image of CNH exhibits the bright spots with sizes of *ca.* 0.20 nm, ascribed to the loading of single atom Fe on CNH. The as-prepared CNH with single-atom Fe dispersion exhibits the excellent catalytic performance for olefins sulfonation, yielding β-ketosulfones under the condition of room temperature and normal pressure using visible light and/or near-infrared light. It is proposed that O_0^- and singlet oxygen $^1O_2$, which are generated by reduction of molecular oxygen using photoinduced electrons, together with photoinduced holes participate in the sulfonation of olefins to produce β-ketosulfones.

5. CONCLUSION AND OUTLOOK

Nowadays an increasing number of single-atom photocatalysts are designed and fabricated toward the emerging reactions yielding the highly desirable chemicals and/or energy carriers. These chemicals and energy carriers are conventionally synthesized under harsh conditions at a high cost. In contrast, single-atom photocatalysts could achieve outstanding activities, selectivity, and/or stabilities toward these reactions in mild conditions by using clean and renewable solar energy. A series of advanced characterization methods, e.g., aberration-corrected scanning transmission electron microscopy (AC-STEM), synchrotron radiation-based X-ray absorption spectroscopy (XAS), *in situ* Fourier transform infrared spectroscopy (FT-IR), and *in situ* ESR spectroscopy, are integrated with DFT-based calculations to uncover the insightful and overall structure−performance relationship for single-atom photocatalysts. Besides, detailed and in-depth photocatalytic mechanisms for these reactions are also explored.

Though many breakthroughs have been made in the above field, there are still many challenging obstacles to overcome. For instance, the rational design and synthesis of appropriate single-atoms (e.g., Fe, Ni, Ru, Rh, Pd, Ag, Pt, and Au) with desirable coordination environments (*e.g,* M-N$_4$, M-P$_3$, M-N/O, and M-N/P) showing high activity and selectivity toward specific reactions is of great importance. Besides, it is highly desirable to seek suitable strategies for achieving strong metal—support interactions in single-atom photocatalysts, assuring long-term stable activity and selectivity. For instance, supports with abundant coordination sites (e.g., N$_4$, P$_3$, N/O, and N/P) should be designed and synthesized for anchoring large amounts of single atoms as active sites. Moreover, supports with sufficient cation/anion vacancies can also be utilized to stabilize suitable single atoms to achieve strong metal—support interactions. Furthermore, more approaches should be discovered for the controllable, scaled-up, and cost-effective production of single-atom photocatalysts via eco-friendly routes. On the other hand, a variety of powerful *in situ* or *operando* characterization techniques, *in situ* transmission electron microscopy (TEM), *in situ* X-ray photoelectron spectroscopy (XPS), and *in situ* Raman spectroscopy, can be adopted to disclose the real-time morphologies, structures, compositions, and surface chemical states of photocatalysts as well as intermediate/product compositions and contents for important reaction processes. The above measurements and calculations can be further utilized to understand the true structure—activity relationship for these photocatalysts as well as the actual and precise reaction mechanisms. Moreover, an increasing advancement of computation methods permits better integration of experimental and computational approaches to elaborate the structure—activity correlation and/or reaction mechanisms for single-atom photocatalysts. Furthermore, it is of great significance to achieve a high-throughput screening of novel photocatalysts via theoretical computations, followed by experimental design and fabrication of these photocatalysts toward specific reactions. The acquired knowledge and achievements are anticipated to tremendously advance the widespread utilization of high-performance and brand-new single-atom photocatalysts in the near future.

■ AUTHOR INFORMATION

Corresponding Authors

Jingrun Ran — *School of Chemical Engineering & Advanced Materials, The University of Adelaide, Adelaide, SA 5005, Australia*; Email: jingrun.ran@adelaide.edu.au

Shi-Zhang Qiao — *School of Chemical Engineering & Advanced Materials, The University of Adelaide, Adelaide, SA 5005, Australia;* ⊙ orcid.org/0000-0002-4568-8422; Email: s.qiao@adelaide.edu.au

Authors

Bingquan Xia — *School of Chemical Engineering & Advanced Materials, The University of Adelaide, Adelaide, SA 5005, Australia*

Yanzhao Zhang — *School of Chemical Engineering & Advanced Materials, The University of Adelaide, Adelaide, SA 5005, Australia*

Mietek Jaroniec — *Department of Chemistry and Biochemistry & Advanced Materials and Liquid Crystal Institute, Kent State University, Kent, Ohio 44242, United States of America;* ⊙ orcid.org/0000-0002-1178-5611

Complete contact information is available at:

■ REFERENCES

(1) Reisner, E. When does organic photoredox catalysis meet artificial photosynthesis? *Angew. Chem., Int. Ed.* **2019**, *58*, 3656−3657.

(2) Ran, J.; Zhang, J.; Yu, J.; Jaroniec, M.; Qiao, S. Z. Earth-abundant cocatalysts for semiconductor-based photocatalytic water splitting. *Chem. Soc. Rev.* **2014**, *43*, 7787−7812.

(3) Brimioulle, R.; Lenhart, D.; Maturi, M. M.; Bach, T. Enantioselective catalysis of photochemical reactions. *Angew. Chem., Int. Ed.* **2015**, *54*, 3872−3890.

(4) Fang, X.; Kalathil, S.; Reisner, E. Semi-biological approaches to solar-to-chemical conversion. *Chem. Soc. Rev.* **2020**, *49*, 4926−4952.

(5) Nair, V.; Muñoz-Batista, M. J.; Fernández-García, M.; Luque, R.; Colmenares, J. C. Thermo-photocatalysis: Environmental and energy applications. *ChemSusChem* **2019**, *12*, 2098−2116.

(6) Nguyen, V.-H.; Nguyen, B.-S.; Jin, Z.; Shokouhimehr, M.; Jang, H. W.; Hu, C.; Singh, P.; Raizada, P.; Peng, W.; Shiung Lam, S.; Xia, C.; Nguyen, C. C.; Kim, S. Y.; Le, Q. V. Towards artificial photosynthesis: Sustainable hydrogen utilization for photocatalytic reduction of CO$_2$ to high-value renewable fuels. *Chem. Eng. J.* **2020**, *402*, 126184.

(7) Ran, J.; Zhu, B.; Qiao, S. Z. Phosphorene co-catalyst advancing highly efficient visible-light photocatalytic hydrogen production. *Angew. Chem., Int. Ed.* **2017**, *56*, 10373−10377.

(8) Akhundi, A.; Habibi-Yangjeh, A.; Abitorabi, M.; Rahim Pouran, S. Review on photocatalytic conversion of carbon dioxide to value-added compounds and renewable fuels by graphitic carbon nitride-based photocatalysts. *Catal. Rev.: Sci. Eng.* **2019**, *61*, 595−628.

(9) Rahman, M. Z.; Davey, K.; Qiao, S.-Z. Carbon, nitrogen and phosphorus containing metal-free photocatalysts for hydrogen production: Progress and challenges. *J. Mater. Chem. A* **2018**, *6*, 1305−1322.

(10) Jones, W.; Burnett, J. W. H.; Shi, J.; Howe, R. F.; Wang, X. Improving photocatalytic energy conversion via NAD(P)H. *Joule* **2020**, *4*, 2055−2059.

(11) Zhou, C.; Shi, R.; Waterhouse, G. I. N.; Zhang, T. Recent advances in niobium-based semiconductors for solar hydrogen production. *Coord. Chem. Rev.* **2020**, *419*, 213399.

(12) You, B.; Han, G.; Sun, Y. Electrocatalytic and photocatalytic hydrogen evolution integrated with organic oxidation. *Chem. Commun.* **2018**, *54*, 5943−5955.

(13) Xia, B.; Zhang, Y.; Shi, B.; Ran, J.; Davey, K.; Qiao, S. Z. Photocatalysts for hydrogen evolution coupled with production of value-added chemicals. *Small Methods* **2020**, *4*, 2000063.

(14) Wang, Q.; Warnan, J.; Rodríguez-Jiménez, S.; Leung, J. J.; Kalathil, S.; Andrei, V.; Domen, K.; Reisner, E. Molecularly engineered photocatalyst sheet for scalable solar formate production from carbon dioxide and water. *Nat. Energy* **2020**, *5*, 703−710.

(15) Wu, X.; Li, J.; Xie, S.; Duan, P.; Zhang, H.; Feng, J.; Zhang, Q.; Cheng, J.; Wang, Y. Selectivity control in photocatalytic valorization of biomass-derived platform compounds by surface engineering of titanium oxide. *Chem.* **2020**, *6*, 3038−3053.

(16) Dilla, M.; Moustakas, N. G.; Becerikli, A. E.; Peppel, T.; Springer, A.; Schlögl, R.; Strunk, J.; Ristig, S. Judging the feasibility of TiO$_2$ as photocatalyst for chemical energy conversion by quantitative reactivity determinants. *Phys. Chem. Chem. Phys.* **2019**, *21*, 13144−13150.

(17) Gao, Y.-J.; Li, X.-B.; Wang, X.-Z.; Zhao, N.-J.; Zhao, Y.; Wang, Y.; Xin, Z.-K.; Zhang, J.-P.; Zhang, T.; Tung, C.-H.; Wu, L.-Z. Site- and spatial-selective integration of non-noble metal ions into quantum dots for robust hydrogen photogeneration. *Matter* **2020**, *3*, 571−585.

(18) Zhao, Y.; Zhang, S.; Shi, R.; Waterhouse, G. I. N.; Tang, J.; Zhang, T. Two-dimensional photocatalyst design: A critical review of recent experimental and computational advances. *Mater. Today* **2020**, *34*, 78−91.

(19) Guayaquil-Sosa, J. F.; Serrano-Rosales, B.; Valadés-Pelayo, P. J.; de Lasa, H. Photocatalytic hydrogen production using mesoporous TiO$_2$ doped with Pt. *Appl. Catal., B* **2017**, *211*, 337−348.

(20) Kumaravel, V.; Mathew, S.; Bartlett, J.; Pillai, S. C. Photocatalytic hydrogen production using metal doped TiO$_2$: A review of recent advances. *Appl. Catal., B* **2019**, *244*, 1021−1064.

(21) Ganguly, P.; Harb, M.; Cao, Z.; Cavallo, L.; Breen, A.; Dervin, S.; Dionysiou, D. D.; Pillai, S. C. 2D nanomaterials for photocatalytic hydrogen production. *ACS Energy Lett.* **2019**, *4*, 1687−1709.

(22) Xia, B.; Ran, J.; Chen, S.; Song, L.; Zhang, X.; Jing, L.; Qiao, S.-Z. A two-dimensional metal-organic framework accelerating visible-light-driven H$_2$ production. *Nanoscale* **2019**, *11*, 8304−8309.

(23) Ran, J.; Qu, J.; Zhang, H.; Wen, T.; Wang, H.; Chen, S.; Song, L.; Zhang, X.; Jing, L.; Zheng, R.; Qiao, S.-Z. 2D metal organic framework nanosheet: A universal platform promoting highly efficient visible-light-induced hydrogen production. *Adv. Energy Mater.* **2019**, *9*, 1803402.

(24) Ran, J.; Wang, H.; Jin, H.; Ling, C.; Zhang, X.; Ju, H.; Jing, L.; Wang, J.; Zheng, R.; Qiao, S.-Z. Metallic MoN ultrathin nanosheets boosting high performance photocatalytic H$_2$ production. *J. Mater. Chem. A* **2018**, *6*, 23278−23282.

(25) Su, D. W.; Ran, J.; Zhuang, Z. W.; Chen, C.; Qiao, S. Z.; Li, Y. D.; Wang, G. X. Atomically dispersed Ni in cadmium-zinc sulfide quantum dots for high-performance visible-light photocatalytic hydrogen production. *Sci. Adv.* **2020**, *6*, No. eaaz8447.

(26) Ran, J.; Zhang, H.; Qu, J.; Xia, B.; Zhang, X.; Chen, S.; Song, L.; Jing, L.; Zheng, R.; Qiao, S.-Z. Atomically dispersed single Co sites in zeolitic imidazole frameworks promoting high-efficiency visible-light-driven hydrogen production. *Chem. - Eur. J.* **2019**, *25*, 9670−9677.

(27) Wang, L.; Xia, M.; Wang, H.; Huang, K.; Qian, C.; Maravelias, C. T.; Ozin, G. A. Greening ammonia toward the solar ammonia refinery. *Joule* **2018**, *2*, 1055−1074.

(28) Qiu, P.; Xu, C.; Zhou, N.; Chen, H.; Jiang, F. Metal-free black phosphorus nanosheets-decorated graphitic carbon nitride nanosheets with C-P bonds for excellent photocatalytic nitrogen fixation. *Appl. Catal., B* **2018**, *221*, 27−35.

(29) Zhao, Y.; Zhao, Y.; Shi, R.; Wang, B.; Waterhouse, G. I. N.; Wu, L. Z.; Tung, C. H.; Zhang, T. Tuning oxygen vacancies in ultrathin TiO$_2$ nanosheets to boost photocatalytic nitrogen fixation up to 700 nm. *Adv. Mater.* **2019**, *31*, No. e1806482.

(30) Zhao, Y.; Zheng, L.; Shi, R.; Zhang, S.; Bian, X.; Wu, F.; Cao, X.; Waterhouse, G. I. N.; Zhang, T. Alkali etching of layered double hydroxide nanosheets for enhanced photocatalytic N$_2$ reduction to NH$_3$. *Adv. Energy Mater.* **2020**, *10*, 2002199.

(31) Xu, F.; Meng, K.; Cheng, B.; Wang, S.; Xu, J.; Yu, J. Unique s-scheme heterojunctions in self-assembled TiO$_2$/C$_5$PbBr$_3$ hybrids for CO$_2$ photoreduction. *Nat. Commun.* **2020**, *11*, 4613.

(32) Wang, J.; Heil, T.; Zhu, B.; Tung, C.-W.; Yu, J.; Chen, H. M.; Antonietti, M.; Cao, S. A single Cu-center containing enzyme-mimic enabling full photosynthesis under CO$_2$ reduction. *ACS Nano* **2020**, *14*, 8584−8593.

(33) Jo, W.-K.; Moru, S.; Tonda, S. A green approach to the fabrication of a TiO$_2$/NiAl-LDH core-shell hybrid photocatalyst for efficient and selective solar-powered reduction of CO$_2$ into value-added fuels. *J. Mater. Chem. A* **2020**, *8*, 8020−8032.

(34) Gao, C.; Chen, S.; Wang, Y.; Wang, J.; Zheng, X.; Zhu, J.; Song, L.; Zhang, W.; Xiong, Y. Heterogeneous single-atom catalyst for visible-light-driven high-turnover CO$_2$ reduction: The role of electron transfer. *Adv. Mater.* **2018**, *30*, 1704624.

(35) Tang, J.-H.; Sun, Y. Visible-light-driven organic transformations integrated with H$_2$ production on semiconductors. *Mater. Adv.* **2020**, *1*, 2155−2162.

(36) Han, G.; Sun, Y. Visible-light-driven organic transformations on semiconductors. *Mater. Today Phys.* **2021**, *16*, 100297.

(37) Liu, Q.; Wu, L.-Z. Recent advances in visible-light-driven organic reactions. *Natl. Sci. Rev.* **2017**, *4*, 359−380.

(38) Chu, C.; Zhu, Q.; Pan, Z.; Gupta, S.; Huang, D.; Du, Y.; Weon, S.; Wu, Y.; Muhich, C.; Stavitski, E.; Domen, K.; Kim, J. H. Spatially separating redox centers on 2D carbon nitride with cobalt single atom for photocatalytic H$_2$O$_2$ production. *Proc. Natl. Acad. Sci. U. S. A.* **2020**, *117*, 6376−6382.

(39) Kim, H.-I.; Choi, Y.; Hu, S.; Choi, W.; Kim, J.-H. Photocatalytic hydrogen peroxide production by anthraquinone-augmented polymeric carbon nitride. *Appl. Catal., B* **2018**, *229*, 121−129.

(40) Zeng, X.; Liu, Y.; Kang, Y.; Li, Q.; Xia, Y.; Zhu, Y.; Hou, H.; Uddin, M. H.; Gengenbach, T. R.; Xia, D.; Sun, C.; McCarthy, D. T.; Deletic, A.; Yu, J.; Zhang, X. Simultaneously tuning charge separation and oxygen reduction pathway on graphitic carbon nitride by polyethylenimine for boosted photocatalytic hydrogen peroxide production. *ACS Catal.* **2020**, *10*, 3697−3706.

(41) Xiao, X.; Gao, Y.; Zhang, L.; Zhang, J.; Zhang, Q.; Li, Q.; Bao, H.; Zhou, J.; Miao, S.; Chen, N.; Wang, J.; Jiang, B.; Tian, C.; Fu, H. A promoted charge separation/transfer system from Cu single atoms and C$_3$N$_4$ layers for efficient photocatalysis. *Adv. Mater.* **2020**, *32*, 2003082.

(42) Zhou, P.; Chao, Y.; Lv, F.; Wang, K.; Zhang, W.; Zhou, J.; Chen, H.; Wang, L.; Li, Y.; Zhang, Q.; Gu, L.; Guo, S. Metal single atom strategy greatly boosts photocatalytic methyl activation and C-C coupling for the coproduction of high-value-added multicarbon compounds and hydrogen. *ACS Catal.* **2020**, *10*, 9109−9114.

(43) Gao, C.; Low, J.; Long, R.; Kong, T.; Zhu, J.; Xiong, Y. Heterogeneous single-atom photocatalysts: Fundamentals and applications. *Chem. Rev.* **2020**, *120*, 12175−12216.

(44) Zhao, Y.; Zhang, T. Dynamic changes of single-atom Pt- C$_3$N$_4$ photocatalysts. *Sci. Bull.* **2020**, *65*, 1055−1056.

(45) Yin, P.; Yao, T.; Wu, Y.; Zheng, L.; Lin, Y.; Liu, W.; Ju, H.; Zhu, J.; Hong, X.; Deng, Z.; Zhou, G.; Wei, S.; Li, Y. Single cobalt atoms with precise N-coordination as superior oxygen reduction reaction catalysts. *Angew. Chem., Int. Ed.* **2016**, *55*, 10800−10805.

(46) Jiao, L.; Jiang, H.-L. Metal-organic-framework-based single-atom catalysts for energy applications. *Chem.* **2019**, *5*, 786−804.

(47) Li, Y.; Li, B.; Zhang, D.; Cheng, L.; Xiang, Q. Crystalline carbon nitride supported copper single atoms for photocatalytic CO$_2$ reduction with nearly 100% co selectivity. *ACS Nano* **2020**, *14*, 10552−10561.

(48) Li, X.; Bi, W.; Zhang, L.; Tao, S.; Chu, W.; Zhang, Q.; Luo, Y.; Wu, C.; Xie, Y. Single-atom Pt as co-catalyst for enhanced photocatalytic H$_2$ evolution. *Adv. Mater.* **2016**, *28*, 2427−2431.

(49) Wang, J.; Li, Z.; Wu, Y.; Li, Y. Fabrication of single-atom catalysts with precise structure and high metal loading. *Adv. Mater.* **2018**, *30*, 1801649.

(50) Yang, Y.; Li, F.; Chen, J.; Fan, J.; Xiang, Q. Single Au atoms anchored on amino-group-enriched graphitic carbon nitride for photocatalytic CO$_2$ reduction. *ChemSusChem* **2020**, *13*, 1979−1985.

(51) Zhang, H.; Lu, X. F.; Wu, Z. P.; Lou, X. W. D. Emerging multifunctional single-atom catalysts/nanozymes. *ACS Cent. Sci.* **2020**, *6*, 1288−1301.

(52) Huang, H.; Shen, K.; Chen, F.; Li, Y. Metal-organic frameworks as a good platform for the fabrication of single-atom catalysts. *ACS Catal.* **2020**, *10*, 6579−6586.

(53) Wang, B.; Cai, H.; Shen, S. Single metal atom photocatalysis. *Small Methods* **2019**, *3*, 1800447.

(54) Wang, Q.; Zhang, D.; Chen, Y.; Fu, W.-F.; Lv, X.-J. Single-atom catalysts for photocatalytic reactions. *ACS Sustainable Chem. Eng.* **2019**, *7*, 6430−6443.

(55) Liu, L.; Corma, A. Metal catalysts for heterogeneous catalysis: From single atoms to nanoclusters and nanoparticles. *Chem. Rev.* **2018**, *118*, 4981−5079.

(56) Zeng, L.; Xue, C. Single metal atom decorated photocatalysts: Progress and challenges. *Nano Res.* 2020, DOI: 10.1007/s12274-020-3099-8.

(57) Liu, J.-C.; Tang, Y.; Wang, Y.-G.; Zhang, T.; Li, J. Theoretical understanding of the stability of single-atom catalysts. *Natl. Sci. Rev.* **2018**, *5*, 638−641.

(58) Li, J.; Guan, Q.; Wu, H.; Liu, W.; Lin, Y.; Sun, Z.; Ye, X.; Zheng, X.; Pan, H.; Zhu, J.; Chen, S.; Zhang, W.; Wei, S.; Lu, J. Highly active and stable metal single-atom catalysts achieved by strong electronic metal-support interactions. *J. Am. Chem. Soc.* **2019**, *141*, 14515−14519.

(59) Zhang, Y.; Xia, B.; Ran, J.; Davey, K.; Qiao, S. Z. Atomic-level reactive sites for semiconductor-based photocatalytic CO_2 reduction. *Adv. Energy Mater.* **2020**, *10*, 1903879.

(60) Zhang, L.; Long, R.; Zhang, Y.; Duan, D.; Xiong, Y.; Zhang, Y.; Bi, Y. Direct observation of dynamic bond evolution in single-atom Pt/C_3N_4 catalysts. *Angew. Chem., Int. Ed.* **2020**, *59*, 6224−6229.

(61) Gawande, M. B.; Fornasiero, P.; Zbořil, R. Carbon-based single-atom catalysts for advanced applications. *ACS Catal.* **2020**, *10*, 2231−2259.

(62) Fang, X.; Shang, Q.; Wang, Y.; Jiao, L.; Yao, T.; Li, Y.; Zhang, Q.; Luo, Y.; Jiang, H.-L. Single Pt atoms confined into a metal-organic framework for efficient photocatalysis. *Adv. Mater.* **2018**, *30*, 1705112.

(63) Yi, L.; Lan, F.; Li, J.; Zhao, C. Efficient noble-metal-free Co-NG/TiO_2 photocatalyst for H_2 evolution: Synergistic effect between single-atom Co and N-doped graphene for enhanced photocatalytic activity. *ACS Sustainable Chem. Eng.* **2018**, *6*, 12766−12775.

(64) Zeng, Z.; Su, Y.; Quan, X.; Choi, W.; Zhang, G.; Liu, N.; Kim, B.; Chen, S.; Yu, H.; Zhang, S. Single-atom platinum confined by the interlayer nanospace of carbon nitride for efficient photocatalytic hydrogen evolution. *Nano Energy* **2020**, *69*, 104409.

(65) Zhao, Q.; Yao, W.; Huang, C.; Wu, Q.; Xu, Q. Effective and durable Co single atomic cocatalysts for photocatalytic hydrogen production. *ACS Appl. Mater. Interfaces* **2017**, *9*, 42734−42741.

(66) Zhao, Q.; Sun, J.; Li, S.; Huang, C.; Yao, W.; Chen, W.; Zeng, T.; Wu, Q.; Xu, Q. Single nickel atoms anchored on nitrogen-doped graphene as a highly active cocatalyst for photocatalytic H_2 evolution. *ACS Catal.* **2018**, *8*, 11863−11874.

(67) Cao, Y.; Chen, S.; Luo, Q.; Yan, H.; Lin, Y.; Liu, W.; Cao, L.; Lu, J.; Yang, J.; Yao, T.; Wei, S. Atomic-level insight into optimizing the hydrogen evolution pathway over a Co_1-N_4 single-site photocatalyst. *Angew. Chem., Int. Ed.* **2017**, *56*, 12191−12196.

(68) Zhou, P.; Lv, F.; Li, N.; Zhang, Y.; Mu, Z.; Tang, Y.; Lai, J.; Chao, Y.; Luo, M.; Lin, F.; Zhou, J.; Su, D.; Guo, S. Strengthening reactive metal-support interaction to stabilize high-density Pt single atoms on electron-deficient g-C_3N_4 for boosting photocatalytic H_2 production. *Nano Energy* **2019**, *56*, 127−137.

(69) Lv, X.; Wei, W.; Li, F.; Huang, B.; Dai, Y. Metal-free B@g-CN: Visible/infrared light-driven single atom photocatalyst enables spontaneous dinitrogen reduction to ammonia. *Nano Lett.* **2019**, *19*, 6391−6399.

(70) Liu, S.; Wang, Y.; Wang, S.; You, M.; Hong, S.; Wu, T.-S.; Soo, Y.-L.; Zhao, Z.; Jiang, G.; Jieshan, Q.; Wang, B.; Sun, Z. Photocatalytic fixation of nitrogen to ammonia by single Ru atom decorated TiO_2 nanosheets. *ACS Sustainable Chem. Eng.* **2019**, *7*, 6813−6820.

(71) Zhang, W.; Peng, Q.; Shi, L.; Yao, Q.; Wang, X.; Yu, A.; Chen, Z.; Fu, Y. Merging single-atom-dispersed iron and graphitic carbon nitride to a joint electronic system for high-efficiency photocatalytic hydrogen evolution. *Small* **2019**, *15*, 1905166.

(72) Li, J.; Liu, P.; Tang, Y.; Huang, H.; Cui, H.; Mei, D.; Zhong, C. Single-atom Pt-N_3 sites on the stable covalent triazine framework nanosheets for photocatalytic N_2 fixation. *ACS Catal.* **2020**, *10*, 2431−2442.

(73) Guo, X. W.; Chen, S. M.; Wang, H. J.; Zhang, Z. M.; Lin, H.; Song, L.; Lu, T. B. Single-atom molybdenum immobilized on photoactive carbon nitride as efficient photocatalysts for ambient nitrogen fixation in pure water. *J. Mater. Chem. A* **2019**, *7*, 19831−19837.

(74) Yang, H.; Liu, Y.; Luo, Y.; Lu, S.; Su, B.; Ma, J. Achieving high activity and selectivity of nitrogen reduction via Fe-N_3 coordination on iron single-atom electrocatalysts at ambient conditions. *ACS Sustainable Chem. Eng.* **2020**, *8*, 12809−12816.

(75) Zhang, H.; Wei, J.; Dong, J.; Liu, G.; Shi, L.; An, P.; Zhao, G.; Kong, J.; Wang, X.; Meng, X.; Zhang, J.; Ye, J. Efficient visible-light-driven carbon dioxide reduction by a single-atom implanted metal-organic framework. *Angew. Chem., Int. Ed.* **2016**, *55*, 14310−14314.

(76) Zheng, Y.-W.; Chen, B.; Ye, P.; Feng, K.; Wang, W.; Meng, Q.-Y.; Wu, L.-Z.; Tung, C.-H. Photocatalytic hydrogen-evolution cross-couplings: Benzene C-H amination and hydroxylation. *J. Am. Chem. Soc.* **2016**, *138*, 10080−10083.

(77) Zhang, N.; Li, X.; Ye, H.; Chen, S.; Ju, H.; Liu, D.; Lin, Y.; Ye, W.; Wang, C.; Xu, Q.; Zhu, J.; Song, L.; Jiang, J.; Xiong, Y. Oxide defect engineering enables to couple solar energy into oxygen activation. *J. Am. Chem. Soc.* **2016**, *138*, 8928−8935.

(78) Zhou, L.; Martirez, J. M. P.; Finzel, J.; Zhang, C.; Swearer, D. F.; Tian, S.; Robatjazi, H.; Lou, M.; Dong, L.; Henderson, L.; Christopher, P.; Carter, E. A.; Nordlander, P.; Halas, N. J. Light-driven methane dry reforming with single atomic site antenna-reactor plasmonic photocatalysts. *Nat. Energy* **2020**, *5*, 61−70.

(79) Wen, J.; Yang, X.; Sun, Z.; Yang, J.; Han, P.; Liu, Q.; Dong, H.; Gu, M.; Huang, L.; Wang, H. Biomimetic photocatalytic sulfonation of alkenes to access β-ketosulfones with single-atom iron site. *Green Chem.* **2020**, *22*, 230−237.

(80) He, T.; Zhang, C.; Zhang, L.; Du, A. Single Pt atom decorated graphitic carbon nitride as an efficient photocatalyst for the hydrogenation of nitrobenzene into aniline. *Nano Res.* **2019**, *12*, 1817−1823.

(81) Chu, C.; Huang, D.; Zhu, Q.; Stavitski, E.; Spies, J. A.; Pan, Z.; Mao, J.; Xin, H. L.; Schmuttenmaer, C. A.; Hu, S.; Kim, J.-H. Electronic tuning of metal nanoparticles for highly efficient photocatalytic hydrogen peroxide production. *ACS Catal.* **2019**, *9*, 626−631.

(82) Lu, Y.; Huang, Y.; Zhang, Y.; Cao, J.-j.; Li, H.; Bian, C.; Lee, S. C. Oxygen vacancy engineering of Bi_2O_3/$Bi_2O_2CO_3$ heterojunctions: Implications of the interfacial charge transfer, no adsorption and removal. *Appl. Catal., B* **2018**, *231*, 357−367.

(83) Hu, S.; Qu, X.; Li, P.; Wang, F.; Li, Q.; Song, L.; Zhao, Y.; Kang, X. Photocatalytic oxygen reduction to hydrogen peroxide over copper doped graphitic carbon nitride hollow microsphere: The effect of Cu(I)-N active sites. *Chem. Eng. J.* **2018**, *334*, 410−418.

(84) Romero, N. A.; Margrey, K. A.; Tay, N. E.; Nicewicz, D. A. Site-selective arene C-H amination via photoredox catalysis. *Science* **2015**, *349*, 1326−1330.

(85) Chu, X.; Qu, Y.; Zada, A.; Bai, L.; Li, Z.; Yang, F.; Zhao, L.; Zhang, G.; Sun, X.; Yang, Z. D.; Jing, L. Ultrathin phosphate-modulated Co phthalocyanine/g-C_3N_4 heterojunction photocatalysts with single Co-N_4(II) sites for efficient O_2 activation. *Adv. Sci.* **2020**, *7*, 2001543.

(86) Shiraishi, Y.; Takeda, Y.; Sugano, Y.; Ichikawa, S.; Tanaka, S.; Hirai, T. Highly efficient photocatalytic dehalogenation of organic halides on TiO_2 loaded with bimetallic Pd-Pt alloy nanoparticles. *Chem. Commun.* **2011**, *47*, 7863−7865.

(87) McTiernan, C. D.; Pitre, S. P.; Scaiano, J. C. Photocatalytic dehalogenation of vicinal dibromo compounds utilizing sexithiophene and visible-light irradiation. *ACS Catal.* **2014**, *4*, 4034−4039.

(88) Wu, W.; Cui, E.; Zhang, Y.; Zhang, C.; Zhu, F.; Tung, C.-H.; Wang, Y. Involving single-atom silver(0) in selective dehalogenation by AgF under visible-light irradiation. *ACS Catal.* **2019**, *9*, 6335−6341.

(89) Niwa Si, S.; Eswaramoorthy, M.; Nair, J.; Raj, A.; Itoh, N.; Shoji, H.; Namba, T.; Mizukami, F. A one-step conversion of benzene to phenol with a palladium membrane. *Science* **2002**, *295*, 105−107.

(90) Chen, X.; Zhang, J.; Fu, X.; Antonietti, M.; Wang, X. Fe-g-C_3N_4-catalyzed oxidation of benzene to phenol using hydrogen peroxide and visible light. *J. Am. Chem. Soc.* **2009**, *131*, 11658−11659.

(91) Grirrane, A.; Corma, A.; Garcia, H. Highly active and selective gold catalysts for the aerobic oxidative condensation of benzylamines

to imines and one-pot, two-step synthesis of secondary benzylamines. *J. Catal.* **2009**, *264*, 138−144.

(92) Kumar, R.; Gleißner, E. H.; Tiu, E. G. V.; Yamakoshi, Y. C₇₀ as a photocatalyst for oxidation of secondary benzylamines to imines. *Org. Lett.* **2016**, *18*, 184−187.

(93) Wang, Q.; Li, J.; Tu, X.; Liu, H.; Shu, M.; Si, R.; Ferguson, C. T. J. J.; Zhang, K. A. I. I.; Li, R. Single atomically anchored cobalt on carbon quantum dots as efficient photocatalysts for visible light-promoted oxidation reactions. *Chem. Mater.* **2020**, *32*, 734−743.

(94) Zhou, P.; Zhang, Q.; Xu, Z.; Shang, Q.; Wang, L.; Chao, Y.; Li, Y.; Chen, H.; Lv, F.; Zhang, Q.; Gu, L.; Guo, S. Atomically dispersed Co-P₃ on CdS nanorods with electron-rich feature boosts photocatalysis. *Adv. Mater.* **2020**, *32*, 1904249.

(95) Akri, M.; Zhao, S.; Li, X.; Zang, K.; Lee, A. F.; Isaacs, M. A.; Xi, W.; Gangarajula, Y.; Luo, J.; Ren, Y.; Cui, Y.-T.; Li, L.; Su, Y.; Pan, X.; Wen, W.; Pan, Y.; Wilson, K.; Li, L.; Qiao, B.; Ishii, H.; Liao, Y.-F.; Wang, A.; Wang, X.; Zhang, T. Atomically dispersed nickel as coke-resistant active sites for methane dry reforming. *Nat. Commun.* **2019**, *10*, 5181.

(96) Ren, D.; Song, Z.; Li, L.; Liu, Y.; Jin, F.; Huo, Z. Production of 2,5-hexanedione and 3-methyl-2-cyclopenten-1-one from 5-hydroxymethylfurfural. *Green Chem.* **2016**, *18*, 3075−3081.

(97) Ni, C.; Zhang, L.; Hu, J. Synthesis of fluorinated *β*-ketosulfones and gem-disulfones by nucleophilic fluoroalkylation of esters and sulfinates with di- and monofluoromethyl sulfones. *J. Org. Chem.* **2009**, *74*, 3767−3771.

(98) Chen, J.; Allyson, Z. G.; Xin, J. R.; Guan, Z.; He, Y. H. Photo-mediated decarboxylative ketonization of atropic acids with sulfonyl hydrazides: Direct access to *β*-ketosulfones. *Adv. Synth. Catal.* **2020**, *362*, 2045−2051.

Chapter 7: Conclusion and Perspective

7.1 Conclusions

This thesis is focused on the design, synthesis, and application of novel nanomaterials for solar-driven production of valuable chemicals and the mechanism study of these photocatalysis processes. Based on the works in this thesis, conclusions can be drawn as follow:

1. Two-dimensional nanomaterials, including transition metal-based metal-organic frameworks and metal phosphorus trisulfide, which possess ultrathin layered structures, could be utilised as an excellent platform for improving photocatalytic performances toward hydrogen production. The 2D Co-MOF, Ni-MOF and FePS$_3$ play key roles in improving the photocatalytic activity of the main photocatalyst by providing sufficient reactive sites and facilitating charge separation and transfer. Since the light-harvesting ability and band structure of these nanomaterials vary, probing into the origin of the structure-performance relationship and finding out a universal strategy for designing and screening outstanding high-performance photocatalysts are of great importance for research on solar-to-hydrogen transformation.

2. Considering most research focused on using the photo-induced electrons to realize the solar-driven hydrogen evolution, the drawback is that the simultaneously formed photoexcited holes have been neglected. It is significant to utilise the photogenerated holes to react with abundantly available hole scavengers, such as biomass, biomass-derived intermediates and plastic wastes, to produce value-added chemical products. It is worthwhile developing high-performance photocatalyst for realising the simultaneous production of hydrogen and valuable chemical products.

3. Thanks to the abundant reactive sites and adjustable coordination environments, novel singe-atom-based photocatalysts exhibit excellent performance for various solar-driven reactions. The combination of fabricating single-atom photocatalysts and adapting for emerging reactions, together with exploring the origin of performance-structure relationships of excellent photocatalysts will significantly broaden the boundary of solar-driven applications.

7.2 Perspectives

Photocatalysis on energy conversion and storage is a complicated process, involving optical, electrical, and chemical processes. To sustain the development of solar energy transition for renewable energy supply, more efforts need to be made to the development of high-performance photocatalysts to overcome the challenging obstacles, such as low quantum yield, poor selectivity toward target products, and low conversion efficiency. To this end, theoretical calculations and advanced characterization techniques are useful for the comprehensive understanding of the solar-driven reactions of energy transformation. Probing the mechanism of the solar-driven conversion is to better understand the origin of the structure-performance relationship of the photocatalysts for hydrogen production and is expected to be extended to the other photocatalytic reactions. Ideally, the massive computation could also be employed to guide the design and synthesis of photocatalysts for reactions producing specific products, not just hydrogen, but also value-added chemicals. The combination of searching for high-performance photocatalysts and improving solar-driven reaction efficiency will be of great benefit to the development of solar energy conversion for achieving the aim of carbon neutrality. Hopefully, affordable, stable and durable photocatalysts will be developed and utilized for practical scaled-up production of valuable chemical products in the near future.

Appendix: Publications during the PhD candidature

(1) Bingquan Xia; Bowen He; Jianjun Zhang; Laiquan Li; Yanzhao Zhang; Jiaguo Yu; Jingrun Ran; Shi-Zhang Qiao. $TiO_2/FePS_3$ S-scheme heterojunction for greatly raised photocatalytic hydrogen evolution, *Adv. Energy Mater.* **2022,** submitted.

(2) Bingquan Xia; Yi Yang; Yanzhao Zhang; Yang Xia; Mietek Jaroniec; Jiaguo Yu; Jingrun Ran; Shi-Zhang Qiao. Metal–organic framework with atomically dispersed $Ni–N_4$ sites for greatly-raised visible-light photocatalytic H_2 production. *Chem. Eng. J.* **2022**, 431, 133944.

(3) Bingquan Xia; Yanzhao Zhang; Jingrun Ran; Mietek Jaroniec; Shi-Zhang Qiao. Single-atom photocatalysts for emerging reactions. *ACS Cent. Sci.* **2021**, 7, 39-54.

(4) Bingquan Xia; Yanzhao Zhang; Bingyang Shi; Jingrun Ran; Kenneth Davey; Shi-Zhang Qiao. Photocatalysts for hydrogen evolution coupled with production of value‐added chemicals. *Small Methods* **2020**, 4, 2000063.

(5) Bingquan Xia; Jingrun Ran; Shuangming Chen; Li Song; Xuliang Zhang; Liqiang Jing; Shi-Zhang Qiao. A two-dimensional metal–organic framework accelerating visible-light-driven H_2 production. *Nanoscale* **2019**, 11, 8304-8309.

(6) Yanzhao Zhang; Dazhi Yao; Bingquan Xia; Haolan Xu; Youhong Tang; Kenneth Davey; Jingrun Ran; Shi-Zhang Qiao. Res2 nanosheets with in situ formed sulfur vacancies for efficient and highly selective photocatalytic CO_2 reduction. *Small Sci.* **2021**, 1, 2000052.

(7) Laiquan Li; Cheng Tang; Yao Zheng; Bingquan Xia; Xianlong Zhou; Haolan Xu; Shi-Zhang Qiao. Tailoring selectivity of electrochemical hydrogen peroxide generation by tunable pyrrolic‐nitrogen‐carbon. *Adv. Energy Mater.* **2020**, 10, 2000789.

(8)   Yanzhao Zhang; <u>Bingquan Xia</u>; Jingrun Ran; Kenneth Davey; Shi Zhang Qiao. Atomic-level reactive sites for semiconductor‐based photocatalytic CO_2 reduction. *Adv. Energy Mater.* **2020**, 10, 1903879.

(9)   Dazhi Yao; Cheng Tang; Laiquan Li; <u>Bingquan Xia</u>; Anthony Vasileff; Huanyu Jin; Yanzhao Zhang; Shi‐Zhang Qiao. In situ fragmented bismuth nanoparticles for electrocatalytic nitrogen reduction. *Adv. Energy Mater.* **2020**, 10, 2001289.

(10)   Laiquan Li; Cheng Tang; <u>Bingquan Xia</u>; Huanyu Jin; Yao Zheng; Shi-Zhang Qiao. Two-dimensional mosaic bismuth nanosheets for highly selective ambient electrocatalytic nitrogen reduction. *ACS Catal.* **2019**, 9, 2902-2908.

(11)   Jingrun Ran; Hongping Zhang; Jiangtao Qu; <u>Bingquan Xia</u>; Xuliang Zhang; Shuangming Chen; Li Song; Liqiang Jing; Rongkun Zheng; Shi-Zhang Qiao. Atomically dispersed single Co sites in zeolitic imidazole frameworks promoting high‐efficiency visible‐light‐driven hydrogen production. *Chem. Eur. J.* **2019**, 25, 9670-9677.